Rete di Idee

Rete di Idee 2025

XIII EDIZIONE

Atti del Convegno
21-23 novembre 2025

RETE DI IDEE 2025

XIII EDIZIONE

ATTI DEL CONVEGNO

Catania, 21-23 novembre 2025

a cura di Marco Fausto Anfuso e Bruno D'Arrigo

Indice

Classe di Scienze Sociali

Classe di Scienze Umane

Classe di Scienze e Tecnologia

Classe di Scienze della Vita

Prefazione

Rete di Idee è un progetto nato nel 2012 da un'esigenza collettiva di confronto e di scambio, coordinato annualmente dalla Rete Italiana dellɜ Allievɜ delle Scuole e degli Istituti di Studi Superiori Universitari (RIASISSU). È infatti l'esperimento di alcune e alcuni giovani studiosi provenienti da Scuole Superiori universitarie diffuse in tutta Italia, mossi dall'aspirazione di riunire i propri saperi e le proprie esperienze di ricerca, così ponendoli al servizio gli uni degli altri. La Rete e le Scuole hanno infatti la finalità precipua di promuovere la cultura e la ricerca accademica integrando metodi e conoscenze da diverse discipline per affrontare le complesse questioni del contemporaneo. Il tutto all'interno di un modello di comunità accademica **integrata**, animato da un contesto collegiale e residenziale vivo e pulsante, che diventa bacino spontaneo di una commistione di saperi. L'interdisciplinarità è il cuore della missione educativa delle scuole, quale principio in grado di esplorare e cogliere le **interrelazioni** e le **interazioni** tra discipline, approcci scientifici e metodologici.

È tuttavia necessario che questo quadro sin qui delineato si innesti all'interno di una cornice ben più grande: i grandi problemi della nostra epoca (la tutela ambientale e le sfide climatiche; le disuguaglianze; la disoccupazione e la precarietà; gli scenari di conflitto) riportano oggi in prima linea la riflessione sull'adozione di un approccio interdisciplinare. Si tratta di fenomeni complessi e stratificati, che rifuggono un'indagine di studio aridamente lineare e parziale. Per queste ragioni, sviluppare un orizzonte culturale all'insegna dell'interdisciplinarietà costituisce una sfida e un dovere sociale nei confronti di un modello che incentiva la *competizione* individuale: un rinnovato modello solidaristico di *comprensione* e *cooperazione*. E proprio verso questa prospettiva – cui deve muoversi oggi la ricerca accademico-scientifica – le Scuole Superiori e la Riasissu costituiscono una "buona pratica" nel panorama accademico italiano.

Rete di Idee permette di cogliere appieno il nucleo essenziale di questo approccio interdisciplinare e dialogico: si tratta infatti di un concorso – organizzato a cadenza annuale – aperto a tutti gli allievi e le allieve delle Scuole aderenti alla Rete. Come da bando, ogni partecipante può presentare un proprio elaborato scientifico inedito, indipendentemente dal proprio

percorso di studi: così, abbattendo le barriere di un approccio accademico isolato e settoriale, è sviluppata una trattazione libera, flessibile e capace di coniugare linguaggi diversi (giuridico, economico, umanistico, tecnologico). Gli elaborati sono presentati in una delle quattro diverse classi di concorso (Scienze Sociali; Scienze e Tecnologia; Scienze Umane e Scienze della Vita) e sottoposti ad una fase di *peer review*. La valutazione è svolta interamente da soci della Rete in due commissioni indipendenti, in modo tale che l'autore e il revisore non conoscano l'identità l'uno dell'altro e che non vi sia coincidenza tra le istituzioni di appartenenza degli stessi. Sulla base delle revisioni operate dalle due diverse commissioni – mediate tra loro – per ogni elaborato viene attribuito un punteggio ed è conseguentemente stilata una graduatoria tra gli articoli con punteggio più alto per ogni classe.

Si riportano di seguito gli elaborati vincitori per l'edizione 2025, tenutasi presso Villa San Saverio, sede della Scuola superiore di **Catania**, in data **23-25 novembre 2025**.

Classe di Scienze Sociali

Sequencing or Gradualism? Democratization Trajectories in the Post-Conflict Contexts of Rwanda and Bosnia and Herzegovina

Veronica Viero

Abstract

This paper analyzes the impact that different post-conflict democratization strategies have on long-term democratic trajectories, focusing on the conflicting objectives of democratization and peacebuilding. This exploratory research, which relies on a qualitative approach, applies the method of comparative process tracing to the cases of Bosnia and Herzegovina and Rwanda. Rwanda exemplifies the sequencing strategy, prioritizing stability and state-building before democratization, while Bosnia is an example of gradualist strategy, pursuing peace and democracy simultaneously. The most-different systems design allows the testing of contrasting approaches in comparable post-conflict contexts.

By combining qualitative analysis with empirical evidence from V-Dem indices (electoral democracy, clean elections, participatory democracy, rule of law), the paper shows the nonlinear relationship between peace, elections, and democratic consolidation. Findings reveal that Bosnia's premature elections, driven by external actors, exacerbated ethnic divisions and entrenched nationalist elites, resulting in a fragile democracy. Conversely, Rwanda's delayed liberalization ensured governance stability but entrenched an authoritarian regime, limiting political pluralism.

By offering a diachronic comparison and tracing how key events such as peace agreements, elections and international interventions shaped institutional outcomes, this work contributes new evidence to debates on post-conflict democratization. The results underscore the importance of context-sensitive approaches to achieve sustainable democratic outcomes in post-conflict settings, challenging the assumption that early elections automatically foster robust democracy.

Keywords: post-conflict democratization, gradualism, sequencing, electoral timing, conflicting objectives.

I. INTRODUCTION ON DEMOCRATIZATION AND PEACEBUILDING: THE ISSUE OF CONFLICTING OBJECTIVES

Drawing from Dahl's minimal definition, democracy can be understood as a political system in which representatives are periodically chosen through free and fair elections, and political actors engage in peaceful public competition for voter support. This system must also be underpinned by a sufficient degree of civil and political rights to ensure meaningful participation and contestation[1]. Democratization, then, refers to the process of moving towards a closer representation of this concept, involving a transition towards greater adherence to democratic principles[2].

For defining peace, we adopt Galtung's concept of *negative peace*, which he defines as the absence of both direct and structural violence[3]. Peacebuilding, as conceptualized by BoutrosGhali[4], involves post-conflict activities aimed at identifying and supporting structures that can consolidate this state of peace and prevent a relapse into conflict.

While democracy and peace are often portrayed as complementary, their relationship can become complicated during periods of democratization. Democratic systems are generally valued for providing peaceful, transparent, and inclusive mechanisms for the transfer and distribution of power[5]. Moreover, the *Democratic Peace Theory* suggests that democratic states are less likely to go to war with one another, due to both structural and normative motivations. Consequently, regions with a high density of democratic states experience a lower incidence of inter-state war. This explains why support for democratization has been central in international peacebuilding efforts since 1990. However, even if it is true that peace is a feature of democratic regimes, it appears only in consolidated democracies, while the delicate state of transition towards democracy contains considerable destabilizing potential[6]. Therefore, we can affirm

---

[1] DAHL R. A., *Polyarchy: Participation and Opposition*, Yale University Press, London, 1971.
[2] J. GALTUNG, "Violence, Peace, and Peace Research", in *Journal of Peace Research*, 6(3), 1969, pp. 167-191.
[3] BOUTROS-GHALI B., *An agenda for peace: Preventive diplomacy, peacemaking and peace-keeping (A/47/277 - S/24111)*, United Nations, 1992.
[4] *Ibidem.*
[5] MROSS K., "First peace, then democracy? Evaluating strategies of international support at critical junctures after civil war", in *International Peacekeeping*, 26(2), 2018, pp. 190-215.
[6] MANSFIELD E. D., SNYDER J., "Pathways to war in democratic transitions", in *International Organization*, 63(2), 2009, pp. 381-390.

that the *Democratic Peace Theory* cannot be used to predict or understand the behaviour of states undergoing the complex process of post-conflict democratization[7].

The process of democratization itself, particularly in post-conflict environments, can create tensions between the goals of democracy and peace, and this is the reason why we talk about *conflicting objectives.*

We define conflicting objectives as the clash of two competing goals, whereby the achievement of one goal is impaired by the achievement of the other goal[8]. Following the distinction theorized by Spanger and Wolff we can distinguish between intrinsic and extrinsic conflicting objectives: the first emerge when different elements of democracy promotion clash, while the second emerge when the goal of democracy promotion interferes with other objectives of foreign policy[9]. According to this distinction, we classify democratization and peacebuilding as extrinsic conflicting objectives.

As a matter of fact, transitioning from a post-war authoritarian regime to a democratic system often involves significant social, political, and institutional upheaval. During this process, the pursuit of democracy (e.g., fostering open contestation and participation) may at times conflict with the immediate need to maintain stability and prevent the re-emergence of violence.

Elections, for example, are the core element of a democracy and are also central to peace process, establishing a peaceful and legitimate post-war order. Yet, electoral competition could emphasize differences, reinforcing existing cleavages that are particularly delicate in a country that is still involved in reconciliation process among its parts after a war[10]. In fact, despite their essential role, post-war elections have often sharpened these tensions, deviating from the objective of peace[11].

What has been described so far raises a question about the ways of dealing with these objectives. To achieve a more robust and consolidated democracy in the medium and long term, should both democracy and peace be pursued simultaneously, despite the risk that democratic elections might undermine stability? Or should the establishment of democracy be postponed

---

[7] BERBERICH A., "Post-Conflict Democratization: Rwanda's Illiberal Democracy", in *Proceedings of GREAT Day*, 2010(1), 2011.

[8] GRIMM S., LEININGER J., "Not all good things go together: conflicting objectives in democracy promotion", in *Conflicting Objectives in Democracy Promotion*, Routledge, 2017, pp. 3-26.

[9] WOLFF J., SPANGER H. J., "Democracy promoters' conflicting objectives: The research agenda", in *The Comparative International Politics of Democracy Promotion*, Routledge, 2013, pp. 3-36.

[10] MROSS K., *First peace, then democracy*, cit

[11] BERBERICH A., *Post-Conflict Democratization*, cit.

until full peace is achieved, acknowledging the challenges of sustaining peace in the absence of democratic governance?

To deal with the issue of these two specific conflicting objectives, scholars have suggested over time different approaches, exemplified in the theories of *sequencing* and *gradualism.*

II. ANALYSIS OF THE LITERATURE ON SEQUENCING AND GRADUALISM

Sequencing was first made popular by Fareed Zakaria[12], Edward Mansfield and Jack Snyder[13]. These scholars agree on the importance of prioritizing a strategy focused on preventing the recurrence of violence, therefore they argue for postponing national elections with universal suffrage until the rule of law and a well-functioning state capable of ensuring peace are firmly established. According to this approach, external actors should be primarily concerned with providing a stable environment to avoid post-conflict struggles that could be stressed by the democratic competition[14]. Establishing a well-functioning state with capable institutions and a solid capacity to develop and implement effective policies represents a necessary precondition which appears to be essential in a perspective of a prudent approach to democracy promotion[15].

In contrast, *gradualism* aims at simultaneously pursuing peacebuilding and democratization in post-conflict societies, without prioritizing peace over democracy[16]. This perspective critiques the most contentious aspect of sequencing theory, which is the expectation that authoritarianism should lay the groundwork for democracy after achieving peace. Autocrats are, in fact, unable to engage in the second phase of state-building, which is the development of an effective state bureaucracy that can carry out the many functions of a modern state[17]. Indeed, Carothers argues that sequentialism would be used by external actors as a façade in

---

[12] ZAKARIA F., "The Rise of Illiberal Democracy", in *Foreign Affairs*, 76(6), 1997, pp. 22-43.
[13] MANSFIELD E. D., SNYDER J., *Electing to fight: Why emerging democracies go to war*, Cambridge, MIT Press, 2007.
[14] MROSS K., *First peace, then democracy*, cit
[15] MANSFIELD E. D., SNYDER J., "Exchange: The Sequencing 'Fallacy'", in *Journal of Democracy*, 18(3), 2007, pp. 5-9.
[16] CAROTHERS T., "How democracies emerge: The 'sequencing' fallacy", in *Journal of Democracy*, 18(1), 2007, pp. 12-27.
[17] MIGDAL J. S., "State building and the non-nation-state", in *Journal of International Affairs*, 2004, pp. 17-46.

order to maintain friendly relations with autocratic governments, under the guise of fostering long-term democratization. Theorists of gradualism also highlight that having experience with political pluralism, even if flawed or conflictual, helps the country to build a democratic awareness, useful for the future[18].

Comparing sequencing and gradualism, we can affirm that the latter seems to embody a more optimistic viewpoint on the democratization process, while sequencing theorists describe the democratization process as intrinsically violent and potentially explosive. However, sequencing theorists are comparatively more optimistic about the ability of autocratic regimes to implement reforms aimed at fostering the rule of law and creating conditions for competitive free elections. One basic criticism of this theory is that sequencing seems to depend on «benevolent dictators who use their power to focus on national development rather than personal gain»[19]. Mansfield and Snyder[20] respond to this criticism by saying that of course dictators are not the actors that will implement well-sequenced reforms leading to a democracy. This role, indeed, has to be played by moderate groups that seek to curtail the power of the authoritarian elite, as it happened, for example, in South Africa.

The debate on which is the best strategy remains open; however, both theories assume that the existence of elections represents the ultimate emblem of democratic achievement. This has led to the belief among policymakers that the presence of elections marks the successful completion of the democracy-promotion process[21]. However, evidence shows that elections can be strategically manipulated, since this strategical manipulation of elections represents one of the new subtle strategies used to lead a country toward democratic backsliding without publicly tarnishing its global image or evading electoral monitoring[22]. Based on the above, the presence of elections alone does not determine a country's level of democracy. Elections must, in fact, be *free and fair*, a concept that is difficult to define and measure, as it involves subjective judgments. Databases such as V-Dem and Polity IV rely on expert coding, which is nonetheless prone to biases stemming from improved communication technologies, motivated beliefs, and media or academic coverage of the issue[23].

---

[18] *Ibidem.*
[19] FUKUYAMA F., "Is there a proper sequence in democratic transitions?", in *Current History*, 110(739), 2011, p. 309.
[20] MANSFIELD E. D., SNYDER J., *Exchange: The Sequencing*, cit.
[21] BERBERICH A., *Post-Conflict Democratization*, cit.
[22] BERMEO N., "On democratic backsliding", in *Journal of Democracy*, 27(1), 2016, pp. 5-19.
[23] LITTLE A. T., MENG A., "Measuring democratic backsliding", in *PS: Political Science & Politics*, 2023, pp.

Aware of the limitations and potential fallibility of these subjective indicators, which generally tend to overestimate the level of democratic backsliding, we nonetheless consider them to be a fundamental measure for assessing the democratic quality of a country. Observing the trends of these indicators can thus provide interesting insights into the impacts that the two different strategies, sequencing and gradualism, have had on the democratic state of a country previously affected by conflict, in the medium and long term.

III. STUDY CASE SELECTION

To investigate the divergent impacts of sequencing and gradualism in post-conflict democratization, this study adopts a comparative case study design focusing on Rwanda and Bosnia and Herzegovina. The selection of these two cases follows a most-different systems logic with similar post-conflict conditions, allowing for a meaningful comparison of contrasting strategies in comparable contexts of severe internal conflict during the 1990s.

Both countries experienced severe ethnic violence during their conflicts, making them emblematic cases for post-conflict democratization studies: Rwanda experienced an internal war that led to the genocide of the Tutsi, while Bosnia underwent an interethnic war among Bosniaks, Croats, and Serbs, culminating in the Srebrenica genocide. In the aftermath of these atrocities, both nations faced immense challenges in rebuilding their political and social structures. These shared characteristics establish a common ground for exploring how the chosen democratization strategies influenced their trajectories towards democracy and assessing their medium and long-term impacts on the quality of democracy.

Bosnia-Herzegovina represents a paradigmatic case of gradualist approach, where democratization and peacebuilding have been pursued simultaneously. Rwanda, conversely, is an example of sequencing, where stability was prioritized over democratization, with peace and state-building preceding efforts aimed at achieving political pluralism.

Although Bosnia and Rwanda represent relatively similar cases of internal conflict, the two countries differ significantly in terms of culture, economy, and especially for the different roles that external actors played in each case. Acknowledging these caveats, which prevent a full

1-13.

isolation of the impact that gradualism and sequencing strategies had on subsequent democratic outcomes, it is important to note that the current state of democracy in these countries is also shaped by factors not considered here. In general, determining the specific factors that contributed to a higher quality of democracy is challenging due to the *attribution gap* caused by the interplay of different situations and instruments involved[24].

Despite these limitations, an exploratory comparison remains valuable. Examining the divergent paths these nations followed after their respective wars and analysing their current democratic conditions can yield insightful perspectives. The choice between these strategies, while insufficient to fully encompass the complexity of factors that have determined democratic success or failure, nonetheless serves as a crucial element of the puzzle, offering a more comprehensive understanding of the broader picture.

The following sections will separately analyze each country, focusing on the steps that led to peacebuilding and democratization.

3.1. Gradualism in Bosnia and Herzegovina

The Bosnian War arose from deep ethnic tensions that intensified after the collapse of Yugoslavia and lasted five years (1992-1995). The declaration of independence by Bosnia and Herzegovina sparked conflict among its three main ethic groups: Bosniaks (Muslims), Croats and Serbs. In mid-1995, the Muslim inhabitants of the Bosnian town of Srebrenica became the victims of one of the worst massacres in Europe since the Second World War. The international community played a crucial role in the Bosnian War, with the United Nations imposing sanctions, delivering humanitarian aid, and establishing safe zones, though often criticized for its limited effectiveness.

The strategy of gradualism in the Bosnian case can be identified through the analysis of the official documents that brought the war to an end. In the Resolution 1031 (1995) adopted by the Security Council we can find a broader understanding of peacebuilding, which incorporates the need for democratic elections: «The Security Council welcomes the agreement by the

[24] CARAMANI D. (a cura di), *Comparative Politics*, Oxford, Oxford University Press, 2023.

Organization for Security and Cooperation in Europe (OSCE) to adopt and put in place a programme of elections for Bosnia and Herzegovina»[25].

The resolution also included the implementation of the Dayton Agreement, which marked the end of the Bosnian War. It is significant to note that this Peace Agreement also includes the intention to establish a «representative government and ensure the progressive achievement of democratic goals»[26]. The Dayton Peace Agreement served two functions, as a legal accord ending the war and as a rough blueprint for building a stable, peaceful and democratic state[27]. Thus, the objectives of peace and democracy were pursued simultaneously. However, some scholars argue that the democratisation and the conflict stabilization neutralized each other, and thus the most tragic mistake of BiH post-conflict efforts was the introduction of democratic contestation at a very early stage[28].

The Agreement, indeed, provided guidelines for the elections' timing, which is central in our discourse: «Elections shall take place on a date six months after entry into force of this Agreement or, if the OSCE determines a delay necessary, no later than nine months after entry into force»[29].

The timing of the November 1996 elections in Bosnia, for instance, was not dictated by events on the ground, but it was rather the answer to the Clinton administration's need to show progress in the Balkans, in time for mid-term elections in the United States[30]. Therefore, as Crocker and Hampson noted, the Bosnian election is highly controversial because the United States and its Western allies avoided taking a stance on either partition or unity[31]. Instead, they convinced the parties to accept both options. This decision delayed the war's ultimate outcome, turning the election into the solution in the suspended Bosnian peace process. Moreover, the choice of going for premature elections reflects the quick results required by international

---

[25] UNITED NATIONS SECURITY COUNCIL, *Resolution 1031 (1995)*, adopted by the Security Council at its 3607th meeting, 15 December 1995.

[26] DAYTON PEACE AGREEMENT, *General Framework Agreement for Peace in Bosnia and Herzegovina*, 1995.

[27] PERRY V., "At cross purposes? Democratization and peace implementation strategies in Bosnia and Herzegovina's frozen conflict", in *Human Rights Review*, 10(1), 2009, pp. 35-54.

[28] HUSKIĆ A., "Democratisation against Democracy: Assessing the Failure of Statebuilding in Bosnia and Herzegovina", in SARAJLIĆ E., MARKO D. (a cura di), *State or Nation*, 2011, pp. 67-92.

[29] DAYTON PEACE AGREEMENT, *General Framework,* cit.

[30] REILLY B., "Timing and sequencing in post-conflict elections", in *Building Sustainable Peace: Timing and Sequencing of Post-Conflict Reconstruction and Peacebuilding*, 2016, pp. 72-86.

[31] CROCKER C. A., HAMPSON F. O., "Making peace settlements work", in *Foreign Policy*, 104, 1996, pp. 54-71.

donors as a tangible sign of progress that will inevitably lead to the creation of some kind of legitimate government[32].

Based on what it has been said, we can assert that the choice of democratic gradualism in Bosnia was neither driven by local demands nor rooted in specific preconditions, but was instead shaped by the interests of the international actors involved in the conflict, particularly the United States.

As a consequence of Dayton's compressed electoral timetable, opposition parties were denied the opportunity to organize themselves as credible alternatives to the ruling nationalists[33]. At the same time, as argued by David Rieff, the electorate, still fractured and traumatized by the recently ended conflict, appealed to what is described as *the politics of hatred and revenge*[34]. The elections, far from being free and fair, saw the electoral struggle among the same political elites that had led the three ethnic groups throughout the war[35]. The new order established by the Dayton Agreements, in fact, had the effect of turning ethnicity into the sole relevant criterion of social organization of post-war Bosnia[36]. As expected, the result was again the dominance of illiberal elites who won playing the nationalist card[37].

3.2. Sequencing in Rwanda

Rwanda suffered near-total collapse during the genocide of 1994, after the devastating war that involved Hutu and Tutsi. The Resolution 995 adopted by the Security Council in November 1994 focus primarily on international justice stressing the need for international cooperation to strengthen the courts and judicial system of Rwanda. The main goal was to achieve national reconciliation as well as the restoration and maintenance of peace, while democratization is not even mentioned[38]. Given also the failure of Rwanda's previous experience with democracy, it is understandable why international observers have concluded that Rwanda was not ready for

[32] REILLY B., *Timing and sequencing*, cit
[33] DONAIS T., "Division and democracy: Bosnia's post-Dayton elections", 1999.
[34] RIEFF D., "Abandoning Bosnia--again", in *Newsweek*, 128(12), 1996, p. 63.
[35] HUSKIĆ A., *Democratisation against Democracy*, cit.
[36] DONAIS T., *Division and democracy,* cit
[37] MANSFIELD E. D., SNYDER J., *Electing to fight,* cit.
[38] UNITED NATIONS SECURITY COUNCIL, *Resolution 995 (1994)*, adopted by the Security Council at its 3544th meeting, 9 June 1994

democracy[39], going against the Bush perspective according to which «it is the practice of democracy that makes a nation ready for democracy»[40]. Decision-makers clearly chose stability over immediate democracy; as a consequence, in Rwanda elections were postponed for nine years. In a clear sequentialist perspective, the Rwandan Patriotic Front (RPF) leader and current president of Rwanda Paul Kagame affirmed his viewpoint on the risk that early elections would create a bigger problem: divide people who are already divided[41]. The RPF deliberately postponed the advancement of multi-party elections, using the additional time to carry out grassroots operations and reinforce its dominance in Rwandan politics[42]. This highlights an unintended consequence of sequentialism: delaying the complete opening of the political process until specific preconditions are satisfied enables the ruling party to exploit its advantageous position within the political landscape[43].

Finally, in May 2003 the new Constitution that was adopted and framed the democratisation process, which should have been achieved in compliance with national unity and reconciliation. The Constitution also includes, among its fundamental principles, the eradication of the loosely defined crime of *divisionism*[44]. Although the measure is intended to prevent a revival of the ethnically driven politics of the pre-genocide era, it has been criticised for placing excessive restrictions of the activity of opposition political parties[45]. A striking example of this was the arrest of Pasteur Bizimungu, who served as Rwanda's president from 1994 to 2000. Shortly after founding his opposition political party, the Party for Democracy and Renewal (PDR), the Rwandan government swiftly banned the party, labelling it as divisionist and Bizimungu was subsequently sentenced to a 15-year prison term[46].

Along with the new Constitution, presidential and parliamentary elections were held as well. However, these elections were overshadowed by political arrests, enforced disappearances, and

---

[39] UVIN P., "Wake up. Some policy proposals for the international community in Rwanda", Tufts University, 2003.

[40] George W. Bush, Remarks by the President at the 20th Anniversary of the National Endowment for Democracy, Washington DC, November 6, 2003.

[41] MISSER F., *Vers un nouveau Rwanda?*, Paris, Karthala, 1995, pp. 82-86.

[42] HUMAN RIGHTS WATCH, *Preparing for elections: Tightening control in the name of unity*, New York, Human Rights Watch, 2003.

[43] BERBERICH A., *Post-Conflict Democratization*, cit.

[44] REPUBLIC OF RWANDA, *Constitution of the Republic of Rwanda of 2003*, Official Gazette of the Republic of Rwanda, Kigali, 2003

[45] HUMAN RIGHTS WATCH, *Preparing for elections,* cit.

[46] INTERNATIONAL CRISIS GROUP, *Rwanda at the End of Transition: A Necessary Political Liberalisation*, Nairobi/Brussels, 2002.

voter intimidation[47]. The ideological pillars proclaimed by the post-2003 regime were national unity, reconciliation, the repression of genocide, and ensuring security[48]. While they were inclusive in principle, the elections in Rwanda offered minimal pluralism, restricting political choice for the population and undermining meaningful vertical accountability[49].

It can be concluded that the 2003 "democratic" elections served as a façade to legitimize the RPF's dominance, which had characterized Rwandan political life since the end of the genocide.

Following Diamond's criteria[50], Rwanda could be considered a hybrid regime, combining authoritarian and democratic elements. More specifically, the characteristics described so far allow us to categorize Rwanda within the framework of electoral authoritarianism[51]. Electoral authoritarianism represents a modern form of non-democratic regime that employs key instruments of liberal democracy, such as regular elections, to sustain its authoritarian grip on power[52]. These kinds of regimes resemble democratic systems, having a constitution, holding elections, having parliaments, courts, local governments, and accountability agencies.

However, political violence remains a defining symptom of electoral authoritarianism[53].

3.3. Comparing two paths: post-conflict trajectories

To analyze and compare the medium- and long-term impacts of gradualism and sequencing strategies on the democratic trajectories of Rwanda and Bosnia-Herzegovina, this section adopts a comparative process tracing approach grounded in the analysis of specific indicators. The study relies on data from sources such as V-Dem, which provides insights into the quality of democracy.

---

[47] EUROPEAN PARLIAMENT, *Report: Ad-hoc delegation to observe the presidential election in Rwanda on Monday, 25 August 2003. Committee on Development and Cooperation*, PE 326.764, 2003.
[48] RAFTI M., *A perilous path to democracy: political transition and authoritarian consolidation in Rwanda*, Antwerp, Institute of Development Policy and Management, University of Antwerp, 2007.
[49] NDI, *Assessment of Rwanda's pre Election Political Environment and the Role of Political Parties*, Kigali, 2003.
[50] DIAMOND L., "Elections without democracy: Thinking about hybrid regimes", in *Journal of Democracy*, 13(2), 2002, pp. 21-35.
[51] SCHEDLER A., "The logic of electoral authoritarianism", in *Electoral Authoritarianism: The Dynamics of Unfree Competition*, 1(6), 2006.
[52] LINDBERG S. L., "Why do Opposition Parties Boycott Elections", in SCHEDLER A. (a cura di), *Electoral Authoritarianism: The Dynamics of Unfree Competition*, Colorado, 2006.
[53] RAFTI M., *A perilous path,* cit.

The temporal scope of the analysis extends from the onset of the conflicts in the early 1990s to 2023, with particular attention to key benchmark years. Specifically, the analysis focuses on the immediate post-conflict period (1995 for Bosnia and 1994 for Rwanda), the year following the first elections (1997 for Bosnia and 2004 for Rwanda), and three additional years (2010, 2017, and 2023) to trace the evolution of these processes over time.

Recognizing that democracy cannot be reduced to the mere occurrence of elections, this investigation emphasizes the interplay between the often-conflicting objectives of peace and democracy. Democracy is understood here in line with Dahl's minimalist definition, which highlights the centrality of electoral processes. Consequently, the selected indices primarily reflect the mechanisms and quality of elections as a measure of democratic development.

The first index analyzed is the *Electoral Democracy Index*, which evaluates the extent to which the ideal of electoral democracy is realized in its fullest sense[54].

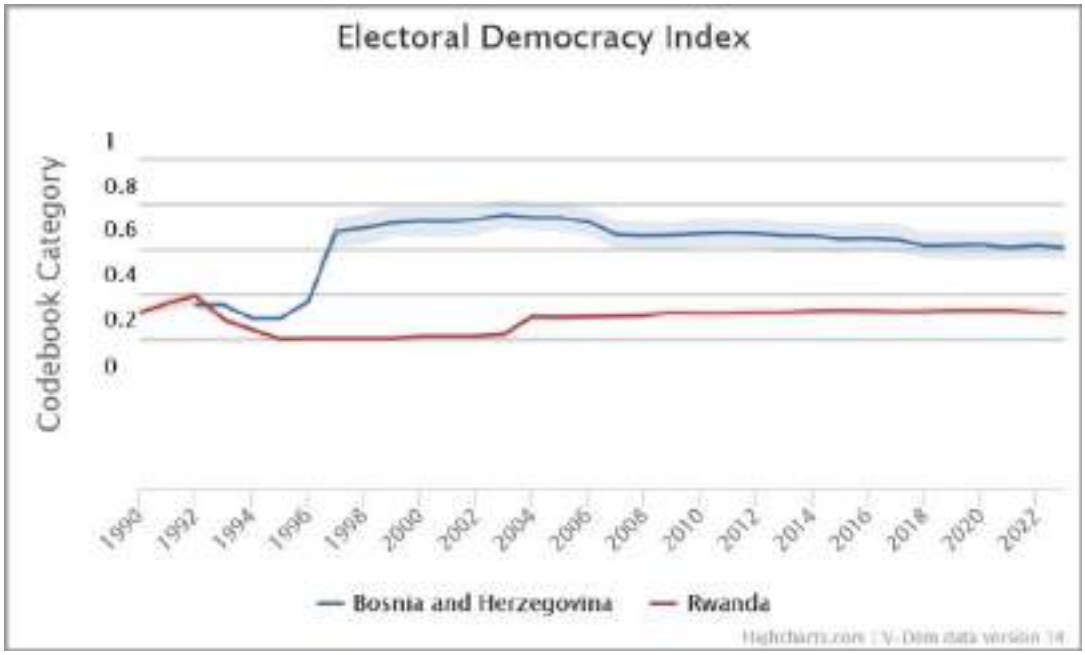

Figure 1 – Electoral Democracy Index (V-Dem Institute)

[54] The electoral principle of democracy seeks to embody the core value of making rulers responsive to citizens, achieved through electoral competition for the electorate's approval under circumstances when suffrage is extensive; political and civil society organizations can operate freely; elections are clean and not marred by fraud or systematic irregularities; and elections affect the composition of the chief executive of the country. In between elections, there is freedom of expression and an independent media capable of presenting alternative views on matters of political relevance. *Scale:* Interval, from low to high (0-1) (V-Dem Institute).

Years/Key Events	*Bosnia and Herzegovina*	*Rwanda*
After the conflict	0.19 (1995)	0.14 (1994)
First elections	0.58 (1997)	0.20 (2004)
2010	0.57	0.22
2017	0.54	0.22
2023	0.51	0.21

Table 1 – Electoral democracy Index

Based on these data we can affirm that Bosnia and Herzegovina achieved higher levels of electoral democracy initially, as a direct consequence of the first election, but then struggled to sustain this progress over time. Rwanda, on the other hand, maintained a consistently low level of electoral democracy.

The second chosen index is the *Clean Elections Index,* which evaluates the extent to which elections can be considered free and fair[55].

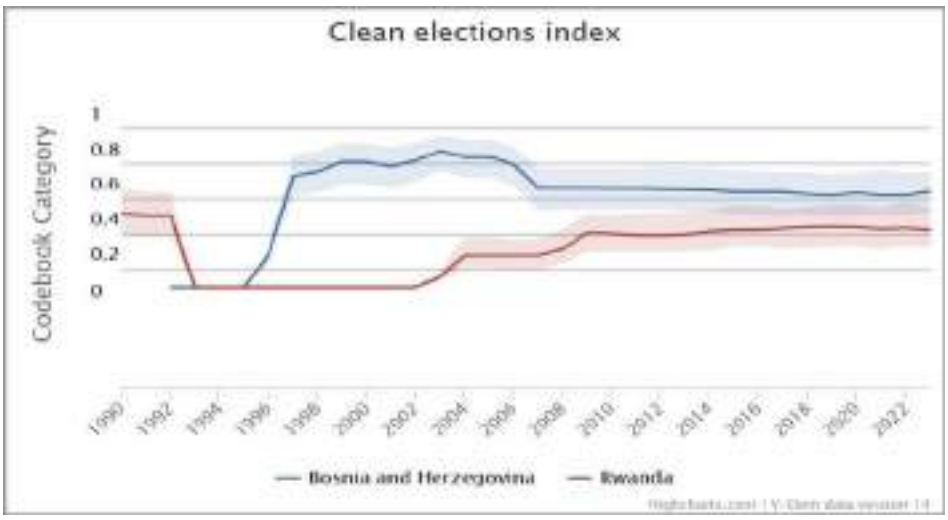

Figure 2 – Clean Elections Index (V-Dem Institute)

[55] Free and fair connotes an absence of registration fraud, systematic irregularities, government intimidation of the opposition, vote buying, and election violence. *Scale:* Interval, from low to high (0-1) (V-Dem Institute).

Years/ Key events	*Bosnia and Herzegovina*	*Rwanda*
After the conflict	0 (1995)	0 (1994)
First elections	0.63 (1997)	0.18 (2004)
2010	0.56	0.31
2017	0.54	0.34
2023	0.54	0.33

Table 2 – Clean Elections Index

As underlined by the Co-ordinator for International Monitoring (CIM), the election day of 14 September 1996 in Bosnia went «technically well, but the general climate in which the elections took place was in some cases below the minimum standards of the OSCE Copenhagen Commitments»[56]. However, the CIM emphasised that the elections, although characterised by imperfections, took place in such a way that they provide a first and cautious step for the democratic functioning of the governing structures of Bosnia and Herzegovina. If this was true up to a certain point, it is important to clarify that since 2007 there has actually been a decline in the Clean Election Index in Bosnia. This decline continued until the 2022 elections, where the EOM assessed the campaign environment as marked by political impasse, mistrust in institutions, and divisive rhetoric, with limited public debate and biased media coverage reducing voter awareness. Despite orderly election day procedures, issues like vote secrecy and inconsistent safeguards during counting raised concerns[57].

In reference to the elections held in Rwanda in 2003, the report produced by the ad-hoc delegation of the European Union states that the elections were conducted peacefully and without violent incidents; however, the EU Election Observation Mission regrets some elements of intimidation noted during the electoral operations and was concerned about disappearances, arrests and police questioning of opponents[58]. What we observe from the

[56] CO-ORDINATOR FOR INTERNATIONAL MONITORING (CIM), *Second Statement: The Elections in Bosnia and Herzegovina*, Pehlivanusa 3/11, Sarajevo, 17 September 1996, p.1.
[57] ODIHR, *Election Observation Mission Final Report, 2022*, Organization for Security and Co-operation in Europe, 2022.
[58] EUROPEAN PARLIAMENT, *Report: Ad-hoc delegation,* cit.

analysis of various reports and data is that, over the years, the trend shows some improvement, but not significant ones.

The *Participatory Democracy Index* emphasizes active participation by citizens in all political processes, electoral and non-electoral.

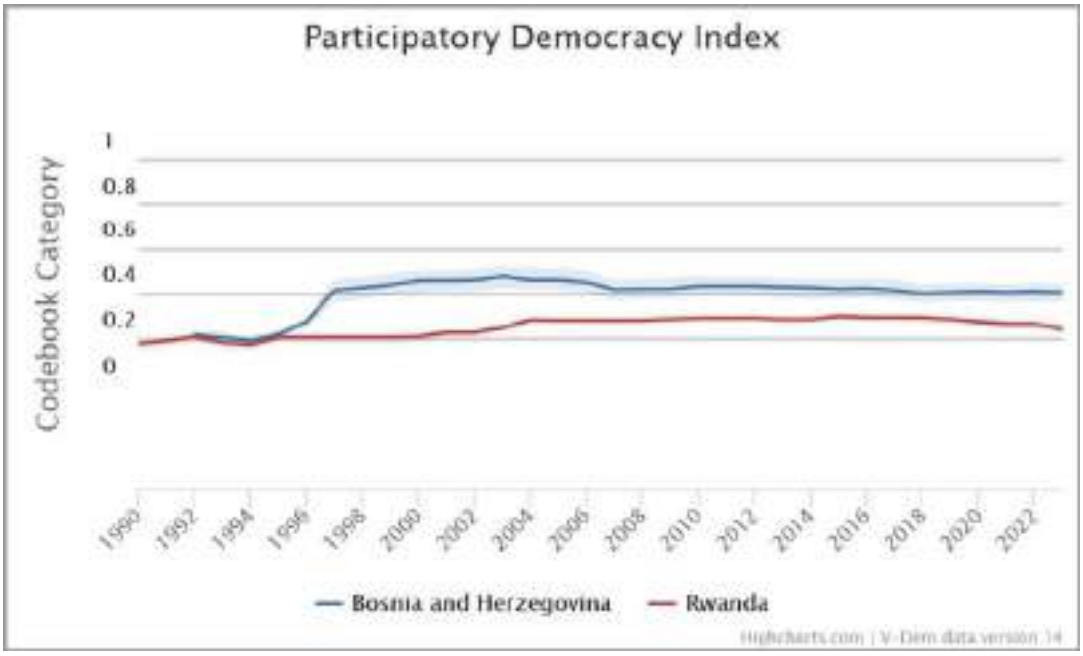

Figure 3 – Participatory Democracy Index (Data: V-Dem Institute)

Years/ Key events	*Bosnia and Herzegovina*	*Rwanda*
After the conflict	0.12 (1995)	0.07 (1994)
First elections	0.32 (1997)	0.19 (2004)
2010	0.34	0.19
2017	0.32	0.2
2023	0.31	0.14

Table 3 – Participatory Elections Index

In this case as well, Bosnia reports better results, particularly due to the role of an active civil society. However, the overall level of civil society participation in both countries remains extremely low. In Bosnia women are underrepresented in politics and government and LGBT+

people are marginalized in formal political life[59]. In Rwanda the Constitution requires the president to appoint Senate members to represent historically marginalized communities. However, the ban on asserting ethnic identity in politics obscures the extent of such representation, hampering disadvantaged groups from organizing independently and advocating for their rights[60].

Finally, the *Rule of Law Index* evaluates the extent to which laws are transparently, independently, predictably, impartially, and equally enforced, and to what extent the actions of government officials comply with the law.

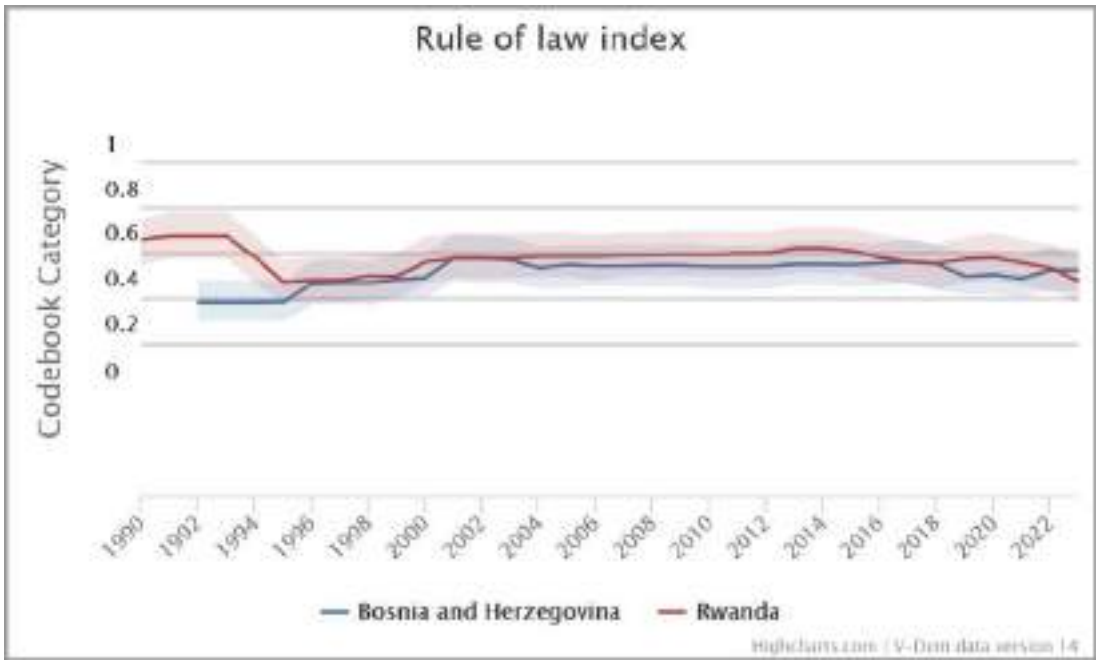

Figure 4 - Rule of Law Index (Data: V-Dem Institute)

Years/ Key events	*Bosnia and Herzegovina*	*Rwanda*
After the conflict	0.29 (1995)	0.48 (1994)
First elections	0.37 (1997)	0.49 (2004)
2010	0.44	0.49
2017	0.46	0.47

[59] FREEDOM HOUSE, *Bosnia and Herzegovina: Freedom in the World 2024*, 2024.
[60] FREEDOM HOUSE, *Rwanda: Freedom in the World 2024*, 2024.

2023	0.43	0.38

Table 4 – Rule of Law Index

The data shows that Bosnia, despite little improvements, continues to struggle with a fragmented legal and political system, ethnic divisions and political interference in the judiciary. The results of the two countries are roughly the same, with a slight overall advantage for Rwanda.

What emerges from this exploratory comparison is that, despite being a flawed democracy, Bosnia has achieved better results, thus supporting the theory according to which gradualism favors democratic development. On the other hand, sequencing in Rwanda has been a failure from the point of view of democratization. However, the data relating to the Rule of law in Rwanda seem to suggest that, from the point of view of government effectiveness, the strategy pursued has brought better results than those in Bosnia.

According to the World Bank Group data Rwanda has made impressive progress in controlling corruption, becoming one of the African states with the lowest levels of perceived corruption[61], while in Bosnia corruption is often cited as one of the main obstacles to the country's development[62].

IV. CONCLUSIONS

The experiences of Rwanda and Bosnia and Herzegovina underscore the complexities of democratization in post-conflict contexts, particularly when it intersects with the conflicting objective of peacebuilding. Despite the different strategies adopted, what emerges from an analysis of both countries is a flawed democracy in the short-term, characterized by the continued dominance of conflict-era leaders.

The way in which the reconciliation process was structured certainly also influenced the democratic transition. In Bosnia, in fact, the achievement of peace came from a reaffirmation

[61] WORLD BANK GROUP, *Worldwide Governance Indicators: Interactive data access*, The World Bank, 2023.
[62] FREEDOM HOUSE, *Bosnia and Herzegovina,* cit.

of ethnic groups, which share political roles, and from a geographical division of the territory. On the contrary, in Rwanda the reconciliation process involved the abolition of any presumed ethnic distinction.

In Rwanda, the prioritization of stability over immediate democratization led to delayed elections and to the establishment of an authoritarian system, underpinned by electoral authoritarianism. This approach achieved substantial control over corruption and ensured a more stable governance framework, yet it stifled political pluralism and restricted civil liberties, leaving the country entrenched in a hybrid regime.

Bosnia, on the other hand, pursued simultaneous democratization and peacebuilding under significant international influence. The gradualist approach, while initially bringing to higher levels of electoral democracy, was marred by premature elections driven by external actors' timelines rather than local readiness. This strategy perpetuated ethnic divisions, reinforced by the Dayton Agreement's institutionalization of ethnic quotas, which undermined long-term democratic consolidation. Bosnia's democracy remains fragile, with declining trust in institutions, persistent corruption, and limited civic engagement.

The comparative analysis highlights that both cases reveal the risks of mistimed democratization efforts. Premature elections in Bosnia and delayed elections in Rwanda illustrate how either extremes can destabilize democratization efforts.

In conclusion, the trade-offs between peace and democratization are neither linear nor easily resolvable. The longer a country defers necessary democratic reforms, as in Rwanda, the greater the risk of entrenching hybrid regimes[63]. Conversely, rushing democratization without addressing underlying societal fractures, as in Bosnia, can result in fragile democratic institutions.

Future strategies should adopt a context-sensitive approach that balances the imperatives of peace, inclusivity, and gradual democratization to address the local needs and to foster sustainable outcomes in post-conflict societies.

[63] SILVA-LEANDER S., "On the Danger and Necessity of Democratisation: Trade-offs between short-term stability and long-term peace in post-genocide Rwanda", in *Third World Quarterly*, 29(8), 2008, pp. 1601-1620.

REFERENCES

BERBERICH A., "Post-Conflict Democratization: Rwanda's Illiberal Democracy", in *Proceedings of GREAT Day*, 2010(1), 2011.

BERMEO N., "On democratic backsliding", in *Journal of Democracy*, 27(1), 2016, pp. 5-19.

BOUTROS-GHALI B., *An agenda for peace: Preventive diplomacy, peacemaking and peacekeeping (A/47/277 - S/24111)*, United Nations, New York, 1992.

CARAMANI D. (a cura di), *Comparative Politics*, Oxford, Oxford University Press, 2023.

CAROTHERS T., "How democracies emerge: The 'sequencing' fallacy", in *Journal of Democracy*, 18(1), 2007, pp. 12-27.

CO-ORDINATOR FOR INTERNATIONAL MONITORING (CIM), *Second Statement: The Elections in Bosnia and Herzegovina*, Pehlivanusa 3/11, Sarajevo, 17 September 1996.

CROCKER C. A., HAMPSON F. O., "Making peace settlements work", in *Foreign Policy*, 104, 1996, pp. 54-71.

DAHL R. A., *Polyarchy: Participation and Opposition*, Yale University, London, 1971.

DAYTON PEACE AGREEMENT, *General Framework Agreement for Peace in Bosnia and Herzegovina*, 1995.

DIAMOND L., "Elections without democracy: Thinking about hybrid regimes", in *Journal of Democracy*, 13(2), 2002, pp. 21-35.

DONAIS T., "Division and democracy: Bosnia's post-Dayton elections", 1999.

EUROPEAN PARLIAMENT, *Report: Ad-hoc delegation to observe the presidential election in Rwanda on Monday, 25 August 2003. Committee on Development and Cooperation*, PE 326.764, 2003.

FREEDOM HOUSE, *Bosnia and Herzegovina: Freedom in the World 2024*, 2024.

FREEDOM HOUSE, *Rwanda: Freedom in the World 2024*, 2024.

FUKUYAMA F., "Is there a proper sequence in democratic transitions?", in *Current History*, 110(739), 2011.

GALTUNG J., "Violence, peace, and peace research", in *Journal of Peace Research*, 6(3), 1969, pp. 167-191.

GRIMM S., LEININGER J., "Not all good things go together: conflicting objectives in democracy promotion", in *Conflicting Objectives in Democracy Promotion*, Routledge, 2017, pp. 3-26.

HUMAN RIGHTS WATCH, *Preparing for elections: Tightening control in the name of unity*, New York, Human Rights Watch, 2003.

HUSKIĆ A., "Democratisation against Democracy: Assessing the Failure of Statebuilding in Bosnia and Herzegovina", in SARAJLIĆ E., MARKO D. (a cura di), *State or Nation*, 2011, pp. 67-92.

INTERNATIONAL CRISIS GROUP, *Rwanda at the End of Transition: A Necessary Political Liberalisation*, Nairobi/Brussels, 2002.

LINDBERG S. L., "Why do Opposition Parties Boycott Elections", in SCHEDLER A. (a cura di), *Electoral Authoritarianism: The Dynamics of Unfree Competition*, Colorado, 2006.

LITTLE A. T., MENG A., "Measuring democratic backsliding", in *PS: Political Science & Politics*, 2023, pp. 1-13.

MANSFIELD E. D., SNYDER J., *Electing to fight: Why emerging democracies go to war*, MIT Press, Cambridge, 2007.

MANSFIELD E. D., SNYDER J., "Exchange: The Sequencing 'Fallacy'", in *Journal of Democracy*, 18(3), 2007, pp. 5-9.

MANSFIELD E. D., SNYDER J., "Pathways to war in democratic transitions", in *International Organization*, 63(2), 2009, pp. 381-390.

MIGDAL J. S., "State building and the non-nation-state", in *Journal of International Affairs*, 2004, pp. 17-46.

MISSER F., *Vers un nouveau Rwanda?*, Karthala, Paris, 1995, pp. 82-86.

MROSS K., "First peace, then democracy? Evaluating strategies of international support at critical junctures after civil war", in *International Peacekeeping*, 26(2), 2018, pp. 190-215.

NDI, *Assessment of Rwanda's pre Election Political Environment and the Role of Political Parties*, Kigali, 2003.

O'DONNELL G., SCHMITTER P. C., WHITEHEAD L. (a cura di), *Transitions from Authoritarian Rule: Comparative Perspectives*, vol. 3, JHU Press, Baltimore, 1986.

ODIHR, *Election Observation Mission Final Report, 2022*, Organization for Security and Cooperation in Europe, 2022.

PERRY V., "At cross purposes? Democratization and peace implementation strategies in Bosnia and Herzegovina's frozen conflict", in *Human Rights Review*, 10(1), 2009, pp. 35-54.

RAFTI M., *A perilous path to democracy: political transition and authoritarian consolidation in Rwanda*, Institute of Development Policy and Management, University of Antwerp, Antwerp, 2007.

REILLY B., "Timing and sequencing in post-conflict elections", in *Building Sustainable Peace: Timing and Sequencing of Post-Conflict Reconstruction and Peacebuilding*, 2016, pp. 72-86.

REPUBLIC OF RWANDA, *Constitution of the Republic of Rwanda of 2003*, Official Gazette of the Republic of Rwanda, Kigali, 2003

RIEFF D., "Abandoning Bosnia--again", in *Newsweek*, 128(12), 1996, p. 63.

SCHEDLER A., "The logic of electoral authoritarianism", in *Electoral Authoritarianism: The Dynamics of Unfree Competition*, 1(6), 2006.

SILVA-LEANDER S., "On the Danger and Necessity of Democratisation: Trade-offs between short-term stability and long-term peace in post-genocide Rwanda", in *Third World Quarterly*, 29(8), 2008, pp. 1601-1620.

UNITED NATIONS SECURITY COUNCIL, *Resolution 1031 (1995)*, adopted by the Security Council at its 3607th meeting, 15 December 1995.

UNITED NATIONS SECURITY COUNCIL, *Resolution 995 (1994)*, adopted by the Security Council at its 3544th meeting, 9 June 1994.

UVIN P., "Wake up. Some policy proposals for the international community in Rwanda", Tufts University, Medford, 2003.

WOLFF J., SPANGER H. J., "Democracy promoters' conflicting objectives: The research agenda", in *The Comparative International Politics of Democracy Promotion*, Routledge, 2013, pp. 3-36.

WORLD BANK GROUP, *Worldwide Governance Indicators: Interactive data access*, The World Bank, 2023.

ZAKARIA F., "The Rise of Illiberal Democracy", in *Foreign Affairs*, 76(6), 1997, pp. 22-43.

Air pollution reduction policies in Europe, the case of Padua

Gaia Bordoni

Abstract

This paper analyses the level of air pollution across Europe and takes into account the role of cities to reduce the emission of nocive pollutants in the environment. Moreover, a specific section is dedicated to the case study of the city of Padua, which was nominated as part of the 100 cities for the Zero City Missions programme activated by Europe thanks to Horizon EU funds.

Keywords: Air pollution, Urban context, Sustainable cities, environmental transition, European Green Deal, Agenda 2030, Padua and Net Zero City Mission.

INTRODUCTION

Air pollution represents one of the main threats to human health, it is the cause of multiple diseases, both mental and physical, and premature deaths. Moreover, air pollution reflects on the quality of soil and biodiversity, thus should be considered in a wider perspective including air, water and soil as a whole and interconnected system. As for the European case, 97% of the population is exposed to the concentration of particulate matter and other nocive air pollutants[1].

This paper focuses on the NetZeroCity Mission policy application to the city of Padua, as it represents a practical example of territorial implementation of European projects and its contents are relevant in terms of green and just transition, environmental policy integration and the creation of collaborative and multilevel networks.

The paper is structured into three sections, which aim at providing a comprehensive standpoint over air pollution issues and the policies implemented by the European Union to confront these problems and respect international binding agreements. Section I provides insights about air pollution levels among European cities and provides an extensive list of the most alarming indicators. Section II outlines the legal framework of air pollution management in Europe and provides information regarding policy instruments to achieve climate neutrality and comply with Agenda 2030 goals. Section III examines the case of the city of Padua and its NetZeroCity Mission programme - which is part Horizon Europe research programme and of the wider Green Deal strategy.

Methodology used in this paper relies both on quantitative and qualitative information: on the one hand, European, national and city legal acts are analyzed; on the other hand, a specific research on data and statistical reports has been conducted to better understand the problems relating with air pollution in Europe.

[1] Council of the European Union, 2025, https://bit.ly/4iM8OFH

I. AIR QUALITY IN MAJOR EUROPEAN CITIES AND RELEVANT INDICATORS

1.1. Main air pollutants in Europe

As reported by the World Health Organization, the main pollutants include[2]:

- Particulate matter
- Ammonia
- Methane
- Ozone
- Nitrogen oxides
- Sulphur dioxide
- Non-methane volatile organic compounds

Each of them is harmful by itself and some can react with each other through chemical processes, thus becoming particulate matter or ozone. Particulate matter represents the most nocive and alarming pollutant: $PM_{2,5}$ can enter the lungs and the blood stream, causing serious health problems.

1.2. Health problems related to acute exposure to air pollutants

Almost 448 million people live in Europe, representing 5,6% of the world's population[3]. As for the level of urbanization, 39% of European population lives in a city, 36% in towns and suburbs and 25% in rural areas[4]. Even though since 1990 emissions of the main air pollutants have decreased significantly as shown in *Table 1*, in 2021 most of the European urban population was exposed to high levels of air pollutants capable of damaging to health.

[2] World Health Organization, *Air pollution*, https://bit.ly/4imEvFG.

[3] European Union, *Facts and Figures on the European Union*, https://bit.ly/4iD4LvL.

[4] EUROSTAT, *Urban-Rural Statistics*, 2022, https://bit.ly/4kMrAP4.

Specifically, 97% of the European urban population was exposed to concentrations of fine particulate matter ($PM_{2.5}$) above the latest guidelines of the World Health Organization (WHO).

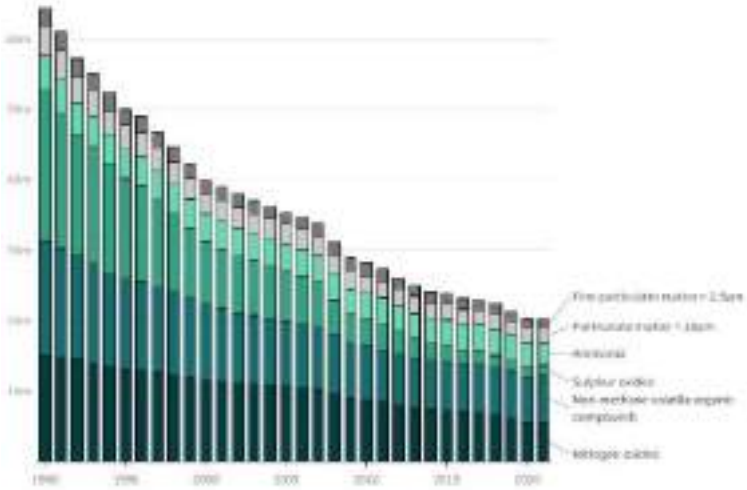

Table 1 - Emissions in tonnes between 1990 and 2020, European Environment Agency (EEA) [5]

Exposure to air pollution can lead to major respiratory and cardiovascular diseases: heart disease and stroke are the most common causes of premature deaths attributable to air pollution, followed by lung diseases and lung cancer. In 2022, Europe registered 239.000 premature deaths due to $PM_{2,5}$ exposure[6] as shown in *Table 2*; moreover, in 2021, exposure to nitrogen dioxide above the guideline level set by WHO was considered responsible for 49.000 premature deaths, while acute exposure to ozone caused 24.000 premature deaths[7].

[5] European Environment Agency (EEA), *env_air_emis*, 2024, https://bit.ly/4bIeNJf.
[6] European Environment Agency (EEA), *Premature deaths due to exposure to fine particulate matter in Europe*, 2024, https://bit.ly/41BEGFW.
[7] European Environmental Agency (EEA), *Air quality in Europe 2022 – Health impacts of air pollution in Europe*, 2023, https://bit.ly/4hAjvdu.

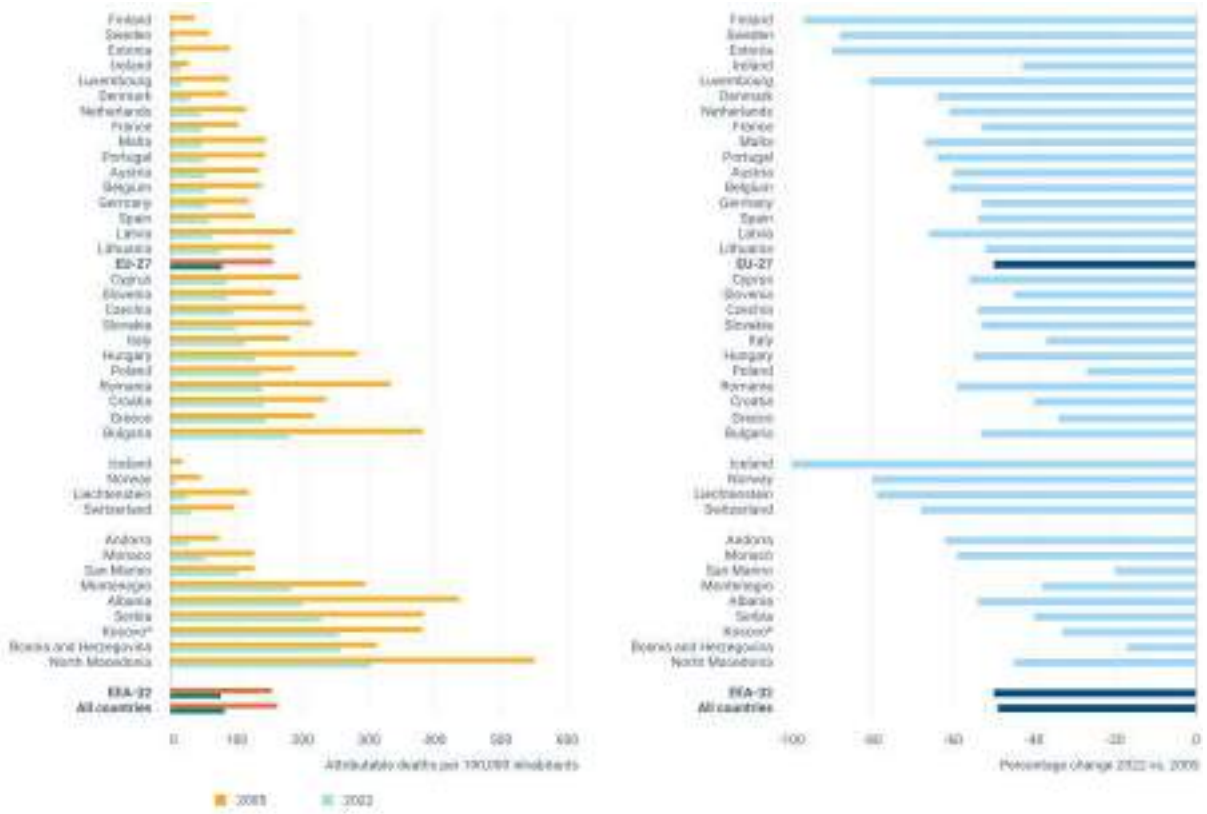

Table 2 - Premature deaths normalized by population attributable to exposure to $PM_{2,5}$ at country level in 2005 and 2022, and percentage of change.

Breathing air containing toxins can also cause morbidity and diseases and significant costs on the health care sector. In 2019, exposure to $PM_{2,5}$ led to 175.702 years lived with disability (YLDs) due to chronic obstructive pulmonary disease in 31 European countries. In the same year of reference, exposure to NO_2 led to 175.070 YLDs due to diabetes mellitus[8] in 31 European countries; finally, 12.253 people across 23 European countries were admitted to the hospital with lower respiratory infections resulting from acute exposure to ozone[9].

[8] Type 2 Diabetes.

[9] European Environmental Agency (EEA), Air quality in Europe 2022 – Health impacts of air pollution in Europe, cit.

1.3 Air quality in European cities

1.3.1. European cities overview

Table 3 reports the various sources of the air pollutants PM_{10}, $PM_{2,5}$, ammonia, sulphur dioxide, non-methane volatile organic compounds and nitrogen oxides. Agriculture and energy consumption represent the biggest contributors to air pollution in Europe.

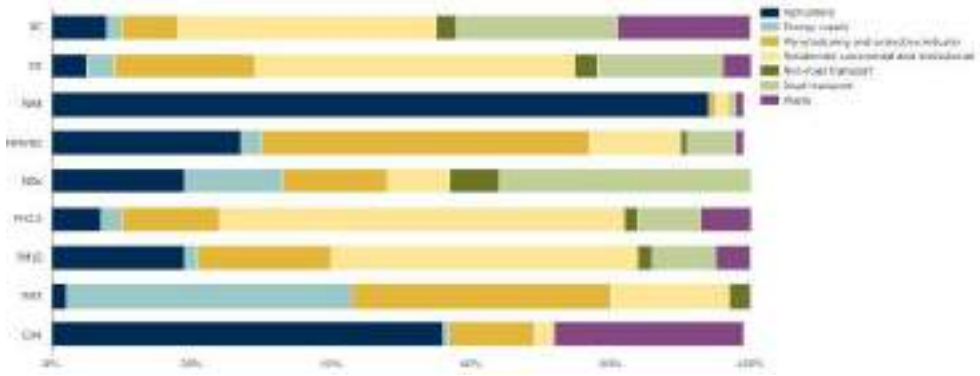

Table 3 - Contributors to EU-27 emissions of BC, CO, NH_3, NMVOCs, NOx, primary PM_{10}, primary $PM_{2,5}$, SO_2 and CH_4 from the main source sectors in 2020 [10]

As for the air quality in European cities, *Figure 1* shows the level of pollution with $PM_{2,5}$. Cities in the north and west of Europe tend to have lower concentrations of $PM_{2,5}$, while cities towards the east and south tend to have higher concentrations.

Figure 1 - $PM_{2,5}$ annual mean concentration, µg/m3, 2021-2022[11]

[10] European Environmental Agency (EEA), *Contributions to EU-27 emissions of BC, CO, NH_3, NMVOCs, NOx, primary PM_{10}, primary $PM_{2.5}$, SO_2 and CH_4 from the main source sectors in 2020*, 2024, https://bit.ly/4bIjD9p.
[11] European Environment Agency (EEA), European city air quality viewer, 2024, https://bit.ly/4iD9GNf.

Between 2021 and 2022 four European cities exceeded the current European limit of 25 micrograms of fine particulate matter for cubic metres of air: Slavonski Brod (Croatia), Nowy Sacz and Piotrków Trybunalski (Poland), and Cremona (Italy). On the contrary, ten European cities made it under 5 micrograms of $PM_{2,5.}$ per cubic metre: Narva and Tallinn in Estonia, Tampere in Finland, Reykjavik in Iceland, Faro and Funchal in Portugal, Umeå, Uppsala, Norrköping and Stockholm in Sweden.

1.3.2. Italian cities

European City Air Quality Viewer takes into account 372 European cities' average concentration levels of $PM_{2,5}$ over the past two calendar years. Among the 20 most polluted cities of the sample, 9 are situated in the northern part of Italy as reported in *Table 4*: Cremona, Vicenza, Padova, Venezia, Piacenza, Torino, Bergamo, Brescia, Treviso.

City name	Country	Rank	Fine particulate matter in ug/m3	Population in the city
Treviso	Italy	359	20,7	85456
Brescia	Italy	360	20,7	196340
Bergamo	Italy	361	20,9	120783
Torino	Italy	362	21,0	857910
Zory	Poland	363	21,8	62456
Czestochowa	Poland	364	21,9	222292
Ioannina	Greece	365	21,9	80371
Piacenza	Italy	366	22,2	104260
Venezia	Italy	367	22,6	258685
Padova	Italy	368	22,7	210077
Vicenza	Italy	369	23,0	109855
Cremona	Italy	370	23,3	72399
Nowy Sacz	Poland	371	24,0	83896
Slavonski Brod	Croatia	372	26,5	52836

Table 4 - Air in European cities, from the cleanest to the most polluted [12]

Italian cities most affected by air pollution are situated in the Po Valley, which is a densely populated and highly industrialised region. Moreover, the Po Valley is surrounded by the Alps in the north and the Apennines to the south, thus creating a natural basin and microclimate trapping pollutants[13].

Finally, as for the city of Padua, the situation is particularly alarming since even areas reporting the lowest mean annual $PM_{2,5}$ concentration show levels that are invariably much

[12] European Environment Agency (EEA), *European city air quality viewer*, cit.
[13] European Space Agency (ESA), Air pollution fluctuations over the Po Valley, 2024, https://bit.ly/4iI3pPP.

higher than the annual average value (10 µg/m^3) indicated as the quality limit by WHO as reported in *Table*

5.

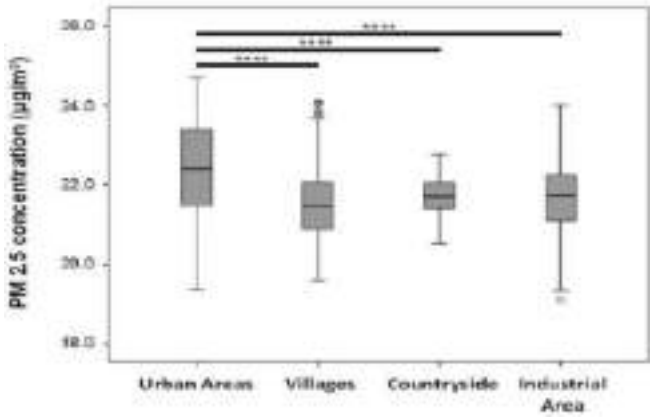

Table 5 - $PM_{2,5}$ concentrations in the different territorial types of the Province of Padua, each box represents second and third quartile, reporting the median value[14].

Emissions concerning the city of Padua mostly relate to the building sector, which was responsible for 73% of the CO_2 emissions in 2021 as reported in *Table 6*. This sector includes energy consumption of private and public buildings and urban equipments[15]. Transportation is responsible for 23% of the total emissions, while 4% is related to waste.

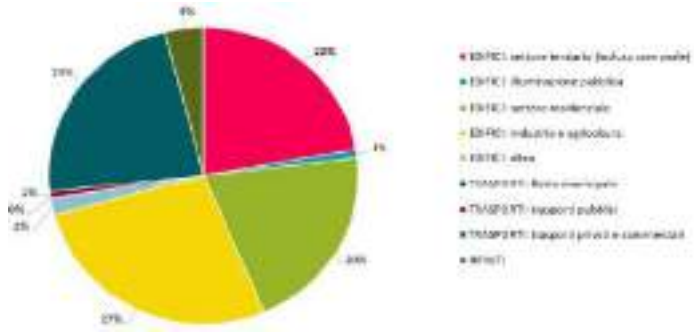

Table 6 - Padua's emissions in 2021 divided by sector (tCO_2eq) [16]

II. EUROPEAN LEGAL FRAMEWORK ON AIR POLLUTION AND SUSTAINABLE CITIES

[14] F. Tateo, F. Grassivaro,M. Ermani, M. Puthenparampil & P. Gallo, *PM2,5 levels strongly associate with multiple sclerosis prevalence in the Province of Padua, Veneto Reion, North-East Italy*. Multiple Sclerosis Journal 25(13), 2018, p.p. 1719-1727

[15] Example: street lighting.

[16] Comune di Padova, *Climate City Contract, Piano d'Azione per la Neutralità Climatica al 2030*, 2023.

2.1. Europe's commitment to reduce air pollution

Europe's commitment to providing practical action and taking effective measures to solve climate change and stop environmental air pollution is visible both at the international and local level, the following chapters analyse these two levels of action.

2.1.1. Agenda 2030 and Green Deal

The European Union took part in major international agreements and conferences during the last decades. In 1992 Europe participated in Rio de Janeiro's United Nations Conference on Environment and Development and subsequently signed Agenda21 (a non-binding action plan of the United Nations promoting sustainable development), the Statement of Forest Principles, the Rio Declaration on Environment and Development, and the following Conventions: UNFCCC (United Nations Framework Convention on Climate Change), CBD (Convention on Biological Diversity) and UNCCD (United Nations Convention to Combat Desertification).

In 1997, Europe - as a signatory of UNFCCC - took part in the Kyoto Protocol, which introduced a legally binding emission reduction target for developed countries. Moreover, the European Union played a central role during the United Nations Climate Change Conference (COP21), which was held in Paris in December 2015. Europe signed the Paris Agreement in October 2016 and as part of its Nationally Determined Contributions (NDCs) it endorsed the objective of achieving a climate-neutral EU by 2050 and adopted a long-term low greenhouse gas emission development strategy.

Furthermore, in 2015 Europe took part in the ONU's General Assembly held in New York and committed to Agenda 2030 goals. Reducing air pollution and tackling the diminution of cities' environmental impact responds to goals III *Good Health and Wellbeing*; VII *Affordable and Clean Energy*; X *Reduced Inequalities*; XI *Sustainable Cities and Communities*; XIII *Climate action* of Agenda 2030.

2.1.2. Europe's commitment to reduce air pollution

In order to implement international agreements, the European Commission set a series of measures requiring an active and operative role of the member states. Specifically, in 2019 the European Commission set out its communication entitled "The European Green Deal", which represents an ambitious roadmap designed to respond to Agenda 2030 commitment and that

represents: «(...) a new growth strategy that aims to transform the EU into a fair and prosperous society, with a modern, resource-efficient and competitive economy where there are no net emissions of greenhouse gases in 2050 and where economic growth is decoupled from resource use»[17].

The European Green Deal also addresses the problem of air pollution, thus stating that «To protect Europe's citizens and ecosystems, the EU needs to better monitor, report, prevent and remedy pollution from air, water, soil, and consumer products. To achieve this, the EU and Member States will need to look more systematically at all policies and regulations»[18].

In this respect, the European Commission announced the adoption of a zero pollution action plan for air, water and soil in 2021 and in that exact year the "Pathway to a Healthy Planet for All - EU Action Plan: Towards Zero Pollution for Air, Water and Soil" communication was delivered. This plan sets out a vision for 2050 to be achieved by a staged approach. In September 2021, the WHO (World Health Organization) updated its Air Quality Guidelines and highlighted new evidence about effects occurring at low levels of exposure to air pollution and formulated lower air quality guideline levels for particulate matter (PM_{10} and $PM_{2,5}$) and for nitrogen dioxide compared to previous guidelines[19]. The following year, in May 2022, the 8th Environment Action Programme (EAP) to 2030 entered into force, it represents Europe's action programme to achieve United Nations' 2030 Agenda and represents Green Deal's implementation plan.

Finally, in 2024 the revised Ambient Air Quality Directive[20] entered into force. The Directive took into account the latest WHO recommendations and reports on air quality standards and applied them to Europe's 2030 action plan to achieve zero pollution by 2050. The new Directive cut the allowed annual limit value for $PM_{2,5}$ by more than a half and lowered the allowable levels for the following air pollutants: nitrogen dioxide and nitrogen oxides, sulphur dioxide, ozone, carbon monoxide, benzene, benzo(a)pyrene, arsenic, cadmium, nickel, and lead. The Directive provides member States guidance regarding monitoring and fitness checks programmes and requires standardised measurement techniques. Finally, the Directive both takes into account the role of local authorities and ensures that people suffering from health

[17] European Commission, *The European Green Deal, COM(2019) 640 final*, 2019, https://bit.ly/4ikpHrd.
[18] European Commission, *The European Green Deal, COM(2019) 640 final*, cit.
[19] World Health Organization (WHO), *WHO global air quality guidelines – Particulate matter (PM2,5 and PM10), ozone, nitrogen dioxide, sulfur dioxide and carbon monoxide*, 2021, https://bit.ly/4kCcxY9.
[20] Directive Of The European Parliament And Of The Council On Ambient Air Quality And Cleaner Air For Europe, *2024/2881*, http://data.europa.eu/eli/dir/2024/2881/oj.

damages due to air pollution have the right to be compensated in the case of a violation of European air quality rules.

2.2. Urban regulation

2.2.1. Pact of Amsterdam

In 2016 the Urban Agenda for the EU was launched thanks to the Pact of Amsterdam and in 2021 it was reconfirmed as a valuable initiative with the Ljubljana Agreement. The Urban Agenda for the EU represents a multilevel working method for urban policy and «(...) strives to involve Urban Authorities in the design of policies, to mobilise Urban Authorities for the implementation of EU policies, and to strengthen the urban dimension in these policies»[21].

The Urban Agenda for the EU focuses on three policy making pillars for its implementation: i) better regulation; ii) better funding; iii) better knowledge. It also aims at realising the full potential of urban areas, establishing an integrated approach and contributing to territorial cohesion by reducing socioeconomic gaps, and involving urban authorities in the design of policies[22]. As for the operational framework of the Urban Agenda for the EU, it sets the designation of 12 Priority Themes (among which air pollution is given high consideration), the creation of Thematic Partnerships as an instrument for multilevel and cross-sectoral cooperation, Impact Assessments to reduce conflicting impacts of EU legislation on Urban Areas and burdensome implementation at local and regional level, and the exchange of knowledge and experiences as well as monitoring results.

The Urban Agenda for the EU focused on the following pollutants which have been proven to have a negative impact in urban environments: Particulate Matter, NOx, Non-exhaust trafficrelated particles, SOx and NOx produced from shipping in coastal areas and port cities, ammonia, particulate matter emissions to air from biomass heating and emissions from construction sites.

[21] Urban Agenda For The EU, *Pact Of Amsterdam*, 2016, https://bit.ly/4iJZ12J.
[22] Urban Agenda For The EU, *Pact Of Amsterdam*, cit.

Finally, the Urban Agenda for the EU raised attention to the need to improve coordination between different levels of governance and the involvement of citizens in urban policy development[23].

2.2.2. Horizon Europe

The last part of this section is dedicated to the Horizon Europe programme. An attentive analysis of this project is required as Padua's NetZeroCity plan - which represents the specific case study taken into account in this essay - is part of it.

Horizon 2020 was Europe's research and innovation funding programme from 2014 to 2020, with a budget of nearly €80 billion. Subsequently, the Horizon Europe funding amount for the period 2021-2027 was raised to €95.5 billion - €5.4 billion of which are destined to the Next Generation EU to foster recovery from COVID-19 crisis and make Europe more resilient for the future, while €4.5 billion are an additional reinforcement - [24] . The proposal was made as part of the next EU long-term budget, the Multiannual Financial Framework (MFF). Horizon Europe represents the key funding programme for research and innovation: it aims at supporting the implementation of European policies, achieving global challenges and the creation of open and high-quality scientific knowledge.

Compared to the previous version[25], the new Horizon Europe created a European Innovation Council, set a series of European Missions, introduced a new approach to partnerships and an open science policy. Horizon Europe states five mission areas, which take into account i) the adaptation to climate change, including societal transformation; ii) cancer; iii) healthy oceans, seas, coastal and inland waters; iv) climate-neutral and smart cities; v) soil health and food[26]. As for the role of cities, the mission board stated the creation of 100 climate-neutral cities by 2030; selected European cities will be assisted in their transformation towards climate neutrality by 2030, thus becoming innovation hubs and creating a benefiting quality of life for the citizens.

---

[23] European Union, *Urban Agenda for the EU*, https://bit.ly/4hrDtXM.

[24] European Union, *Horizon Europe fundings*, https://bit.ly/4kHHIRM.

[25] European Union, *Horizon 2020*, https://bit.ly/4bJAaKc.

[26] European Parliament And The Council, HORIZON EUROPE – *The Framework Programme for Research and Innovation, laying down its rules for participation and dissemination, and repealing Regulations (EU)*, No 1290/2013 and (EU) No 1291/2013, 2021, https://eur-lex.europa.eu/eli/reg/2021/695/oj.

The NetZeroCities project will help cities overcome institutional and cultural barriers and provide a platform accessible to all aggregating new and existing tools, resources and expertise[27]. NetZeroCities also comprehends a series of Pilots to test innovative ideas, twinning programmes and two City Panels[28].

III. PADUA AND NETZEROCITY MISSION

3.1. Selection process

NetZeroCities is a four-year project launched in October 2021 to support the delivery of the European Mission aiming at making 100 Cities climate-neutral by 2030. Cities aspiring to be part of the programme had to undertake an *Expression of Interest* process run by the European Commission in the late 2021 and early 2022. Overall, 377 cities applied and the 100 cities selected represent 12% of the European population[29].

Selected cities were admitted to the NetZeroCities programme and supported through the process of developing a Climate City Contract (CCC), which is a politically binding contract and an expression of commitment between the city, its stakeholders and the citizens to pursue climate neutrality by 2030. Among the 112 selected cities, 9 are Italian: Bergamo, Bologna, Florence, Milan, Padua, Parma, Prato, Rome and Turin[30].

3.2. Padua's Climate City Contract

3.2.1. Levels of governance

In September 2024 the Municipality of Padua presented its CCC, the strategic document aiming at decarbonizing the city by 2030[31]. To put into action the CCC the Municipality referred to two different levels of governance: a vertical one comprehending the Veneto Region, energy distributors, Ministries, national agencies and the other eight Italian cities of the

[27] European Union, *NetZero City Mission*, 2022 https://bit.ly/4kGjO9d.
[28] The Practitioner Panel for technical and administrative staff and the Strategic Panel for Mayors, Deputy Mayors ad high-level decision makers.
[29] IREN, *9 città italiane saranno a zero emissioni entro il 2030*, 2022, https://bit.ly/41MzyPv.
[30] European Union, *Net Zero City Mission, Meet the cities*, https://netzerocities.eu/mission-cities/.
[31] Università Degli Studi Di Padova, *Padova Carbon Neutral entro il 2030: presentato alla Commissione Europea il Climate City Contract*, https://bit.ly/4iIbQut.

Mission; an horizontal one referring to territorial actors (such as the University of Padua and both private and public local actors). *Figure 2* and *Figure 3* represent the vertical and horizontal governance of the CCC.

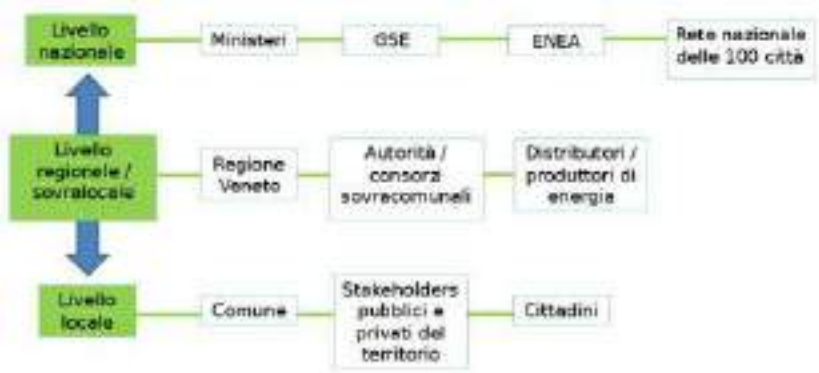

Figure 2 - Vertical governance of Padua's CCC

Figure 3 - Horizontal governance of Padua's CCC

The Mission is headed by the Mayor and the Councillor for the Environment, who identified the general directions for achieving climate neutrality by 2030. The Environment and Territorial Sector and the Financial Resources Sector are responsible for coordinating, implementing and monitoring the CCC. Also, an intersectoral working group was activated in 2022 and a specific support office will take care of the operative aspects, such as communication and information to the citizens and organization of meetings between local actors.

3.2.2. Map of the stakeholders

As for the stakeholders involved in the CCC, they are divided into the following categories: technological / infrastructure, research and education, organization, institutional, financial, political and social. The city of Padua analysed the level of interest and the influence of each

stakeholder towards the CCC. Specifically, the level of influence relates to the capacity of each stakeholder to reduce the emissions, while the level of interest is defined by the stakeholder's engagement in the plan.

Stakeholders were addressed by the Municipality of Padua through a participatory process at the initial phase of CCC: 30 local actors discussed together to define barriers and opportunities towards achieving climate neutrality. During the following stages stakeholders had the opportunity to prepare Climate Agreements, thus setting specific and impactful actions. To this date, 36 Climate Agreements have been signed and it is still possible to present applications for the stakeholders.

Furthermore, the Municipality of Padua in accordance with the stakeholders who signed Climate Agreements identified 13 strategic actions[32] which will integrate present actions. In addition, between 2021 and 2022 the city of Padua planted 10.000 trees[33]; to maximize carbon emissions' reduction, 55.000 more trees will be planted by 2030.

Finally, participatory methods were taken into action by the organization of 3 District Councils, 4 public meetings open to the whole community, several bilateral and technical meetings and educational activities in many schools of Padua. The CCC elaborated by the Municipality of Padua held in high regard the role of the population and city users (like University students and commuters). Many of the actions and projects which will be implemented will be preceded by consultations and surveys organized by the Psychology Department of the University of Padua (FISPPA). Citizens' involvement will also be facilitated by the introduction of carbon neutrality mediators, who will act in neighbourhoods, schools and companies.

More information about both the stakeholders and their classification and the Climate Agreements can be found in *Annex 1*.

[32] Strategic actions include: i) Energy upgrading of civil and industrial buildings; ii) Electrification of vehicle fleet; ii) District heating of civil and industrial buildings; iv) SMART Project - Metropolitan Tramway Network System; v) Photovoltaic on civil and industrial buildings and activation of energy communities; vi) Replacement of boilers in civil buildings and generators in industrial buildings; vii) Mobility management; viii) TPL Electric Buses; ix) Introduction of a new Low Emission Zone; x) Actions to favour cycling; xi) Promotion for the purchase of certified electricity; xii) Communication and information of citizens and agencies; xiii) Improvement of waste collection.

[33] Settore Verde Parchi e Agricoltura Urbana - Comune Di Padova, https://padova10000alberi.it/.

3.2.3. Action plan towards Padua's climate neutrality

Padua's action plan presents 26 impact paths, which refer to 5 main areas: energetic systems, mobility and transports, waste and circular economy, green infrastructures and built environment. Impact paths describe the ways in which the Municipality and the stakeholders will work to achieve climate neutrality. The 26 impact paths will result in a reduction of 857,006 tonnes of CO2, that, together with the objectives of existing strategies (those included in the PAESC, approved by the City Council in 2021) - equal to 168,017 tons of CO2. This will bring the to a reduction of almost 80% of the emissions detected in 2021. The most relevant sectors in terms of direct impacts are those of the Built Environment and Mobility, which together represent 87% of the emission gap reduction targets.

Details about the impact paths are reported in *Annex 2*.

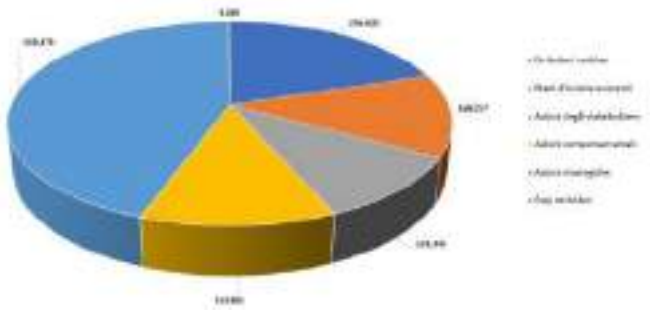

Table 7 - Actions contributing to the achievement of climate neutrality [34]

Policy instruments comprehend communication campaigns, nudging, experiential paths, incentives forms and participatory balances. Communication campaigns will be modelled on the socioeconomic characteristics of the population of reference and the language adopted will fit the different cultural segments of the citizenship. Nudging actions will be defined after analyzing survey reports by FISPPA and will also include bonus spendable in shops or to buy public services. Experiential paths aim at making people personally prove the advantages of carbon neutrality: these paths will favour citizens' acceptance of the policies implemented and their propensity to change habits. Incentives are directed to economically disadvantaged families to defeat energetic poverty and help them environmentally upgrade their homes. As for the participatory budget, neighbourhoods and district councils will be provided an annual fund to finance local projects and activities. Finally, a focus working group will work on policies regarding food to reduce waste and promote food sustainability.

[34] Climate City Contract – Piano d'azione per la neutralità climatica al 2030, cit.

IV. CONCLUSIONS

Europe's engagement to become the first carbon-neutral continent is innovative and in line with international climate standards to face climate change. In this regard, the role of cities and local communities as hubs of innovation and practice action is central. The NetZeroCity Mission programme analyzed in this paper is an excellent opportunity to ensure the foundations of a sustainable future for the young generations. Cities commitment is vital and proactive, thus taking into account the role of numerous stakeholders and the opportunities offered by an organized multilevel governance framework.

As for the case of Padua, the CCC presented is being evaluated by the European Commission and will take practical action in the following months. In this regard, the high involvement of the University and the provision of both a precise agenda and evaluation system represent key points to achieve climate neutrality by 2030.

BIBLIOGRAPHY

Journal articles

F. TATEO, F. GRASSIVARO,M. ERMANI, M. PUTHENPARAMPIL & P. GALLO, *PM2,5 levels strongly associate with multiple sclerosis prevalence in the Province of Padua, Veneto Reion, North-East Italy*. Multiple Sclerosis Journal 25(13), 2018, p.p. 1719-1727 doi:10.1177/1352458518803273.

Web sites

COMUNE DI PADOVA; *Settore Verde Parchi e Agricoltura Urbana* - Padova 1000 alberi: https://padova10000alberi.it/

COUNCIL OF THE EUROPEAN UNION, *Air pollution in the EU: facts and figures*; January 30, 2025 https://www.consilium.europa.eu/en/infographics/air-pollution-in-the-eu/

EUROPEAN ENVIRONMENT AGENCY (EEA); *Premature Deaths due to exposure to fine particulate matter in Europe*; December 10, 2024: https://bit.ly/41BEGFW

EUROPEAN UNION; *Horizon 2020*: https://bit.ly/4bJAaKc

EUROPEAN UNION; *Net Zero City* Mission - Meet the cities; https://netzerocities.eu/mission-cities/

EUROPEAN UNION; *Urban Agenda for the EU*; https://urbanagenda.urban-initiative.eu/partnerships/air-quality

EUROPEAN SPACE AGENCY (ESA); *Air pollution fluctuations over the Po Valley*; February 13, 2024: https://bit.ly/4iI3pPP

IREN; *9 città italiane saranno a zero emissioni entro il 2030*; May 9, 2022; https://bit.ly/41MzyPv

UNIVERSITÀ DEGLI STUDI DI PADOVA; *Padova Carbon Neutral entro il 2030: presentato alla Commissione Europea il Climate City Conctract*. UniPadova sostenibile: https://bit.ly/4iIbQut

WORLD HEALTH ORGANIZATION; *Air pollution*: https://www.who.int/health-topics/air-pollution#tab=tab_1

EUROPEAN UNION; *Urban Agenda for the EU*: https://urbanagenda.urban-initiative.eu/partnerships/air-quality

Legal Acts

COMUNE DI PADOVA; *Climate City Contract - Piano d'Azione per la Neutralità Climatica al 2030*. 2023

EUROPEAN PARLIAMENT AND COUNCIL OF EUROPE; *Directive of the European Parliament and of the Council on Ambient air quality and cleaner air for Europe*, 2881; November 20, 2024; http://data.europa.eu/eli/dir/2024/2881/oj

EUROPEAN COMMISSION; *The European Green Deal. Communication from the Commission.* Brussels. (2019) https://bit.ly/4ikpHrd

URBAN AGENDA FOR THE EU; *Pact of Amsterdam*; May 30, 2016

EUROPEAN PARLIAMENT AND THE COUNCIL OF EUROPE; *Horizon Europe – The Framework Programme for Research and Innovation, laying down its rules for participation and dissemination, and repealing Regulations (EU)* No 1290/2013 and (EU) No 1291/2013; April 28, 2021: https://eur-lex.europa.eu/eli/reg/2021/695/oj

EUROPEAN UNION; *Net Zero City Mission. EU Missions for climate-neutral & smart cities, concrete solutions for our greatest challenges*. (2022, April 28). Retrieved from https://bit.ly/4kGjO9d

Data

EUROPEAN ENVIRONMENT AGENCY (EEA), *From European city air quality viewer*; August 21, 2024, https://bit.ly/4iD9GNf

EUROSTAT, *Air pollutants by source sector*; Semptember 27, 2024; https://ec.europa.eu/eurostat/databrowser/product/page/ENV_AIR_EMIS

EUROSTAT, *Urban-Rural Europe - Introduction*; 2022:

https://ec.europa.eu/eurostat/statistics-explained/index.php?title=Urbanrural_Europe__introduction

EUROPEAN ENVIRONMENT AGENCY (EEA). *Air quality in Europe 2022 - Health impacts of air pollution in Europe*, 2022; November 20, 2023; https://bit.ly/4hAjvdu

EUROPEAN ENVIRONMENT AGENCY (EEA). *Contributions to EU-27 emissions of BC, CO, NH_3, NMVOCs, NOx, primary PM_{10}, primary $PM_{2.5}$, SO_2 and CH_4 from the main source sectors in 2020*; Semptember 20, 2024; https://bit.ly/4bIjD9p

EUROPEAN UNION. *Facts and Figures on the European Union*; https://european-union.europa.eu/principles-countries-history/facts-and-figures-europeanunion_en

WORLD HEALTH ORGANIZATION (WHO). (2021). *WHO global air quality guidelines - Particulate matter (PM2,5 and PM10), ozone, nitrogen dioxide, sulfur dioxide and carbon monoxide.* Genéve: World Health Organization. https://bit.ly/4kCcxY9

ANNEX I

In Annex I are reported the list of stakeholders indicated by the Climate City Contract of the Municipality of Padua. Information was retrieved from the official text, which can be found at the following link:

https://www.comune.padova.it/sites/default/files/attachment/Action%20Plan_ITA%20rev%20ott24.pdf

Stakeholders map

The following tables report the list of CCC stakeholders; they have been classified using 5 main categories (technical, research and education, organization, institutional, financial, political, social and behavioural). Moreover, the Municipality of Padua stated their level of interest and their capacity to decrease emissions. Specifically, the level of interest takes into account the submission of a Climate Agreement, the participation to complementary activities which contribute to decrease the climate impact, and the participation to workshops and meetings organized by the Municipality of Padua.

Source: Climate City Contract – Padua, pp. 40-43

A-3.2: Mappatura degli stakeholders coinvolti nel percorso di neutralità climatica			
Sistema di riferimento	**Stakeholders**	**Livello di influenza sull'abbattimento delle emissioni**	**Livello di interesse**
Tecnologico/ Infrastrutturale	AcegasApsAmga	Molto alto	Alto: ha sottoscritto un Accordo per il Clima
	ARD Ravizzello	Medio - Basso	Alto: ha sottoscritto un Accordo per il Clima
	Birra Peroni SpA	Medio	Alto: ha sottoscritto un Accordo per il Clima
	Busitalia Veneto	Molto alto	Alto: ha sottoscritto un Accordo per il Clima
	Enel Distribuzione	Molto alto	Medio-alto: ha sottoscritto un protocollo d'intesa per l'adeguamento della rete elettrica
	Fondazione CRC	Medio	Alto: ha sottoscritto un Accordo per il Clima
	Galileo Visionary District	Basso	Medio-alto: è membro del Council of Innovation
	Interporto Padova SpA	Alto	Alto: ha sottoscritto un Accordo per il Clima
	Italchimica srl	Medio	Alto: ha sottoscritto un Accordo per il Clima
	Lundbeck Italia SpA	Medio	Alto: ha sottoscritto un Accordo per il Clima
	Padova Hall	Medio	Alto: ha sottoscritto un Accordo per il Clima
	Paradigma	Medio- basso	Medio-alto: è membro del Council of Innovation
	Poste Italiane SpA	Alto	Alto: ha sottoscritto un Accordo per il Clima
	Variaco srl	Medio	Alto: ha sottoscritto un Accordo per il Clima
	Net Center	Basso	Alto: ha sottoscritto un Accordo per il Clima
Ricerca & Formazione	Fondazione Fenice	Medio - Basso	Medio-alto: ha partecipato al percorso per la carbon neutrality È membro del Council of Innovation
	Galileo Visionary District	Medio - Basso	Medio-alto: è membro del Council of Innovation
	Le Village by CA	Medio	Medio-alto: è membro del Council of Innovation
	1173 srl	Basso	Alto: ha sottoscritto un Accordo per il Clima
	Università di Padova	Molto alto	Molto alto: ha sottoscritto un Accordo per il Clima Ha sottoscritto un Protocollo d'intesa con il Comune per la neutralità climatica

A-3.2: Mappatura degli stakeholders coinvolti nel percorso di neutralità climatica			
Sistema di riferimento	**Stakeholders**	**Livello di influenza sull'abbattimento delle emissioni**	**Livello di interesse**
			È membro del Council of Innovation È sottoscrittore del Manifesto CERS
	SMACT Competence Center	Medio	Alto: ha sottoscritto un Accordo per il Clima È membro del Council of Innovation
	R2M Solution	Alto	Alto: ha sottoscritto un Accordo per il Clima
	EURAC	Alto	Alto: ha sottoscritto un Accordo per il Clima
Organizzativo	ANACI Padova	Alto	Alto: ha sottoscritto un Accordo per il Clima
	ANCE Padova	Medio	Alto: ha sottoscritto un Accordo per il Clima
	APPE Padova	Medio	Alto: ha sottoscritto un Accordo per il Clima
	ASCOM Padova	Medio	Alto: ha sottoscritto un Accordo per il Clima È sottoscrittore del Manifesto CERS
	CNA Padova	Medio	Alto: ha sottoscritto un Accordo per il Clima Ha sottoscritto un protocollo d'intesa per la Smart City
	Coldiretti Padova	Medio	Medio-alto: ha partecipato al percorso per la carbon neutrality È sottoscrittore del Manifesto CERS
	Confagricoltura Padova	Medio	Medio: è sottoscrittore del Manifesto CERS
	Confapi Padova	Medio	Alto: ha sottoscritto un Accordo per il Clima È sottoscrittore del Manifesto CERS
	Confartigianato Imprese Padova	Medio	Alto: ha sottoscritto un Accordo per il Clima È sottoscrittore del Manifesto CERS
	Confindustria Veneto Est	Alto	Molto alto: ha sottoscritto un Accordo per il Clima È membro del Council of Innovation È sottoscrittore del Manifesto CERS
	Infocamere	Medio	Alto: ha sottoscritto un Accordo per il Clima
	Ordine degli Architetti di Padova	Medio	Medio: ha partecipato al percorso per la carbon neutrality
	Ordine degli Ingegneri di Padova	Medio	Medio: ha partecipato al percorso per la carbon neutrality

A-3.2: Mappatura degli stakeholders coinvolti nel percorso di neutralità climatica			
Sistema di riferimento	**Stakeholders**	**Livello di influenza sull'abbattimento delle emissioni**	**Livello di interesse**
	Ordine dei Periti Industriali della Provincia di Padova	Medio	Medio: ha partecipato al percorso per la carbon neutrality
Istituzionale/ Regolatorio	ARPA Veneto	Medio - Alto	Alto: ha sottoscritto un Accordo per il Clima
	Camera di Commercio Padova	Alto	Molto alto: ha sottoscritto un Accordo per il Clima È membro del Council of Innovation È sottoscrittore del Manifesto CERS
	Consorzio di Bacino Padova Centro	Alto	Alto: ha sottoscritto un Accordo per il Clima
	Provincia di Padova	Alto	Alto: ha sottoscritto un Accordo per il Clima
Finanziario	Banca Etica	Alto	Alto: ha sottoscritto un Accordo per il Clima
	BCC Veneta	Alto	Alto: ha sottoscritto un Accordo per il Clima
	Cherry Bank	Alto	Alto: ha sottoscritto un Accordo per il Clima
Istituzionale/ Politico	Ministeri	Molto alto	Medio: coinvolto nel percorso della carbon neutrality con la rete italiana delle città della Mission
	Regione Veneto	Alto	Medio-alto: ha partecipato al percorso per la carbon neutrality e avviato collaborazioni con il Comune
Sociale e comportamentale	ACLI Padova	Medio	Alto: ha sottoscritto un Accordo per il Clima
	ADL Cobas	Basso	Medio: ha partecipato al percorso per la carbon neutrality
	Associazione dei Biologi del Veneto	Basso	Alto: ha sottoscritto un Accordo per il Clima
	ASVESS	Medio - Basso	Alto: è sottoscrittore del Manifesto CERS
	CAI Padova	Basso	Medio: ha partecipato al percorso per la carbon neutrality
	CISL	Basso	Medio: ha partecipato al percorso per la carbon neutrality
	Comune di quartiere	Medio	Medio-alto: hanno partecipato al percorso per la carbon neutrality Hanno avviato percorsi per l'attuazione di misure
	CSV Padova e Rovigo	Medio - Alto	Alto: ha sottoscritto un Accordo per il Clima È sottoscrittore del Manifesto CERS

A-3.2: Mappatura degli stakeholders coinvolti nel percorso di neutralità climatica			
Sistema di riferimento	**Stakeholders**	**Livello di influenza sull'abbattimento delle emissioni**	**Livello di interesse**
	Diocesi di Padova	Medio	Medio-alto: ha partecipato al percorso per la carbon neutrality È sottoscrittore del Manifesto CERS
	Fondazione Teatro Stabile del Veneto	Basso	Alto: ha sottoscritto un Accordo per il Clima
	Legambiente Padova	Medio	Medio: ha partecipato al percorso per la carbon neutrality
	UPU Padova	Basso	Medio: ha partecipato al percorso per la carbon neutrality
	Italia Nostra	Basso	Medio: ha partecipato al percorso per la carbon neutrality
	Slow Food	Basso	Medio: ha partecipato al percorso per la carbon neutrality
	SPI CGIL	Basso	Medio: ha partecipato al percorso per la carbon neutrality

Climate Agreemnents

To realize the CCC the city has put into action the creation of "Climate Agreements" between the city itself and stakeholders. Committing to a Climate Agreement means that the stakeholder will actively participate through a series of practical actions, thus contributing to achieving the Zero Emissions goal. To this day, 36 Climate Agreements have been submitted and participation is still open.

Here is a list of the 36 stakeholders who signed a Climate Agreement (source: Climate City Contract – Padua; pp. 99-100):

1. AcegasApsAmga (società soggetta a direzione e coordinamento di Hera S.p.A. che opera nei servizi ambientali e idrici, nella distribuzione di gas ed energia elettrica nel Nordest, nonché nell'illuminazione pubblica e riqualificazione energetica in tutto il territorio nazionale)
2. ACLI Padova (Associazioni Cristiane dei Lavoratori Italiani, associazione di promozione sociale italiana);
3. ANACI Padova (Associazione Nazionale Amministratori Condominiali e Immobiliari di Padova);
4. ANCE Padova (Associazione Nazionale Costruttori Edili, costituisce l'organizzazione economica di categoria in rappresentanza dell'imprenditoria dell'edilizia e dei comparti affini a livello provinciale)
5. APPE (Associazione Provinciale Pubblici Esercizi della Provincia di Padova);
6. ARD Raccanello S.p.A. (società privata che produce una gamma completa di prodotti per l'edilizia: idropitture murali per interni, grassello di calce, finiture ad elevate prestazioni per esterni, ai prodotti per l'applicazione del cappotto agli edifici);
7. ARPA Veneto (Agenzia Regionale per la Prevenzione e la Protezione Ambientale del Veneto);
8. ASCOM Padova (associazione dei commercianti della Provincia di Padova)
9. Associazione dei Biologi del Veneto (Associazione impegnata nella promozione scientifica con la realizzazione di iniziative scientifiche, culturali, ricreative, di formazione e sensibilizzazione rivolte agli associati, ai giovani, alle scuole e alla cittadinanza sui temi della salute e della tutela ambientale)
10. Banca Etica (operatore finanziario)
11. BCC Veneta Credito Cooperativo (operatore finanziario)
12. Busitalia Veneto (società operante in Veneto che svolge servizi urbani ed extraurbani di trasporto pubblico nelle province di Padova e Rovigo)

13. Camera di Commercio di Padova (ente pubblico che svolge, nell'ambito della circoscrizione territoriale provinciale, funzioni di interesse generale per il sistema delle imprese e i consumatori e promuove lo sviluppo dell'economia provinciale)
14. Cherry Bank (operatore finanziario)
15. CNA Padova (Confederazione Nazionale dell'Artigianato e della Piccola e Media Impresa, associazione di imprese la cui mission è dare valore all'artigianato e alla piccola e media impresa)
16. Confapi Padova (Associazione delle Piccole Medie Imprese di Padova)
17. Confartigianato Imprese Padova (associazione di categoria che supporta le piccole imprese artigiane nella Provincia di Padova)
18. Confindustria Veneto Est (associazione di categoria che riunisce gli imprenditori delle province di Venezia, Padova, Rovigo e Treviso)
19. CSV di Padova e Rovigo (organizza, gestisce ed eroga servizi di supporto tecnico, 99 2030 Climate Neutrality Action Plan formativo ed informativo agli Enti del Terzo Settore con particolare riguardo alle Organizzazioni di Volontariato)
20. EURAC (centro di ricerca che affronta le maggiori sfide del futuro: mantenere sane le società, promuovere ambienti intatti, promuovere l'energia sostenibile e sviluppare sistemi politici e sociali ben funzionanti)
21. Fondazione Teatro Stabile del Veneto (gestisce alcuni teatri, tra i quali il Teatro Verdi di Padova)
22. Lundbeck Italia S.p.A. (società del Gruppo Lundbeck, leader internazionale in ambito farmaceutico)
23. Infocamere SCpA (società delle Camere di Commercio per l'innovazione digitale)
24. Interporto Padova S.p.A. (centro logistico intermodale di eccellenza che progetta e realizza infrastrutture e servizi per la logistica e il trasporto)
25. Italchimica S.r.l. (azienda che crea prodotti di detergenza, disinfezione e cosmesi innovativi e sostenibili per la qualità di vita delle persone e la cura del pianeta)
26. Net Center (polo direzionale ed alberghiero situato nella zona di Padova Est)
27. Fondazione OIC Onlus (Fondazione dell'Opera Immacolata Concezione che un punto di riferimento per l'accoglienza delle persone fragili)
28. Padova Hall S.p.A. (società partecipata dal Comune che ha per oggetto l'acquisto, la vendita, la permuta, la gestione, la locazione, la sublocazione, l'amministrazione di beni immobili e mobili)

29. Birra Peroni S.p.A. (società produttrice di birre con un importante stabilimento a Padova)
30. Poste Italiane S.p.A. (impresa pubblica che opera nei settori dei servizi postali, assicurativi e finanziari, nei servizi di monetica, telecomunicazioni, telegrafici e di telematica pubblica, nonché, recentemente nel settore dell'energia, e di operazioni di riscossione, e di raccolta del risparmio postale)
31. Provincia di Padova (ente locale territoriale, è una provincia italiana del Veneto e la più popolata della regione)
32. R2M Solution S.r.l. (società di ingegneria specializzata in consulenza integrata e multidisciplinare nell'ambito del real estate)
33. SMACT Competence Center (uno degli 8 Centri di Competenza industria 4.0 nati in Italia su impulso del Ministero dello Sviluppo Economico come partnership pubblicoprivata)
34. Università di Padova (università statale italiana fondata nel 1222, fra le più antiche al mondo)
35. Varisco S.r.l. (azienda privata che progetta, produce e distribuisce pompe di tipo professionale per l'industria e per il drenaggio)
36. 1173 S.r.l. (start up che si occupa di strumenti per l'efficientamento del patrimonio edilizio).

ANNEX II

Impact paths

The 26 impact paths have been divided into 5 main areas of action: energetic systems, mobility and transports, waste products and circular economy, green infrastructures and built environment. Impact paths describe the way in which both the Municipality of Padua and stakeholders are going to achieve climate neutrality. Direct impacts have been estimated taking into account benefits coming from stakeholders' actions and report how many emissions are going to be eliminated; while, indirect impacts report co-benefits coming from these virtuous behaviours and programmes. The 26 impact paths will bring a reduction of 857.006 tons of CO2.

Source: Climate City Contract – Padua; pp. 45-46

B-I.1: Percorsi d'impatto					
Campo d'azione	Leva sistemica	Cambiamento a breve termine (1-2 anni)	Cambiamento a lungo termine (3-4 anni)	Impatti diretti	Impatti indiretti (co-benefici)
	sociale	coinvolgimento delle cittadinanze	iniziative per un coinvolgimento capillare		
Stakeholder che contribuiscono a processi d'impatto sopra elencati: AcegasApsAmga, ACLI, APPE					
Infrastrutture verdi e soluzioni NBS*	Tecnologia	Applicazione di nuove tecnologie in ambito NBS	Ulteriore sviluppo di progetti pilota a livello locale con potenziale di scalabilità	1.905 ton CO_{2eq}	Aumento dei posti di lavoro, riduzione degli impatti da eventi climatici estremi
	Democrazia e partecipazione	Identificazione di partnership strategiche locali per lo sviluppo di soluzioni innovative	Ulteriore coinvolgimento strategico per progetti su larga scala		Aumento della competitività, aumento delle sinergie territoriali
	Finanza	Monitoraggio dei risultati raggiunti per implementare nuove soluzioni	Investimenti con orizzonte temporale lungo		Attrazione di capitali per l'adattamento ai cambiamenti climatici
	Governance & Policy	Allineare la normativa locale con gli obiettivi nazionali ed europei	Definizione di standard sostenibili per lo sviluppo del territorio		Miglioramento della permeabilità dei suoli e della capacità adattiva del territorio
	Innovazione sociale	Partecipazione della cittadinanza in progetti di sviluppo NBS	Supporto [illegible] nell'identificazione delle criticità e nello sviluppo di soluzioni efficienti		Miglioramento della vivibilità cittadina, maggiore partecipazione dei cittadini nella vita pubblica
Stakeholder che contribuiscono a processi d'impatto sopra elencati: Comune di Padova, BCC Veneta, Provincia di Padova, Cherry Bank					
Ambiente costruito	Tecnologia	Sviluppi tecnologici nell'efficientamento edilizio	Ulteriori sviluppi tecnologici garantiranno edifici con prestazioni in continuo miglioramento	574.693 ton CO_{2eq}	Miglioramento della qualità abitativa, miglioramento della vivibilità degli spazi interni, aumento del valore complessivo dell'immobile
	Democrazia e partecipazione	Incremento del processo partecipativo per la riqualificazione degli edifici privati	Costante coinvolgimento della cittadinanza e del settore di riferimento nel processo di transizione ecologica dell'intero comparto		Aumento degli spazi di partecipazione
	Finanza	Definizione di nuovi modelli economico-finanziari per la riqualificazione di edifici ed impianti vetusti	Ulteriori incentivi finanziari per sostenere la transizione verso un modello di edilizia più efficiente e piena attuazione e scalabilità dei nuovi modelli identificati		Aumento della competitività tecnologica, creazione posti di lavoro, attrazione di nuovi capitali
	Apprendimento e competenze	Formazione rivolta ai settori interessati ed ai cittadini	La formazione continua garantirà un miglioramento continuo del settore edilizio privato		Coinvolgimento e sensibilizzazione verso nuove pratiche sostenibili
	Governance & Policy	Normative sull'efficienza energetica degli edifici in linea con la regolamentazione UE	Definizione di standard minimi per le riqualificazioni e per i nuovi edifici		Migliori performance energetico-ambientali del patrimonio edilizio, aumento del valore degli immobili
	Innovazione sociale	Definizione di programmi che garantiscano la riqualificazione energetica dell'edilizia residenziale pubblica	Ulteriori programmi di inclusione a favore di soggetti e categorie con particolari fragilità		Riduzione dei fenomeni di povertà energetica, miglioramento del comfort per le persone più vulnerabili
Stakeholder che contribuiscono a processi d'impatto sopra elencati: AcegasApsAmga, Italchimica, Lundbeck, Varisco, Comune di Padova, Università di Padova, APPE, Infocamere, Facciolo, BCC Veneta, Parcon, Banca Etica, Padova Hall, Cherry Bank, Net Center, Teatro Stabile, Fondazione CIC, Poste Italiane, ASCOM					

* Le azioni relative alla sezione "Infrastrutture verdi e soluzioni NBS" sono da intendersi quali azioni di compensazione e come parte di una strategia per la gestione delle emissioni residuali della città "hard to abate" (v. sezione B-2.3).

Classe di Scienze Umane

“Animali a raccolta”: l’imposizione dei nomi in *aleth*. 1,342. Uno “sfortunato” neologismo giuridico nell’*Alethia* di Claudio Mario Vittorio

Federico Catania

Abstract:

Il presente studio mira a offrire un’analisi approfondita di una neoformazione, *vocitamen,* adoperata da Claudio Mario Vittorio nell’*Alethia* (1,342), parafrasi biblica latina esametrica del libro della Genesi (sino a *Gen* 19,26) composta intorno al V sec. d.C. Il neologismo lessicale, impiegato nel passo in cui Adamo impone i nomi agli animali (*Gen* 2,19-20), è stato tradizionalmente interpretato come semplice variante di *nomen*. Mediante un approccio filologico e comparativo, che integra l’analisi dell’ipotesto biblico (*Vetus Latina*, in questo caso), l’esegesi patristica (in particolare Filone, Origene, Ambrogio e Agostino), e una rassegna di attestazioni poetiche e grammaticali tardoantiche e medievali, il lavoro intende proporre un’ampliata valutazione lessicografica del lemma. L’indagine mostra come *vocitamen* vada inteso non come semplice designazione nominale, ma come “convocazione solenne” densa di implicazioni giuridiche e sacrali, che riflettono un modello di sovranità antropologica ispirato alla regalità razionale dell’uomo creato a immagine di Dio. La scelta del lemma risponde a precise esigenze poetiche e teologiche: rappresentare Adamo non solo come colui che nomina, ma come soggetto che esercita una funzione di sovranità linguistica e ontologica, in continuità con la creatività divina. Questo contributo mette in luce la sofisticata strategia espressiva del parafraste marsigliese, che, attraverso una forma lessicale inedita, traduce in versi un concetto dottrinalmente centrale. L’articolo si propone così di valorizzare un elemento sinora trascurato, restituendo complessità e profondità all’opera vittoriana, e offrendo nuove prospettive per lo studio della poesia cristiana tardoantica.

Parole-chiave: *Alethia*, Claudio Mario Vittorio, imposizione dei nomi, latino tardo, parafrasi biblica.

INTRODUZIONE

La parafrasi biblica veterotestamentaria[1], *Alethia,* di Claudio Mario Vittorio, retore marsigliese[2], databile tra il 435 e il 450 d.C.[3], propone, come oramai ben noto, una riscrittura in versi degli episodi narrati nel libro della Genesi, dalla creazione sino alla distruzione di Sodoma e Gomorra (*Gen* 19,26)[4]. Allo stato attuale delle ricerche[5], il poema, realizzato con finalità didattico-retoriche[6], risulta composto delle seguenti quattro sezioni: *Precatio* introduttiva in 126 vv., primo libro in 547 vv., secondo libro in 558 vv. e terzo libro in 789 vv.

Il *liber primus*, in 547 esametri, si apre con un'esposizione dei principi teologici del Cristianesimo. Attraverso l'uso di un'immagine iniziale efficace e connotata, l'*Auctor* interviene, facendo rifulgere la luce nelle tenebre e immettendo nel mondo i *semina rerum.* Vengono, quindi, riproposte le opere realizzate, secondo la letterale successione temporale. Giunti al sesto giorno, desiderando Dio, per bontà, che qualcuno goda di cotanta bellezza, decide di formare l'uomo. In una digressione

[1] In merito all'inquadramento del genere letterario, rimando ad A. V. Nazzaro, "Riscritture metriche di testi biblici e agiografici in cerca del genere negato", in *Auctores Nostri* 4, 2006, pp. 435-439; A. V. Nazzaro, "Motivi e forme nella poesia cristiana antica tra Scrittura e Tradizione Classica", in *Motivi e forme della poesia cristiana antica tra scrittura e tradizione classica*, XXXVI Incontro di studiosi dell'antichità cristiana (Roma, 3-5 maggio 2007), Roma 2008, pp. 9-56.

[2] Intorno alla questione dell'identificazione del parafraste con il retore marsigliese Claudio Mario Vittorio, rimando a S. Papini, *Claudio Mario Vittorio, La Verità*, introduzione, traduzione e note a cura di S. Papini, Roma 2006, pp. 5-6; A. V. Nazzaro, *Claudio Mario Vittorio*, in *NDPAC*, 2, Genova- Milano 2007, pp. 3060-3063; U. Martorelli, *Redeat Verum. Studi sulla tecnica poetica dell'Alethia di Claudio Mario Vittorio*, Stoccarda 2008, p. 14; M. Cutino, *L'Alethia di Claudio Mario Vittorio: la parafrasi biblica come forma di espressione teologica*, Roma 2009, p. 10; I. D'Auria, *Claudio Mario Vittorio, ALETHIA, Precatio e primo libro*. *Introduzione, testo latino, traduzione e commento, a cura di I. D'Auria*, Napoli 2014, pp. 11-14; T. K. Treichel*, Alethia. Claudius Marius Victorius; eingeleitet, übers. und kommentiert von Thomas Kuhn-Treichel*, Basel 2018, pp. 10-13.

[3] M. Cutino, "Struttura, significato e modalità parafrastiche dell'Alethia di Claudio Mario Vittorio", in *Motivi e forme della poesia cristiana antica tra scrittura e tradizione classica*, XXXVI Incontro di studiosi dell'antichità cristiana (Roma, 3-5 maggio 2007), Roma 2008, p. 456. Rimando alla bibliografia per ulteriori approfondimenti.

[4] S. Papini, *La Verità*, cit., pp. 7-9.

[5] In merito alle varie proposte critiche circa l'originale estensione del poema e la divisione in libri, rimando a U. Martorelli, *Redeat Verum,* cit., pp. 15-16; M. Cutino, *L'Alethia* cit., pp. 37-56; I. D'Auria, *Alethia*, cit., pp. 16-22; D. H. Abosso, *Translation and commentary on Claudius Marius Victor's Alethia 3.1- 326*, Illinois 2015, p. 3 (n. 8); T. K. Treichel, *Alethia,* cit., p. 22 (n. 30).

[6] In merito alla caratterizzazione dell'*Alethia* rimando a M. Roberts, *Biblical Epic and Rhetorical Paraphrase in Late Antiquity*, Liverpool 1985, p. 86; D. J. Nodes, *Doctrine and exegesis in Biblical Latin poetry*, Leeds 1993, p. 12; F. Stella, *Poesia e teologia. L'Occidente latino tra IV e VIII secolo*, Milano 2001, pp. 93 ss.; Nazzaro 2007, 42 ss.; U. Martorelli, *Redeat Verum,* cit., pp. 204 ss.; M. Cutino, *L'Alethia* cit., pp. 224 ss.; R. Green, "Victorius' Vergil: Comments on a passage of the Alethia", in *Millennium* 7, 2010, pp. 54-55; D. Weber, "Die Alethia des Claudius Marius Victorius und ihr Verhältnis zu Lukrez", in V. Zimmerl-Panagl (ed.), *Dulce melos 2. Lateinische und griechische Dichtung in Spätantike, Mittelalterund Neuzeit*, Pisa 2013, pp. 198 ss.; I. D'Auria, *Alethia*, cit., pp. 51-52; D. H. Abosso, *Translation and commentary*, cit., p. 10; T. K. Treichel, *Die «Alethia» des Claudius Marius Victorius*: *Bibeldichtung zwischen Epos und Lehrgedicht*, Berlin 2016, pp. 177 ss. Una sintesi si trova in E. Falcon, *La théologie de l'histoire dans l'Alethia de Claudius Marius Victorius (Ve s.): entre ruptures et alliances*. *Traduction des Livres I, II et III a cura di E. Falcon*, Strasbourg 2024, pp. 8-15.

programmatica che ben dà prova della consapevolezza del parafraste di realizzare un'opera poetica appartenente a un preciso genere letterario[7], Vittorio avverte di doversi discostare dal dettato biblico e approfondisce la questione del sesto e settimo giorno, quest'ultimo da considerarsi "momento attivo"[8] e segno di completamento dell'opera. Quindi, il marsigliese torna alla parafrasi genesiaca, menzionando l'affidamento all'uomo del paradiso terrestre da lavorare e custodire, il divieto divino di cibarsi del frutto dell'albero del bene e del male e l'ordine di richiamo degli animali, mediante l'impiego di un lessico militare - vengono disposti, organizzati, armati come schiera dal *deus dux*[9] e denominati (vv. 305-355). Tuttavia, poiché Adamo non riesce a individuare qualcuno che gli somigli tra gli animali, Dio lo fa addormentare e crea dalla sua costola la donna, ovvero Eva (avviene un'anticipazione del nome rispetto al dettato genesiaco, ma per il resto è aderente all'ipotesto – vv. 355-387)[10]. A questa scena profondamente intrisa di stilemi della letteratura erotica, si oppone la seguente ingenuità di Eva che, a causa della tentazione del serpente, induce il primo uomo alla violazione del precetto divino (vv. 387-395). Scoperti, giacché Adamo, interrogato, confessa, ha inizio il "processo" di Dio[11] (vv. 471-519): Dio, associato al Giove olimpico, giudice, *omnipotens* (come il *deus* virgiliano) dà l'avvio alla *quaestio* (un'indagine processuale), interroga i testimoni ed emette una *sententia.* Il *liber* si conclude con la cacciata dei protoplasti dall'Eden e con la clausola escatologica, ben inquadrata nell'economia della «teologia della misericordia»[12], intorno alla possibilità di arrivo di un *alter lignum* in responsione oppositiva e salvifica a quello della "tentazione"[13]. Questa breve premessa, certamente non esaustiva ma fondamentale per introdurre la questione da affrontare, offre un quadro entro cui contestualizzare e collocare il neologismo di cui si intende trattare.

[7] A. V. Nazzaro, *Riscritture metriche,* cit., pp. 397 ss.
[8] D. J. Nodes, *Doctrine,* cit., 100-107.
[9] I. D'Auria, *Alethia*, cit., pp. 256 ss.
[10] I. D'Auria, "La creazione della donna (*Gen* 2, 21-24) nella parafrasi biblica di Claudius Marius Victorius (*Alethia* 1, 355-387)", in *Dalla civiltà classica all'umanesimo*, Napoli 2014, pp. 83-104.
[11] I. D'Auria, "Il giudizio divino (*Gn* 3, 10 - 19) nella riscrittura esametrica di Claudio Mario Vittorio (*Alethia*1, 471-519)", in *Vetera Christianorum* 44, 2007, pp. 33-57.
[12] M. Cutino, *L'Alethia* cit., p. 63.
[13] La prima identificazione del frutto proibito con la mela si rinviene proprio in un poema di parafrasi biblica, ovvero il poema dell'*Heptateuchos*, cfr. M. R. Petringa, "Adamo ed Eva e il frutto proibito nel poema dell'Heptateuchos (*gen.* 64-90). Testo critico, traduzione e commento", in *Commentaria Classica. Studi di filologia greca e latina* 4, 2017, p. 109.

I. LA NOMINAZIONE DEGLI ANIMALI: TRA POESIA PARAFRASTICA ED ESEGESI PATRISTICA

1.1. L'*impositio nominum* nella riscrittura vittoriana

Innanzitutto, intendo riprodurre il passaggio secondo il testo dell'edizione a cura di P. F. Hovingh (Mar. Victor *aleth.* 1,341-343)[14]:

«iussit adesse deus proprioque obedire tyranno, summaque post generum vocitamina dicere partis nomina ceu famulis rebus quo figeret Adam;»[15]

341 oboedire (*corr.* P[4])

Fornisco anche l'ipotesto genesiaco del versetto parafrasato ai vv. 342-343, secondo le versioni della *Vetus Latina* di Fischer[16] e della *Vulgata* di Weber[17]:

***Vet. Lat. Gen* 2,20:** «Et post haec vocavit Adam nomina omnium pecorum et omnium avium caeli et omnium bestiarum agri et secundum quod vocavit ea Adam hoc est nomen eorum usque in hodiernum diem ipsi autem Adae nondum fuit adiutorium simile illi».

***Vulg. Gen* 2,20:** «appellavitque Adam nominibus suis cuncta animantia et universa volatilia caeli et omnes bestias terrae Adam vero non inveniebatur adiutor similis eius».

Il passaggio genesiaco in esame, coincidente con l'*impositio nominum* e la sottomissione della fauna al controllo dell'uomo (*Gen* 2,19-20), si presenta parafrasato mediante un intervento di *amplificatio*

[14] P. F. Hovingh, *Claudii Marii Victorii Alethia*, *cura et studio P. F. Hovingh*, CChL 128, Turnhout 1960, p. 141.
[15] Riporto la traduzione tratta da S. Papini, *La Verità*, cit., p. 56: «Dio ordinò a tutti gli animali (*omne animal* v. 399) [...] di presentarsi e di obbedire al proprio signore e, dopo che tutti i generi furono chiamati, ordinò ad Adamo di dare i nomi, per stabilirli, a quegli esseri che erano stati partoriti, in quanto erano suoi servi». Anche I. D'Auria, *Alethia*, cit., p. 93, non si discosta moltissimo: «Dio comandò a ogni animale (*omne animal* v. 399) [...] di presentarsi e di obbedire al proprio signore e, successivamente, ordinò ad Adamo di pronunciare ad alta voce rivolto agli esseri generati i nomi dei loro generi in maniera da imporre il nome alle cose come se fossero a lui asservite».
[16] B. Fischer, *Vetus Latina*. *Die Reste der altlateinischen Bibel nach P. Sabatier neu gesammelt und herausgegeben von der Erzabtei Beuron*, 2, *Genesis*, *herausgegeben von B. Fischer*, Freiburg 1951-1954, pp. 50-51.
[17] R. Weber, *Biblia sacra iuxta Vulgatam versionem*, *adiuvantibus B. Fischer - I. Gribomont - H. F. D. Sparks - W. Thiele, recensuit et brevi apparatu critico instruxit R. Weber*, Stuttgart 2007[5] (1969[1]), p. 10.

retorica in cui Dio convoca gli animali della terra affinché Adamo gli possa imporre dei nomi, secondo la loro specie. Il v. 342 offre una forma *vocitamina*[18] che da parte di diversi studiosi è stata interpretata e tradotta quale forma di *variatio* poetica per *nomina*[19]. In effetti, se si volge uno sguardo alle traduzioni più recenti, tale valore appare riproposto anche da Treichel[20], il quale traduce *vocitamina* con "bezeichnungen", evidenziando un'incongruenza nella traduzione di Papini (vd. n. 15), ove si evincerebbe una attività di nominazione precedente a quella dell'uomo realizzata da Dio[21]. In realtà tale interpretazione, risultato, tuttavia, di un fraintendimento da parte dello studioso, non sarebbe altamente problematico. Infatti, sebbene oramai concordi nell'attribuire ad Adamo l'attività di *impositio nominum* rivolta agli animali, l'ambiguità dell'ipotesto aveva, invero, indotto alcuni Padri all'interpretazione contraria, secondo la quale Dio avrebbe posto Adamo nelle condizioni di saper pronunciare il "nome proprio" di ciascuna creatura[22]. Infine, nell'intento di fornire un quadro completo delle proposte traduttive, appare inserirsi nella medesima scia anche Falcon[23], la quale, rendendo

[18] Così si legge nel *Parisinus Latinus* 7558 (IX sec., f. 54^{v}), conservato a Parigi nella Bibliothèque Nationale de France. Nelle precedenti edizioni solo G. Morel, *Cl. Marii Victoris oratoris Massiliensis, ALHQEIAS, seu Commentationum in Genesin lib. III. Epigrammata Varia vetusti cuiusdam auctoris, inter quae sunt et aliquot psalmi versibus redditi*, Parisiis 1560, p.18 accoglie *vocitamina*: I. Gagny, *Christiana et docta divi Alchimi Aviti Viennensis archiepiscopi, et Claudii Marii Victoris Oratoris Massiliensis, poëmata, aliaque non poenitenda*, 1536, p. 188 (ripreso anche da G. Fabricius, *Poetarum veterum Ecclesiasticorum Opera Christiana, et operum reliquiae atque fragmenta*, Basileae 1564, p. 318 e J. P. Migne, *Claudii Marii Victoris commentariorum in Genesin libri tres*, PL 61, Parisiis 1847, p. 945), invece, accoglie un v. 342 profondamente alterato *scilicet ut cunctis bene congrua nomina rebus / inderet*: ... Per una disamina approfondita relativa alla tradizione manoscritta e alle edizioni critiche rimando a I. D'Auria, *Alethia*, cit., pp. 57-59 e a E. Falcon, *La théologie,* cit., pp. 8-12.

[19] Rimando a C. Schenkl, *Claudii Marii Victoris oratoris Massiliensis Alethia*, CSEL 16, Vindobonae 1888, p. 162 o P. F. Hovingh, *Alethia*, cit., p. 295: «*vocitamen* i. q. *vocamen*».

[20] Riporto la traduzione dei vv. 341-343 tratta da T. K. Treichel, *Alethia,* cit., p. 117: «(darum also) befahl Gott allen zu kommen und ihrem Herrn zu gehorchen, und (gebot) Adam danach, erste Gattungsbezeichnungen zu sagen, damit er den gewonnenen Dingen wie Dienern Namen beilege».

[21] T. K. Treichel, *Alethia,* cit., p. 116 (n.103): «Ich fasse *partis nomina ... quo figeret Adam* als Nebensatz auf, wobei ich *quo* mit Schenklis Index grammaticae et elocutionis s.v. 494 wie *ut* übersetze. Ganz anders *Papini*: „Dopo che tutti i generi furono chiamati, ordinò ad Adamo di dare i nomi, per stabilirli, a quegli esseri che erano stati partoriti, in quanto erano suoi servi" (die Übersetzung ist inhaltlich problematisch, weil sie den Eindruck erweckt, Gott habe zuerst die Gattungen mit Namen gerufen, was nach Gen 2,19f ja erst Adam tut)».

[22] C. Schiano, "La genesi del linguaggio: memorie lucreziane in Cyrano de Bergerac", in *Atene e Roma* 8, 2014, p. 251 (n.42) «A ben vedere, il modo in cui si esprime il testo biblico [...] conserva dei margini di ambiguità: [...] «Proprio quello è il suo nome» perché così ha scelto Adamo, o perché Adamo è stato messo da Dio nelle condizioni di riconoscerne il nome naturale? Verso quest'ultima interpretazione sembra pendere una parte rilevante della patristica (cfr. Clem. al. *Strom*. I 21, 135, 3; Eus. *PE* XI, 6, 9-10; Jo. chrys. *in Gen*. XIV 4-5, PG 53, 116)». Anche Flavio Giuseppe sembra suggerire una possibile interpretazione, cfr. G. Büsing, "Beobachtungen zum Verständnis der erzählten Namengebung in Gen 2, 19 f.", in *Bibel und Midrasch: zur Bedeutung der rabbinischen Exegeese für die Bibelwissenschaft*, 22, pp. 191208.

[23] Riporto la traduzione dei vv. 341-343 tratta da E. Falcon, *La théologie,* cit., p. 51: «Dieu enjoignit de se présenter et d'obéir à leur vrai souverain, puis à Adam, de déterminer les appellations globales des espèces afin qu'il impose un nom aux êtres ainsi mis au monde comme à ses serviteurs».

summa… vocitamina con "les appellations globales", mira a intendere una prima formulazione da parte del protoplasto dei nomi "generici" e una seconda dei nomi specifici.

1.2. La sovranità di Adamo nella tradizione dei Padri

L'episodio proposto si propone quale momento essenziale nell'economia della teologia vittoriana, profondamente influenzata, come sarà esposto, dalle precedenti interpretazioni esegetiche. Attribuire un nome significa cogliere l'essenza stessa di ciò che si nomina. Secondo la tradizione biblica e patristica[24], tale capacità non nasce dall'uomo, ma da Dio, che la trasmette all'uomo quando lo crea "a sua immagine". In questa luce si comprende la scena di Adamo che nomina gli animali: un atto che, nella lettura di Filone e Origene, riflette la partecipazione umana a un sapere divino, radicato nella conoscenza originaria del creatore. Agostino, nel *De Magistro*, radicalizza questa prospettiva, sostenendo che la vera comprensione non viene dalle parole, ma dallo Spirito che abita nell'uomo e che è Cristo stesso, inteso come Verità vivente. È Lui che rende intelligibile il mondo, aprendo nel cuore umano la via alla conoscenza autentica. Ancora, nel *De Opificio* di Filone[25], influenzato dalla dottrina platonica delle idee, l'uomo originario viene inteso come il compimento perfetto dell'ideale: dotato di ragione, intelligenza, moralità e bellezza. Lo spazio in cui egli vive viene descritto attraverso un'immagine politica: è una sorta di ordinamento statale, in cui l'uomo svolge la funzione di sovrano, la legge naturale funge da diritto, e tutte le realtà appaiono come soggetti governati. L'assegnazione dei nomi agli animali diviene un'allegoria della regalità e dell'intelligenza sovrana dell'uomo primordiale[26]. Si evince, pertanto, un evidente ribadimento del fatto che l'uomo deterrà la sovranità sugli animali, come affermato altrove in *Gen* 1,28 e nel *Sal* 8[27] oltre che l'aspetto della partecipazione dell'uomo all'esercizio del dominio divino (cfr. *Sal* 147,4; *Is* 40,26)[28]. Dal punto di vista storico, inoltre, l'atto del "nominare" appare pregnante e ben significativo, poiché «attribuire un nome a qualcuno o a qualcosa è praticamente sempre, nel Vicino Oriente antico, un segno di sovranità da parte di un superiore nei confronti di un inferiore»[29]. Se, adesso, ci volgiamo all'esegesi ambrosiana e

[24] E. Falcon, *La théologie,* cit., p. 203.
[25] G. Büsing, *Beobachtungen zum Verständnis*, cit., p. 200.
[26] G. Büsing, *Beobachtungen zum Verständnis*, cit., p. 200: «Filone ha in mente una corte regale, quando descrive la scena (*Op*. 148)».
[27] P. Colella, "La Costola di Adamo: Gen. 2, 18-24", in *Apollinaris*, 67 3-4, 1994, p. 859.
[28] J. C. Gertz, *Das Alte Testament Deutsch. 1, Das erste Buch Mose, Genesis: die Urgeschichte Gen 1-11. übers. und erklärt von Jan Christian Gertz*, Göttingen 2018, p. 123.
[29] J. A. Soggin, *Genesi*, *a cura di J. A. Soggin*, Genova 1991, p. 72. Così anche G. von Rad, *Das Alte Testament deutsch, IV: Das erste Buch Mose. Genesis Kapitel XXV,19-L,26*, *übers. & erkl. G. von Rad*, Göttingen 1953, p. 67.

agostiniana, tenute ben a mente dal marsigliese[30], è possibile trarre ulteriori spunti di riflessione utili alla valutazione complessiva del contesto considerato. Innanzitutto, il vescovo di Milano, nel tentativo di giustificare l'evidente incongruenza circa il richiamo di Dio dei soli animali selvatici e degli uccelli e la successiva imposizione dei nomi a questi due gruppi e, in più, agli animali domestici non convocati (*Gen* 2,19-20), propone l'idea di una collaborazione tra Dio e uomo: Dio è colui che presenta all'uomo ciò che proviene dalla sfera dell'alterità, della natura indomita o del cielo; al contrario, spetta all'uomo il compito di raccogliere, ordinare e classificare gli animali domestici, cioè quelli già integrabili nella sua sfera di dominio. Dunque, mentre il primo atto di raccolta è da attribuirsi all'azione sovrana di Dio, il secondo dipende dalla diligenza dell'uomo[31]. Ancora, in un passo successivo, Ambrogio, che adotta un'esegesi di tipo allegorico e associa le bestie ai moti irrazionali dell'anima (*Parad.* 11,51-52), riconosce una facoltà superiore conferita all'uomo: la capacità di discernere, attraverso il giudizio prudente, l'essenza e la natura di ogni creatura. Dio stesso ha condotto davanti a lui tutti gli esseri viventi, affinché potesse constatare che la propria intelligenza li sovrastava tutti. Tuttavia, venendo meno all'obbedienza, l'uomo è caduto, pretendendo di sostituire alla fedeltà all'ordine divino la propria volontà autonoma[32]. Per Agostino, invece, Dio ha inteso manifestare all'uomo la sua superiorità sugli animali conducendo al suo cospetto tutte le creature viventi, per osservare come egli le avrebbe chiamate e quali nomi avrebbe loro assegnato. Attraverso questo gesto simbolico, si evidenzierebbe la preminenza dell'essere umano su tutte le bestie irrazionali: una superiorità fondata sulla ragione, poiché solo la facoltà razionale consente di distinguere, giudicare e denominare ciascun essere secondo la propria natura[33]. Tuttavia, aggiunge, mirando a spiegare come siano stati condotti gli animali al cospetto di Adamo e non sembrando influenzare il nostro parafraste, che Dio non ha radunato le fiere, né è scaturito da una nube un comando udito e compreso da queste. Dio muove tutte le cose nel tempo, non per azione diretta, ma tramite il ministero degli angeli. Questi, partecipando al Verbo divino, comprendono ciò che dev'essere compiuto e agiscono nel mondo visibile secondo la volontà eterna[34]. Pertanto, sulla base di questo introduttivo quadro esplicativo, appare ben chiaro, come già individuato da D'Auria (vd. n. 11), che la trattazione dell'episodio ben si conformi a una riscrittura in versi caratterizzata dall'utilizzo di stilemi di natura giuridica e militare.

[30] Per una sommaria trattazione delle fonti esegetiche adoperato, rinvio a I. D'Auria, *Alethia*, cit., pp. 39 ss.
[31] Ambr. *Parad.* 11,49.
[32] Ambr. *Parad.* 11,52.
[33] Aug. *gen. c. Manich.* 2,11,16.
[34] Aug. *gen. ad litt.* 9,14,24.

II. LA NEOFORMAZIONE *VOCTITAMEN*

2.1. Riflessioni intorno a un neologismo poetico vittoriano

Quanto sopra riportato, ovvero ipotesto genesiaco ed esegesi patristica, consente di ben contestualizzare l'episodio parafrasato, offrendoci, quindi, la possibilità di approfondire e ben chiarificare l'uso del neologismo lessicale *vocitamen*, rendendone adeguatamente il significato e le peculiarità semantiche. A proposito dell'interpretazione della neoformazione, D'Auria[35] sostiene che *vocitamen* sia una forma deverbale da una base *vocito* con valore intensivo, da intendersi con "chiamare ad alta voce". In più, l'espressione «vocitamina dicere», rafforzata da *summa*, indicherebbe una convocazione solenne degli animali, nominati per genere. L'osservazione della studiosa appare, tuttavia, insufficiente: rendendo perifrasticamente il lessema ("chiamare ad alta voce" - vd. n. 15), di fatto, svilisce la pregnanza di un neologismo poetico, riducendolo soltanto a un incremento del volume della voce necessario al coinvolgimento del gruppo di animali. È indubbio che, a causa della scarsità di menzioni nelle fonti lessicografiche e di attestazioni successive, la possibilità di individuare un'alternativa di traduzione è stata fortemente disincentivata, attribuendo alla forma il significato di "nome".

Desiderando, pertanto, vagliare più attestazioni, al fine di cogliere maggiormente la pregnanza della neoformazione, si propone il seguente itinerario. Innanzitutto, appare ben utile far riferimento a un autore ben noto al *Massiliensis*, ovvero Giovenco[36], ad esempio in Iuvenc. 4,360: «Et pariter luctu oppressam vocitare sororem»; 4,694: «Heliam vocitare putat. Tum concitus unus»[37]. La seconda attestazione potrebbe aver giocato un ruolo decisivo, nell'intendimento da parte di D'Auria della neoformazione *vocitamen,* in quanto il costrutto «magna...voce vocabat» (Iuvenc. 4,692), viene poi sostituito al v. 694 con il solo *vocitare*, quasi volendone, mediante l'uso di una sola forma, riprodurre interamente il significato[38]. Se, allora, si effettua una ricerca delle attestazioni all'interno della prosa

[35] I. D'Auria, *Alethia*, cit., pp. 253-254. La studiosa riporta anche tutte le attestazioni successive d'età altomedievale, conferendo al lemma (sulla base di quanto riportato dal Du Cange) sempre e solo i significati di *vocabulum, nomen, appellatio.*

[36] I. D'Auria, *Alethia*, cit., p. 39 (ma per gli esempi vedi anche le pagine seguenti).

[37] D. De Gianni, *Iuvencus. Evangeliorum Liber Quartus*. Introduzione, testo criticamente riveduto, traduzione e commento a cura di D. De Gianni, Stuttgart: Steiner, 2020, p. 399 (riferendosi a Iuvenc. 4,694): «L'intensivo sostituisce la forma semplice *uocare* [...]. Negli epici classici e nella poesia esametrica latina *uocitare*, colloquiale come in genere tutte le forme intensive, è quasi del tutto assente».

[38] Iuvenc. 4,692-694: «Et Christus magna genitorem voce vocabat / Hebraeae in morem linguae; sed nescia plebes / Heliam vocitare putat...».

tecnica e grammaticale, si rinviene un'attestazione particolarmente significativa e dirimente, in grado di fornire una chiave interpretativa illuminante: Paul. Fest. p. 251: «citare enim vocitare est». Soffermandoci sulla valenza giuridica del verbo *citare*[39], è possibile cogliere una suggestione tale da poter sollecitare una nuova ricerca volta a indagare, innanzitutto, i derivati nominali della base *vocare*. A proposito di questi, risulta proficuo segnalare un riferimento di natura grammaticale (morfologia derivazionale), tale da porre innanzi una interessante valutazione, ovvero Virg. gramm. *epist.* 1,111,21: «Sunt tamen quaedam nomina quae duas per omnia declinationes habere noscuntur ut laetitia laetamen, vocatio vocamen». Si riscontra, pertanto, una consapevolezza nella possibilità di individuare due formazioni deverbali, su cui, probabilmente è possibile fornire qualche altra informazione. Effettuando una ricerca lessicografica sul Forcellini, si avverte come *vocamen*[40]e *vocatio*[41], pur mantenendo un significato primario affine, in virtù della comune radice e ricostruzione etimologica, probabilmente a causa del differente suffisso derivativo e di specifiche questioni extralinguistiche, si diversificano in merito alla possibilità di accogliere accezioni differenti. Essendo ancor più specifici, la forma *vocatio* si specializza, accogliendo differenti significati traslati[42], mentre la forma *vocamen* si limita a mantenere il proprio significato più diretto.

A questo punto si intende indagare la possibilità che tale significato traslato sia, in effetti, stato accolto anche nei derivati deverbali del frequentativo *vocito*. Innanzitutto, nel latino medievale[43], è possibile rinvenire un significato estensivo attribuito al sostantivo *vocitatio* ("convocazione, raccolta"), tale per cui sarebbe possibile interpretare un naturale slittamento per la neoformazione presa in esame. Infatti, svolgendo una ricerca in merito alle attestazioni poetiche delle forme *vocatio* e *vocitatio*, si riscontra che soltanto la prima perviene e solo a partire dall'età umanistica: Stefan. *opus metr.* 2,190: «Compatiens populis, quos pura vocatio traxit»; Quatrar. *bursa* 1,121: «Non hesit cuntis natura vocatio rebus»; Berni *carm*. 8,12: «Virgo, quam celebri vocatione». Certamente, non stupisce che accanto alle

[39] «...plerumque technice de magistratibus in re publica et re iudiciaria i. q. arcessere, convocare, evocare, excire, in ius vocare, adesse iubere, accusare sim». (*ThlL* 3, 1200,38-40).

[40] Forcellini IV, p. 550: «VŎCĀMEN, ĭnis, n. 3. (voco) nomen, appellatio».

[41] Forcellini IV, p. 550: «VŎCĀTĬO (vocacio), ōnis, f. 3. (voco) Vocatio pro vacatio. V. VACO, VACATIO. - Vocatio est actus vocandi, [...] Speciatim est invitatio ad cenam, [...] Item actio vocandi in jus, [...] Item, apud Ecclesiasticos scriptores, actio divina, qua quis ad veram religionem vocatur ac proinde ad vitam aeternam, [...] Item electio divina ad aliquod munus, dos divinitus immissa».

[42] Tra questi ricordo quello giuridico e in particolare la costruzione polirematica «in ius vocatio». A tal proposito A. Berger, *Encyclopedic dictionary of Roman law*, Philadelphia 1952 riporta *ad loc.*: «*In ius vocatio.* The summons of a debtor by the plaintiff to appear in iure (before the magistrate) where the plaintiff will claim his right».

[43] DMLBS *ad loc.*: «*vocitatio* [LL = address], **1** name, designation [...].; **2** (act of) summoning, summons, citation».

forme con suffisso derivativo in *-tio* compaia in poesia una forma iterativa con suffisso *-en* (*-mina*) ben comoda metricamente e di maggior pregnanza semantica[44].

2.2. Su alcune attestazioni di *vocitamen-vocitare* nel latino medievale

Posta questa premessa, si intende offrire alcuni passi esemplificativi circa il valore da attribuire alla neoformazione vittoriana *vocitamen*, tentando di integrare quanto affermato da D'Auria (vd. n. 35) in merito alle attestazioni del lessema in età altomedievale. Innanzitutto, non appare superfluo segnalare che la forma intensiva *vocitare* viene adoperata anche in un'altra occasione da Vittorio e in maniera altamente significativa, con sfumatura giuridico-militare: *aleth.* 2,518: «Non vocitante deo, propria qui voce trementem». Soltanto l'ordine[45] di Dio, infatti, consente a Noè, "nuovo Adamo secondo i santi Padri"[46], e alla sua famiglia di abbandonare l'arca, a seguito del ritiro delle acque prodotte dal diluvio universale. A questo punto, non intendendo escludere che il lessema possa intendere anche semplicemente il "nome", giacché il significato della base è evidente, è possibile, tuttavia, riscontrare alcune peculiari sfumature tali da arricchire la pregnanza semantica di siffatta neoformazione.

Innanzitutto, è di notevole interesse segnalare alcune attestazioni nelle quali, seppur il sostantivo miri a designare un soggetto, quest'ultimo appare esser destinatario di una "speciale relazione", in quanto scelto o in stretto rapporto con Dio o Cristo. Ad esempio, nella *Vita Sancti Galli confessoris*, una vita metrica di dubbia attribuzione, dedicata a un monaco del IX sec., San Gallo[47], la forma di nostro interesse appare ben due volte: al v. 925 (MGH *Poetae* 2, p. 452): «horum si lector gestis vocitamina nosse»; e al v. 1366 (MGH *Poetae* 2, p. 463): «presbiter adveniens vocitamine Willimar atque». Se nel primo caso si tratta dei nomi di due leviti particolarmente cari e apprezzati dal santo uomo e portati assieme a lui al sinodo indetto; nel secondo si tratta del nome di un presbitero quasi inviato da Dio per

[44] Il suffisso *-men* viene considerato dal colorito più antico e venerando nella lingua poetica, cfr. A. Lunelli (ed.), *La lingua poetica latina*, Bologna 1974, p. 99 (si tratta della traduzione del saggio di H. H. Jannsen "De Kenmerken der Romeinsche dichtertaal"); ancora i neologismi in *-mina* vengono creati per comodità metrica (p. 163), in più sono comode le forme iterative del verbo (p. 162), cfr. A. Lunelli (ed.), *La lingua poetica latina*, cit. (si tratta della traduzione del saggio di M. Leumann "Die lateinische Dichtersprache").

[45] Appare significativo, infatti, che Papini abbia reso il costrutto *non vocitante deo* con «se non l'ordina Dio», cfr. S. Papini, *La Verità*, cit., p. 89. Treichel e Falcon, probabilmente, banalizzano: il primo opta per «Wenn Gott nicht ruft», cfr. T. K. Treichel, *Alethia,* cit., p. 183; la seconda per «tant que cela n'a pas été prononcé par Dieu», cfr. E. Falcon, *La théologie,* cit., p. 95.

[46] Cfr. S. Papini, *La Verità*, cit., p. 84 (n. 18): «Il titolo, applicato a Noè, di «primo genitore» è da spiegarsi in virtù dell'alleanza stabilita da Dio con la sua discendenza. Si tratta di un'idea elaborata già da Filone (*Quaestiones sulla Genesi* 2, 17; 2, 45; 2, 66 [...])».

[47] E. Dümmler, *Vita Galli metrica*, *edidit E. Dümmler*, MGH *Poetae 2*, 1884, p. 266.

sostenere il monaco provato dalle lotte. Ancora nel Carme 5 del vescovo Radbodo di Treviri al v. 64 (MGH *Poetae* 4, p. 171), anch'essa una vita metrica databile al X sec. e dedicata a Lebuino, apostolo dei Sassoni[48], viene adoperata la forma *vocitamen* nel contesto della spiegazione "etimologica" del nome dell'"inviato" di Dio: difatti dall'unione di "caro amico" e di "di Cristo" si ottiene l'appellativo del santo: «Haec duo si copules, sancti vocitamen adimples». *Nel Liber prefigurationum Christi et Ecclesie*, poema anonimo di 2670 esametri, di uso scolastico, databile alla fine dell'XI secolo, consistente in una riscrittura e un'esegesi di tipo tipologico dalla Genesi al libro dei Maccabei[49], è possibile rinvenire alcuni elementi significativi: al v. 512 del *liber Genesis,* «Sancta Rebecca suo quod de vocitamine signat»; e al v. 1438 del *liber Iudices,* «est equidem Christo vocitamen "iusticie sol"»[50]. Nel primo caso si tratta del nome di Giacobbe, dato da Rebecca, quale prefigurazione di Cristo, nel secondo del nome di Sansone, il cui nome "sole di popoli" è accostabile a quello di Cristo "sole di giustizia".

Dopo questa prima rassegna che non sembra discostarsi eccessivamente, se non per una lieve sfumatura contenutistica, intendo offrire alcune attestazioni di *vocitamen/vocitare* ove si evince una specifica connotazione sacrale nell'atto di "chiamata", ovvero un'invocazione. Ad esempio, nel *De bellis Parisiacae urbis* del monaco Abbone di San Germano, poema databile al X sec. che narra dell'assedio di Parigi da parte dei Normanni[51], al v. 400 (MGH *Poetae* 4, p. 91), la forma *vocitantibus* in «Germanum respondet et urbs vocitantibus ipsum», allude a coloro che, in un momento di grave lutto e afflizione, ove il popolo si percuote per il dolore e soffre, invocano il santo Germano, onorato e venerato, il cui nome risuona per tutta Parigi a seguito delle accorate suppliche prodotte. Più significativo è il valore che assume *vocitare* nella *Visio Wettini* di Valafrido Strabone, opera in versi ascrivibile al IX sec. e riguardante la narrazione delle visioni dell'oltretomba avute dal monaco Wetti sul punto di morte[52]. Al v. 914 (MGH *Poetae* 2, p. 332), infatti, in «me vocitare iubet residensque infigere cerae», la forma verbale allude all'atto di convocazione del giovane Valafrido da parte del monaco che, dopo le visioni avute, pur ammalato, non mostrando segni di deperimento e richiamando tutti alla preghiera e a chiedere perdono, ordina che quanto visto venga messo per iscritto a memoria futura. Infine, a suggellare questo breve percorso si pone l'ultima testimonianza, molto probante sia a

[48] P. von Winterfeld, *Radbodus Traiectensis episcopus, Carmina*, *edidit P. von Winterfeld*, *MGH* Poetae 4,1, 1899, p. 161.

[49] S. Leroy, "Le Liber prefigurationum Christi et Ecclesie: un commentaire de la Bible en hexamètres actyliques", in *Pragmatique du commentaire* 2018, pp. 245-261.

[50] Si rinvia *ad loc.* a G. Dinkova – Brunn, *Liber prefigurationum Christi et ecclesie. Liber de gratia Novi Testamenti cura et studio Greti Dinkova-Bruun*, CC CM 195, Turnhout 2007, pp. 3-115.

[51] P. von Winterfeld, *Radbodus*, cit., pp. 71-73.

[52] E. Dümmler, *Vita Galli metrica*, cit., pp. 259-260.

livello semantico, sia perché la forma occupa la stessa posizione nell'esametro della forma *vocitamina* in *aleth.* 1,342. Si tratta del carme 32 in distici elegiaci del *Codex epistolarum Tergernseensium* di Froumund, opera che il monaco benedettino dell'XI sec. compose, combinando lettere e liriche[53]: al v. 43 (MGH *epp.* 3, p. 82) nello stico esametrico «Vos iterum revoco vocitamine valde preclaro», all'interno di un "canto" di addio, l'autore, in un'ultima manifestazione d'amore, riproponendo quanto svolto sino ad allora, convoca i ragazzi in una solenne adunanza, ammonendo loro a continuare a seguire i propri insegnamenti e a dedicare maggiore attenzione alla composizione di *carmina* invece che dilettarsi con giochi incapaci di eguagliare i primi nello spessore formativo. Tale ultima testimonianza poetica, preziosa per la posizione occupata nell'esametro da *vocitamine*, per il senso che la forma assume anche in relazione al successivo *confluite pueri...* (v. 44), nonché anche per l'accorata difesa della poesia, offre un terreno fertile per l'ultimo e decisivo passo in avanti.

2.3 *Vocitamen*: uno sfortunato neologismo giuridico?

A questo punto, a seguito di tale indagine e di tali riscontri, è possibile giungere ad alcune conclusioni. Innanzitutto, se ci si rivolge all'ipotesto genesiaco, appare evidente che Vittorio stia parafrasando la *Vetus* e non la *Vulgata*, in quanto il quasi-stico «summaque post generum vocitamina» (v. 342) non è altro che una forma di *amplificatio* con valenza ecfrastica[54] del sintagma *post haec* in *Gen* 2,20 – assente nella *Vulgata*[55]. In effetti, un altro elemento che induce a considerare tale uso esclusivo, nel passo in esame, è l'uso nel v. 339 di *adhuc* che rende ἔτι, presente nell'*Itala* ma assente in altre versioni e nella *Vulgata*[56]. Inoltre, appare significativo, volgendo l'attenzione verso il *liber Genesis* del poema dell'*Heptateuchos*[57], che al v. 42, che parafrasa proprio *Gen* 2,20 («Ilicet exhibitis animantum ex ordine turbis»), compaia la locuzione *ex ordine*, comoda metricamente e di fatto ricorrente in poesia nella medesima posizione, la quale, considerando che l'ipotesto del poema suddetto è quello della *Vetus Latina*[58], potrebbe, in questo caso, non intendere solamente una "disposizione in ordine", ma,

[53] Rimando a K. Strecker, *Codex epistolarum Tergernseensium. Froumund*, *edidit K. Strecker*, *MGH* epp. 3, 1925, pp. V ss.
[54] M. Roberts, *Biblical Epic*, cit., pp. 190 ss.; U. Martorelli, *Redeat Verum,* cit., pp. 67 ss.; T. K. Treichel, *Die «Alethia»*, cit., pp. 107-113.
[55] Sulla questione dell'ipotesto adoperato dal parafraste, la critica più recente riconosce un uso combinato di *Vetus Latina* e *Vulgata*, cfr. ad esempio I. D'Auria, *Alethia*, cit., pp. 52-57; D. H. Abosso, *Translation and commentary,* cit., p. 6; T. K. Treichel, *Die «Alethia»*, cit., pp. 15-21.
[56] M. Cutino, *L'Alethia* cit., p. 123 (n. 105).
[57] Per un inquadramento complessivo dell'opera rimando a M. R. Petringa, *Il poema dell'Heptateuchos. Itinera philologica tra tardoantico e alto medioevo*, Catania 2016.
[58] M. R. Petringa, *Il poema dell'Heptateuchos*, cit., p. 29.

traducendo a calco e integrando il *post haec* dell'ipotesto, alludere a "dopo il comando"[59], conferendo una sfumatura di tipo giuridico al passo, anche sulla base dell'esegesi dei Padri. Il che ben si giustificherebbe, considerando che il parafraste adopera poco dopo delle espressioni giuridiche (*formatur e noxale)* ai vv. 65 e 68[60]. Inoltre, e non da ultimo, l'uso del verbo *dicere* in *aleth.* 1,342, seppur intenda l'atto del nominare, non escludo alluda a una seconda creazione[61] "umana" operata da Adamo: come infatti, secondo l'etimologia varroniana (riproposta anche da Cicerone)[62] il console nomina (ovvero "crea") il dittatore affinché questi intervenga per una specifica situazione "speciale", allo stesso modo Dio nomina (crea) Adamo rendendolo "capace" di straordinarie prerogative.

A questo punto, appare ben chiaro che, a causa di un ipotesto estremamente succinto e sintetico, a fine di maggiore perspicuità e chiarezza, il parafraste intende esplicitare la natura di quanto detto prima, adoperando una neoformazione alquanto pregna di significato. Le traduzioni di Treichel e di Falcon sacrificano la valenza di *post* quale preposizione impropria (svilendo anche l'*amplificatio* operata in relazione al sintagma della *Vetus*), reggente un accusativo neutro plurale (*pro singulari*) e attribuiscono ad Adamo una duplice azione di chiamata, diversificata in una preparatoria-generica e in una attiva-specifica. In effetti, soltanto la Papini ha conservato nella sua resa traduttiva tale funzione morfosintattica di *post*, ovviando, attraverso una formula più libera, al problema della corretta traduzione del neologismo. A mio avviso, inoltre, la scelta della Papini, oltre a essere adeguata, in quanto rispettante l'ipotesto e la volontà amplificativa dell'intervento di Vittorio, non è stata adeguatamente compresa da Treichel (vd. n. 21), a causa di un fraintendimento tra le accezioni del "chiamare / dire il nome" e "chiamare / convocare".

Pertanto, semplicemente descrivendo la scena di *Gen* 2,19-20, si evince come da parte di Dio avvenga una vera e propria convocazione di tutti gli animali di fronte ad Adamo, affinché questi possa compiere l'*impositio nominum*. A partire dall'attestazione di Paolo Diacono, la forma *vocitare* starebbe per *citare* che, nella sua accezione giuridica, come mostrato, intenderebbe diverse azioni come *convocare* o *in ius vocare.* L'*in ius vocatio* (vd. n. 45), secondo quanto sopra illustrato, non era altro che una pratica legale, consistente nel convocare qualcuno in tribunale: per essere ancor più precisi (e sintetici) una persona poteva richiamarne un'altra davanti a un magistrato per risolvere una controversia legale. Di

[59] Cfr. *ThlL*, 9,2 957,76-958-50.

[60] M. R. Petringa, *Adamo ed* Eva, cit., pp. 108 e 110. Sui contatti tra l'*Alethia* e il poema dell'*Heptateuchos*, seppur non si possa stabilire la priorità cronologica tra i due, rinvio a K. Pollmann, "Der sogenannte Heptateuchdichter und die Alethia des Claudius Marius Victorius. Anmerkungen zur Datierungsfrage und zur Imitationsforschung", in *Hermes* 120, 1992, p. 498 e a M. R. Petringa, *Il poema dell'Heptateuchos*, cit., pp. 26-27.

[61] *ThlL*, 5,1 982,16-17.

[62] Varro *ling.* 5, 82; Cic. *rep.* 1, 63.

conseguenza, considerando anche l'impostazione teologica dell'opera[63], è possibile intravedere in Dio quell'essere che vanta un diritto sui convocati, anche perché sono stati creati da Lui, e che li conduce di fronte a un *alter auctor*, ovvero Adamo (*dictator*, in quanto "creato" da Dio), affinché, quasi come secondo creatore dia nome, ovvero vita e riconoscimento, agli animali della terra. Il neologismo *vocitamen*, pertanto, in considerazione della scena, dell'ipotesto, delle successive attestazioni che fanno emergere una connotazione giuridico-sacrale nonché di "adunanza", sarebbe da tradursi come "convocazione", mantenendo quella notazione giuridica ben confermata dallo stile del poeta e già riconosciuta all'interno del passo in esame (vd. n. 11). Tale scelta stilistica vittoriana, considerando la pressoché totale assenza di attestazioni poetiche delle forme *vocatio* e *vocitatio,* sarebbe, inoltre stata dettata dalla volontà di introdurre un "neologismo giuridico" in poesia, probabilmente sfortunato e non affermatosi, differenziandolo dal *simplex vocamen*, col significato di *nomen*. Per quanto riguarda l'accostamento dell'aggettivo *summa*, non lo riferirei al volume della *vox*[64], bensì, riaccostandomi alla traduzione della Papini, all'adunanza generale di tutte le creature (non escluderei, tuttavia, che l'aggettivo possa far riferimento al *summus auctor,* vd. ad esempio *aleth.* 1,193-194, poiché è Lui a compiere la convocazione).

Pertanto, a conclusione di quanto sopra sostenuto, intendendo *post* come preposizione impropria e *vocitamina* come "convocazione/chiamata a raccolta" tradurrei i vv. 341-343 con «ordinò che ogni animale (*omne animal* v. 399) si presentasse innanzi al proprio signore e gli obbedisse, e, quindi che, dopo la convocazione generale delle specie, Adamo, come se fossero creature a lui sottoposte, creasse i nomi di quanti erano stati generati, per stabilirli».

[63] M. Cutino, *L'Alethia* cit., pp. 57-76.
[64] I. D'Auria, *Alethia*, cit., p. 253.

CONCLUSIONI

Il presente lavoro mira a inserirsi nel filone di studi legati alla valorizzazione della produzione parafrastica d'età tardoantica, gettando uno sguardo sulle peculiarità linguistiche e sulle particolarità lessicali, particolarmente pregnanti e veicolo di innovazione linguistica nonché, in taluni di casi, di esplicita evidenza esegetica. Lo studio in questione, a partire da un caso di neoformazione, operazione ben frequente nella poesia parafrastica[65], intende ricostruire, a partire dalla letteratura critica, dal costante ricorso all'ipotesto di partenza e dal vaglio di peculiari attestazioni del lemma, le ragioni tali da motivare una scelta stilistica, forse sottostimata e che, in virtù di un riuso successivo, può, invece, esser testimone di una fortuna dell'*Alethia* non ancora validata. Di fronte a una banalizzazione di intendimento, che di fatto tradisce quanto il passo intende esprimere, la forma che, a quanto si evince dagli studi lessicografici, seppur riadoperata, ha mantenuto quasi esclusivamente il significato di *nomen*, in relazione alle modalità stilistiche del *Massiliensis,* può essere riabilitata, arricchendone le peculiarità semantiche, come "sfortunato" neologismo giuridico, coniato al fine di poter esprimere suddetta sfumatura, evitando di inserire un sostantivo ben più prosastico e non aderente ai gusti intellettuali desiderati e perseguiti.

Appare fondamentale sottolineare ancora una volta come il parafraste utilizzi strumenti espressivi e retorici per adattare l'ipotesto biblico ai gusti intellettuali dell'epoca, mediante l'adozione di stilemi estremamente ricercati e ben connotati. Si evince, chiaramente, la necessità di confrontarsi con l'ipotesto di riferimento al fine di poter adeguatamente interpretare e valutare le scelte semantiche, nonché la consapevolezza di trovarsi innanzi a un'opera, forse fortunata, ma finora non ampiamente attenzionata. In conclusione, si ribadisce che questa proposta intende essere considerata un intervento criticamente chiarificatore, un'ipotesi volta a valorizzare il preziosismo linguistico del retore Vittorio e le particolarità contraddistinguenti la sua *langue* e *facies* poetica.

[65] Rimando, ad esempio, ad alcuni studi: M. R. Petringa, "Le attestazioni del verbo clepto nel latino tardo e medievale", in P. Molinelli, P. Cuzzolin, C. Fedriani (Édité par), *Latin Vulgaire - Latin Tardif 10*, Actes du Xe Colloque International sur le latin vulgaire et tardif, (Bergamo, 5-9 septembre 2012), Bergamo 2014, pp. 615-626; M. R. Petringa, "Particolarità lessicali nel poema dell'Heptateuchos", in *Commentaria Classica. Studi di filologia greca e latina* 5, 2018, pp. 57-60; M. R. Petringa, "L'aggettivo innumerosus nel poema dell'Heptateuchos (*exod.* 7)", in *Commentaria Classica. Studi di filologia greca e latina* 8, 2021, pp. 215-222.

SIGLE E ABBREVIAZIONI

DMLBS = R. E. Latham - D. R. Howlett - R. K. Ashdowne (edd.), *Dictionary of Medieval Latin from British Sources*, Oxford 1975-2013.

Du Cange = *Glossarium mediae et infimae Latinitatis*, ... editio nova aucta ... a L. Favre, 10 voll., Niort 1883-1887.

Forcellini = E. Forcellini, *Lexicon totius Latinitatis* [...], I-VI, (II impr. anast. IV ed., Patavii 1864-1926), Bononiae 1965.

ThlL = Thesaurus linguae Latinae, 1900 -

BIBLIOGRAFIA

Abosso D. H., *Translation and commentary on Claudius Marius Victor's Alethia 3.1- 326*, Illinois, 2015.

Berger A., *Encyclopedic dictionary of Roman law*, Philadelphia 1952.

Büsing G., "Beobachtungen zum Verständnis der erzählten Namengebung in Gen 2, 19 f.", in G. Bodendorfer, e M. Millard (edd.), *Bibel und Midrasch: zur Bedeutung der rabbinischen Exegeese für die Bibelwissenschaft, Forschungen zum Alten Testamento* 22, Tubinga 1998, pp. 191-208.

Colella P., "La Costola di Adamo: Gen. 2, 18-24", in *Apollinaris*, 67 3-4, 1994, pp. 847-875.

Cutino M., "Struttura, significato e modalità parafrastiche dell'Alethia di Claudio Mario Vittorio", in *Motivi e forme della poesia cristiana antica tra scrittura e tradizione classica*, XXXVI Incontro di studiosi dell'antichità cristiana (Roma, 3-5 maggio 2007), Roma 2008, pp. 455-485.

—, *L'Alethia di Claudio Mario Vittorio: la parafrasi biblica come forma di espressione teologica*, Roma 2009.

De Gianni D., Iuvencus. *Evangeliorum Liber Quartus. Introduzione, testo criticamente riveduto, traduzione e commento a cura di D. De Gianni*, Stuttgart 2020.

D'Auria I., "Il giudizio divino (*Gn* 3, 10 - 19) nella riscrittura esametrica di Claudio Mario Vittorio (*Alethia* 1, 471-519), in *Vetera Christianorum* 44, 2007, pp. 33-57.

—, *Claudio Mario Vittorio, ALETHIA, Precatio e primo libro. Introduzione, testo latino, traduzione e commento, a cura di I. D'Auria*, Napoli 2014.

—, "La creazione della donna (*Gen* 2, 21-24) nella parafrasi biblica di Claudius Marius Victorius (*Alethia* 1, 355-387)", in *Dalla civiltà classica all'umanesimo*, Napoli 2014, pp. 83-104. Dinkova – Brunn G., *Liber prefigurationum Christi et ecclesie. Liber de gratia Novi Testamenti cura et studio Greti Dinkova-Bruun*, CC CM 195, Turnhout 2007.

Dümmler E., *Vita Galli metrica*, edidit E. Dümmler, *MGH Poetae* 2, 1884, pp. 428-473.

Fabricius G., *Poetarum veterum Ecclesiasticorum Opera Christiana, et operum reliquiae atque fragmenta: Thesaurus catholicae et orthodoxae Ecclesiae, et Antiquitatis religiosae, ad utilitatem iuventutis scholasticae: Collectus, emendatus, digestus, et Commentario quoque expositus, diligentia et studio Georgii Fabricii Chemnicensis, per Ioannem Oporinum*, Basileae 1564, pp. 307-349.

Falcon E., *La théologie de l'histoire dans l'Alethia de Claudius Marius Victorius (Ve s.)*: *entre ruptures et alliances*. *Traduction des Livres I, II et III a cura di E. Falcon*, Strasbourg 2024. Fischer B., *Vetus Latina. Die Reste der altlateinischen Bibel nach P. Sabatier neu gesammelt und herausgegeben von der Erzabtei Beuron, 2, Genesis*, *herausgegeben von B. Fischer*, Freiburg 1951-1954.

Gagny I., *Christiana et docta divi Alchimi Aviti Viennensis archiepiscopi, et Claudii Marii Victoris Oratoris Massiliensis, poëmata, aliaque non poenitenda*. *Per Ioannem Gaigneium Parisinum Theologum e vetustissimis librariis in lucem asserta, suoque nitori restituta, quorum catalogum*

proxima pagella indicabit. Vaeneunt Lugduni a Vincentio Portonario. Cum privilegio Regio ad quadriennium 1536, pp. 166-249.

Gertz J.C., *Das Alte Testament Deutsch. 1, Das erste Buch Mose, Genesis: die Urgeschichte Gen 1-11. übers. und erklärt von Jan Christian Gertz,* Göttingen 2018.

Green R., "Victorius' Vergil: Comments on a passage of the Alethia", in *Millennium* 7, 2010, pp. 51-66.

Hovingh P. F., *Claudii Marii Victorii Alethia*, *cura et studio P. F. Hovingh*, CChL 128, Turnhout 1960, pp. 115-193.

Leroy S., "Le Liber prefigurationum Christi et Ecclesie: un commentaire de la Bible en hexamètres dactyliques", in *Pragmatique du commentaire* 2018, pp. 245-261.

Lunelli A. (ed.), *La lingua poetica latina,* Bologna 1974.

Martorelli U., *Redeat Verum. Studi sulla tecnica poetica dell'Alethia di Claudio Mario Vittorio*, Stoccarda 2008.

Migne J. P., *Claudii Marii Victoris commentariorum in Genesin libri tres,* PL 61, Parisiis 1847, pp. 937-970.

Morel G., *Cl. Marii Victoris oratoris Massiliensis, ALHQEIAS, seu Commentationum in Genesin lib. III. Epigrammata Varia vetusti cuiusdamauctoris, inter quae sunt et aliquot psalmi versibus redditi. Hilarii Pictaviensis episc. Genesis. Cypriani, Genesis et Sodoma. Dracontii, De opere sex dierum. Omnia versibus, nunc primum e vetustis codicibus expressa*, apud Guil. *Morelium, in Graecis typographum Regium. Privilegio Regis*, Parisiis 1560, pp. 1-72. Nazzaro A. V., "Riscritture metriche di testi biblici e agiografici in cerca del genere negato", in *Auctores Nostri* 4, 2006, pp. 397-439.

—, *Claudio Mario Vittorio,* in *Nuovo Dizionario patristico e di antichità cristiane,* vol. 2, Genova-Milano 2007, pp. 3060-3063.

—, “Motivi e forme nella poesia cristiana antica tra Scrittura e Tradizione Classica”, in *Motivi e forme della poesia cristiana antica tra scrittura e tradizione classica*, XXXVI Incontro di studiosi dell’antichità cristiana (Roma, 3-5 maggio 2007), Roma 2008, pp. 9-56.

Nodes D. J., *Doctrine and exegesis in Biblical Latin poetry*, Leeds 1993.

Papini S., *Claudio Mario Vittorio, La Verità, introduzione, traduzione e note a cura di S. Papini*, Roma 2006**.**

Petringa M. R., “Le attestazioni del verbo clepto nel latino tardo e medievale”, in P. Molinelli, P. Cuzzolin, C. Fedriani (Édité par), *Latin Vulgaire - Latin Tardif 10, Actes du Xe Colloque International sur le latin vulgaire et tardif*, (Bergamo, 5-9 septembre 2012), Bergamo 2014, pp. 615-626.

—, *Il poema dell'Heptateuchos. Itinera philologica tra tardoantico e alto medioevo*, Catania 2016.

—, “Adamo ed Eva e il frutto proibito nel poema dell’Heptateuchos (gen. 64-90). Testo critico, traduzione e commento”, in *Commentaria Classica. Studi di filologia greca e latina* 4, 2017, pp. 105-118.

—, “Particolarità lessicali nel poema dell’Heptateuchos”*,* in *Commentaria Classica. Studi di filologia greca e latina* 5, 2018, pp. 57-60*.*

—, “L’aggettivo innumerosus nel poema dell’Heptateuchos (*exod.* 7)”*,* in *Commentaria Classica. Studi di filologia greca e latina* 8, 2021, pp. 215-222.

Pollmann K., “Der sogenannte Heptateuchdichter und die Alethia des Claudius Marius Victorius. Anmerkungen zur Datierungsfrage und zur Imitationsforschung”, in *Hermes* 120, 1992, pp. 490-501.

Roberts M., *Biblical Epic and Rhetorical Paraphrase in Late Antiquity*, Liverpool 1985.

Schenkl C., *Claudii Marii Victoris oratoris Massiliensis Alethia*, CSEL 16, Vindobonae 1888, pp. 335-498.

Schiano C., “La genesi del linguaggio: memorie lucreziane in Cyrano de Bergerac”, in *Atene e Roma* 8, 2014, pp. 239-256.

Soggin J.A., *Genesi, a cura di J. A. Soggin*, Genova 1991.

Stella F., *Poesia e teologia. L'Occidente latino tra IV e VIII secolo*, Milano 2001.

Strecker K., *Codex epistolarum Tergernseensium. Froumund*, *edidit* K. Strecker, *MGH epp.* 3, 1925.

Treichel T. K., *Die «Alethia» des Claudius Marius Victorius: Bibeldichtung zwischen Epos und Lehrgedicht*, Berlin 2016.

—, *Alethia. Claudius Marius Victorius*; *eingeleitet, übers. und kommentiert von Thomas Kuhn Treichel*, Basel 2018.

von Rad G., *Das Alte Testament deutsch, IV: Das erste Buch Mose. Genesis Kapitel XXV,19-L,26, übers. & erkl. G. von Rad,* Göttingen 1953.

von Winterfeld P., *Radbodus Traiectensis episcopus, Carmina*, *edidit P. von Winterfeld*, *MGH Poetae* 4,1, 1899, pp. 161-173.

Weber D., “Die Alethia des Claudius Marius Victorius und ihr Verhältnis zu Lukrez”, in V. Zimmerl-Panagl (ed.), *Dulce melos 2. Lateinische und griechische Dichtung in Spätantike, Mittelalterund Neuzeit*, Akten des 5. Internationalen Symposiums, (Wien, 25.-27. November 2010), Pisa 2013, pp. 183-199.

Weber R., *Biblia sacra iuxta Vulgatam versionem*, a*diuvantibus B. Fischer - I. Gribomont - H. F. D. Sparks - W. Thiele, recensuit et brevi apparatu critico instruxit R. Weber, editionem quintam emendatam retractatam praeparavit R. Gryson*, Stuttgart 2007[5] (1969[1]).

RECLAIMING THE SACRED: SPRITITUALITY IN THE INTERSECTIONAL PRAXIS OF THE KURDISH WOMEN'S LIBERATION MOVEMENT

Evita Guerra

Abstract

This study investigates the integral role of spirituality within the Kurdish Women's Liberation Movement, positing spirituality as a critical ethical, epistemic, and political vector for emancipatory praxis. Contesting dominant secular and rationalist frameworks that frequently marginalize spirituality as either anachronistic or regressive, the movement undertakes a profound reclamation of the sacred, understood as a site of counter-memory, suppressed epistemologies, and communal ethical life. Employing the theoretical interventions of Silvia Federici and Abdullah Öcalan, this inquiry historicizes the processes of spiritual dispossession concomitant with the advent of patriarchal capitalist modernity. Central to this analysis is the conceptualization of *Jineolojî* — a revolutionary epistemology formulated to recuperate women's knowledge and spiritual agency. Empirically grounded in the political praxis of Rojava, the Kurdish Women's Movement exemplifies the integration of spirituality within intersectional frameworks that interlink gender, ethnicity, ecology, and class. This contribution extends contemporary debates in decolonial feminism and political ontology by articulating spirituality not as a residual superstition but as a constitutive dimension of transformative political subjectivity and collective liberation.

Keywords: Kurdish Women's Liberation Movement; Spirituality and Politics; Jineolojî; Intersectionality; Decolonial Feminism; Patriarchy and Capitalism.

I. INTRODUCTION: THEORETICAL FOUNDATIONS AND SPIRITUAL POLITICS

The marginalization of spirituality within contemporary political theory and feminist praxis has been predicated upon a secularist rationality that dichotomizes reason and faith, rendering the sacred as obsolete or antithetical to emancipatory politics[1]. This paper challenges such epistemic exclusions by examining spirituality as a foundational dimension of the Kurdish Women's Liberation Movement's praxis. Far from being a vestigial or regressive element, spirituality emerges as an ethical horizon and a locus of resistance that fundamentally reconfigures political ontology and emancipatory possibility[2].

Ernst Bloch's philosophy of hope, as articulated in *The Principle of Hope*[3], provides a critical theoretical framework for apprehending this dimension. Bloch elucidates hope as a temporal and ontological force — an anticipatory consciousness that engenders a "not-yet" realm of possibility. Religion and spirituality, in this schema, possess latent utopian potentialities, functioning as repositories of critique against present conditions and as catalysts for radical transformation. The Kurdish Women's Movement's engagement with the sacred can thus be understood as enacting a Blochian praxis, wherein myth, memory, and imagination coalesce to sustain political struggle and forge alternative futures.

In dialogue with this, Silvia Federici's materialist feminist historiography reveals the gendered violence inherent in the epistemic and spiritual dispossession wrought by early modern capitalist formations[4]. Her analysis of the witch hunts explicates how women's embodied knowledge and spiritual authority were systematically targeted to facilitate the subjugation of female bodies and labor within patriarchal capitalist structures. Abdullah Öcalan's theorization of civilizational ruptures further historicizes these processes, delineating the successive disjunctions that severed matriarchal, relational cosmologies in favor of hierarchical, patriarchal orderings[5].

---

[1] T. ASAD, *Formations of the Secular: Christianity, Islam, Modernity*, Stanford University Press, Stanford, 2003, pp.1-26.
[2] A. ÖCALAN, *Liberating Life: Woman's Revolution*, International Initiative Edition, Cologne, 2013, pp. 19-25.
[3] E. BLOCH, *The Principle of Hope*, 3 vols., MIT Press, Cambridge (MA), 1986, p.1376.
[4] FEDERICI S., *Caccia alle streghe, guerra alle donne*, Ombre Corte, Verona, 2015, p.23.
[5] A. ÖCALAN, *Liberating Life,* cit., pp.18-21.

Within this theoretical constellation, the Kurdish Women's Movement's articulation of *Jineolojî* emerges as a radical epistemic and ethical intervention. It endeavors not only to recuperate suppressed knowledges but also to instantiate a mode of knowing that transcends the ontological ruptures of modernity, reintegrating spirituality as a lived ethical praxis[6]. The following analysis traces this trajectory — from historical dispossession through epistemic restoration to the concrete political praxis embodied in Rojava — thereby advancing a conception of sacred intersectionality that enriches contemporary debates in decolonial feminist theory and praxis.

II. THE WITCH-HUNT AND THE HISTORICAL DISPOSSESSION OF WOMEN'S SPIRITUALITY

Silvia Federici's materialist feminist analysis offers a decisive intervention into the historical understanding of the witch hunts, reinterpreting them not as aberrant episodes of medieval superstition but as a structured and violent process embedded within the political economy of early capitalism. In her seminal work *Caliban and the Witch*[7], Federici reveals that the persecution of women accused of witchcraft was neither arbitrary nor culturally anomalous. Rather, it constituted a key moment in the reorganization of gender relations and spiritual life that accompanied the rise of capitalist modernity. Women targeted during the witch hunts were not marginal figures; they were often midwives, herbalists, and community healers — custodians of pre-capitalist, communal, and non-patriarchal knowledge systems rooted in cyclical time, bodily autonomy, and a cosmological understanding of life's interconnectedness[8].

Crucially, Federici situates these events within the broader framework of what Marx describes as «primitive accumulation»[9]: the violent disembedding of people from traditional lifeways in order to create a proletariat suitable for wage labor and capitalist discipline. In this view, the witch hunt

[6] KONGRA STAR, "Epistemology and Spirituality" in *Jineolojî: The Science of Women*, Kongra Star Publications, Rojava, 2020.
[7] S. FEDERICI, *Caliban and the Witch: Women, the Body and Primitive Accumulation*, Autonomedia, New York, 2004.
[8] S. FEDERICI, *Caliban and the Witch*, ivi, pp-184-194.
[9] K. MARX, *Capital. A Critique of Political Economy*, vol. 1, trans. by B. Fowkes, Penguin Books, London, 1990 [ed. or. *Das Kapital*, 1867], pp.871-872.

emerges not as a residual practice of premodern religious intolerance but as a deliberate mechanism of social engineering aligned with the foundational imperatives of capitalist development. It targeted not only specific women but also the symbolic and epistemological order in which their roles were embedded. As Federici explains, the destruction of female-centered spiritualities and the criminalization of healing practices served to undermine communal resistance and eliminate alternative forms of life that were incompatible with the emerging capitalist rationality[10].

The witch, as a figure, embodied a direct challenge to the consolidation of patriarchal capitalism. Her capacity to heal, her access to reproductive knowledge, and her mediation between human and non-human realms represented a mode of authority that was irreducible to either the market or the state. This figure had to be disempowered — materially, epistemologically, and spiritually — to clear the ground for a new social ontology. «The witch hunt was an essential aspect of primitive accumulation and the transformation of the body into a work-machine»[11], Federici writes, underscoring the way in which women's bodies were conscripted into the emerging logic of capitalist production. This transformation was not limited to economic restructuring; it simultaneously enacted a profound spiritual rupture, in which female autonomy, sacred knowledge, and non-dualistic cosmologies were delegitimized and replaced with rationalist, mechanistic, and patriarchal paradigms[12].

What Federici terms the «housewifization» of women[13] — a process by which women were confined to reproductive labor within the domestic sphere — marked a profound epistemic shift. The enclosure of women's labor was accompanied by the enclosure of their symbolic and spiritual functions. No longer mediators of knowledge and healing, women were reconstituted as dependents within the nuclear family, defined by their relation to male breadwinners and subordinated to institutional religious and scientific authorities. This reconfiguration of gendered roles reflected and reinforced the broader shift from a sacred and relational cosmology to one dominated by abstraction, hierarchy, and control. As Federici notes, the rise of capitalist modernity necessitated the destruction

[10] S. FEDERICI, *Caliban and the Witch*, cit., pp.168-171.
[11] S. FEDERICI, *Caliban and the Witch*, ivi, p.170.
[12] S. FEDERICI, *Caliban and the Witch*, ivi, pp.174-176.
[13] S. FEDERICI, *Caliban and the Witch*, ivi, pp. 27, 75-77, 180-183.

of alternative life-worlds, particularly those grounded in feminine spirituality and embodied forms of knowledge[14].

The ontological violence of the witch hunts thus extended far beyond the persecution of individuals. It entailed the suppression of entire systems of meaning that had structured premodern life. The relational, cyclical, and animistic understandings of existence upheld by these women were systematically delegitimized, rendering nature inert, labor external, and life desacralized. In Federici's account, modernity is not simply a shift in economic or political structures, but a cosmological reordering in which the sacred is displaced and knowledge is abstracted from ethical, embodied, and communal existence[15]. This process can be further understood through the lens of Robert Nichols's concept of «desecration»[16], which he defines as the removal of sacredness from land, life, or community in order to render it available for appropriation. In Nichols's formulation, desecration is not a byproduct of secularization but a political act intrinsic to the logic of dispossession. Desecration transforms relational worlds into abstractable resources, preparing them for commodification or domination. The witch hunts, in this light, were not merely cultural attacks on spirituality, but material enactments of desecration that enabled the reconstitution of women's labor, bodies, and cosmologies into forms legible and exploitable by emerging capitalist orders[17]. This analysis resonates with Abdullah Öcalan's critique of patriarchal civilization[18]. Öcalan similarly identifies the disenchantment of the world and the suppression of sacred, feminine-centered cosmologies as central to the history of domination. Both thinkers call for a reconstitution of the sacred within social and political life, seeing in this reintegration the possibility of a genuinely emancipatory future.

In this light, the witch hunts can be understood as a crucible in which modern capitalist subjectivity was forged: rational, disenchanted, and disembodied. Yet in exposing the historical and political construction of this subjectivity, Federici invites a reawakening of suppressed spiritual and epistemological traditions. The memory of the witch — the healer, the midwife, the wise woman

[14] S. FEDERICI, *Caliban and the Witch*, ivi, pp.177-180.
[15] S. FEDERICI, *Caliban and the Witch*, ivi, pp.181-182.
[16] R. NICHOLS, *Theft is Property!: Dispossession and Critical Theory*, Duke University Press, Durham 2020, pp. 29-34.
[17] R. NICHOLS, *Theft is Property,* ivi, pp.83-85.
[18] A. ÖCALAN, *Liberating Life,* cit., pp.25-27.

continues to haunt the margins of modernity, suggesting not only what was lost, but also what might yet be reclaimed.

III. SPIRITUAL RUPTURE AND THE LOGIC OF DOMINATION

Abdullah Öcalan[19] offers a profound rethinking of the historical development of patriarchy and the ontological ruptures that have reshaped human consciousness and social organization. Central to his analysis is the notion of three major civilizational ruptures, each marking a decisive break in the relationship between society, spirituality, and gendered power. These ruptures collectively trace the progressive disenchantment of life and the increasing institutionalization of hierarchy, abstraction, and systemic violence. Through this lens, Öcalan not only critiques capitalist modernity but also historicizes its roots within a broader trajectory of spiritual and material dispossession.

The first rupture, according to Öcalan[20], occurred with the violent dismantling of Neolithic communal societies, many of which were organized around egalitarian, eco-spiritual, and womancentered cosmologies. These early communities, often described as matristic or gynocentric rather than matriarchal in a domineering sense, were shaped by a reverence for fertility, the cyclical rhythms of nature, and a sacred understanding of the feminine principle. Rather than centralized power, social cohesion was maintained through collective responsibility, mutual care, and spiritual embeddedness within the natural world. However, with the rise of male-dominated warrior castes and emerging theocratic hierarchies, these life-affirming social systems were gradually dismantled. The symbolic displacement of the goddess by a male divine figure initiated what Öcalan terms a «spiritual rupture» — a systematic devaluation and demonization of the sacred feminine that laid the groundwork for later forms of gendered domination[21]. This transformation echoes what Federici describes as the ideological groundwork for the capitalist reorganization of society, where spiritual and bodily autonomy — particularly women's — had to be destroyed to make way for patriarchal control.

[19] A. ÖCALAN, *Liberating Life,* ivi.
[20] A. ÖCALAN, *Liberating Life,* ivi, pp.19-21.
[21] Ibidem.

The second rupture unfolds with the consolidation of class-based societies and the institutionalization of monotheistic religions. In this phase, the divine is rendered distant, masculine, and transcendent, severing sacredness from the immanent, embodied world. Religious authority becomes monopolized by patriarchal institutions, and the figure of the woman is increasingly excluded from sacred narratives and positions of spiritual power. Öcalan[22] identifies this moment as the beginning of the colonization of women — not solely in economic or political terms, but symbolically and spiritually. Woman is recast as subordinate, her body desacralized, and her spiritual functions either erased or demonized. This aligns closely with Federici's[23] analysis of the witch hunts, in which religious ideology functioned as a legitimizing force for the suppression of communal, non-institutional spiritualities that were often maintained by women. Both thinkers highlight the role of religion in the historical marginalization of women, emphasizing how institutionalized faith systems served as instruments of patriarchal domination.

The third rupture is consummated with the advent of capitalist modernity, which replaces the spiritual with the rational, the symbolic with the instrumental, and the sacred with the commodified. Here, Öcalan[24] argues, the disenchantment of the world reaches its apex: positivist science and industrial rationality become hegemonic epistemologies, while spirituality is relegated to the private sphere or dismissed altogether as irrational. In contrast to earlier epochs, where the sacred was demonized, modernity deems it irrelevant. The result is a profound alienation, as individuals become severed from ancestral knowledge, ecological belonging, and communal life-worlds. «Capitalist modernity is the most refined form of power and exploitation», Öcalan asserts, «it colonizes the spirit of society and individuals alike»[25]. This spiritual colonization does not operate merely through economic mechanisms or ideological coercion, but through a deep restructuring of meaning itself. The rupture is thus not only material but ontological, producing subjects who are alienated from the sacred dimensions of existence and thus more easily governed by market logic and technocratic control.

Öcalan's triadic schema allows us to view the historical marginalization of women and the sacred not as isolated incidents, but as phases in a *longue durée* of civilizational transformation. His

[22] A. ÖCALAN, *Liberating Life*, ivi, pp.32-35.
[23] S. FEDERICI, *Caliban and the Witch*, cit.
[24] A. ÖCALAN, *Liberating Life*, cit., pp. 51-55.
[25] A. ÖCALAN, *Liberating Life,* ivi, p.25.

analysis converges with feminist critiques, such as those of Federici, in recognizing that the suppression of women's spiritual and communal authority has been essential to the consolidation of hierarchical and capitalist forms of power. What is required, then, is not merely resistance at the level of economics or politics, but a cosmological reorientation, a healing of the rift between the sacred and the social, the feminine and the political, the embodied and the spiritual.

IV. JINEOLOGJI AS EPISTEMIC AND ETHICAL RESTORATION

In response to this history of rupture, the Kurdish Women's Movement has articulated *Jineolojî* as both a critique and a constructive project. Far from being a new discipline in the conventional sense, *Jineolojî* represents a philosophical and epistemological insurgency. As Sebahat Tuncel writes, «*Jineolojî* is a call to re-examine the basis of knowledge, its sources, and the power structures it serves. It is a science for life, not for power»[26]. It seeks to undo the legacy of epistemic violence by reactivating suppressed forms of knowing, particularly those grounded in women's experience, oral history, myth, and spiritual practice[27].

As articulated in the *Jineolojî Journal*, «Jineolojî is not a repetition of the sciences developed within the framework of power and the state; it is the creation of a new science that questions and transforms life in all its dimensions»[28]. *Jineolojî* does not aim to replicate existing sciences by inserting gender as a category, as it critiques any form of scientific rationalism that accompanies capitalist modernity, that is complicit in the domination of life. Indeed, modern science, far from being neutral, has systematically excluded intuitive, affective and relational knowledge forms. *Jineolojî* , instead, calls into question the very foundations of modern knowledge. In this framework, the sacred is not an object of belief but a method of relational knowing. Spirituality is understood as the living connection between individuals, communities, and the natural world; as an ethical orientation grounded in care, responsibility, and memory.

This reclamation of the sacred is also a political act. It challenges the colonial-capitalist notion of the self as autonomous and extractive, proposing instead a relational subjectivity grounded in

[26] S. TUNCEL, "Jineolojî: The Science of Women and Life", in *Jineolojî Journal*, vol. 1, no. 1, 2018, p.6.
[27] Ibidem.
[28] S. TUNCEL, "Jineolojî: The Science of Women and Life", ivi, p.7.

reciprocity. Through *Jineolojî*, the movement reclaims not only epistemic agency but ontological depth, embedding political resistance in a larger cosmology of life-affirming values.

Educational programs based on *Jineolojî* have played a key role in transforming the political consciousness of women and communities in Northern Syria and beyond. These institutions foster spaces where knowledge is not transmitted hierarchically but cultivated through dialogue, reflection, and practice. The return to oral traditions, myth, and ritual is not nostalgic but strategic: it reweaves the social fabric through stories that center women, nature, and community as sacred and interdependent.

V. FROM STRUGGLE TO SACRED PRAXIX

The practical articulation of the Kurdish Women's Liberation Movement's principles occurs most tangibly in the autonomous Democratic Autonomous Administration of North and East Syria (AANES), commonly known as Rojava. Here, the movement has institutionalized a model known as democratic confederalism, a decentralized, stateless political system based on grassroots democracy, ecological sustainability, and gender liberation. Öcalan's model draws inspiration from Murray Bookchin's libertarian municipalism[29] but grounds it in the cultural, historical, and material realities of the Kurdish people and their long history of dispossession and resistance.

The political system in Rojava is organized through communes, councils, and democratic assemblies at the neighborhood, district, and regional levels. These are not simply administrative structures but function as participatory spaces in which political decisions are made collectively and often begin with collective reflection. Each commune includes a co-chair system — one male, one female — to ensure gender parity, and committees dedicated to justice, education, ecology, and health. The principle of dual power is realized through parallel women's structures, such as the umbrella organization Kongra Star, which ensures autonomous decision-making by women while remaining connected to the broader political fabric[30].

[29] M. BOOKCHIN, *The Ecology of Freedom: The Emergence and Dissolution of Hierarchy*, AK Press, Oakland, 2005, p.129.
[30] D. DIRIK, *The Kurdish Women's Movement: History, Theory, Practice*, London, Pluto Press, 2022, pp. 188-190.

Jineolojî plays a critical role in shaping these institutions. For example, women's academies established throughout Rojava offer political education grounded in *Jineolojî.* These academies facilitate reflection on patriarchy, capitalism, colonialism, and the internalization of domination, using both theoretical texts and embodied learning practices. They also incorporate ancestral healing rituals, storytelling, and oral histories as epistemic sources, making them spaces of spiritual, intellectual, and political transformation[31].

In practice, intersectionality and ecological consciousness are translated into daily governance. Communal cooperatives are organized around sustainable agriculture and local economic resilience, with an emphasis on ecological harmony rather than industrial productivity. The village of Jinwar, for instance, is an all-women ecovillage built on feminist principles where women live communally, cultivate land collectively, and raise children in a space free from patriarchal and state violence. Jinwar is not only a social experiment but a living testimony to the possibility of feminist ecological autonomy[32].

Legal justice is also reimagined through the implementation of peace and reconciliation committees that resolve conflicts without resorting to punitive incarceration. These committees often begin proceedings with ethical-spiritual reflection and prioritize collective healing, especially in cases involving gender-based violence. The integration of spirituality into the resolution of conflict reflects a commitment to restoring social harmony rather than enforcing state-sanctioned punishment.

The Rojava model challenges the neoliberal and statist separation of political, economic, ecological, and spiritual life. Instead, it proposes an integrated system in which ethical and communal values are inseparable from governance. The slogan «democracy without the state» is practiced not as utopian rhetoric but as a daily reality structured through embedded, relational forms of care and political engagement.

Ceremonies to honor martyrs are central moments of collective spiritual and political life. As often expressed in the movement: «The remembrance of martyrs is the memory of our values. It is not mourning, but a promise to continue life in freedom»[33]. These events do not replicate state-

[31] S. TUNCEL, "Jineolojî: The Science of Women and Life", cit., pp.5-15.

[32] M. KNAPP, A. FLACH, E. AYBOGA, *Revolution in Rojava: Democratic Autonomy and Women's Liberation in Syrian Kurdistan*, Pluto Press, London, 2016, pp.45-47.

[33] Movement source, n.d.; cited in D. DIRIK, *The Kurdish Women's Movement,* cit., p. 191.

sponsored nationalist rites; rather, they evoke a sense of ethical continuity, binding the past, present, and future in a sacred temporality. Healing is also collective: storytelling, music, and ritual are used to address trauma, restore dignity, and affirm belonging.

Spirituality in Rojava is not dictated by dogma but enacted in daily life. It informs ecological practices, such as reforestation and communal agriculture, which are guided by a view of the earth as alive and interconnected. It also shapes gender relations, challenging both institutional patriarchy and internalized forms of domination.

This integration of spirituality into governance and social reproduction constitutes a form of sacred politics. It does not seek to install a theocracy, but to reimagine the political as rooted in care, memory, and cosmic balance. It is a living example of what Öcalan describes as a society with soul, where freedom is measured not only by institutional arrangements but by the depth of ethical life.

VI. TOWARD A SACRED INTERSECTIONALITY

The Kurdish Women's Movement presents a compelling rearticulation of intersectionality, which is not confined to juridical categories or institutional recognition but anchored in lived experience, cosmological knowledge, and collective ethical life. This reconceptualization reflects what Kimberlé Crenshaw originally identified in her foundational work on Black feminist legal theory: intersectionality as the analytical recognition of how overlapping structures of power — such as race, gender, and class — interact to create compounded forms of marginalization. Crenshaw's intervention highlighted the failure of single-axis frameworks to capture the complexity of Black women's experiences within legal and political institutions[34].

Yet, in the praxis of the Kurdish Women's Movement, intersectionality is not simply an analytic tool; it becomes a mode of being, a spiritual and relational understanding of existence that foregrounds the entanglement of oppressions across axes of gender, colonialism, class, ecological destruction, and epistemic erasure. This sacred intersectionality resonates with María Lugones' notion of the *coloniality of gender*[35], in which colonialism is seen as a civilizational rupture that

[34] K. CRENSHAW, "Mapping the Margins: Intersectionality, Identity Politics, and Violence Against Women of Color", in *Stanford Law Review*, vol. 43, no. 6, 1991, pp. 1241–1299.
[35] M. LUGONES, "The Coloniality of Gender", in *Worlds & Knowledges Otherwise*, Spring, 2010, pp. 4-7.

imposed European gender binaries while simultaneously destroying Indigenous cosmologies, lifeworlds, and relational ontologies. For Lugones, decolonial feminism must recover these severed relationalities through both political and spiritual praxis.

The political genealogy of Kurdish women can thus be read as a project of ontological repair. The framework of *Jineolojî*, or the "science of women," is emblematic of this undertaking: it centers embodied knowledge, oral histories, ecological stewardship, and spirituality as foundational sources of both resistance and world-making. In this view, the woman is not only a gendered subject but, as Abdullah Öcalan argues, the *first colonized being*[36], the bearer of a cosmology that was violently displaced by hierarchical civilizations. The recovery of this cosmology is not symbolic; it is insurgent. It requires rebuilding not only communal autonomy, but an entire ontological orientation rooted in mutuality, place, and sacred responsibility.

This understanding of structural harm and reclamation is enriched by Robert Nichols' theory of *recursive dispossession*[37]. Nichols argues that dispossession should not be seen merely as the loss of property, but as the constitutive logic of modern property regimes: «dispossession is not the opposite of property, but its condition»[38]. Recursive dispossession refers to the repeated and institutionalized practices by which communities are stripped of land, identity, and spiritual grounding — only for these losses to be reinscribed through legal, economic, and epistemic frameworks. The historical and ongoing dispossession of Kurdish women — from land, language, kinship, and the sacred — must therefore be read not as isolated acts of violence but as the recursive infrastructure of modernity itself. In reclaiming these dimensions of life, the Kurdish Women's Movement subverts the foundational grammar of domination.

In this light, the political horizon articulated by the Kurdish Women's Movement can be understood through Massimiliano Tomba's concept of *insurgent universality*[39]. Tomba critiques the dominant, homogenizing conception of universality derived from Western liberalism, proposing instead a universality "from below": a form of collective political reason that arises from situated struggles and enacts an alternative temporality, one grounded in historical interruption rather than

[36] A. ÖCALAN, *Liberating Life,* cit., pp.57-58.
[37] R. NICHOLS, *Theft is Property*, cit., defined pp.8-9, genealogy pp.33-34, structural context pp. 91-92.
[38] R. NICHOLS, *Theft is Property,* ivi, p. 19.
[39] M. TOMBA, *Insurgent Universality: An Alternative Legacy of Modernity,* Oxford University Press, Oxford, 2019, pp. 24-30.

linear progress. Insurgent universality is not imposed from above; it emerges from the cracks of the present and the reactivation of suppressed knowledges and solidarities[40].

The Kurdish Women's Movement is an embodiment of this insurgent universality. Rather than appealing to abstract rights or global governance, it builds a revolutionary universalism from the specificity of Kurdish women's historical experience, spiritual cosmologies, and anti-statist communal politics. It proposes an alternative world order not by negating difference, but by weaving together relational autonomy, ecological responsibility, and spiritual embeddedness. This praxis does not universalize through abstraction but through resonance with Indigenous, decolonial, and feminist movements across the globe.

Woman, within this sacred intersectionality, becomes a planetary figure: not an essentialized category, but a node of historical and cosmological rupture whose healing is necessary for the liberation of all. As Donna Haraway notes in her theory of *situated knowledges*[41], truth emerges not from detached objectivity, but from embodied, accountable positionality. *Jineolojî* builds precisely on this logic, namely that knowledge is not extracted; it is cultivated through relation, care, and spiritual presence.

Land, similarly, is not an inert resource but a sacred presence. Class is not merely a structural position, but a disfiguration of reciprocal moral economies. Spirituality, in this context, reveals these interwoven dimensions not merely as analytical tools, but as ontological realities. The sacred is not a remnant of the past, but the ground from which a future politics can emerge.

Thus, the Kurdish Women's Movement challenges both secular liberal feminism and state-centered revolutionism. It offers instead a sacred intersectionality, one that recognizes the multiple and recursive forms of dispossession while grounding liberation in ethical life, cosmological reweaving, and insurgent political imagination. This is not only a regional resistance but a profound contribution to a planetary rethinking of feminism, revolution, and universal emancipation.

---

[40] M. TOMBA, *Insurgent Universality,* ivi, pp. 23-24.

[41] D. HARAWAY, "Situated Knowledges: The Science Question in Feminism and the Privilege of Partial Perspective", in *Feminist Studies*, vol. 14, no. 3, 1988, pp. 575–599.

VII. CONCLUSION: RECLAIMING THE SACRED FOR LIBERATION

The Kurdish Women's Liberation Movement fundamentally reshapes spirituality and politics by rejecting modernity's-imposed divisions between the sacred and secular, personal and political, embodied and abstract. Rather than retreating into nostalgia or essentialism, it enacts a forwardlooking ethical-political spirituality that confronts the ontological premises of political modernity. This challenge opposes the rationalist, disenfranchised worldview of capitalist modernity and proposes a mode of being rooted in relationality, cosmology, and collective memory.

Far from being private consolation or cultural ornament, spirituality within this movement is a potent counter-hegemonic force resisting the historical dispossession endured by women, Indigenous peoples, and colonized communities. As ontological resistance, it breaks the recursive logic of dispossession[42] — the ongoing appropriation of marginalized knowledges, lands, and bodies under the guise of progress — by rooting struggle in a lived relation to land, history, and community.

The movement expands Kimberlé Crenshaw's concept of intersectionality beyond its juridical origins, showing that gendered oppression is inseparable from colonialism, capitalism, and ecological destruction. By embedding intersectionality in a sacred cosmology, it grounds liberation in relational and ethical life, echoing María Lugones' critique of colonial genderity and Donna Haraway's insistence on situated, embodied knowledge.

This synthesis produces *sacred intersectionality*, a framework recognizing oppression as both structural and cosmological. Woman is reimagined not only as a gendered category but as the first colonized subject, bearer of suppressed ontologies, and midwife of alternative futures. Through *Jineolojî*, new epistemologies emerge rooted in oral traditions, ecological interdependence, and the re-sacralization of life — knowledge born from lived struggle, care, and community.

Viewed through Massimiliano Tomba's concept of insurgent universality, the Kurdish Women's Liberation Movement contests dominant capitalist temporalities and universalisms. Drawing on plural temporalities and subaltern experiences, it articulates emancipatory politics grounded in suppressed histories and communal bonds. The universal here is not a homogenizing ideal but a horizon of interconnected struggles.

[42] R. NICHOLS, *Theft is Property*, cit., defined pp.8-9, genealogy pp.33-34, structural context pp. 91-92.

Today, this vision unfolds dynamically amid a world beset by ecological crises, patriarchal violence, political repression, and spiritual alienation. Kurdish women assert leadership through grassroots activism, democratic autonomy projects, and collective resilience — challenging authoritarian regimes and entrenched patriarchies across Kurdistan and neighboring regions. The Free Women's Movement (TJA) mobilizes thousands around the philosophy of *Jin, Jiyan, Azadî* (Women, Life, Freedom), organizing education, protests, and community initiatives even under severe state repression.

New platforms uniting Kurdish women's organizations signal growing solidarity and political strength, aimed at forging unity and liberation that transcend national borders. Their struggle embodies resistance not only to direct violence but to the fragmentation, commodification, and spiritual dispossession of late modernity. This spiritual-political praxis envisions collective subjectivation rooted in ethical and cosmological re-embedding, cultivating new ways of living, vocabularies of dignity, and conditions for collective flourishing.

By reclaiming the sacred as politics' foundation, the Kurdish Women's Liberation Movement insists that true liberation must be total — material, epistemic, and ontological. It offers a revolutionary framework deeply attuned to contemporary crises and aspirations, illuminating pathways toward justice, healing, and enduring freedom.

REFERENCES

ASAD T., *Formations of the Secular: Christianity, Islam, Modernity*, Stanford University Press, Stanford, 2003.

BLOCH E., *The Principle of Hope*, 3 vols., MIT Press, Cambridge (MA), 1986. BOOKCHIN M., *The Ecology of Freedom: The Emergence and Dissolution of Hierarchy*, AK Press, Oakland, 2005.

BUTLER J., *Undoing Gender*, Routledge, New York, 2004.

CRENSHAW K., "Mapping the Margins: Intersectionality, Identity Politics, and Violence Against Women of Color", in *Stanford Law Review*, vol. 43, no. 6, 1991, pp. 1241–1299.

DIRIK D., *The Kurdish Women's Movement: History, Theory, Practice*, London, Pluto Press, 2022.

FEDERICI S., *Caccia alle streghe, guerra alle donne*, Ombre Corte, Verona, 2015.

FEDERICI S., *Caliban and the Witch: Women, the Body and Primitive Accumulation*, Autonomedia, New York, 2004.

GUTIÉRREZ G., *A Theology of Liberation: History, Politics, and Salvation*, Orbis Books, Maryknoll, 1973.

HABERMAS J., "Religion in the Public Sphere", in *European Journal of Philosophy*, vol. 14, no. 1, 2006, pp. 1–25.

HARAWAY D., "Situated Knowledges: The Science Question in Feminism and the Privilege of Partial Perspective", in *Feminist Studies*, vol. 14, no. 3, 1988, pp. 575–599.

HOOKS B., *All About Love: New Visions*, William Morrow, New York, 2000.

JONGERDEN J., AKKAYA A. H., "The Kurdish Movement: A New Generation of Activists and the Struggle for Autonomy", in *European Journal of Turkish Studies*, no. 14, 2012.

KONGRA STAR, *Jineolojî: The Science of Women*, Kongra Star Publications, Rojava, 2020.

KNAPP M., FLACH A., AYBOGA E., *Revolution in Rojava: Democratic Autonomy and Women's Liberation in Syrian Kurdistan*, Pluto Press, London, 2016.

LUGONES M., "The Coloniality of Gender", in *Worlds & Knowledges Otherwise*, Spring, 2010, pp. 1–17.

LUGONES M., "Toward a Decolonial Feminism", in *Hypatia*, vol. 25, no. 4, 2010, pp. 742–759.

MARX K., *Capital. A Critique of Political Economy*, vol. 1, trans. by B. Fowkes, Penguin Books, London, 1990 [ed. or. *Das Kapital*, 1867].

MIGNOLO W. D., *The Darker Side of Western Modernity: Global Futures, Decolonial Options*, Duke University Press, Durham, 2011.

NICHOLS R., *Theft is Property!: Dispossession and Critical Theory*, Duke University Press, Durham, 2020.

ÖCALAN A., *Liberating Life: Woman's Revolution*, International Initiative Edition, Cologne, 2013.

TAYLOR C., *A Secular Age*, Harvard University Press, Cambridge (MA), 2007.

TOMBA M., *Insurgent Universality: An Alternative Legacy of Modernity*, Oxford University Press, Oxford, 2019.

TUNCEL S., "Jineolojî: The Science of Women and Life", in *Jineolojî Journal*, vol. 1, no. 1, 2018, pp. 5–15.

Classe di Scienze e Tecnologia

Quantum correlations: a geometric perspective

Andrea Zingarofalo

Abstract

Quantum correlations lie at the heart of the conceptual revolution brought by quantum theory. Their study is motivated not only by foundational questions—such as the nature of locality, realism, and causality—but also by their central role in quantum technologies, from device-independent protocols to quantum computing and cryptography. This thesis provides an accessible introduction to the landscape of quantum correlations and their geometric structure, with a particular focus on the minimal scenario. The first chapter outlines the physical and philosophical motivations behind the problem and sets the stage for the study of quantum correlations as constrained probabilistic models. The second chapter introduces the formal framework of Bell scenarios and the sets of local, quantum, and no-signaling correlations, emphasizing the importance of convexity and the distinction between classical and quantum models. The final chapter adopts a geometric perspective to study the quantum set, especially its boundaries and faces, where the tension between locality and quantum predictions becomes evident. Both analytical and numerical tools are discussed, including the NPA hierarchy and semidefinite programming relaxations, which are used to characterize and certify the quantum nature of correlations.

Keywords: quantum physics, correlations, nonlocality, Bell's theorem, convex geometry.

I. INTRODUCTION AND MOTIVATIONS

Over the past century, quantum mechanics has established itself as one of the most successful and farreaching theories in the history of science. Its predictive power has been confirmed with astonishing precision across a wide range of physical phenomena, from the behavior of subatomic particles to the properties of condensed matter systems. Additionally, new models widening the understanding of our surrounding were constructed from quantum physics. The Standard Model of particle physics, within the framework of quantum field theory, represents a milestone achievement for the natural sciences, it is the most complete account of the physical world that we have so far. From a pragmatic point of view, quantum theory (QT) led to the so-called *first quantum revolution*, where devices exploiting the laws of quantum mechanical systems were invented, like the transistor and the laser, which consequently led to further developments and applications in areas of science like chemistry, biology, medicine, engineering and computing, with a huge impact in the economy and culture of our society, and virtually every aspect of contemporary human life.

Beyond its empirical success, QT has fundamentally reshaped our understanding of the physical world, challenging classical notions of *determinism*, *locality*, and *realism*. The counterintuitive features of quantum mechanics—superposition, entanglement, and measurement-induced collapse—have stimulated profound conceptual debates and motivated some of the most important foundational questions in physics [8, 36, 46].

Among these, the nature of quantum correlations stands out as a central theme. In 1935, The seminal paper by Einstein, Podolsky, and Rosen (EPR) [24] famously questioned the completeness of quantum mechanics, highlighting a paradox that arises when considering entangled states shared between spatially separated systems. The EPR argument [7, 14, 15, 47] rested on the assumption of $_{local}$*realism*: the idea that physical properties exist prior to and independent of measurement, and that no influence can travel faster than light. If one accepts these assumptions, QT appears to allow for instantaneous correlations between distant events, which Einstein famously referred to as "spooky action at a distance."

This tension was brought into sharp focus by John Bell in 1964 [11]. Bell formulated a precise mathematical inequality—now known as Bell's inequality—that must be satisfied by any theory obeying local realism. He then showed that quantum mechanics predicts violations of this inequality in certainentangledsystems. Bell'stheoremthusmarksafundamentalturningpointinourunderstanding of nature: it proves that no local hidden variable theory can reproduce all the predictions of quantum mechanics. These predictions have since been confirmed experimentally [5, 6, 20, 59], with increasing

precision and sophistication [32, 62], leaving little doubt that quantum theory exhibits an intrinsic form of *nonlocality*[1].

The discovery of quantum nonlocality prompted a renewed interest in the structure of correlations allowed by different physical theories. In particular, researchers began to explore the space of possible correlations among distant parties performing local measurements [16, 60]. From this perspective, each class of physical theories—classical, quantum, and no-signaling—defines a distinct set of achievable correlations. The classical (or local) set forms a polytope characterized by deterministic strategies and convex combinations thereof. The no-signaling set, which includes all correlations consistent with relativistic causality, forms a larger polytope encompassing both classical and quantum correlations. The set of quantum correlations, however, occupies a rich intermediate position: it is convex but not a polytope, and exhibits a highly nontrivial boundary structure.

A powerful way to study quantum correlations is through their *geometric* representation in probability space. This approach was pioneered by B. S. Tsirelson in the 1980s, who characterized the set of quantum correlations in terms of the Hilbert space formalism of quantum theory. In what is now known as Tsirelson's theorem [19], he provided explicit bounds on the strength of quantum violations of Bell inequalities, showing that these bounds are strictly stronger than classical, but weaker than the no-signaling constraints. Tsirelson's work laid the foundation for a geometric approach to quantum nonlocality, enabling a deeper understanding of the shape and structure of the quantum set Q.

This geometric perspective plays a central role in foundational investigations. One of the major open questions in the foundations of quantum theory is whether quantum mechanics is uniquely singled out by simple physical or information-theoretic principles. In recent decades, several reconstruction programs have attempted to derive the formalism of quantum theory from axioms such as continuity, reversibility, and tomographic locality [18, 31, 38, 55]. Other approaches seek to understand quantum correlations by embedding them within a broader landscape of logically consistent theories, asking whether quantum theory is *an island in theoryspace* [1, 40]. Principles like *information causality* [50],

[1] Throughout this work, we use the term *nonlocality* to refer specifically to the empirical violation of a Bell inequality. This notion is standard in the physics literature, where Bell nonlocality denotes statistical correlations that cannot be explained by any local hidden variable model. It is important to emphasize, however, that Bell's theorem—and the corresponding definition of locality—rests on precise assumptions, including *statistical independence*, *realism*, and a form of *relativistic causality*. The interpretation and physical justification of "locality" involved, remain subjects of ongoing debate. In particular, the extent to which Bell inequality violations conflict with the principles of special relativity depends on one's interpretative framework and assumptions about the ontology of quantum theory. These foundational questions, which have been explored extensively in both the physics and philosophy of science communities since Bell's original work, lie beyond the scope of this thesis. For further discussion, see e.g. [30, 39, 48].

macroscopic locality [45], and *local orthogonality* [27] have been proposed to distinguish quantum correlations from more general no-signaling ones. In this context, the structure of the set Q reflects deep physical constraints, and understanding its geometry provides a window into the fundamental properties of quantum theory itself.

In recent decades, this perspective has also proved to be of growing *practical* relevance. The nonlocal correlations predicted by quantum mechanics have become a key resource in quantum information science. *Device-independent* protocols [52, 61] exploit quantum nonlocality to guarantee security or functionality without relying on the internal workings of the devices used. These include deviceindependent quantum key distribution [2, 25, 41], randomness certification [53], and self-testing of quantum states and measurements [65]. Furthermore, the structure of quantum correlations plays a role in quantum computing and complexity theory, where it can lead to computational speed-ups [4, 34], and in the design of quantum networks [66] and the future quantum internet [35, 58, 70]. Understanding the geometry of the quantum set is thus not only essential for foundational clarity, but also for technological advancement.

II. CLASSICAL, QUANTUM AND NO-SIGNALING CORRELATIONS

2.1. The device-independent paradigm

In many areas of science, it is often fruitful to analyze systems by focusing solely on their observable input-output behavior, abstracting away from their internal mechanisms. This strategy, commonly referred to as the *black-box approach*, is particularly powerful in quantum information theory, where it underpins the *device-independent (DI) paradigm* [52, 61]. In this framework, quantum devices are treated as opaque systems whose internal workings are unknown or untrusted. All that is accessible to the experimenter is the statistical behavior of the devices in response to various inputs.

In this thesis, we adopt this perspective to investigate the implications of quantum theory in bipartite Bell scenarios, where two spatially separated parties—traditionally named Alice and Bob—interact with uncharacterized devices. By analyzing the observable input-output correlations produced in such settings, we can uncover deep insights into the structure of quantum correlations, the limitations of classical models, and the potential for certifying quantum resources in a device-independent manner. Consider a bipartite experimental setting involving two space-like separated parties, traditionally named Alice and Bob. Each party is located in a distinct laboratory, such that no communication can occur between them during the execution of the experiment. In particular, the choice of measurement setting by one party cannot be signaled to the other. This condition can be enforced by ensuring that the measurement events are space-like separated in accordance with special relativity: if Alice's choice of setting x and Bob's choice y are made after they are causally disconnected, then neither party can influence the other's measurement outcome.

In each run of the experiment, Alice and Bob each choose one of m possible measurement settings, denoted $x, y \in \{1, \ldots, m\}$, and obtain outcomes $a, b \in \{1, \ldots, k\}$, respectively. The experiment is characterized statistically by the joint conditional probability distribution

$$P(a, b|x, y), \tag{II.1}$$

which gives the probability of obtaining outcomes a and b when the measurement settings x and y are chosen.

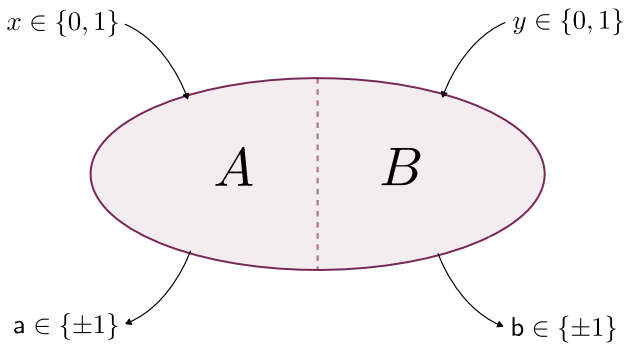

Figure II.1: Pictorial representation of the CHSH scenario. From [10].

This abstract framework is known as a *Bell scenario*, and it encapsulates the notion of a *black-box model*, in which each party inputs a setting and receives an output. A Bell scenario with outcome alphabet of size k, and m measurement settings per party is specified by k^2m^2 conditional probabilities, one for each possible combination of inputs and outputs.

The collection of all such probabilities defines what is called a *behavior*:

$$\boldsymbol{P} := \{P(a,b|x,y)\}_{a,b,x,y}. \tag{II.2}$$

Each behavior $\boldsymbol{P}$ is a point in the space $\mathbb{R}^{k^2m^2}$. However, physical realizability imposes two fundamental constraints:

$$\text{Positivity:} \quad P(a,b|x,y) \geq 0, \quad \forall a,b,x,y \tag{II.3a}$$

$$\text{Normalization:} \quad \sum_{a,b} P(a,b|x,y) = 1, \quad \forall x,y. \tag{II.3b}$$

These conditions ensure that the behavior $\boldsymbol{P}$ is a valid probability distribution for each choice of settings. The set of all points $\boldsymbol{P}$ satisfying these constraints defines a convex subset of $\mathbb{R}^{k^2m^2}$ known as the *behavior space* $\mathcal{P}$, with

$$\dim \mathcal{P} = (k^2-1)m^2. \tag{II.4}$$

A particularly important case is the simplest nontrivial Bell scenario, known as the *CHSH scenario*, where $m = 2$ and $k = 2$. In this case, Alice and Bob each have two possible measurement settings, $x, y \in \{0, 1\}$, and each measurement yields one of two outcomes, conventionally labeled $a, b \in \{\pm 1\}$. This scenario has been extensively studied in both theoretical and experimental contexts, and plays a central role in the investigation of quantum nonlocality.

Remark 1. While the discussion above is restricted to the bipartite case ($n = 2$), the framework can be naturally generalized to *multipartite* or *generalized Bell scenarios*, where n spatially separated

parties share a global system and independently choose local measurements. The corresponding behavior is then a conditional distribution

$$P(a_1, \ldots, a_n | x_1, \ldots, x_n) := P(\boldsymbol{a}, \boldsymbol{x}), \tag{II.5}$$

and the behavior space $\mathcal{P}_n$ is embedded in $\mathbb{R}^{k^n m^n}$, subject to similar positivity and normalization constraints.

2.2. Different types of correlations

The existence of a given physical model behind the correlations obtained in a Bell scenario translates into additional constraints on the behaviors $\boldsymbol{P}$. We consider three main types of correlations:

1. no-signaling correlations
2. local correlations
3. quantum correlations.

2.2.1. No-signaling correlations

A foundational principle shared by both classical and quantum physics is the *no-signaling principle*, which asserts the impossibility of instantaneous information transfer between spatially separated systems:

Principle 1 (No-signaling principle). *The transmission of information requires a physical carrier that departs from the sender after the message has been chosen.*

This principle encapsulates the empirical fact thatc ommunication necessitates a physical medium — such as acoustic waves, electromagnetic radiation, or material particles—to convey information. Since such carriers propagate through space-time, and special relativity prohibits any influence from propagating faster than the speed of light in vacuum, causal signaling between space-like separated events is forbidden. Consequently, in scenarios involving two distant parties, if their respective inputs are chosen after they become space-like separated, the input selected by one party cannot influence the measurement outcome obtained by the other.

In operational terms, this implies that the marginal probability distribution of one party's outcomes must be independent of the other party's input choice:

$$P(a|x,y) := \sum_{b=1}^{k} P(a,b|x,y) \overset{NS}{=} P(a|x), \qquad \forall a,x,y. \tag{II.6a}$$

$$P(b|x,y) := \sum_{a=1}^{k} P(a,b|x,y) \overset{NS}{=} P(b|y), \qquad \forall b,x,y. \tag{II.6b}$$

Equivalently,

Definition 1. A conditional probability distribution $P(a,b|x,y)$ over outcomes $a,b \in \{1,\ldots,k\}$ and inputs (measurement settings) $x,y \in \{1,\ldots,m\}$ is said to be *no-signaling* if it satisfies the following constraints:

$$\sum_{b=1}^{k} P(a,b|x,y) = \sum_{b=1}^{k} P(a,b|x,y'), \qquad \forall a,x,y,y', \tag{II.7a}$$

$$\sum_{a=1}^{k} P(a,b|x,y) = \sum_{a=1}^{k} P(a,b|x',y), \qquad \forall b,x,x',y. \tag{II.7b}$$

The set of all such distributions is called the *no-signaling set*, denoted by NS.

These constraints guarantee that neither Alice nor Bob can use their choice of measurement setting to influence, and thus communicate with, the other party.

The no-signaling principle plays a pivotal role in quantum information theory and the foundations of quantum mechanics. It serves as a universal constraint on physically realizable correlations and is essential for delineating the boundary between quantum and post-quantum theories. In particular, while quantum correlations always satisfy the no-signaling conditions, the converse is not true: some no-signaling correlations, such as those described by the *Popescu-Rohrlich (PR) box*, exceed the strength of quantum correlations and are not physically realizable within quantum theory [56]. The canonical PR box is defined by the conditional probabilities

$$P_{PR}(a,b|x,y) := \begin{cases} \frac{1}{2} & \text{if } ab = (-1)^{xy}, \\ 0 & \text{otherwise,} \end{cases} \tag{II.8}$$

where $a,b \in \{-1,1\}, x,y \in \{0,1\}$.

Thus, the no-signaling principle not only encodes a fundamental causal structure of physical theories, but also imposes stringent operational constraints on any observed statistical correlations.

2.2.2. Local correlations

The concept of *local causality* was introduced by John Bell as a formulation of the relativistic principle that influences cannot travel faster than light. In Bell's words [13]:

A theory will be said to be locally causal if the probabilities attached to values of local beables[2] in a space-time region 1 are unaltered by specification of values in a space-like separated region 2, when what happens in the backward light cone of 1 is already sufficiently specified.

This principle expresses the idea that events in one region of spacetime should not be directly influenced by choices or events occurring in a distant, space-like separated region — provided that all relevant past information is already accounted for. More precisely, once a complete specification of all physical influences in the past light cone of region 1 is given, any additional information from region 2 should be redundant in determining the probabilities for events in region 1.

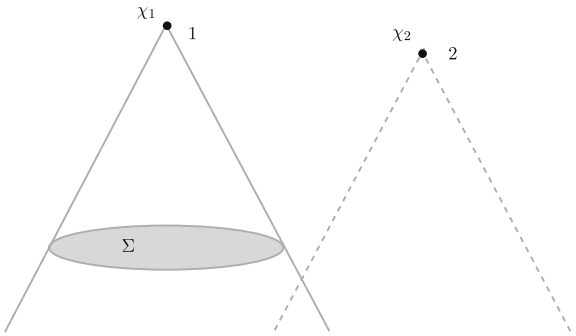

Figure II.2: According to Bell's notion of local causality, the probability of an event χ_1 in region 1, conditioned on a complete specification C_Σ of events in a spacetime slice Σ within its backward light cone, should be unaffected by additional conditioning on a space-like separated event χ_2 outside the future of Σ. From [47].

In a typical Bell experiment, although Alice and Bob are located at distant, space-like separated regions, they may still share information from a common past. This shared information could consist of pre-established strategies, shared randomness, or any other correlated data originating from events within their mutual backward light cones. To formally account for such pre-existing correlations, one introduces a variable λ, commonly referred to as a *hidden variable*, which encodes all relevant data accessible to both parties before the measurements are chosen.

According to the principle of local causality, measurement outcomes should be determined solely by local causes. That is, the outcome observed by each party depends only on their local measurement setting and on the shared hidden variable λ, and not on the distant party's setting or outcome. This assumption leads to factorize of the conditional on λ joint probability distribution in the form

[2] The term *beable*, introduced by John Bellin[12], refers to elements of a physical theory that are supposed to correspond to objective features of reality — what "is" rather than what is merely "observed." Unlike *observables* in standard quantum mechanics, which are associated with measurement outcomes, beables are intended to describe the physical state of a system independently of observation.

$$P(a,b|x,y,\lambda) = P(a|x,\lambda)P(b|y,\lambda), \tag{II.9}$$

where $P(a|x,\lambda)$ and $P(b|y,\lambda)$ are valid probability distributions, describing the local response of each party given the hidden variable. Then, it is natural to state that

Definition 2. A joint probability distribution $P(a,b|x,y)$ is said to be *local* if it can be expressed as a convex mixture of product distributions conditioned on a shared hidden variable λ. That is,

$$P(a,b|x,y) = \int_\Lambda d\lambda\, Q(\lambda)P(a|x,\lambda)P(b|y,\lambda), \tag{II.10}$$

where:

- λ is a hidden variable, drawn from a probability distribution $Q(\lambda)$ over some measurable space Λ;
- $P(a|x,\lambda)$ and $P(b|y,\lambda)$ are local response functions, representing valid conditional probability distributions for Alice and Bob, respectively.

The set of all probability distributions that admit such a decomposition defines the *local set* L.

In this formulation, Alice's and Bob's outcomes depend only on their local settings and the shared variable λ, in line with the requirement of relativistic local causality.

Remark 2. It is essential to emphasize that locality is a property of the model, not of the hidden variable. The hidden variable λ may encode any kind of shared information, but the requirement of locality is that the responses of Alice and Bob depend only on their respective inputs, once λ is fixed.

A particularly relevant class of local models is that of the *deterministic strategies*, where for each value of λ the response functions $P(a|x,\lambda)$ and $P(b|y,\lambda)$ take values in $\{0,1\}$. That is, for each λ, the outputs are deterministically fixed functions of the inputs:

$$a = f_A(x,\lambda), \qquad b = f_B(y,\lambda). \tag{II.11}$$

We now prove that deterministic local hidden-variable (LHV) models are equivalent in their expressive power to general (stochastic) LHV models when it comes to describing local correlations. This means that any correlation achievable by a stochastic LHV model can also be achieved by a deterministic one, provided the hidden variable itself can encompass additional randomness.

Proposition 1. *Every local behavior $\mathbf{P} \in \mathcal{L}$ generated by a general (stochastic) local hidden-variable model can also be generated by a deterministic local hidden-variable model.*

Proof. Let us start with a general local behavior $\mathbf{P}$ defined by (II.10), with stochastic response functions $P(a|x,\lambda)$ and $P(b|y,\lambda)$, and a hidden variable distribution $Q(\lambda)$. We aim to construct an equivalent deterministic model.

First, define a new, augmented hidden variable

$$\lambda' := (\lambda, \mu_A, \mu_B), \tag{II.12}$$

where $\mu_A, \mu_B \in [0, 1]$ are independent uniformly distributed random numbers. These additional random numbers will serve to "determinize" the local probabilistic choices.

Next, we define new deterministic response functions, $P'(a|x, \lambda')$ for Alice and $P'(b|y, \lambda')$ for Bob. For Alice, we use her original stochastic response function $P(a|x, \lambda)$ to build a cumulative distribution function (CDF)

$$F(a|x, \lambda) := \sum_{a_0 \leq a} P(a_0|x, \lambda). \tag{II.13}$$

Using this, we construct Alice's new deterministic response function

$$P'(a|x, \lambda') := \begin{cases} 1 & \text{if } F(a-1|x, \lambda) \leq \mu_A < F(a|x, \lambda), \\ 0 & \text{otherwise.} \end{cases} \tag{II.14}$$

Here, $F(a-1|x, \lambda)$ for the smallest outcome a is taken to be 0. This construction ensures that for a fixed λ and a random μ_A, $P'(a|x, \lambda')$ assigns 1 to exactly one outcome a, thus making the response deterministic. A similar construction applies for Bob, using μ_B to define $P'(b|y, \lambda')$.

Finally, we define the new distribution over the augmented hidden variable λ' as

$$Q'(\lambda') := Q(\lambda). \tag{II.15}$$

Now, let's verify that this deterministic model recovers the predictions of the original stochastic model. The joint probability $P'(a, b|x, y)$ in the new deterministic model is

$$P'(a, b|x, y) = \int_\Lambda d\lambda \int_0^1 d\mu_A \int_0^1 d\mu_B \; P'(a|x, \lambda, \mu_A) P'(b|y, \lambda, \mu_B) Q(\lambda).$$

Due to the independence of μ_A and μ_B, we can separate the integrals:

$$P'(a, b|x, y) = \int_\Lambda d\lambda \left(\int_0^1 d\mu_A \; P'(a|x, \lambda, \mu_A) \right) \left(\int_0^1 d\mu_B \; P'(b|y, \lambda, \mu_B) \right) Q(\lambda).$$

Consider the inner integral for Alice:

$$\int_0^1 d\mu_A \; P'(a|x, \lambda, \mu_A).$$

By definition of $P'(a|x, \lambda')$ in (II.14), this integral is 1 if μ_A falls within the interval $[F(a-1|x, \lambda), F(a|x, \lambda))$, and 0 otherwise. The length of this interval is $F(a|x, \lambda) - F(a-1|x, \lambda)$, which by definition of the CDF (II.13) is precisely $P(a|x, \lambda)$. So,

$$\int_0^1 \mathrm{d}\mu_A \, P'(a|x,\lambda,\mu_A) = P(a|x,\lambda).$$

and a similar result holds for Bob.

Substituting these back into the expression for $P'(a,b|x,y)$, one obtains

$$P'(a,b|x,y) = \int_\Lambda \mathrm{d}\lambda \, Q(\lambda) P(a|x,\lambda) P(b|y,\lambda). \tag{II.16}$$

This is exactly the expression for the general stochastic local behavior $\boldsymbol{P}$ given by (II.10).

This construction, originally introduced by Fine [26], shows that every stochastic local model can be simulated by a deterministic one by incorporating the necessary randomness into the definition of the hidden variable itself.

Correlations that do not admit a decomposition of the form (II.10) are called *nonlocal*. This can only occur in scenarios with at least two inputs and two outputs ($m,\ k \geq 2$); otherwise, all behaviors in P can be modeled locally.[3]

2.2.3. Quantum correlations

Finally, we consider the set of behaviors achievable in quantum mechanics.

Definition 3. For a given Bell scenario, the *quantum set* $\boldsymbol{Q}$ of quantum behaviors corresponds to the elements of $\mathcal{P}$ that can be written as

$$P(a,b|x,y) = \mathrm{Tr}\left((\hat{M}^A_{a|x} \otimes \hat{M}^B_{b|y}) \rho_{AB} \right), \tag{II.17}$$

where $\hat{\rho}_{AB}$ is a density operator acting in the bipartite Hilbert space $\mathcal{H}_A \otimes \mathcal{H}_B$ of unspecified dimension, $\hat{M}^A_{a|x}$, ($\hat{M}^B_{b|y}$) are Positive Operator-Valued Measures (POVM) elements on $\mathcal{H}_A$ ($\mathcal{H}_B$) characterizing Alice's (Bob's) measurements.

Note that the operators $\hat{M}^A_{a|x}$ and $\hat{M}^B_{b|y}$ are not necessarily orthogonal projectors. The only requirement is that they are normalized positive semidefinite operators, i.e.,

$$\hat{M}^A_{a|x}, \hat{M}^B_{b|y} \geq 0, \qquad \sum_{a=1}^{k} \hat{M}^A_{a|x} = \mathbb{1}_A, \quad \sum_{b=1}^{k} \hat{M}^B_{b|y} = \mathbb{1}_B. \tag{II.18}$$

[3] Nonlocal correlations can only arise in Bell scenarios where both the number of measurement settings and the number of outcomes per party satisfy $m,\ k \geq 2$. If $m = 1$, each party performs only one measurement, so the observed behavior reduces to a fixed joint distribution $P(a,\ b)$. In this case, any correlation — no matter how strong — can be reproduced by a local model, since there is no dependence on measurement choices. Likewise, if $k = 1$, the outputs are fixed, rendering the correlations trivial ($a = a_0,\ b = b_0$ and $P(a_0,\ b_0|x,\ y) = 1\ \forall x,\ y$). Thus, both measurement choice and outcome variability are essential for revealing nonlocality.

Remark 3. The fact that the dimensions of the Hilbert space is left unspecified is significant for several reasons. First, it ensures that the players' strategies are not artificially constrained. In particular, the shared quantum state $\hat{\rho}_{AB}$ need not represent only entanglement between the parties: it may also include arbitrary local (separable) information.
Second, this flexibility allows us to adopt two important simplifications without loss of generality:

1. Purification of the state: any mixed state $\hat{\rho}_{AB}$ shared by the players can be viewed as the reduced state of a larger pure state $|\psi\rangle$ defined on an extended Hilbert space (purification theorem).
2. Projective measurements: any general measurement described by a Positive Operator-Valued Measurerement (POVM) can be implemented as a projective measurement (i.e., one using orthogonal projection operators) on a larger Hilbert space. This follows from Naimark's dilation theorem [68], which guarantees that for any POVM, there exists an extended space in which the same measurement statistics can be obtained via a standard projective measurement.

That is, we can equivalently write a quantum behavior as

$$P(a,b|x,y) = \langle\psi|\,\hat{\Pi}^{A}_{a|x} \otimes \hat{\Pi}^{B}_{b|y}\,|\psi\rangle\,, \tag{II.19}$$

where $|\psi\rangle \in \mathcal{H}_A \otimes \mathcal{H}_B$ and

$$\hat{\Pi}^{A}_{a|x}\hat{\Pi}^{A}_{a'|x} = \delta_{aa'}\hat{\Pi}^{A}_{a|x}, \qquad \sum_{a}\hat{\Pi}^{A}_{a|x} = \mathbb{1}_A, \tag{II.20a}$$

$$\hat{\Pi}^{B}_{b|y}\hat{\Pi}^{B}_{b'|y} = \delta_{bb'}\hat{\Pi}^{B}_{b|y}, \qquad \sum_{b}\hat{\Pi}^{B}_{b|y} = \mathbb{1}_B. \tag{II.20b}$$

A different definition of quantum behaviors is also possible, where instead of imposing a tensor product structure between Alice's and Bob's systems, we merely require that their local operators commute [67]:

Definition 4. A behavior $\boldsymbol{P} \in \mathcal{P}$ belongs to the set Q' of *commuting-operator quantum correlations* if there exist:

- a Hilbert space $\mathcal{H}$,
- a quantum state $|\psi\rangle \in \mathcal{H}$,
- families of positive operators $\{\hat{\Pi}^{A}_{a|x}\}, \{\hat{\Pi}^{B}_{b|y}\} \subset L(\mathcal{H})$,

such that

$$P(a,b|x,y) = \langle\psi|\,\hat{\Pi}^{A}_{a|x}\hat{\Pi}^{B}_{b|y}\,|\psi\rangle\,, \qquad \text{and} \qquad [\hat{\Pi}^{A}_{a|x}, \hat{\Pi}^{B}_{b|y}] = 0 \quad \forall a,b,x,y. \tag{II.21}$$

In contrast to the standard tensor-product definition of quantum behaviors (defining the set Q), this commuting-operator model does not assume an explicit partitioning of the Hilbert space into local subsystems.

It is easy to see that $Q \subseteq Q'$: in fact, any behavior realized via a tensor-product representation also satisfies the commuting condition, since operators of the form

$$\{\hat{\Pi}^A_{a|x} \otimes \mathbb{1}_B\}, \qquad \{\mathbb{1}_A \otimes \hat{\Pi}^B_{b|y}\}$$

commute.

Whether every commuting-operator model admits a tensor-product representation was long known as Tsirelson's problem [22, 44]. In general,

$$Q \subseteq Q' \subseteq NS, \tag{II.22}$$

but neither inclusion is an equality. For specific scenarios, such as the CHSH case in finite dimensions, it is known that $Q = Q'$. However, in the infinite-dimensional setting, this equivalence fails. In particular, Slofstra [64] showed that Q is not closed, meaning that there exist sequences of quantum behaviors that converge to a point outside Q, although still in $\overline{Q} \subseteq Q'$.

This left open the question of whether the closure $\overline{Q}$ of the quantum set coincides with the commuting-operator set Q'. This question was conclusively resolved by Ji et al. [33], who proved that

$$\overline{Q} \subsetneq Q', \tag{II.23}$$

thereby showing that there exist correlations that can be realized using commuting measurements on a single Hilbert space, but that cannot even be approximated by any tensor-product quantum strategy — not even in infinite dimensions. This result demonstrates that the commuting-operator model is strictly more general than the tensor-product model, and implies that the maximum winning probability of certain multiplayer nonlocal games can differ depending on the chosen quantum model [33].

III. GEOMETRY OF CORRELATIONS

3.1. Geometry of correlations

Let us now consider some geometrical properties of the sets of correlations introduced so far, namely the local set $\mathcal{L}$, the quantum set Q, and the no-signaling set NS.
One can show that any local behavior, i.e., any probability distribution that admits a decomposition as in Eq. (II.10), also admits a quantum realization of the form (II.17), and thus belongs to Q [54]. In this sense, local correlations form a subset of quantum correlations, namely

$$\mathcal{L} \subseteq Q.$$

Moreover, quantum correlations automatically satisfy the no-signaling constraints, since measurements on separate subsystems of a quantum system cannot transmit information instantaneously (*no-communication theorem*). Therefore, it holds

$$Q \subseteq NS.$$

However, both inclusions are known to be strict:

- Bell famously showed that there exist quantum correlations that cannot be reproduced by any local model, i.e., $\mathcal{L} \subsetneq Q$ [11].
- Later, Popescu and Rohrlich demonstrated that there exist hypothetical no-signaling correlations (such as PR-box correlations) that exceed the bounds imposed by quantum theory, i.e., $Q \subsetneq NS$ [56].

In general, we thus have the strict inclusions

$$\mathcal{L} \subsetneq Q \subsetneq NS. \tag{III.1}$$

From a physical perspective, this hierarchy reflects the increasingly general assumptions made about the nature of correlations:

- $\mathcal{L}$ contains all behaviors that can be explained by the only presence of shared classical information, i.e., local hidden variable models;
- Q allows for the use of quantum entanglement and measurements on composite systems;
- NS includes all correlations that obey the relativistic no-signaling constraint, regardless of their physical realizability.

Furthermore, it can be shown that $\dim \mathcal{L} = \dim Q = \dim NS = t$ [51], where

$$t := 2(k-1)m + (k-1)^2 m^2. \tag{III.2}$$

In the case of binary outcomes ($k = 2$), a useful parametrization is given in terms of $2m + m^2$ quantities, collectively called *correlators*, which include both the *correlations*

$$\langle A_x B_y \rangle := \sum_{a,b} ab\, P(a,b|x,y), \tag{III.3a}$$

and the marginals

$$\langle A_x \rangle := \sum_{a} a\, P(a|x), \quad \langle B_y \rangle := \sum_{b} b\, P(b|y). \tag{III.3b}$$

In the CHSH scenario, this change of variables enables the study of a behavior $\boldsymbol{P} \in \mathbb{R}^8$, by representing it in table form, structured as follows:

$$\boldsymbol{P} = \begin{array}{c|c|c} & \langle B_0 \rangle & \langle B_1 \rangle \\ \hline \langle A_0 \rangle & \langle A_0 B_0 \rangle & \langle A_0 B_1 \rangle \\ \langle A_1 \rangle & \langle A_1 B_0 \rangle & \langle A_1 B_1 \rangle \end{array}, \tag{III.4}$$

where each entry corresponds to a specific expectation value or joint probability.

For quantum behaviors, in the CHSH scenario, it is customary to express the measurements performed by Alice and Bob in terms of Hermitian[4] operators $\mathcal{A}_x \in \mathcal{L}(\mathrm{H}_A)$ and $\mathcal{B}_y \in \mathcal{L}(\mathrm{H}_B)$, each with eigenvalues in $\{-1, 1\}$ and defined as

$$\hat{A}_x := \hat{\Pi}^A_{1|x} - \hat{\Pi}^A_{-1|x}, \qquad \hat{B}_y := \hat{\Pi}^B_{1|y} - \hat{\Pi}^B_{-1|y}, \tag{III.5}$$

and satisfy

$$\hat{A}_x^2 = \mathbb{1}_A, \qquad \hat{B}_y^2 = \mathbb{1}_B, \qquad [\hat{A}_x, \hat{B}_y] = 0 \qquad \forall x, y \in \{0,1\}. \tag{III.6}$$

These operators provide a convenient expression for the correlators:

$$\langle A_x B_y \rangle = \mathrm{Tr}\left[(\hat{A}_x \otimes \hat{B}_y)\hat{\rho}_{AB}\right], \tag{III.7a}$$

$$\langle A_x \rangle = \mathrm{Tr}\left[(\hat{A}_x \otimes \mathbb{1}_B)\hat{\rho}_{AB}\right], \tag{III.7b}$$

$$\langle B_y \rangle = \mathrm{Tr}\left[(\mathbb{1}_A \otimes \hat{B}_y)\rho_{AB}\right]. \tag{III.7c}$$

We refer to $(\hat{\rho}, \hat{A}_x, \hat{B}_y)$ as a *realization*, where each realization uniquely determines a correlator vector via the equations above.

Remarkably, the sets $\mathcal{L}$, Q, and NS are all closed, bounded, and convex [54]. This means that if $\boldsymbol{P}_1$

[4] Strictly speaking, quantum observables are represented by self-adjoint operators. In infinite-dimensional Hilbert spaces, Hermitian and self-adjoint operators are not equivalent; however, in the finite-dimensional case considered throughout this thesis, the two notions coincide.

and $\boldsymbol{P}_2$ are elements of any one of these sets, then any convex combination $\mu\boldsymbol{P}_1 + (1-\mu)\boldsymbol{P}_2$ with $0 \le \mu \le 1$ also belongs to the same set. The convexity of the non-signaling set $\mathcal{NS}$ follows directly from the fact that it is defined by linear constraints, which are preserved under convex combinations. As for the local set $\mathcal{L}$, its convexity arises from its construction: it consists of all convex mixtures of deterministic (separable) probability distributions, as described in Eq. (II.10).

We now show that $\mathcal{Q}$ is convex, i.e., if $P(a,b|x,y)$ and $Q(a,b|x,y)$ belong to $\mathcal{Q}$, then their convex combination

$$R(a,b|x,y) := \lambda P(a,b|x,y) + (1-\lambda)Q(a,b|x,y), \quad \text{for } 0 \le \lambda \le 1, \tag{III.8}$$

also belongs to $\mathcal{Q}$.

Proof. Since $P(a,b|x,y)$ and $Q(a,b|x,y)$ are in $\mathcal{Q}$, there exist the quantum realizations

$$P(a,b|x,y) = \mathrm{Tr}\left[(\hat{M}^A_{a|x} \otimes \hat{M}^B_{b|y})\hat{\rho}_1\right], \tag{III.9a}$$

and

$$Q(a,b|x,y) = \mathrm{Tr}\left[(\hat{N}^A_{a|x} \otimes \hat{N}^B_{b|y})\hat{\rho}_2\right], \tag{III.9b}$$

for some states $\hat{\rho}_1, \hat{\rho}_2$ and POVMs $\{\hat{M}^A_{a|x}, \hat{M}^B_{b|y}\}$, $\{\hat{N}^A_{a|x}, \hat{N}^B_{b|y}\}$.

To construct a quantum realization of $R(a,b|x,y)$, consider the new bipartite state:

$$\hat{\rho} := \lambda\hat{\rho}_1 \oplus (1-\lambda)\hat{\rho}_2, \tag{III.10}$$

acting on the direct sum Hilbert space

$$\mathcal{H}_A \otimes \mathcal{H}_B := (\mathcal{H}^1_A \otimes \mathcal{H}^1_B) \oplus (\mathcal{H}^2_A \otimes \mathcal{H}^2_B). \tag{III.11}$$

Similarly, define the block-diagonal measurement operators:

$$\hat{O}^A_{a|x} := \hat{M}^A_{a|x} \oplus \hat{N}^A_{a|x}, \qquad \hat{O}^B_{b|y} := \hat{M}^B_{b|y} \oplus \hat{N}^B_{b|y}. \tag{III.12}$$

By construction, these operators satisfy the completeness conditions:

$$\sum_a \hat{O}^A_{a|x} = \mathbb{1}_A, \qquad \sum_b \hat{O}^B_{b|y} = \mathbb{1}_B. \tag{III.13}$$

Now, computing the probability distribution using this realization:

$$\begin{aligned} R(a,b|x,y) &:= \mathrm{Tr}\left[(\hat{O}^A_{a|x} \otimes \hat{O}^B_{b|y})\hat{\rho}\right] \\ &= \mathrm{Tr}\left[(\hat{M}^A_{a|x} \oplus \hat{N}^A_{a|x}) \otimes (\hat{M}^B_{b|y} \oplus \hat{N}^B_{b|y})(\lambda\hat{\rho}_1 \oplus (1-\lambda)\hat{\rho}_2)\right] \\ &= \lambda\,\mathrm{Tr}\left[(\hat{M}^A_{a|x} \otimes \hat{M}^B_{b|y})\hat{\rho}_1\right] + (1-\lambda)\,\mathrm{Tr}\left[(\hat{N}^A_{a|x} \otimes \hat{N}^B_{b|y})\hat{\rho}_2\right]. \end{aligned}$$

Using the definitions of $P(a,b|x,y)$ and $Q(a,b|x,y)$, we conclude that

$$R(a,b|x,y) = \lambda P(a,b|x,y) + (1-\lambda)Q(a,b|x,y). \tag{III.14}$$

Since we have explicitly constructed a quantum state and measurement scheme that produces $R(a, b|x, y)$, it follows that $\boldsymbol{R} \in$ Q. This proves that the quantum set is convex.

While discussing the geometry of the correlation sets, it is natural to employ standard tools from convex geometry —most notably the notions of boundary points, extremal points, and exposed points. Let $\mathcal{K} \subset \mathbb{R}^d$ be a compact convex set (i.e., closed and bounded). A point $\boldsymbol{u} \in \mathcal{K}$ is called a *boundary point* if it belongs to the topological boundary of $\mathcal{K}$; that is, it does not lie in the interior of the set. A boundary point is said to be *extremal* if it cannot be written as a non-trivial convex combination of other points in $\mathcal{K}$. The set of all extremal points of $\mathcal{K}$ is denoted $\mathcal{K}_{\text{ext}}$. A stronger condition is that of *exposedness*: a point $\boldsymbol{u} \in \mathcal{K}$ is *exposed* if there exists a vector $\boldsymbol{v} \in \mathbb{R}^d$ such that $\boldsymbol{u}$ uniquely maximizes the inner product $\boldsymbol{v} \cdot \boldsymbol{w}$ over all $\boldsymbol{w} \in \mathcal{K}$. That is, the set

$$F_{\boldsymbol{v}} \coloneqq \left\{ \boldsymbol{w} \in \mathcal{K} : \boldsymbol{v} \cdot \boldsymbol{w} = \max_{z \in \mathcal{K}} \boldsymbol{v} \cdot z \right\} \tag{III.15}$$

is reduced to the singleton $\{\boldsymbol{u}\}$. In this case, the hyperplane defined by $\boldsymbol{v} \cdot \boldsymbol{w} = \max_{z \in \mathcal{K}} \boldsymbol{v} \cdot z$ is a *supporting hyperplane* of $\mathcal{K}$, and the set $F_{\boldsymbol{v}}$ is referred to as the *exposed face of* $\mathcal{K}$ *associated to* $\boldsymbol{v}$.

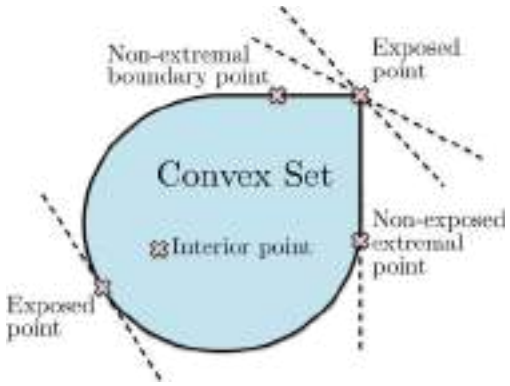

Figure III.1: Different types of points of a compact convex set. From [29].

By construction, we always have the chain of inclusions:

$$\mathcal{K}_{\text{exp}} \subseteq \mathcal{K}_{\text{ext}} \subseteq \mathcal{K}_{\text{bnd}} \subseteq \mathcal{K}, \tag{III.16}$$

and in general, each inclusion is strict. This hierarchy is illustrated in Fig. III.1. An important structural result in convex geometry, known as the *Krein-Milman theorem* [63], states that any compact convex set $\mathcal{K}$ is equal to the convex hull of its extremal points:

$$\mathcal{K} = \text{conv}(\mathcal{K}_{\text{ext}}). \tag{III.17}$$

Hence, optimization of a linear functional over $\mathcal{K}$ always attains its maximum at an extremal point. However, the maximizer need not be unique, nor does it need to be an exposed point. This leads to the distinction between extremal and exposed points: although every exposed point is extremal, the converse is not true in general. Still, a classical result due to Straszewicz [63] shows that in finite-dimensional spaces, the set of exposed points is dense in the set of extremal points. That is, extremal but non-exposed points exist, but they are in a certain sense exceptional.

Remark 4. For polytopes, i.e. convex hulls of finitely many points, this hierarchy collapses: all extremal points are exposed, and they correspond to the vertices of the polytope.

3.2. Bell inequalities

Since the sets $\mathcal{L}$, $\mathcal{Q}$, and $\mathcal{NS}$ are convex, the *hyperplane separation theorem* ensures that any behavior $\boldsymbol{P}' \in \mathbb{R}^I$ lying outside one of these sets can be separated from it by a linear inequality. That is, if $\boldsymbol{P}' \notin \mathcal{K}$, where $\mathcal{K}$ denotes either $\mathcal{L}$, $\mathcal{Q}$, or $\mathcal{NS}$, then there exists a vector $\boldsymbol{\beta} \in \mathbb{R}^I$ and a constant $\beta_{\mathcal{K}} \in \mathbb{R}$ such that

$$\boldsymbol{\beta} \cdot \boldsymbol{P} \leq \beta_{\mathcal{K}} \quad \text{for all } \boldsymbol{P} \in \mathcal{K}, \qquad \text{while} \qquad \boldsymbol{\beta} \cdot \boldsymbol{P}' > \beta_{\mathcal{K}}. \tag{III.18}$$

In the case where $\mathcal{K} \equiv \mathcal{L}$, the inequality

$$\boldsymbol{\beta} \cdot \boldsymbol{P} \leq \beta_{\mathcal{L}} \tag{III.19}$$

is known as a *Bell inequality*. Such inequalities delineate the boundary of the local set and provide a criterion for detecting nonlocality: any behavior that violates a Bell inequality is necessarily nonlocal. The quantity $\beta_{\mathcal{L}}$ is called the *local bound* of the Bell expression $\boldsymbol{\beta}$, and it represents the maximum value that this expression can attain over all local correlations. If the inequality

$$\boldsymbol{\beta} \cdot \boldsymbol{P} \leq \beta_{\mathcal{L}}$$

is known as a *Bell inequality*. Such inequalities delineate the boundary of the local set and provide a criterion for detecting nonlocality: any behavior that violates a Bell inequality is necessarily nonlocal. The quantity $\beta_{\mathcal{L}}$ is called the *local bound* of the Bell expression $\boldsymbol{\beta}$, and it represents the maximum value that this expression can attain over all local correlations. If the inequality

$$\boldsymbol{\beta} \cdot \boldsymbol{P} \leq \beta_{\mathcal{L}}$$

is violated by a quantum behavior $\boldsymbol{P} \in \mathcal{Q}$, then quantum theory exhibits a departure from classical locality. In such cases, the Bell inequality is said to be *violated by quantum mechanics*.
More generally, any inequality of the form

$$\boldsymbol{\beta} \cdot \boldsymbol{P} \leq \beta_{\mathcal{Q}}$$

that holds for all $\boldsymbol{P} \in \boldsymbol{Q}$ is referred to as a *Tsirelson inequality*. Similarly, one defines the *quantum bound* (or *Tsirelson bound*) β_Q as the maximal value of the same expression over the quantum set. These inequalities characterize the boundary of the quantum set within the no-signaling polytope and provide a natural generalization of Bell inequalities when the focus is shifted from classical to quantum correlations.

3.2.1. Bell expressions and Bell operators

We now provide a precise formulation of the relevant concepts. For a given a Bell scenario, let $\mathcal{P}$ denote the set of all admissible behaviors.

Definition 5. A *Bell expression* β is a linear functional on $\mathcal{P}$, which associates to each behavior $\boldsymbol{P} \in \mathcal{P}$ a real number called the *Bell score*

$$\beta(\boldsymbol{P}) \coloneqq \sum_{a,b,x,y} \beta_{a,b,x,y} P(a,b|x,y), \tag{III.20}$$

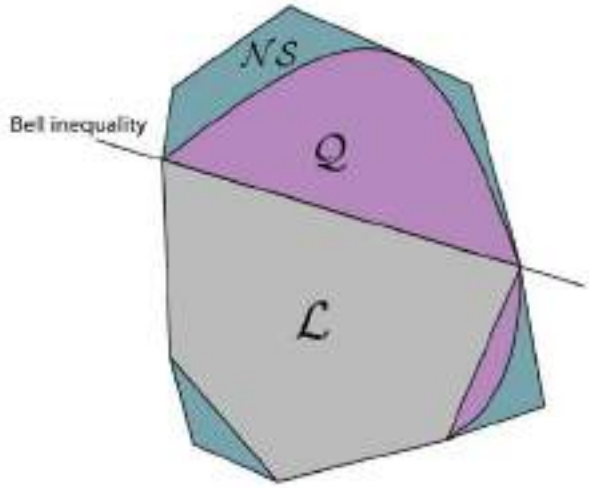

Figure III.2: Relations between the no-signaling, local and quantum set. From [16].

defined by a set of real coefficients $\{\beta_{a,b,x,y}\}$

If the space of behaviors $\mathcal{P}$ is represented as a submanifold of the real vector space $\mathbb{R}^t$, we can associate to each Bell expression β a vector in $\boldsymbol{\beta} \in \mathbb{R}^t$, where the components $\beta_{a,b,x,y}$ are ordered consistently with the representation of behaviors. In this sense, a Bell expression defines a linear map (a covector) on $\mathbb{R}^t$, and evaluating the Bell score translates in computing the Euclidean scalar product

$$\beta(\boldsymbol{P}) = \boldsymbol{\beta} \cdot \boldsymbol{P}. \tag{III.21}$$

If the behavior $\boldsymbol{P}$ arises from a quantum realization $(|\psi\rangle, \{\hat{\Pi}^A_{a|x}\}, \{\hat{\Pi}^B_{b|y}\})$, then associated with the Bell expression $\beta(\boldsymbol{P})$ and the measurement choices, the corresponding *Bell operator* $\hat{S} \in L(\mathcal{H}_A \otimes \mathcal{H}_B)$ is defined as

$$\hat{S} := \sum_{a,b,x,y} \beta_{a,b,x,y} \hat{\Pi}^{A}_{a|x} \otimes \hat{\Pi}^{B}_{b|y}. \tag{III.22}$$

This operator captures the structure of the Bell expression for a fixed choice of measurement operators. The quantum value of the Bell expression is then obtained by computing its expectation value on the given state:

$$\boldsymbol{\beta} \cdot \boldsymbol{P} = \langle \psi | \hat{S} | \psi \rangle . \tag{III.23}$$

As we have seen, in the CHSH scenario ($t = 8$), a behavior $\boldsymbol{P}$ can be parametrized by (III.4), seen as a point in $\mathbb{R}^8$. Then, a general Bell expression is represented as a linear combination of expectation values:

$$\boldsymbol{\beta} \cdot \boldsymbol{P} = \sum_{x} \alpha_x \langle A_x \rangle + \sum_{y} \beta_y \langle B_y \rangle + \sum_{x,y} \gamma_{xy} \langle A_x B_y \rangle,$$

where $\alpha_x, \beta_y, \gamma_{xy} \in \mathbb{R}$ are the components of $\boldsymbol{\beta} \in \mathbb{R}^8$. The corresponding Bell operator, for a given choice of measurements $\{\hat{A}_x\}, \{\hat{B}_y\}$, reads

$$\hat{S} := \sum_{x} \alpha_x \hat{A}_x \otimes \mathbb{1}_B + \sum_{y} \beta_y \mathbb{1}_A \otimes \hat{B}_y + \sum_{x,y} \gamma_{xy} \hat{A}_x \otimes \hat{B}_y. \tag{III.24}$$

Remark 5. Note that:

- In writing $\boldsymbol{\beta} \cdot \boldsymbol{P}$, the vector $\boldsymbol{\beta}$ encodes the functional form of the Bell expression (independent of any physical implementation), and $\boldsymbol{P}$ contains the full set of expectation values generated by a specific behavior —whether classical, quantum, or otherwise.
- In the expression $\langle \psi | \hat{S} | \psi \rangle$, the Bell operator $\hat{S}$ already includes the information on the measurement choices $\{\hat{A}_x\}, \{\hat{B}_y\}$, and the quantum state $|\psi\rangle$ provides the complementary information relative of the quantum realization.

In particular, for a fixed Bell expression β, different choices of observables $\{\hat{A}_x\}, \{\hat{B}_y\}$ give rise to different Bell operators S, which in turn lead to different quantum expectation values. Conversely, for a fixed behavior $\boldsymbol{P}$, the value $\boldsymbol{\beta} \cdot \boldsymbol{P}$ is completely determined by the underlying correlators.

3.2.2. The CHSH inequality

The CHSH inequality, introduced by Clauser, Horne, Shimony, and Holt in 1969 [21], is a Bell inequality formulated for the simplest nontrivial Bell scenario, where $(n, m, k) = (2, 2, 2)$. In this setting, the CHSH inequality is expressed as

$$\langle A_0B_0\rangle + \langle A_0B_1\rangle + \langle A_1B_0\rangle - \langle A_1B_1\rangle \leq 2. \tag{III.25}$$

This inequality is satisfied by all probability distributions that admit a local hidden-variable (LHV) model, i.e., all $\boldsymbol{P} \in \mathcal{L}$.

Proof. Consider a CHSH scenario. In a local theory, the outcome of Alice's measurement depends only on her setting and eventually on a hidden variable λ, and similarly for Bob. Thus, we can represent the outcomes as deterministic functions of the hidden variable λ, $A_x(\lambda), B_y(\lambda) \in \{-1, +1\}$. We define the CHSH quantity $S_{\text{CHSH}}(\lambda)$ as:

$$S_{\text{CHSH}}(\lambda) := A_0(\lambda)B_0(\lambda) + A_1(\lambda)B_0(\lambda) + A_0(\lambda)B_1(\lambda) - A_1(\lambda)B_1(\lambda). \tag{III.26}$$

This can be rearranged as:

$$S_{\text{CHSH}}(\lambda) = A_0(\lambda)(B_0(\lambda) + B_1(\lambda)) + A_1(\lambda)(B_0(\lambda) - B_1(\lambda)). \tag{III.27}$$

Let's analyze the possible values of $S_{\text{CHSH}}(\lambda)$ for any given λ. Since $B_0(\lambda)$ and $B_1(\lambda)$ can only take values of $+1$ or -1,

- If $B_0(\lambda) = B_1(\lambda)$, $(B_0 - B_1)(\lambda) = 0$, and $(B_0 + B_1)(\lambda) = \pm 2$. In this case, $S_{\text{CHSH}}(\lambda) = \pm 2A_1(\lambda)$.
- If $B_0(\lambda) = -B_1(\lambda)$, then $(B_0 - B_1)(\lambda) = \pm 2$, and $(B_0 + B_1)(\lambda) = 0$. In this case, $S(\lambda) = \pm 2A_0(\lambda)$.

Therefore, in all possible scenarios,

$$|S_{\text{CHSH}}(\lambda)| \leq 2 \tag{III.28}$$

Let $Q(\lambda)$ be the probability distribution of the hidden variable $\lambda \in \Lambda$, satisfying $\int_\Lambda \mathrm{d}\lambda\, Q(\lambda) = 1$. The expectation value of S_{CHSH} is given by:

$$\langle S_{\text{CHSH}}\rangle := \int_\Lambda \mathrm{d}\lambda\, S_{\text{CHSH}}(\lambda)Q(\lambda) \tag{III.29}$$

Due to the linearity of expectation values, this can be written as:

$$\langle S_{\text{CHSH}}\rangle = \langle A_0B_0\rangle + \langle A_1B_0\rangle + \langle A_0B_1\rangle - \langle A_1B_1\rangle \tag{III.30}$$

where $\langle A_xB_y\rangle = \int_\Lambda \mathrm{d}\lambda\, A_x(\lambda)B_y(\lambda)\rho(\lambda)$.
Since $|S(\lambda)| \leq 2$ for all λ, we can integrate this inequality over λ:

$$\int_\Lambda \mathrm{d}\lambda\, |S_{\text{CHSH}}(\lambda)|Q(\lambda) \leq 2\int_\Lambda \mathrm{d}\lambda\, Q(\lambda), \tag{III.31}$$

that simplifies to

$$|\langle S_{\text{CHSH}}\rangle| \leq 2. \tag{III.32}$$

$$\langle A_0B_0\rangle + \langle A_1B_0\rangle + \langle A_0B_1\rangle - \langle A_1B_1\rangle \leq 2. \tag{III.33}$$

In quantum mechanics, the CHSH inequality can be violated. The maximal value achievable by quantum correlations is given by the *Tsirelson bound* [19]:

$$\langle A_0B_0\rangle + \langle A_0B_1\rangle + \langle A_1B_0\rangle - \langle A_1B_1\rangle \leq 2\sqrt{2}. \tag{III.34}$$

Proof. Let $\hat{A}_0$, $\hat{A}_1$, $\hat{B}_0$, and $\hat{B}_1$ be Hermitian operators in the CHSH scenario, each with eigenvalues in ± 1. This implies that:

$$\hat{A}_0^2 = \hat{A}_1^2 = \hat{B}_0^2 = \hat{B}_1^2 = \mathbb{1}.$$

Assume furthermore that Alice's observables commute with Bob's ones:

$$[\hat{A}_x, \hat{B}_y] = 0 \qquad \text{for all } x, y \in \{0, 1\},$$

while $[\hat{A}_0, \hat{A}_1] \neq 0$, $[\hat{B}_0, \hat{B}_1] \neq 0$. Define the CHSH Bell operator[5]:

$$\hat{S}_{\text{CHSH}} := \hat{A}_0\hat{B}_0 + \hat{A}_0\hat{B}_1 + \hat{A}_1\hat{B}_0 - \hat{A}_1\hat{B}_1.$$

We wish to compute the maximum possible expectation value $\langle\psi|\hat{S}_{\text{CHSH}}|\psi\rangle$ over all quantum states $|\psi\rangle \in \mathcal{H}_A \otimes \mathcal{H}_B$. To this end, consider the operator norm:

$$\|\hat{C}\|_{\text{sup}} := \sup_{|\psi\rangle} \frac{\|\hat{C}|\psi\rangle\|}{\||\psi\rangle\|}.$$

We evaluate an upper bound on $\|\hat{S}_{\text{CHSH}}\|_{\text{sup}}$ by computing $\hat{S}^2_{\text{CHSH}}$. A direct algebraic manipulation yields:

$$\hat{S}^2_{\text{CHSH}} = 4\mathbb{1} \otimes \mathbb{1} - [\hat{A}_0, \hat{A}_1] \otimes [\hat{B}_0, \hat{B}_1].$$

Using the submultiplicativity of the operator norm, and the fact that all operators involved are bounded with $\|\hat{A}_x\|_{\text{sup}}, \|\hat{B}_y\|_{\text{sup}} \leq 1$, we obtain:

$$\|\hat{S}^2_{\text{CHSH}}\|_{\text{sup}} \leq 4 + \|[\hat{A}_0, \hat{A}_1]\|_{\text{sup}} \cdot \|[\hat{B}_0, \hat{B}_1]\|_{\text{sup}} \leq 8.$$

Since $\hat{S}_{\text{CHSH}}$ is Hermitian,

$$\|\hat{S}_{\text{CHSH}}\|^2_{\text{sup}} = \|\hat{S}^2_{\text{CHSH}}\|_{\text{sup}},$$

and thus:

$$\|\hat{S}_{\text{CHSH}}\|_{\text{sup}} \leq 2\sqrt{2}. \tag{III.35}$$

The latter expression is called a *quantum Bell inequality* or a *Tsirelson inequality*.

[5] To simplify notation, we omit explicit tensor products between operators acting on different subsystems when there is no ambiguity. For instance, expressions like $\hat{A}_x\hat{B}_y$ should be understood as $\hat{A}_x \otimes \hat{B}_y$. This convention will be used throughout the thesis.

The Tsirelson bound is tight: it can be achieved within quantum mechanics. In particular, consider the bipartite maximally entangled state:

$$\left|\phi^+\right\rangle := \frac{1}{\sqrt{2}}(|00\rangle + |11\rangle). \tag{III.36}$$

Let Alice and Bob perform the following projective measurements on their respective subsystems:

$$\hat{A}_0 = \hat{Z}_A, \qquad \hat{A}_1 = \hat{X}_A, \tag{III.37a}$$

$$\hat{B}_0 = \frac{1}{\sqrt{2}}(\hat{Z}_B + \hat{X}_B), \qquad \hat{B}_1 = \frac{1}{\sqrt{2}}(\hat{Z}_B - \hat{X}_B). \tag{III.37b}$$

Here, $\hat{X}_A$ and $\hat{Z}_A$ denote the Pauli $\hat{X}$ and $\hat{Z}$ operators acting on Alice's qubit, while $\hat{X}_B$ and $\hat{Z}_B$ act similarly on Bob's qubit. A straightforward calculation then shows that:

$$\left\langle\phi^+\right| \hat{S}_{\mathrm{CHSH}} \left|\phi^+\right\rangle = 2\sqrt{2}. \tag{III.38}$$

Thus, the quantum correlations arising from these measurements on the entangled state $|\phi^+\rangle$ saturate the Tsirelson bound. The corresponding behavior is represented by the following table

$$\boldsymbol{P}_T := \begin{array}{c|c|c} 1 & 0 & 0 \\ \hline 0 & \frac{1}{\sqrt{2}} & \frac{1}{\sqrt{2}} \\ \hline 0 & \frac{1}{\sqrt{2}} & -\frac{1}{\sqrt{2}} \end{array} \tag{III.39}$$

and it is known as the *Tsirelson behavior* or *Tsirelson point.*

Remark 6. In order to obtain nonlocal correlations from measurements on a quantum state, it is necessary that the latter is entangled. That is, the state cannot be written in the separable form

$$\hat{\rho}_{AB} = \sum_{\lambda} p_\lambda \hat{\rho}_A^\lambda \otimes \hat{\rho}_B^\lambda. \tag{III.40}$$

Indeed, if a state is of such a form, the correlations obtained by performing local measurements on it are given by

$$\begin{aligned} P(a,b|x,y) &= \mathrm{Tr}\left[\sum_{\lambda} p_\lambda (\hat{\rho}_A^\lambda \otimes \hat{\rho}_B^\lambda) \hat{M}_{a|x}^A \otimes \hat{M}_{b|y}^B\right] \\ &= \sum_{\lambda} p_\lambda \,\mathrm{Tr}\left(\hat{\rho}_A^\lambda \hat{M}_{a|x}^A\right) \mathrm{Tr}\left(\hat{\rho}_B^\lambda \hat{M}_{b|y}^B\right) \\ &= \sum_{\lambda} p_\lambda P(a|x,\lambda) P(b|y,\lambda). \end{aligned} \tag{III.41}$$

which is of the local form (II.10). Hence the observation of nonlocal correlations implies the presence of entanglement.

It is interesting to investigate whether this link can be reversed. That is, do all entangled states lead to nonlocality? In the case of pure states, the answer is positive. Specifically, for any entangled pure state, it is possible to find local measurements such that the resulting correlations violate a Bell inequality, in particular, the CHSH inequality. Therefore, all pure entangled states are nonlocal [28]. The only pure states that do not violate Bell inequalities are the product states

$$|\Psi\rangle = |\psi\rangle_A \otimes |\phi\rangle_B .$$

3.2.3. *No-signaling bounds*

We now consider the problem of computing bounds on Bell expressions for no-signaling correlations. Contrary to the case of local and quantum correlations, this turns out to be a rather easy task. To understand why note that once the no-signaling constraints Eq. (II.7) are taken into account, e.g., by introducing a parametrization of the relevant affine subspace $\mathbb{R}^r$, the set $\mathcal{NS}$ of no-signaling behaviors is uniquely determined by the set of k^2m^2 positivity inequalities

$$P(a,b|x,y) \geq 0. \tag{III.42}$$

Since $\mathcal{NS}$ is defined by a finite number of linear inequalities, it is a polytope and can thus be described as the convex hull of a finite set of vertices.

3.2.4. *Local bounds*

Let us now explore how Bell inequalities, i.e., the hyperplanes that define the boundary of the local set $\mathcal{L}$, can be systematically derived. A useful starting point is the observation that local correlations can be represented using *deterministic local hidden-variable models*, as was proved in Prop. 1.

Moreover, since we assume a finite number of measurement inputs and outputs, there are only finitely many deterministic response functions. Each hidden variable λ in a deterministic model corresponds to a complete assignment of outputs to inputs: that is, to a fixed function $x \mapsto a_x$ and $y \mapsto b_y$. Hence, we can identify λ with a tuple

$$\lambda := (a_1, \ldots, a_m, b_1, \ldots, b_m), \tag{III.43}$$

which specifies a deterministic output a_x and b_y for each measurement setting $x, y = 1, \ldots, m$.
The corresponding deterministic behavior $\boldsymbol{D}_\lambda$ is given by:

$$D_\lambda(a,b|x,y) := \delta_{aa_x}\delta_{bb_y}, \tag{III.44}$$

which has value 1 only if a and b are the outputs assigned by λ for the inputs x and y.
There are k^{2m} such deterministic behaviors, where k is the number of possible outputs per party, and m the number of inputs per party. A general behavior $\boldsymbol{P}$ is local if and only if it can be written as a convex combination of these deterministic points:

$$\boldsymbol{P} = \sum_{\lambda} q_{\lambda} \boldsymbol{D}_{\lambda}, \quad \text{with } q_{\lambda} \geq 0, \quad \sum_{\lambda} q_{\lambda} = 1. \tag{III.45}$$

This formulation is powerful, as it transforms the problem of testing locality into a *linear programming (LP) problem*: determining whether a given point $\boldsymbol{P}$ lies within the convex hull of known deterministic points $\boldsymbol{D}_{\lambda}$ under the constraints above. However, because the number of variables (k^{2m}) grows exponentially, solving the LP may become computationally intractable in practice.

Remark 7. Note that since $\mathcal{L}$ is the convex hull of a finite set of points, it is a polytope. By Minkowski's theorem, any polytope can also be represented as the intersection of a finite number of half-spaces. Therefore, there exists a finite set of inequalities of the form:

$$\boldsymbol{\beta}^{i} \cdot \boldsymbol{P} \leq \beta^{i}_{\mathcal{L}}, \quad \forall i \in I, \tag{III.46}$$

such that $\boldsymbol{P} \in \mathcal{L}$ if and only if it satisfies all inequalities in this set. These inequalities are precisely the Bell inequalities, and they define the *facets* of the *local polytope* $\mathcal{L}$. Moreover, the fact that the list of extremal local points is known means that the local bound $\beta_{\mathcal{L}}$ of a Bell inequality can be computed directly, by taking the maximum value over a finite number of deterministic points.

Every linear program admits a dual formulation.[6] The dual LP associated with equation (III.45) has a a natural physical interpretation: it corresponds to searching for a Bell inequality violated by $\boldsymbol{P}$. The dual form can be written as:

$$\begin{aligned} \max_{(\boldsymbol{\beta}, \beta_{\mathcal{L}})} \quad & \boldsymbol{\beta} \cdot \boldsymbol{P} - \beta_{\mathcal{L}} \\ \text{subject to} \quad & \boldsymbol{\beta} \cdot \boldsymbol{D}_{\lambda} - \beta_{\mathcal{L}} \leq 0 \quad \forall \lambda, \\ & \boldsymbol{\beta} \cdot \boldsymbol{P} - \beta_{\mathcal{L}} \leq 1. \end{aligned} \tag{III.47}$$

Then,

- If $\boldsymbol{P} \in \mathcal{L}$, then $\boldsymbol{P}$ satisfies all Bell inequalities, and the optimal value S of the dual problem satisfies $S \leq 0$.
- If $\boldsymbol{P} \notin \mathcal{L}$, then the dual program returns a vector $\boldsymbol{\beta}$ and bound $\beta_{\mathcal{L}}$ such that

$$\boldsymbol{\beta} \cdot \boldsymbol{P} = \beta_{\mathcal{L}} + 1 > \beta_{\mathcal{L}}, \tag{III.48}$$

  i.e., $\boldsymbol{P}$ violates the Bell inequality $\boldsymbol{\beta} \cdot \boldsymbol{P} \leq \beta_{\mathcal{L}}$, which is satisfied by all local points (since it's satisfied by all $\boldsymbol{d}_{\lambda}$).

This demonstrates that solving the dual LP provides an effective method for certifying nonlocality and for explicitly constructing a Bell inequality that $\boldsymbol{P}$ violates.

[6] For a review of convex programs, including linear and semidefinite programs, please refer to S. Boyd, L. Vandenberghe, *Convex Optimization*, Cambridge University Press, 2004.

3.2.5. *Quantum bounds*

Unlike the sets of local and no-signaling correlations, the set Q of quantum correlations is generally not a polytope. This implies that Q cannot be described by a finite number of extremal points or a finite set of linear inequalities. However, some structural features of $\mathcal{L}$ persist within Q.
For instance, all extremal points of $\mathcal{L}$ —i.e., the local deterministic behaviors— are also extremal in Q. Moreover, certain faces of $\mathcal{L}$ are shared with Q. An example is provided by the $(k-1)$-dimensional face defined by the hyperplanes

$$P(a,b|x,y) = 0. \tag{III.49}$$

Although the associated Bell inequalities $P(a,b|x,y) \geq 0$ are never violated by physical correlations, they still define flat regions on the boundary of Q.
In [37], it is shown that some faces of $\mathcal{L}$ correspond to Bell inequalities that are violated by no-signaling correlations but not by quantum ones. These inequalities define common faces between $\mathcal{L}$ and $\mathcal{NS}$ (but not necessarily Q). Previously, an open question remained whether such shared faces could be of maximal dimension, i.e., whether there existed facets of $\mathcal{L}$ that are violated by some $\mathcal{NS}$ behaviors but not by any quantum behavior. This question has since been affirmatively answered in the multipartite (e.g., tripartite) scenario; for instance, the work in [3] demonstrates Bell inequalities (related to the "guess your neighbor's input" game) that correspond to facets of $\mathcal{L}$, are violated by no-signaling correlations, yet yield no quantum advantage (i.e., are not violated by quantum correlations).

3.2.5.1. *Maximizing the norm of the Bell operator*

Let us now focus more specifically on the problem of computing the quantum bound of a Bell expression. Recall that Q as any convex compact set can be described by an infinite system of linear inequalities. Given a Bell expression defined by a vector $\boldsymbol{\beta}$, the quantum set Q can be characterized as the set of conditional probability distributions $\boldsymbol{P} = \{P(a,b|x,y)\}$ satisfying all Tsirelson inequalities of the form:

$$\boldsymbol{\beta} \cdot \boldsymbol{P} \leq \beta_Q. \tag{III.50}$$

The quantity β_Q denotes the quantum bound of the Bell expression and is defined as

$$\beta_Q := \max_{\boldsymbol{P} \in Q} \boldsymbol{\beta} \cdot \boldsymbol{P} = \max_{\hat{S}} \|\hat{S}\|_{\sup}, \tag{III.51}$$

where again $\|S\|_{\sup}$ is the spectral norm of the associated Bell operator

$$\hat{S} := \sum_{a,b,x,y} \beta_{a,b,x,y} \hat{\Pi}^A_{a|x} \hat{\Pi}^B_{b|y}. \tag{III.52}$$

The maximization is performed over all possible quantum realizations of the Bell operator $\hat{S}$, i.e., over all valid measurement operators $\{\hat{\Pi}^A_{a|x}\}$, $\{\hat{\Pi}^B_{b|y}\}$ acting on a bipartite Hilbert space $\mathcal{H}_A \otimes \mathcal{H}_B$.
A straightforward approach to estimate β_Q is to fix a Hilbert space of bounded dimension and optimize the spectral norm $\|\hat{S}\|_{\sup}$ numerically over a parametrized family of Bell operators. However, this method generally provides only a lower bound on β_Q, since:

- it may miss the global optimum;
- there is no guarantee that the optimal violation can be realized in the chosen Hilbert space.

Despite these limitations, such lower bounds are useful for constructing explicit quantum violations of classical Bell inequalities.

3.2.5.2. *The NPA hierarchy*

The previous discussion focused on techniques for establishing lower bounds on β_Q. Now, we shift our attention to methods for determining upper bounds.

For the purpose of device-independent certification, it is advantageous to define *supersets* or *relaxations* of $\boldsymbol{Q}$. This way, any property proven for one of these supersets automatically applies to the entire quantum set. This section introduces a systematic construction of such supersets, characterized by compact and computationally efficient conditions for membership. These conditions were systematically introduced by Navascués, Pironio, and Acín [42, 43] and are thus known as *NPA relaxations*.

The foundation of NPA relaxations lies in the following observation:

Lemma 1. *Let $O \coloneqq \{\hat{O}_1, \ldots, \hat{O}_n\}$ be a set of linear operators, $\hat{O}_i \in L(\mathcal{H}_{AB})$. Then, for any state $|\psi\rangle$, the Hermitian matrix $\Gamma(|\psi\rangle, O)$ of entries*

$$\Gamma_{ij} \coloneqq \langle\psi| \hat{O}_i^\dagger \hat{O}_j |\psi\rangle \tag{III.53}$$

is positive semidefinite.

Proof. For any vector $\boldsymbol{v} \in \mathbb{C}^n$ it holds

$$\boldsymbol{v}^\dagger \Gamma \boldsymbol{v} = \langle\psi| \left(\sum_i v_i^* \hat{O}_i^\dagger\right)\left(\sum_j v_j \hat{O}_j\right) |\psi\rangle \geq 0, \tag{III.54}$$

because any operator of the form $O^\dagger O$ is positive semidefinite. □

Consider a behavior $P \in Q$. We can construct the matrix $\Gamma_1(|\psi\rangle, O_1)$ using the state $|\psi\rangle$ and the collection of $2mk$ projectors:

$$O_1 \coloneqq \left\{\mathbb{1}, \{\hat{\Pi}^A_{a|x}\}, \{\hat{\Pi}^B_{b|y}\}\right\}. \tag{III.55}$$

If the specific state and measurements were known, all entries of Γ_1 could be directly computed. However, in a device-independent scenario, we only assume knowledge of the statistics (the state and projectors are unknown a priori). Therefore, certain entries of Γ_1 are directly determined by the observed behavior. In fact, it results

$$\langle\psi| \hat{\Pi}^A_{a|x} \hat{\Pi}^B_{b|y} |\psi\rangle = P(a,b|x,y), \qquad \langle\psi| \hat{\Pi}^A_{a|x} |\psi\rangle = P(a|x), \qquad \langle\psi| \hat{\Pi}^B_{b|y} |\psi\rangle = P(b|y). \tag{III.56}$$

Other entries, which involve two operators from Alice's side or two from Bob's, do not correspond to directly observed quantities in a Bell test. Nonetheless, Lemma 1 guarantees that these entries can be completed such that $\Gamma_1 \succeq 0$. Conversely, if, after populating the known entries with the observed behavior, it becomes impossible to fill the remaining entries to satisfy $\Gamma_1 \succeq 0$, then it can be conclusively stated that $\boldsymbol{P} \notin \boldsymbol{Q}$.

This describes a necessary condition for a behavior $\boldsymbol{P}$ to be part of the quantum set $\boldsymbol{Q}$. For some specific subsets of the quantum set, this condition is also sufficient. However, generally, it represents only the first step in the NPA hierarchy of criteria. The set of behaviors that satisfy the condition $\Gamma_1 \succeq 0$ is denoted as $\boldsymbol{Q}_1$.

For the subsequent level of the hierarchy, denoted $\nu = 2$, the matrix Γ_2 is constructed using an expanded collection of operators:

$$\mathcal{O}_2 = \mathcal{O}_1 \cup \left\{ \{\hat{\Pi}^A_{a|x}\hat{\Pi}^A_{a'|x'}\}, \{\hat{\Pi}^B_{b|y}\hat{\Pi}^B_{b'|y'}\}, \{\hat{\Pi}^A_{a|x}\hat{\Pi}^B_{b|y}\} \right\}. \tag{III.57}$$

It's understood that all $3(mk)^2$ newly formed operators are added to $\mathcal{O}_1$. The set of behaviors for which $\Gamma_2 \succeq 0$ is denoted $\boldsymbol{Q}_2$. The positivity of Γ_2 is a necessary condition for $\boldsymbol{P} \in \boldsymbol{Q}$, providing a tighter constraint than Γ_1 positivity, though still not generally sufficient. Notably, none of the entries involving operators like $\hat{\Pi}^A_{a|x}\hat{\Pi}^A_{a'|x'}$ are determined by the observed behavior for $a \neq a'$. Nevertheless, these terms impose specific structural requirements on the matrix. For instance:

$$\langle\psi|\,\hat{\Pi}^A_{a|x}\hat{\Pi}^A_{a'|x'}\hat{\Pi}^A_{a''|x'}\,|\psi\rangle = \langle\psi|\,\hat{\Pi}^A_{a|x}\hat{\Pi}^A_{a'|x'}\,|\psi\rangle\,\delta_{a'a''}. \tag{III.58}$$

It can be inferred that the n-th step of this hierarchy involves constructing the matrix Γ_n from the collection of all products of n or fewer projectors. The set of behaviors for which $\Gamma_n \succeq 0$ is denoted $\boldsymbol{Q}_n$. This construction yields a nested sequence of sets:

$$\boldsymbol{Q}_1 \supseteq \boldsymbol{Q}_2 \supseteq \boldsymbol{Q}_3 \supseteq \cdots \supseteq \boldsymbol{Q}_n \supseteq \boldsymbol{Q}'. \tag{III.59}$$

NPA demonstrated the convergence of this hierarchy, proving that $\lim_{n\to\infty} \boldsymbol{Q}_n = \boldsymbol{Q}'$. It's important to note that this convergence is established for $\boldsymbol{Q}'$, not $\boldsymbol{Q}$. In many practical cases, the quantum result is achieved at a finite level n of the hierarchy.

Remark 8. Note that:

- The inherent flexibility in choosing the operator collection $\mathcal{O}$ within Lemma 1 is a key aspect of this hierarchy.
- Adding even a single operator to an existing $\mathcal{O}$ can lead to a tighter bound. The notation $\boldsymbol{Q}_{\mathcal{O}}$ is used to denote the set of behaviors where $\Gamma_{\mathcal{O}} \succeq 0$ for a given collection of operators $\mathcal{O}$.

The fact that the NPA conditions are expressed as semidefinite requirements ($\Gamma \succeq 0$) makes them particularly well-suited for use in *semidefinite programs (SDPs)*. SDPs are the next level of complexity in convex optimization after linear programs. Similar to linear programs, for any given SDP, a dual SDP can be algorithmically constructed, providing simultaneous lower and upper bounds for the desired solution.

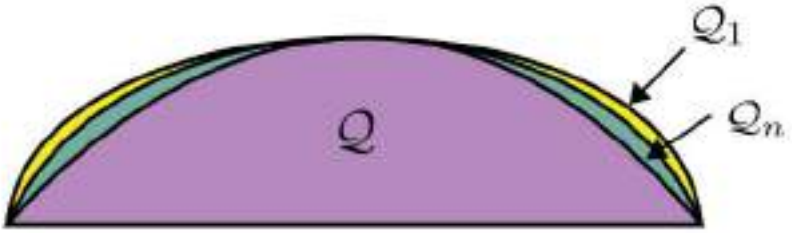

Figure III.3: Hierarchy of sets Q_n generated by the NPA recipe. Each set in the hierarchy approximates better the set of quantum correlations Q. From [16].

The membership problem. Let us describe how the NPA techniques are employed to address the problem of quantum set membership, i.e., determining whether a given behavior $\boldsymbol{P}$ belongs to $\mathcal{Q}$. For any chosen set of operators O, the membership problem can be relaxed to the following optimization:

$$\begin{aligned} \Lambda := \max \quad & \lambda \\ \text{s. t.} \quad & \Gamma - \lambda \mathbb{1} \succeq 0 \\ & \Gamma_{(x,a)} = P(a|x) \\ & \Gamma_{(y,b)} = P(b|y) \\ & \Gamma_{(x,a)(y,b)} = P(a,b|x,y) \end{aligned} \tag{III.60}$$

Here, $\Gamma_{(x,a)}$, $\Gamma_{(y,b)}$, and $\Gamma_{(x,a)(y,b)}$ refers to specific entries of Γ corresponding to the marginal probabilities $P(a|x)$, $P(b|y)$, and the joint probabilities $P(a,b|x,y)$, respectively. The optimization variables are $\lambda \in \mathbb{R}$ and all other entries of the matrix Γ.

Remark 9. These additional entries can be restricted to be real without loss of generality: if a solution Γ_{sol} is found to be positive semidefinite and satisfies the constraints, potentially with complex entries, then its complex conjugate Γ^*_{sol} also satisfies the constraints. Consequently, their real part, $\Gamma = \frac{1}{2}(\Gamma_{\text{sol}} + \Gamma^*_{\text{sol}})$, is also positive semidefinite and satisfies all the imposed constraints.

If the solution to this optimization, Λ, is found to be negative ($\Lambda < 0$), it implies that no positive semidefinite matrix Γ can be constructed while satisfying the given constraints. In such a scenario, it can be definitively concluded that the behavior $\boldsymbol{P} \notin \mathcal{Q}$. Conversely, if a $\Gamma \succeq 0$ is found, it indicates that $\boldsymbol{P} \in \mathcal{Q}_O$. Since $\mathcal{Q}_O$ is a superset of $\mathcal{Q}$ (i.e., $\mathcal{Q}_O \supset \mathcal{Q}$), this condition alone does not definitively prove that $\boldsymbol{P} \in \mathcal{Q}$. The tightness of this assessment can be improved by selecting a larger collection of operators O. The only conclusive method to formally demonstrate that $\boldsymbol{P} \in \mathcal{Q}$ is to explicitly provide a quantum realization of the behavior, specifying the underlying quantum state and measurement projectors (of course, knowing such a realization, the semidefinite program becomes redundant for membership verification).

Maximal violation of a Bell inequality. Next, we consider the problem of determining the maximal violation of a Bell inequality within quantum theory, which represents one of the earliest applications of semidefinite programs in the study of nonlocality, as highlighted in [69]. The goal is to find

$$\begin{aligned} \beta_Q \coloneqq \max \quad & \beta(\boldsymbol{P}) \\ \text{s. t.} \quad & \boldsymbol{P} \in \boldsymbol{Q}. \end{aligned} \tag{III.61}$$

Unless analytical arguments are available, such as those used to derive the Tsirelson bound, this problem cannot be solved efficiently. At best, one can employ heuristic optimization strategies over a restricted class of states and measurements, effectively searching over a subset of $\boldsymbol{Q}$. Due to the heuristic nature of such optimizations, possibly converging to a local maximum, the obtained outcome will satisfy $\beta_{\text{heur}} \leq \beta_Q$.

The NPA techniques provide a systematic way to relax the optimization problem stated in (III.61) into the SDP:

$$\begin{aligned} \beta_\Gamma \coloneqq \max \quad & \beta(\boldsymbol{P}) \\ \text{s. t.} \quad & \Gamma(\boldsymbol{P}) \succeq 0. \end{aligned} \tag{III.62}$$

In this SDP, all entries of the matrix Γ are treated as optimization variables. To ensure a non-trivial solution, all probabilities $P(a,b|x,y)$ that appear in the Bell expression $\beta(\boldsymbol{P})$ must correspond to entries within Γ. This requirement implicitly defines the minimal collection of operators $\boldsymbol{O}$ necessary for the problem. The SDP typically yields both an upper and a lower bound for $\beta(\boldsymbol{P})$, which usually align within numerical precision. Crucially, by optimizing over $\boldsymbol{Q}_O \supseteq \boldsymbol{Q}$, we are guaranteed that the obtained value β_Γ satisfies $\beta_\Gamma \geq \beta_Q$. Increasing the size of the operator collection $\boldsymbol{O}$ will generally lead to a β_Γ that converges more closely to the true β_Q. If β_Γ is found to be equal to an explicitly achievable quantum value (either a numerical β_{heur} from a specific quantum realization or by an exact computation), then we have successfully determined β_Q.

Dual approach. An alternative, dual approach to this hierarchy was developed in [23], drawing upon concepts from *sum-of-squares (SOS) polynomial optimization* [49]. For a given Bell operator $\hat{S}$, the quantum bound β_Q satisfies the condition

$$\hat{\xi} \coloneqq \beta_Q \mathbb{1} - \hat{S} \succeq 0, \tag{III.63}$$

if and only if $\hat{\xi}$ is a positive operator. In the SOS methodology, the objective is to express $\hat{\xi}$ as a sum of squares of polynomials in the measurement operators. By constraining these polynomials to a maximum degree of 2ℓ, this problem transforms into an SDP, yielding progressively tighter bounds as ℓ increases. This SOS hierarchy converges to the quantum set in the limit $\ell \to \infty$.

For certain Bell expressions, finite convergence can be established. When this occurs, it becomes possible to reconstruct a quantum realization of the optimal bound. That is, to explicitly determine the state $|\psi\rangle$ and the measurements $\{\hat{\Pi}^A_{a|x}\}$, $\{\hat{\Pi}^B_{b|y}\}$ that achieve β_Q [43].

Finally, the optimality at a finite level can be confirmed by comparing the upper bound derived from the NPA hierarchy with a lower bound obtained through direct optimization over Bell operators, as previously discussed.

3.2.6. Geometry of correlations in the CHSH scenario

Already in the minimal Bell scenario ($n = k = m = 2$), the structure of the sets of correlations exhibits a remarkably rich geometry. The local set $\mathcal{L}$ consists of the local deterministic behaviors, forming a polytope with 16 vertices (corresponding to deterministic assignments of outputs to inputs) and 24 facets. Among these, 16 correspond to trivial positivity constraints, while the remaining 8 correspond to violations of the CHSH inequality, up to relabeling of inputs and outputs.

The no-signaling set $\mathcal{NS}$, defined by the requirement that neither party can influence the marginal statistics of the other through their choice of input, also forms a polytope, but with a different geometric structure. It has 24 extremal points: the 16 local deterministic ones, and 8 additional nonlocal vertices, all equivalent under symmetries to the PR box (II.8). This behavior maximally violates the CHSH inequality up to the algebraic maximum

$$\beta_{\mathrm{CHSH}} \cdot \boldsymbol{P}_{\mathrm{PR}} = 4. \tag{III.64}$$

This value clearly exceeds the Tsirelson bound $2\sqrt{2}$.

The CHSH expression thus delineates three distinct regions in correlation space:

$$\beta_{\mathrm{CHSH}} \cdot \boldsymbol{P} \leq \begin{cases} 4 & \text{if } \boldsymbol{P} \in \mathcal{NS}, \\ 2\sqrt{2} & \text{if } \boldsymbol{P} \in \mathcal{Q}, \\ 2 & \text{if } \boldsymbol{P} \in \mathcal{L}, \end{cases} \tag{III.65}$$

providing a rare example where a single Bell inequality fully separates three operationally distinct sets of interest. This tri-level structure is visually represented in simplified two-dimensional slices, as in Fig. III.4.

While this coarse-grained representation of the geometry is helpful, the actual structure of the quantum set $\mathcal{Q}$ is far more complex. A fundamental result in this direction was the discovery that the quantum set $\mathcal{Q}$ contains extremal points that are *non-exposed*, i.e., points which cannot be obtained as the unique maximizers of any Bell inequality over $\mathcal{Q}$ [29]. This contrasts sharply with the classical and no-signaling sets, where every extremal point is exposed. The existence of non-exposed points implies that the boundary of $\mathcal{Q}$ is not fully accessible via Bell inequality violations: some quantum behaviors are extremal yet remain invisible to any linear optimization procedure over the set. This fact underscores a fundamental limitation of the Bell inequality framework in fully characterizing quantum correlations.

Additional structural richness is revealed by the existence of so-called *quantum voids*—open regions of the boundary of the no-signaling polytope $\mathcal{NS}$ that remain entirely inaccessible to quantum correlations

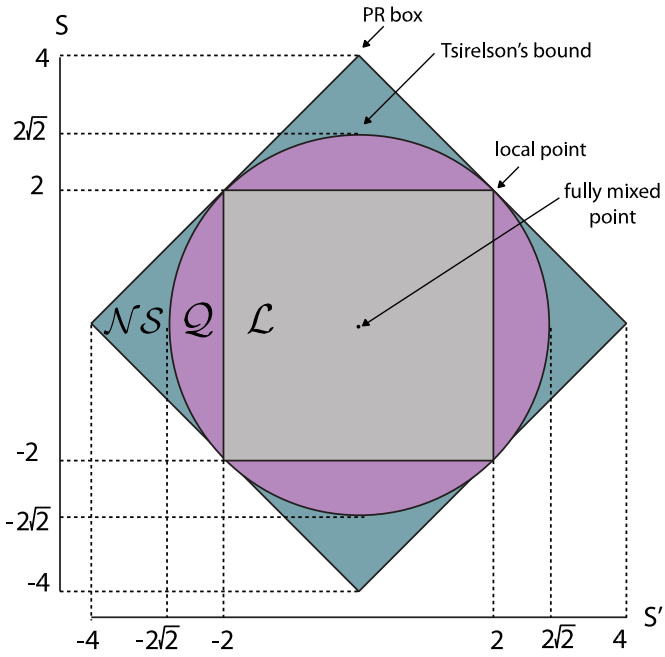

Figure III.4: A two-dimensional section of the no-signaling polytope in the CHSH scenario ($m = k = 2$). The vertical axis represents the CHSH value $\mathcal{S} := \langle \mathcal{S}_{\text{CHSH}} \rangle$, while the horizontal axis represents a symmetry of the CHSH expression $\mathcal{S}$. Local correlations satisfy $|\mathcal{S}| \leq 2$ and $|\mathcal{S}'| \leq 2$. The PR box achieves the algebraic maximum $\mathcal{S} = 4$, while Tsirelson's bound corresponds to $\mathcal{S} = 2\sqrt{2}$, the maximum achievable quantum value. From [16].

[57]. Although the quantum set Q is dense in the interior of NS, meaning that quantum correlations can approximate any interior no-signaling point arbitrarily well, this is not the case for the full boundary. In particular, there exist boundary faces of NS of high dimension—up to six in the CHSH scenario—that are completely disjoint from Q. These quantum voids underscore the sparsity of the quantum set relative to NS, and illustrate that quantum theory does not saturate all the physically allowed no-signaling correlations, even in the limit.

This feature challenges the common intuition that quantum mechanics nearly saturates the space of physically consistent probabilistic theories compatible with relativistic causality.

Surprisingly, despite the general curvature of Q, recent work has shown that some of its facets are flat and shared with the no-signaling polytope [17]. That is, there exist supporting hyperplanes that simultaneously define a face of both Q and NS, indicating that the boundary of the quantum set aligns exactly with the no-signaling polytope in certain directions. These shared facets demonstrate that not all of the boundary of Q is curved, and some portions admit a polyhedral structure —another departure from the naive image of a uniformly smooth body.

Complementary to the phenomenon of non-exposed extremal points, recent results have also uncovered "pointy" extremal points of Q, which lie at the intersection of several tight Bell inequalities [9]. These points locally resemble vertices of a polytope, and although Q itself is not a polytope, these features provide local structures where quantum correlations are highly constrained. This polyhedral-like structure implies that some quantum behaviors can, after all, be fully characterized by a finite set of Bell inequalities—suggesting that the curved geometry of Q coexists with strongly "cornered"

extremal features.

Understanding this geometry is not merely an academic exercise: it is crucial to identifying the principles that distinguish quantum theory from more general no-signaling theories. The subtle interplay between exposed and non-exposed points, between flat and curved facets, and between accessible and inaccessible regions of Q, suggests that any candidate physical principle aiming to recover quantum theory must be sensitive not only to the set's algebraic constraints, but also to its geometric subtleties.

REFERENCES

Aaronson, S., *Is quantum mechanics an island in theoryspace?*, 2004, arXiv: quant-ph/ 0401062 (quant-ph).

Acín, A., Gisin, N., and Masanes, L., "From Bell's theorem to secure quantum key distribution", in: *Physical Review Letters*, 97, 2006, p. 120405, doi: 10.1103/PhysRevLett.97. 120405.

Almeida, M. L. et al., "Guess your neighbor's input: a multipartite nonlocal game with no quantum advantage", in: *Physical Review Letters*, 104, 2010, p. 230404, doi: 10.1103/ PhysRevLett.104.230404.

Anders, J. and Browne, D. E., "Computational power of correlations", in: *Physical Review Letters*, 102, 2009, p. 050502, doi: 10.1103/PhysRevLett.102.050502.

Aspect, A., Dalibard, J., and Roger, G., "Experimental test of Bell's inequalities using timevarying analyzers", in: *Physical Review Letters*, 49, 1982, pp. 1804–1807, doi: 10.1103/ PhysRevLett.49.1804.

Aspect, A., Grangier, P., and Roger, G., "Experimental realization of Einstein-PodolskyRosen-Bohm gedankenexperiment: a new violation of Bell's inequalities", in: *Physical Review Letters*, 49, 1982, pp. 91–94, doi: 10.1103/PhysRevLett.49.91.

Auletta, G., Fortunato, M., and Parisi, G., *Quantum Mechanics*, Cambridge University Press, 2009.

Auletta, G. and Parisi, G., *Foundations and Interpretation of Quantum Mechanics: In the Light of a Critical-historical Analysis of the Problems and of a Synthesis of the Results*, World Scientific, 2001.

Barizien, V. and Bancal, J.-D., "Extremal Tsirelson inequalities", in: *Physical Review Letters*, 133, 2024, p. 010201, doi: 10.1103/PhysRevLett.133.010201.

Barizien, V. and Bancal, J.-D., "Quantum statistics in the minimal Bell scenario", in: *Nature Physics*, 2025, doi: 10.1038/s41567-025-02782-3.

Bell, J. S., “On the Einstein-Podolsky-Rosen paradox”, in: *Physics*, 1, 1964, pp. 195–200, doi: 10.1103/PhysicsPhysiqueFizika.1.195.

Bell, J. S., “The theory of local beables”, in: *Epistemological Letters*, 9, 1975.

Bell, J. S., “La nouvelle cuisine”, in: *Speakable and Unspeakable in Quantum Mechanics*, Cambridge University Press, 2010, pp. 232–248.

Bohm, D., *Quantum Mechanics*, Dover Publications, 1951.

Bohm, D., “A suggested interpretation of the quantum theory in terms of “hidden” variables. I”, in: *Physical Review*, 85, 1952, pp. 166–179, doi: 10.1103/PhysRev.85.166.

Brunner, N. et al., “Bell nonlocality”, in: *Reviews of Modern Physics*, 86, 2014, pp. 839–840, doi: 10.1103/RevModPhys.86.839.

Chen, K.-S. et al., “Quantum correlations on the no-signaling boundary: self-testing and more”, in: *Quantum*, 7, 2023, p. 1054, doi: 10.22331/q-2023-07-11-1054.

Chiribella, G., D’Ariano, G. M., and Perinotti, P., “Informational derivation of quantum theory”, in: *Physical Review A*, 84, 2011, p. 012311, doi: 10.1103/PhysRevA.84.012311.

Cirel’son, B. S., “Quantum generalizations of Bell’s inequality”, in: *Letters in Mathematical Physics*, 42, 1980, pp. 93–100, doi: 10.1007/bf00417500.

Clauser, J. F. and Shimony, A., “Bell’s theorem. Experimental tests and implications”, in: *Reports on Progress in Physics*, 4112, 1978, pp. 1881–1927, doi: 10.1088/0034-4885/41/12/002.

Clauser, J. F. et al., “Proposed experiment to test local hidden-variable theories”, in: *Physical Review Letters*, 23, 1969, pp. 880–884, doi: 10.1103/PhysRevLett.23.880.

Coladangelo, A. and Stark, J., *Unconditional separation of finite and infinite-dimensional quantum correlations*, 2018, arXiv: 1804.05116 (quant-ph).

Doherty, A. C. et al., “The quantum moment problem and bounds on entangled multi-prover games”,in:*Proceedingsofthe2008IEEE23rdAnnualConferenceonComputationalComplexity*, CCC ’08, USA: IEEE Computer Society, 2008, pp. 199–210, doi: 10.1109/CCC.2008.26.

Einstein, A., Podolsky, B., and Rosen, N., “Can quantum-mechanical description of physical reality be considered complete?”, in: *Physical Review*, 4710, 1935, pp. 777–780, doi: 10. 1103/physrev.47.777.

Ekert, A. K., “Quantum cryptography based on Bell’s theorem”, in: *Physical Review Letters*, 67, 1991, pp. 661–663, doi: 10.1103/PhysRevLett.67.661.

Fine, A., “Hidden variables, joint probability, and the Bell inequalities”, in: *Physical Review Letters*, 485, 1982, pp. 291–295, doi: 10.1103/PhysRevLett.48.291.

Fritz, T. et al., “Local orthogonality as a multipartite principle for quantum correlations”, in: *Nature Communications*, 41, 2013, doi: 10.1038/ncomms3263.

Gisin, N., “Bell’s inequality holds for all non-product states”, in: *Physics Letters A*, 1545, 1991, pp. 201–202, doi: 10.1016/0375-9601(91)90805-I.

Goh, K. T. et al., “Geometry of the set of quantum correlations”, in: *Physical Review A*, 97, 2018, p. 022104, doi: 10.1103/PhysRevA.97.022104.

Goldstein, S. et al., “Bell’s theorem”, in: *Scholarpedia*, 610, 2011, p. 8378, doi: 10.4249/ scholarpedia.8378.

Hardy, L., *Quantum theory from five reasonable axioms*, 2001, arXiv: quant-ph/0101012 (quant-ph).

Hensen, B. et al., “Loophole-free Bell inequality violation using electron spins separated by 1.3 kilometres”, in: *Nature*, 5267575, 2015, pp. 682–686, doi: 10.1038/nature15759.

Ji, Z. et al., “MIP* = RE”, in: *Communication ACM*, 6411, 2021, pp. 131–138, doi: 10.1145/ 3485628.

Jozsa, R. and Linden, N., “On the role of entanglement in quantum-computational speed-up”, in: *Proceedings of the Royal Society of London. Series A: Mathematical, Physical and Engineering Sciences*, 4592036, 2003, pp. 2011–2032, doi: 10.1098/rspa.2002.1097.

Kimble, H. J., “The quantum internet”, in: *Nature*, 4537198, 2008, pp. 1023–1030, doi: 10.1038/nature07127.

Laloë, F., *Do We Really Understand Quantum Mechanics?*, 2nd ed., Cambridge University Press, 2019.

Linden, N. et al., “Quantum nonlocality and beyond: Limits from nonlocal computation”, in: *Physical Review Letters*, 9918, 2007, doi: 10.1103/physrevlett.99.180502.

Masanes, L. and Müller, M.P.,“A derivation of quantum theory from physical requirements”, in: *New Journal of Physics*, 136, 2011, p. 063001, doi: 10.1088/1367-2630/13/6/063001.

Maudlin, T., *Quantum Non-Locality and Relativity: Metaphysical Intimations of Modern Physics*, Wiley-Blackwell, 2011.

Müller, M.,“Probabilistic theories and reconstructions of quantum theory”, in: *SciPostPhysics Lecture Notes*, 2021, doi: 10.21468/scipostphyslectnotes.28.

Nadlinger, D. P. et al., “Experimental quantum key distribution certified by Bell’s theorem”, in: *Nature*, 6077920, 2022, pp. 682–686, doi: 10.1038/s41586-022-04941-5.

Navascués, M., Pironio, S., and Acín, A., “Bounding the set of quantum correlations”, in: *Physical Review Letters*, 981, 2007, p. 010401, doi: 10.1103/PhysRevLett.98.010401.

Navascués, M., Pironio, S., and Acín, A., “A convergent hierarchy of semidefinite programs characterizing the set of quantum correlations”, in: *New Journal of Physics*, 107, 2008, p. 073013, doi: 10.1088/1367-2630/10/7/073013.

Navascués, M.et al.,“A Physical Approach to Tsirelson’s Problem”, in: *FoundationsofPhysics*, 428, 2012, pp. 985–995, doi: 10.1007/s10701-012-9641-0.

Navascués, M. and Wunderlich, H., “A glance beyond the quantum model”, in: *Proceedings of the Royal Society A: Mathematical, Physical and Engineering Sciences*, 4662115, 2009, pp. 881–890, doi: 10.1098/rspa.2009.0453.

Nikolić, H., “Quantum mechanics: myths and facts”, in: *Foundations of Physics*, 3711, 2007, pp. 1563–1611, doi: 10.1007/s10701-007-9176-y.

Norsen, T., *Foundations of Quantum Mechanics: An Exploration of the Physical Meaning of Quantum Theory*, Springer International Publishing, 2017.

Norsen, T., “Local causality and completeness: Bell vs. Jarrett”, in: *Foundations of Physics*, 393, 2009, pp. 273–294, doi: 10.1007/s10701-009-9281-1.

Parrilo, P. A., “Semidefinite programming relaxations for semialgebraic problems”, in: *Mathematical Programming*, 962, 2003, pp. 293–320, doi: 10.1007/s10107-003-0387-5.

Pawłowski, M. et al., “Information causality as a physical principle”, en, in: *Nature*, 4617267, 2009, pp. 1101–1104, doi: 10.1038/nature08400.

Pironio, S., “Lifting Bell inequalities”, in: *Journal of Mathematical Physics*, 466, 2005, p. 062112, doi: 10.1063/1.1928727.

Pironio, S., Scarani, V., and Vidick, T., “Focus on device independent quantum information”, in: *New Journal of Physics*, 1810, 2016, p. 100202, doi: 10.1088/1367-2630/18/10/100202.

Pironio, S. et al., “Random numbers certified by Bell’s theorem”, in: *Nature*, 4647291, 2010, pp. 1021–1024, doi: 10.1038/nature09008.

Pitowsky, I., “The range of quantum probability”, in: *Journal of Mathematical Physics*, 276, 1986, pp. 1556–1565, doi: 10.1063/1.527066.

Popescu, S., “Nonlocality beyond quantum mechanics”, in: *Nature Physics*, 104, 2014, pp. 264–270, doi: 10.1038/nphys2916.

Popescu, S. and Rohrlich, D., “Quantum nonlocality as an axiom”, in: *Foundations of Physics*, 243, 1994, pp. 379–385, doi: 10.1007/bf02058098.

Rai, A. et al., “Geometry of the quantum set on no-signaling faces”, in: *Physical Review* $_A$, 99, 2019, p. 032106, doi: 10.1103/PhysRevA.99.032106.

Rohde, P. P., *The Quantum Internet: The Second Quantum Revolution*, Cambridge University Press, Sept. 2021.

Rowe, M. A. et al., “Experimental violation of a Bell’s inequality with efficient detection”, in: *Nature*, 4096822, 2001, pp. 791–794, doi: 10.1038/35057215.

Scarani, V., *Bell Nonlocality*, Oxford University Press, 2019.

Scarani, V., “The device-independent outlook on quantum physics”, in: *Acta Physica Slovaca*, 624, 2012, pp. 347–409, doi: 10.2478/v10155-012-0003-4.

Shalm, L. K. et al., “Strong loophole-free test of local realism”, in: *Physical Review Letters*, 115, 2015, p. 250402, doi: 10.1103/PhysRevLett.115.250402.

Simon, B., *Convexity: An Analytic Viewpoint*, Cambridge Tracts in Mathematics, Cambridge University Press, 2011.

Slofstra, W., “Tsirelson’s problem and an embedding theorem for groups arising from nonlocal games”, in: *Journal of the American Mathematical Society*, 331, 2019, pp. 1–56, doi: 10.1090/jams/929.

Šupić, I. and Bowles, J., “Self-testing of quantum systems: a review”, in: *Quantum*, 4, 2020, p. 337, doi: 10.22331/q-2020-09-30-337.

Tavakoli, A. et al., “Bell nonlocality in networks”, in: *Reports on Progress in Physics*, 855, 2022, p. 056001, doi: 10.1088/1361-6633/ac41bb.

Tsirelson, B., “Some results and problems on quantum Bell-type inequalities”, in: *Hadronic Journal. Supplement*, 84, 1993, pp. 329–345, doi: 10.1016/0370-1573(93)90050-8.

Watrous, J., *The Theory of Quantum Information*, Cambridge University Press, 2018.

Wehner, S., “Tsirelson bounds for generalized Clauser-Horne-Shimony-Holt inequalities”, in: *Physical Review A*, 73, 2006, p. 022110, doi: 10.1103/PhysRevA.73.022110.

Wehner, S., Elkouss, D., and Hanson, R., “Quantum internet: A vision for the road ahead”, in: *Science*, 3626412, 2018, doi: 10.1126/science.aam9288.

Modeling the resonant structure of HD 121617's debris disk

Matteo Raffaelli

Abstract

In this paper I will be modeling the debris disk found around the star HD 121617. This disk is not viewed face-on, rather, it has an inclination of 42° and is rotated by -29°. The important feature of this circumstellar structure made up of dust and planetesimals is that it presents a bright clump. The hypothesis I will be discussing is whether this clump can be explained by a planet whose orbit increased at some point in time. A migrating planet of this kind can gravitationally influence the azimuthal structure of a debris disk through the phenomenon of gravitational resonance. Gravitational resonance consists of an interaction between two bodies orbiting a third, more massive, body. What I will find is that the clump can indeed be explained by a resonance of the type 2:1 and a Neptune-like planet that migrated over the span of 10 million years for 7 astronomical units. The data for the disk comes from observations by the Atacama Large Millimeter Array taken at sub-millimeter. The method used here could be standardized in the future as a way to find planets hidden by circumstellar dust.

Keywords: Data, Modeling, Planets, Resonance, Discovery

I. INTRODUCTION

HD 121617 is a star located 117 parsec away from earth[1]. Observations of HD 121617 in the sub-millimeter range reveal the presence of a debris disk, a structure composed of planetesimals[2] and of micron-sized dust produced through a collisional cascade. According to [3], the star is estimated to be 16 million years old and has a mass of 1.9 solar masses. Recent observations made by the Atacama Large Millimeter Array (ALMA) in 2023 show the presence of a bright clump within the debris disk. Following the methodology outlined in [4]this clump was modeled. In this article a similar clump within Vega's debris disk is attributed to a phenomenon known as gravitational resonance, which occurs between a migrating planet (a planet moving away from its host star) and the surrounding debris disk. This phenomenon, detailed in Chapter 2, arises when two bodies orbit a more massive third body, such as a star. Specifically, when for every p orbits of the first body, the second body completes p+q orbits, it is said that the two bodies are in a p:q resonance[5]. The second body is driven by resonant forces towards certain angular locations of the orbit, which in turn explains the formation of clumps in a debris disk. For instance, a 2:1 resonance can produce two clumps of different density, a pattern that could explain the structure observed in HD 121617's disk. A more in-depth discussion of gravitational resonance can be found in[6]. A well known example of such resonance within our solar system is Neptune's 3:2 resonance, as discussed in [7]. Thefirststepinmodelingtheclump, describedinChapter3, involvescharacterizingitsstructure. Thisisachievedbyextractingaradialprofile, whichrepresentsthedisk'sbrightnessasafunction of distance from the star. Additionaly, an azimuthal profile, showing brightness as a function of angular position, is analyzed. A numerical model, described in (4), is used to simulate the resonance phenomenon more efficiently than traditional N-body simulations.

[1] The parsec is a unit defined as the distance at which an observer should be located to see an astronomical unit as 1 arcsecond.

[2] Astronomical rocky objects with a radius around 1 km.

[3] M. Cure, A. Kospal, A. Moor, et al., "Molecular Gas in Debris Disks around Young A-type Stars", in *The Astrophysical Journal*, 2017.

[4] M. C. Wyatt, "Resonant trapping of planetesimals by planet migration: debris disk clumps and Vega's similarity to the solar system", in *The Astrophysical Journal*, 2003.

[5] This relationship between orbits may also be unrelated to the phenomenon of gravitational resonance.

[6] D. Murrey, F. Stanley, "Solar System Dynamics", *Cambridge University Press*, 1st edition, 2000.

[7] G. Bryden, T. Hidekazu, S. Ida, D. N. C. Lin, "Orbital Migration of Neptune and Orbital Distribution of Trans-Neptunian Objects", in *The Astrophysical Journal*, 2000.

In Chapter 4 the images created by this model and the image of the original disk are compared and the values of key parameters are estimated. The values found for these parameters are: 21 earth's masses for the planet's mass, 58-97 au for the inner and outer boundaries of the disk, 41-48 au for the migration distance of the planet and 0.67 au/Myr for its velocity. The implications of this findings are discussed in Chapter 5.

In summary, this paper integrates the analytical approach from [8], the data found in [9] and the theory of [10] to model the new observations of HD 121617's disk made by ALMA.

[8] M. C. Wyatt, "Resonant trapping of planetesimals by planet migration: debris disk clumps and Vega's similarity to the solar system", in *The Astrophysical Journal*, 2003.

[9] M. Cure, A. Kospal, A. Moor, et al., "Molecular Gas in Debris Disks around Young A-type Stars", in *The Astrophysical Journal*, 2017.

[10] D. Murrey, F. Stanley, "Solar System Dynamics", *Cambridge University Press*, 1st edition, 2000.

II. RESONANT TRAPPING OF PLANETESIMALS BY PLANET MIGRATION

In this chapter the phenomenon of resonant trapping is explained in detail and also the numerical model used in [11] is introduced.

2.1. Planetary resonances in a debris disk

Planetary resonance is a physical phenomenon that is observed when the orbital periods of two bodies that rotate around a third body [12] are related by a ratio of small integers. More precisely, it is said that two bodies are in a p:q resonance when, for every p+q complete orbits of the first body around the central mass, the second body completes p orbits. This particular configuration causes a shift in orbital parameters such as eccentricity and radius. The case modeled in this paper is that of a system composed of a central star of mass m_*, a planet of mass m_{pl} that has migrated with velocity $a¤_{pl}$ and an external debris disk. A planet is said to have migrated when its orbit has increased (or decreased) due to gravitational interactions with the cirmcustellar materials (e.g. gas)[13]. A debris disk is a circumstellar structure made up of planetesimals, more commonly known as asteroids or comets, that are grinded down by collisions and produce dust which can reach micron size, much like the Kuiper belt in our solar system. However, the model used in this analysis considers the disk to be made up of only planetesimals for simplicity. Taking into account Kepler's third law which relates the semi-major axis a and the period T of an orbit to a constant k:

$$\frac{a^3}{T^2} = k \tag{II.1}$$

considering a resonance of (p+q):q, one obtains that such a phenomenon occurs at a semi-major axis of:

$$a_{(p+q):p} = a_{pl}\left(\frac{p+q}{p}\right)^{2/3} \tag{II.2}$$

[11] M. Cure, A. Kospal, A. Moor, et al., "Molecular Gas in Debris Disks around Young A-type Stars", in *The Astrophysical Journal*, 2017.

[12] e.g., Two planets around a star.

[13] The objective of this paper is to model the effects of such migration and not to study its causes.

where $a_{(p+q):p}$ is the radial location of the resonance and a_{pl} is the semi-major axis of the orbit of the planet. Given that in the examined case the planet is migrating at a rate $\dot{a}_{pl}$, the semi-major axis, defined by equation (II.2) at which the resonances occur increases. Therefore, if the planetesimals were not moving, they would be subjected to the planet's resonance only for short period of time. However, an exchange in angular momentum can cause an increase in the planetesimals' orbit as well, so that they get trapped inside the resonance. The planetesimals trapped inside a resonance accumulate and form a clump which is then observable. Table 2.1 reports the relation between the starting semi-major axis of a migrating planet and the moving radial locations of different resonances:

Resonance	(deg)	A	B	C	D_i	D_g	E_i	E_g
2:1 (u)	-(107–79)	···	···	···	$> 1.59a_{pl}$	50% of $a_i > 1.59a_{pl}$	$> 1.59a_{pl}$	50% of $a_i > 1.59a_{pl}$
2:1 (l)	107–79	···	···	···	···	50% of $a_i > 1.59a_{pl}$	···	50% of $a_i > 1.59a_{pl}$
5:3	±60, 180	···	···	···	···	···	$(1.41 - 1.59)a_{pl}$	$(1.41 - 1.59)a_{pl}$
3:2	±90	···	···	$> 1.31a_{pl}$	$(1.31 - 1.59)a_{pl}$	$(1.31 - 1.59)a_{pl}$	$(1.31 - 1.41)a_{pl}$	$(1.31 - 1.41)a_{pl}$
4:3	±60, 180	···	$> 1.21a_{pl}$	$(1.21 - 1.31)a_{pl}$	$(1.21 - 1.31)a_{pl}$	$(1.21 - 1.31)a_{pl}$	$(1.21 - 1.31)a_{pl}$	$(1.21 - 1.31)a_{pl}$

Table II.1: This table shows, in the second column, the azimuthal locations at which planetesimals spend more time, and therefore accumulate, for different resonances. The letters above the next columns represent different regions of the II.2 graph. For each region, a value of semi-major axis is given for each resonance. Planetesimals with a starting semi-major axis greater than this value can get trapped in the resonance.

An intuitive explanation for the formation of the clumps can come from considering the frame corotating with the mean motion of the planet. In this frame, by definition of resonance, the pericenters[14] of the planetesimals' orbits are located at longitudes[15] relative to the planet incremented by (p/q)360° from the previous passage. Furthermore, the planetesimals spend moretimeatrelativelongitudesclosetothepericenterthanatlongitudesclosetotheapocenter[16]. Figure 2.1 shows how the orbits of the planetesimals look like for different resonances in the corotating frame.

The patterns shown in Figure 2.1 are unique but their orientations relative to the planet are not, and can be represented by a single parameter called the planetesimal's resonant argument defined by:

$$\phi = (p+q)\lambda_r - p\lambda_{pl} - q\tilde{\omega}_r \qquad \text{(II.3)}$$

[14] The point of the orbit which is closest to the attracting body.

[15] The angle in the orbital plane that defines a point on the orbit.

[16] The furthes point of the orbit from the attracting body.

In Equation (II.3), λ_r and λ_{pl} are the longitudes of the planetesimal and the planet respectively, and $\tilde{\omega}_r$ is the planetesimal's argument of periapsis[17]. When in resonance, the planetesimal's resonant argument stays constant since an increase in the first term corresponds to a decrease in the second. It is possible to mathematically describe, in the context of the three body problem, the planet's gravitational influence in the form of a scalar potential as the sum of many perturbing terms[18]. Assuming that the orbits of the planet and the planetesimals are coplanar, and that the planet has a circular orbit, these perturbing terms can be written as:

$$R = \frac{Gm_{pl}}{a}\left\{f_{s,1}e^2 + e^q\left[f_d(\alpha) + \frac{f_i(\alpha)}{\alpha}\right]cos\phi\right\} \qquad \text{(II.4)}$$

where $\alpha = a_{pl}/a$, $f_{s,1}$, f_d, and f_i are coefficients corresponding to the secular, resonant direct and resonant indirect parts of the perturbing function, and e is the eccentricity of the planetesimal. The secular part does not depend on mean longitudes, which are the fastest changing orbital parameters, and therefore it is slowly varying. The other terms depend on ϕ, the planetesimal's

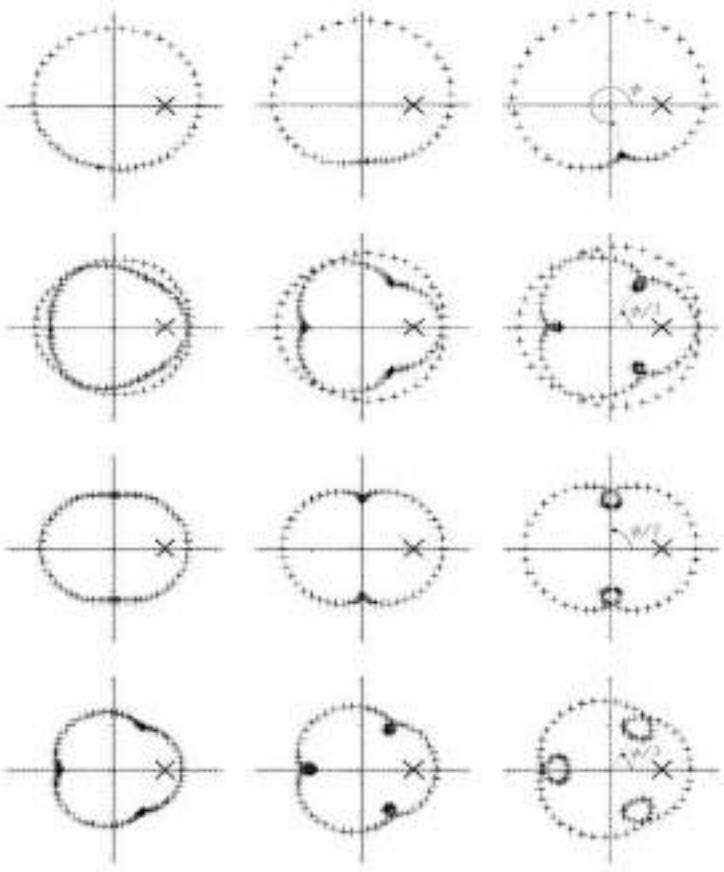

[17] The argument of the periapsis is the angle between the ascending node and the periapsis. The ascending node is the point where the orbit intersects a plane of reference and the orbiting body climbs above this reference plane.
[18] D. Murrey, F. Stanley, "Solar System Dynamics", *Cambridge University Press*, 1st edition, 2000.

Figure II.1: In this image, the position of the planet is represented by the largest cross while the smaller crosses represent the position of a planetesimal at intervals of 1/24 of the planet's orbit. The resonances are, from top to bottom: 2:1, 5:3, 3:2 and 4:3. From left to right the eccentricity of the planetesimal is 0.1, 0.2, and 0.3.

resonant argument, and are called either direct or indirect based on whether they depend on the choice of the origin of the coordinate system or not. The effects of these perturbations on a planetesimal's orbit can be derived using the Langrangian planetary equations. In [19] it is shown, from further analysis of the three body problem, that the influence of a planet causes a libration[20] in the planetesimal's resonant argument of:

$$\phi = \phi_m + \Delta\phi sin(2\pi t/t_\phi) \tag{II.5}$$

where ϕ_m is called the center of libration. The fact that all planetesimals trapped in a resonance have the same center of libration is what causes the azimuthal distribution to be asymmetric. This is due to the fact that there is an increase (decrease) in angular momentum when a conjunctio[21]happens before (after) the planetesimal's apocenter. In other words, the conjunction is pushed towards the apocenter, where the planetesimal would experience no change in its angular momentum[22]. This condition corresponds to: $\phi_m/q = 180°$. However, it is necessary to take into account the fact that the planet is migrating. This means that, even if the conjunction happens at pericenter, there must be an increase in the planetesimal's angular momentum such that it migrates along with the planet. This can be expressed by:

$$\dot{a}_{mig} = \dot{a}_{pl}\left(\frac{p+q}{p}\right)^{2/3} \tag{II.6}$$

The eccentricity of the orbit will also be affected as:

$$e = \sqrt{e_0^2 + \left(\frac{q}{p+q}\right) ln\frac{a}{a_0}} \tag{II.7}$$

where e_0 and a_0 are the starting values of eccentricity and semi-major axis.

[19] D. Murrey, F. Stanley, "Solar System Dynamics", *Cambridge University Press*, 1st edition, 2000.
[20] An oscillation.
[21] The point of the orbit of a planetesimal where it is closest to the influencing planet.
[22] This holds for q=1 resonances.

2.1.1. Trapping probabilities

The probability for the planetesimals of remaining trapped inside different resonances is discussed in[23]. In this paper the RADAU 15th-order integrator program (Everhart 1985)[24] was used to experimentally determine the dependence of the aforementioned probability on certain parameters. What was found is that for a p:q resonance this probability is given by:

$$P = [1 + (X\mu^{-u}\theta)^{Y\mu^{v}}]^{-1} \tag{II.8}$$

where X, u, Y, v are numerical constants that depend on p and q. On the other hand μ and θ are determined by the characteristics of the system:

$$\mu = m_{pl}/m_{*} \tag{II.9}$$

$$\theta = \dot{a}_{pl}\sqrt{a/m_{*}} \tag{II.10}$$

where a is the major semi-axis of the planetesimal. These results are summarized in Figure II.2. In this Figure, values of μ are in the abscissas and values of θ are on the ordinates. The lines are obtained by using Equation (II.8) for a chosen value of the probability. Each triplet of lines belongs to a different resonance. The dotted line corresponds to a probability value of 0.1, the continuous line to 0.5 and the dashed one to 0.9. The dash-dot line represents a probability value of 0.33 of ending up in the 2:1(1) resonance, as explained in the following section.

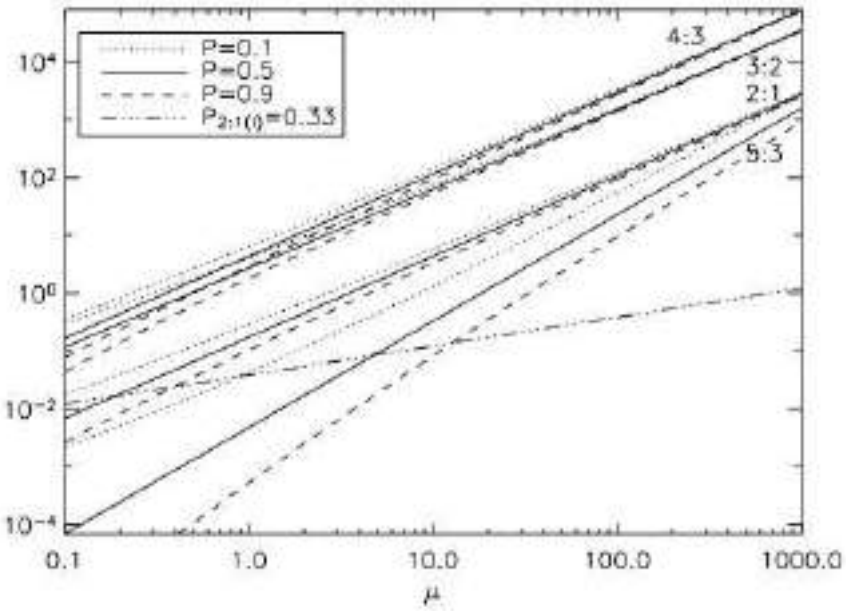

Figure II.2: θ vs μ graph from [2]

[23] M. C. Wyatt, "Resonant trapping of planetesimals by planet migration: debris disk clumps and Vega's similarity to the solar system", in *The Astrophysical Journal*, 2003.

[24] A program to simulate gravitational mechanics.

2.1.2. The 2:1 resonance

The 2:1 resonance plays an important role in this paper since it is the only one that gives rise to a single clump[15]. For values of eccentricity below 0.04 the libration center of this resonance is found at about 180°. For values of eccentricity above 0.04 the libration center can take two values: $\phi_m > 180°$ and $\phi_m < 180°$. This is the so called asymmetric libration which can be physically explained by the fact that perturbations to the orbit also occur if the conjunction is at pericenter. This is because, after a conjunction, the planet is ahead of the planetesimal which is thus forced to increase its angular momentum, as explained before. However, when the planet reaches the 180° mark ahead of the planetesimal, its influence causes a decrease in the planetesimal's angular momentum. Since the planetesimal spends more time at longitudes relative to the planet close to the pericenter, these forces do not cancel out and are not negligible for $q = 1$ resonances, where every pericenter passage occurs at the same relative longitude as the planet. This peculiarity of the 2:1 resonance is studied in [16] where the name 2:1(u) is used when $\phi_m > 180°$ and the name 2:1(l) when $\phi < 180°$. It was found that fewer planetesimals get trapped in the 2:1(l) resonance than in the 2:1(u). The probability of ending in the former resonance is:

$$P_{2:1(l)} = 0.5 - 0.85\theta^{0.5}\mu^{-0.25} \qquad \text{(II.11)}$$

In conclusion, the 2:1 resonance gives rise to two different centers of libration which, in turn, cause two asymmetric clumps, the 2:1(u) being the most populated. If a probability value of 0.33 is set in Equation (II.11), the dash-dot line in graph II.2 is obtained. Below this line the 2:1(u) clump is exactly twice as populated as the 2:1(l) one. The 2:1(u) clump is found at 107°-79° behind the planet and the 2:1(l) one at 107°-79° ahead of it, as reported in table 2.1.

2.2. The physical model

The modelling of HD 121617 was conducted using a software[25] that is explained and used in [26]. This software, starting from a set of initial parameters, produces an image[27] that represents a debris disk viewed face-on which has been subjected to the gravitational influence of a migrating planet.

[25] Written in IDL programming language.

[26] M. C. Wyatt, "Resonant trapping of planetesimals by planet migration: debris disk clumps and Vega's similarity to the solar system", in *The Astrophysical Journal*, 2003.

[27] A 2d-array.

2.2.1. Description of the software

The program is set up in the form of a function that takes in ten parameters and simulates over a series of timesteps the evolution of the system. The parameters are:

- a_{min}: the starting minimum semi-major axis of the distribution of planetesimals composing the debris disk, measured in astronomical units[28] as every other distance parameter.
- a_{max}: the starting maximum semi-major axis of the distribution of planetesimals.
- δ: a parameter determining the number of planetesimals comprised between a semimajor axis a and $a + da$ which is $a^{\delta} da$. This parameter is always set to -0.5.
- n_{pp}: the number of planetesimals included in the simulation. This parameter is chosen based on a trade-of between speed and precision of the simulations.
- a_{pl1}: the starting semi-major axis of the planet.
- a_{pl2}: the final semi-major axis of the planet.
- $\dot{a}_{pl}$: the rate of migration of the planet, measured in astronomical units per million years.
- m_{pl}: the mass of the planet, measured in units of earth's masses.
- m_*: the mass of the star, measured in units of solar masses. In the case of HD 121617 this value is 1.9.
- nt: the number of iterations or timesteps for the simulation, always set to 2.

In this model, the planetesimals are assumed to be massless so that they do not influence the migration of the planet. The starting distribution of the planetesimals is determined by the parameters a_{min}, a_{max} and δ. It is assumed that for the starting orbits of the planetesimals the eccentricities only vary in the range $(0 - 0.01)$, the inclinations in the range $(0 - 0.01)$ rad, and the argument of periastron, longitudes of ascending node and their own longitudes[29] can assume every possible value in the range (0-360°). The position of each of the n_{pp} planetesimals is set up by assigning random values within the described ranges. The planet's initial orbit is determined by the input parameter a_{pl1} and every other parameter is assumed to be zero, i.e.,

[28] An astronomical unit is defined as the average distance of the earth from the sun.
[29] These are all the angles needed to fully determine the position of a body orbiting in a 3d space.

the orbit is circular and belongs to the midplane of the debris disk. The migration of the planet is sustained by a tangential force which produces an acceleration of:

$$\dot{v} = 0.5\dot{a}_{var}\sqrt{GM_*/a^3}$$

where $\dot{a}_{var}$ is the variation of the semi-major axis. The only orbital parameter of the planet that changes during the simulation is its distance from the star.
During each of the timesteps five operations are performed:

1. The location of every resonance is determined through Equation (II.2).
2. For every planetesimal, the program checks whether it passes a resonance and, if so, a random number between 0 and 1 is produced.
3. If the random number is less than the probability of trapping given by Equation (II.8) the planetesimal is considered to be trapped.
4. Equations (II.6) and (II.7) are used to update the planetesimal's orbital parameters.
5. Each planetesimal is assumed to be representative of 9600(p+q) more planetesimals. For each of this new planetesimals, a resonant argument is chosen according to Equation (II.5). The resulting number density (planetesimals per pixel) is normalised dividing by 9600(p+q).

The non resonant planetesimals' orbits remain unchanged unless they are reached by the planet's overlap region[22], defined by:

$$|a/a_{pl}| < 1.3(3 \times 10^{-6}\mu)^{2/7} \qquad \text{(II.12)}$$

This region is chaotic and planetesimals in it would be scattered out. They are therefore removed from the simulation. It is assumed at the end of the simulation that the planet has stopped migrating. The image in Figure II.3 shows a possible result of the program for parameters:

Parameter	Value
amin (au)	50
amax (au)	100
npp	400
apl1 (au)	30
apl2 (au)	50
$\dot{a}_pl$ (Myr/au)	1
m_{pl} (earth's masses)	20

Table II.2: Choice of parameters for an example simulation

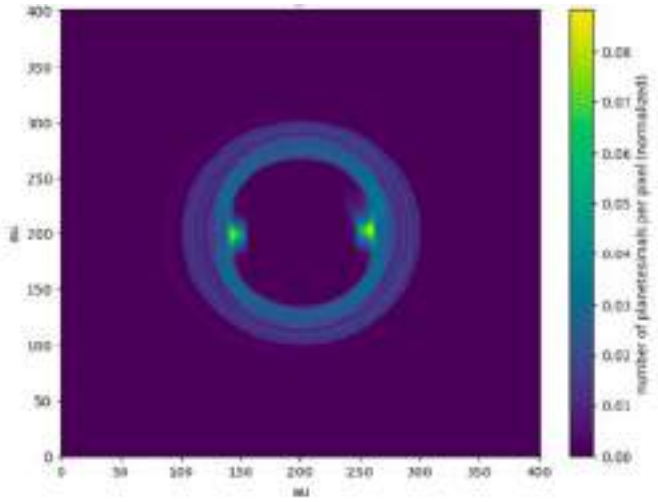

Figure II.3: This image is an example of the output of the numerical model. Two clumps can be seen and could be explained by a 3:2 resonance

The described numerical model is based on statical laws instead of gravitational dynamics which makes it inherently stochastic. However, it is physically coherent and much faster than a gravitational dynamics-based simulation which allows for a more convenient analysis.

III. THE STAR HD 121617

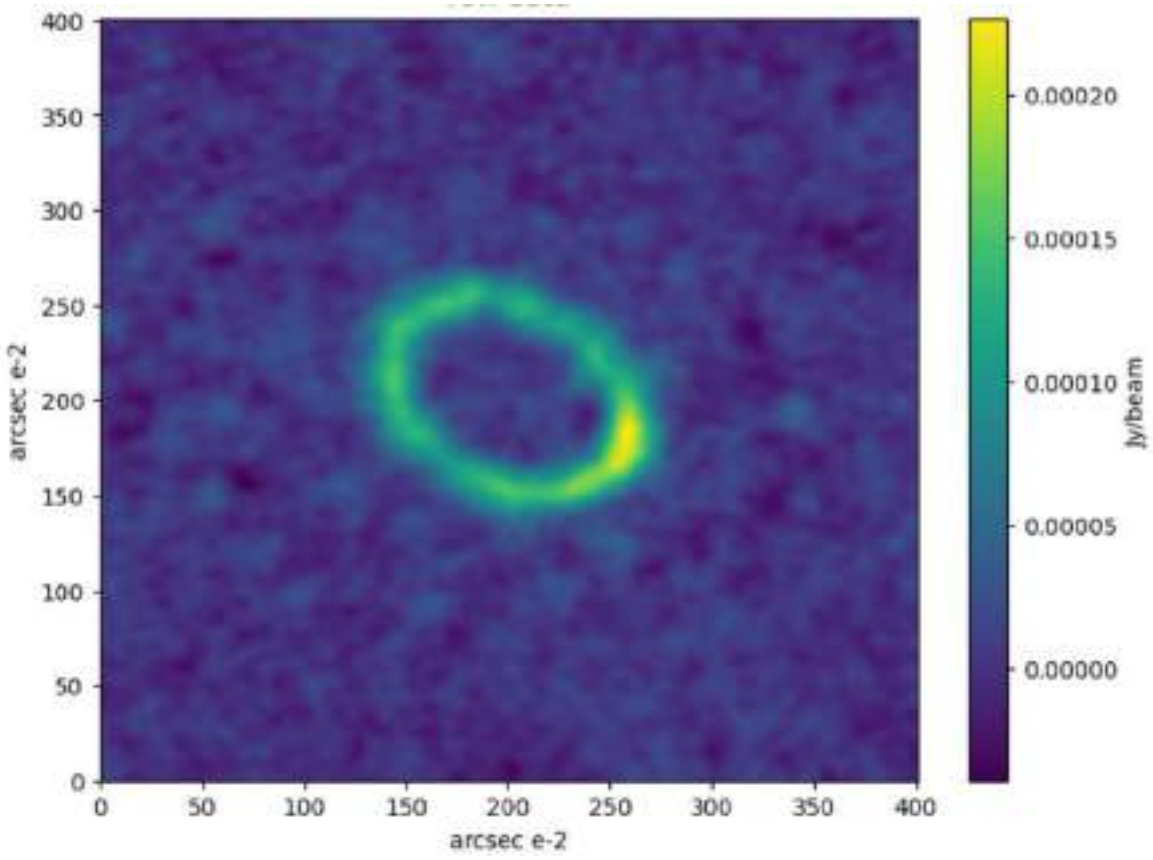

Figure III.1: ALMA's observation of HD 121617's debris disk.

HD 121617 is a main sequence star 117 parsec away from us. Its age is 16 million years [30]. In this chapter the observational data is described. The debris disk is then characterized, firstly by calculating the azimuthal profile and secondly by calculating the radial profile.

3.1. Data collection

The data used in the simulation come in the form of a Flexible Image Transport System (FITS) file that is a typical format for astronomical images. FITS files contain a header that gives information on how to interpret the data. The image opening this chapter was taken on the 28th of April 2023 by ALMA, one of the world's largest Astronomical Interferometers. ALMA is located in the Atacama Desert in Chile because of the perfect weather conditions of low humidity and high elevation characterizing the location. The observation was taken at a frequency of $3.33 \cdot 10^{11}$ Hz in the sub-millimeter. This particular frequency range is chosen because the objective is to observe the debris disk, which has a temperature of around 20 K and

[30] M. Cure, A. Kospal, A. Moor, et al., "Molecular Gas in Debris Disks around Young A-type Stars", in *The Astrophysical Journal*, 2017.

therefore emits at around one THz according to Wien's displacement law. The very bright star in the middle, which has a much higher temperature[31], emits at higher frequencies, thus making it possible to observe the disk without the star. However, the peak obtained from Wein's law is far from the observational frequency (far-infrared). This is because longer frequencies are needed to get through earth's atmosphere. Due to the properties of the observational instrument, the image is convolved with a 2-dimensional Gaussian (the beam), which has two Full Width at Half Maximum (FWHM) of 0.205 au and 0.193 au, and is rotated by an angle of -70°. The unit of measure for the content of each pixel in the image is Janksys per beam. The Janksy is a unit that is used to measure flux-density. It is defined as:

$$1\ Jy = 10^{-26} W \cdot m^{-2} \cdot Hz^{-1} \tag{III.1}$$

For extended sources the most convenient approach is to use units of Jy per beam size, which is the area of the sky in solid angles that the instrument is looking at. The width of a pixel is 1/100 of arcsecond. What the image is showing is the flux density of the radiation emitted by the disk and not its distribution in terms of number of planetesimals per pixel. On the other hand, the latter is what the numerical model generates, as explained in section 2.2.1. To shift between these two quantities some considerations can be made. It makes sense to approximate the emission spectrum of a star with the emission spectrum of a blackbody. This is due to the fact that a star doesn't reflect radiation but rather it produces and emits new photons which makes it similar to a blackbody. It is therefore possible to assume that Stefan-Boltzmann's law, which relates the emitted flux F at the surface to the temperature T, holds for a star:

$$F = \sigma_{SF} T^4 \tag{III.2}$$

The flux $F(r)$ emitted by a spherically symmetrical source at a distance r from its center is proportional to the inverse square $\frac{1}{r^2}$ of the distance. Knowing this, the temperature due to the flux at a distance r will be:

$$T = \left(\frac{F(r)}{\sigma_{SF}}\right)^{\frac{1}{4}} \propto \frac{1}{\sqrt{r}} \tag{III.3}$$

σ_{SF} r

The next assumption needed to convert between units of flux density and mass density is that the planetesimals emit radiation only by reprocessing it and can therefore be considered as

[31] e.g. 6000 K for our sun.

blackbodies as well. Their temperature will be a consequence of the emission of the star and therefore, as previously discussed, proportional to the inverse square root of the distance from the center of the star. The subsequent observed emission of the planetesimals will be in the Rayleigh Jeans region because as explained before, the peak is in the sub-millimeter but the observations are made in the far-infrared. Rayleigh Jeans law states that the emitted flux is proportional to the temperature. The conclusion is that the flux density of the emission of the planetesimals is proportional to the inverse square root of the distance from the center of the star. If two pixels at different distances (r_1 and r_2) from the center contain the same number of planetesimal the further one will emit $(\frac{1}{\sqrt{r_2}} - \frac{1}{\sqrt{r_1}})$ times less. Taking this into account it is possible to make the flux density proportional to the number density and therefore to confront the numerical model image and the observations[32].

3.2. Data analysis

In order to model the disk an analysis through the use of Python programming language was performed.

3.2.1. Disk coordinates

Assuming that the debris disk is circular, it is evident from figure III.1 that the observational point of view is not perpendicular to the orbital plane, because the shape is elliptical. The first logical step of the analysis is then to estimate two rotational angles. One angle determines the inclination of the circle in the sky and the other determines the subsequent rotation around the center. Such a geometric operation transforms a circle into an ellipse. The applied procedure was to filter from the image all the flux below $5e-5$ Jy/beam so that what remained was the shape of the disk and not the surrounding noise. Then all non-zero points were converted to 1 so that they all weighed the same in the subsequent analysis. Next an ellipse was fitted to the transformed dataset using the minimum chi-squared method implemented by the scipy function ”least squares” which uses a trust region reflective algorithm. The fit is shown in Figure III.2

[32] A constant of renormalization will have to be considered for future analysis.

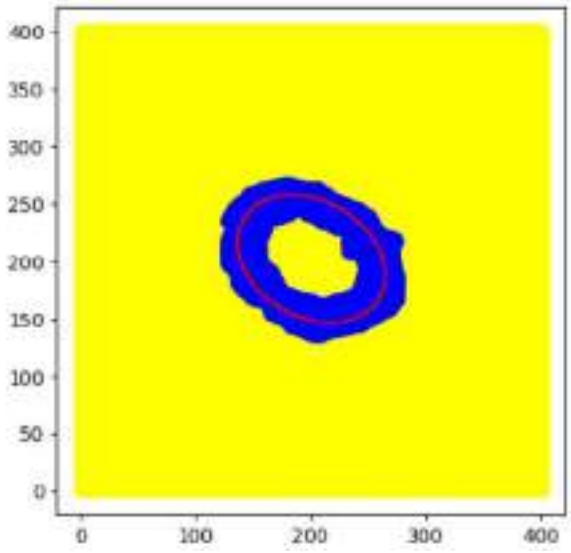

Figure III.2: This image shows the fitted ellipse plotted over the filtered data.

The equation for a rotated ellipse is:

$$\frac{((x-x_c)cos(\theta)+(y-y_c)sin(\theta))^2}{a^2}+\frac{((x-x_c)sin(\theta)-(y-y_c)cos(\theta))^2}{b^2}=1 \qquad \text{(III.4)}$$

where x_c and y_c are the coordinates of the center of the ellipse, θ is the rotation angle with respect to the positive x axis and a and b are the major and minor semiaxes. The obtained parameters are reported in Table III.1. Remembering the assumption that the disk is circular,

Table III.1: Parameters of the fitted ellipse

Parameter	Value	Error
x_c (px)	200	1
y_c (px)	202	1
a (px)	68	1
b (px)	50	1
θ (rad)	-0.52	0.03

the minor axis of the ellipse in reality should have the same length as the major one, its shortness being only an effect of the inclination. Therefore the inclination angle can be obtained through a simple trigonometric computation:

$$\theta_{inc} = arccos\left(\frac{b}{a}\right) \qquad \text{(III.5)}$$

The final values for the angles in degrees are then 42 ± 1 for the inclination and −29 ± 2 for the rotation.

3.2.2. Filtering and noise estimation

The next step needed for the analysis is a function capable of selecting portions of the data following the elliptical profile of the disk. This is possible thanks to the previously estimated parameters. The function allows to filter out a portion of the data reasonably far from the disk, shown in Figure III.3.

It is then assumed that the data in this region are mainly due to the noise[33]. To characterize this noise, all data points are sorted in bins made by dividing the difference between the maximum and minimum fluxes by 100. A Gaussian is then fitted to the bins, as shown in Figure III.4. This process results in a standard deviation for the noise of $1 \cdot 10^{-5}$ Jy/Beam. This value is used as error on the flux of a pixel for the rest of the analysis.

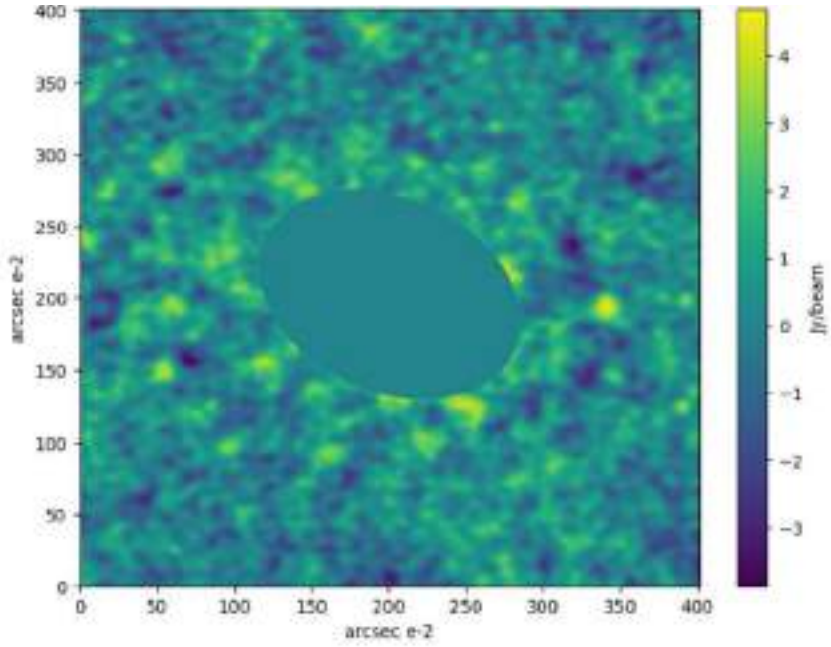

Figure III.3: This image shows the application of a filter to the original image.

3.2.3. The Radial profile

In order to better understand the shape of the disk it is useful to obtain a radial profile, which consists of plotting the flux as a function of the distance from the center. There are two ways of going about this task. The first way consists of using Python's scipy.ndimage package to scale and rotate the image to deproject the ellipse into a circle. Although this method produces a good deprojected image III.5, the stretching and rotating of the image implies that some pixels remain empty and/or that some of the original pixels overlap after the transformation. The

[33] There are some clear flux spots like the one at the center on the right that are probably not due to noise but are actual sources. However, they can be safely ignored since they constitute a small effect overall.

function “affine transform” from scipy.ndimage solves this problem by using spline interpolation at the cost of changing the flux’s distribution with respect to the original image. Obtaining a radial profile from the circular image produced with the described method is straightforward because all it needs to be done is to average the flux over a circular annulus.

The second way of obtaining a radial profile is to use the disk coordinates more cleverly. It is possible to use Equation (III.4) to define an elliptical annulus. A point of the radial profile is then calculated as the average flux over this elliptical annulus. Figure III.6 illustrates this process with annuli of exaggerated width for clarity.

The obtained radial profile of HD 121617 is shown in Figure III.7, from a distance to the star of 0 au to a distance of 250 au.

As expected by looking at the image at the beginning of the chapter, the width of the disk is around 50 au, going from 50 au to a 100 au. The error on each point is given by the value calculated in Section 3.2.2 divided by the square root of the number of points in each annulus, as the propagation for errors requires.

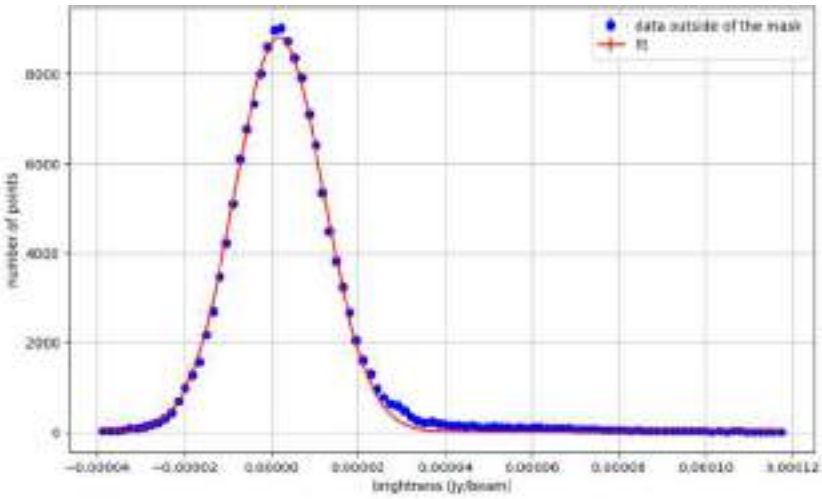

Figure III.4: The Gaussian fitted to the data points.

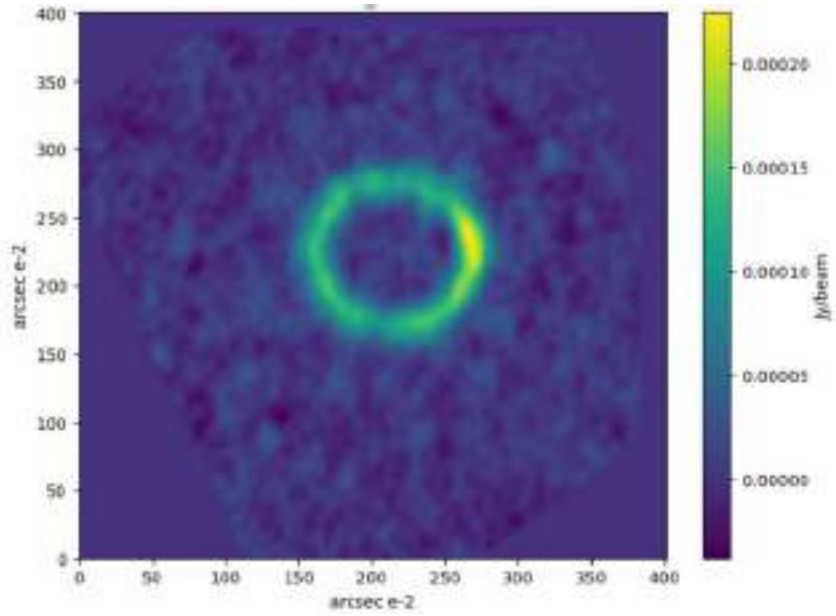

Figure III.5: The deprojected disk.

3.2.4. The azimuthal profile

An azimuthal profile is a plot of the flux as a function of the angle with respect to the positive x-axis of a system where the origin is located in the center of the disk. As for the radial profile there are two ways of fulfilling this task. The first one involves modifying the image and messing with the flux distribution, and thus the second way was used again. The coordinates are converted into elliptical ones by first translating every point about the center of the ellipse, then rotating them by the rotation angle and then stretching them by a factor equal to the eccentricity of the ellipse which represent a rotation in the 3-d space of the inclination angle. The angle of every transformed point was then calculated by taking the arctangent of y divided by x[34].

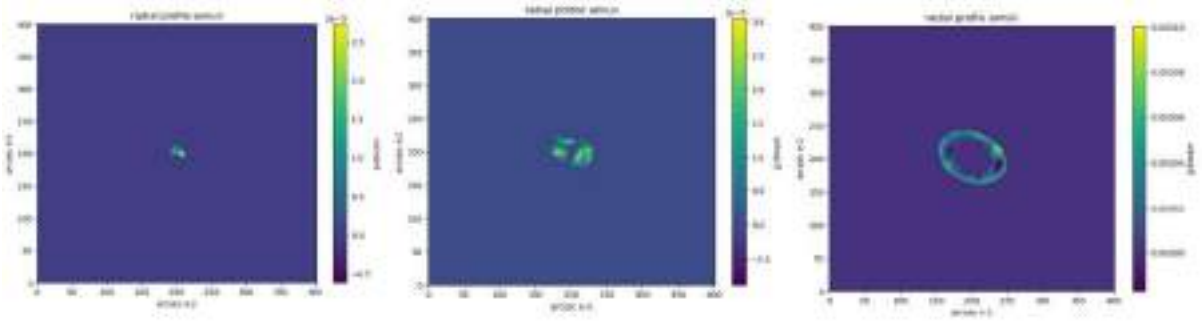

Figure III.6: This image shows the first three annuli over which the flux is averaged by the radial profile function.

[34] The angles are measured starting from the major axis of the fitted ellipse.

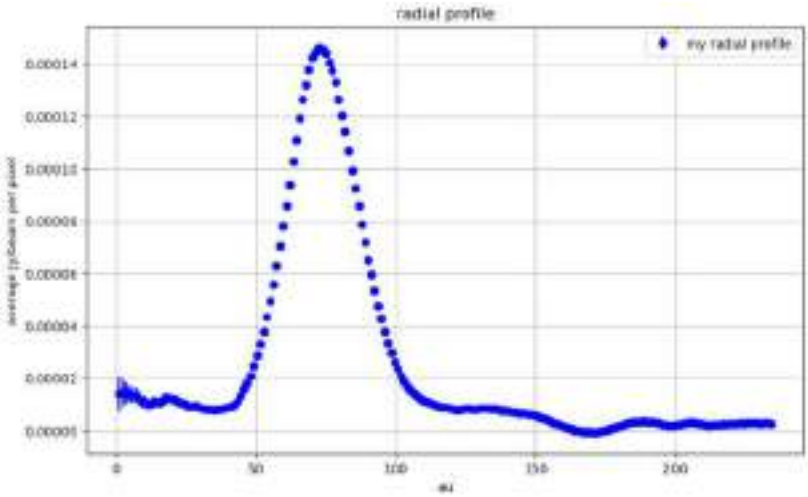

Figure III.7: The radial profile of the disk.

The points were then divided based on their angle in overlapping angular bins centered on every integer from 1 to 360 with a width of 50. The overlapping bins are needed because they produce a much smoother profile with no abrupt changes. A point of the azimuthal profile is then obtained by averaging over the bin. The process is shown in Figure III.8.

In order to obtain a noiseless profile without the loss of important information, two spatial filters, as described in Section 3.2.2 were applied, obtaining the image in Figure III.9.

The azimuthal profiles of the image outside of this mask were plotted to verify that they are indeed oscillating within a range of one standard deviation and thus do not contain any important information, as shown in Figure III.10.

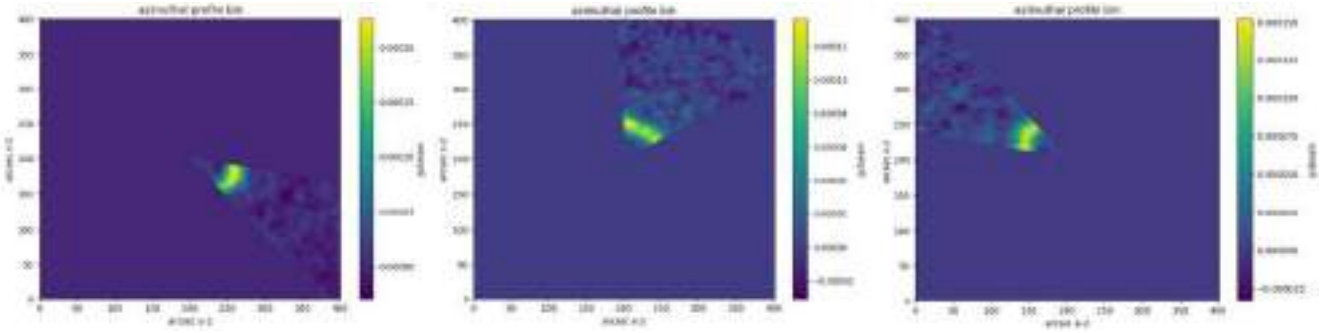

Figure III.8: This image shows the angular bins over which the flux is averaged to obtain the azimuthal profile. The bins are centered at 0°, 90° and 180° respectively.

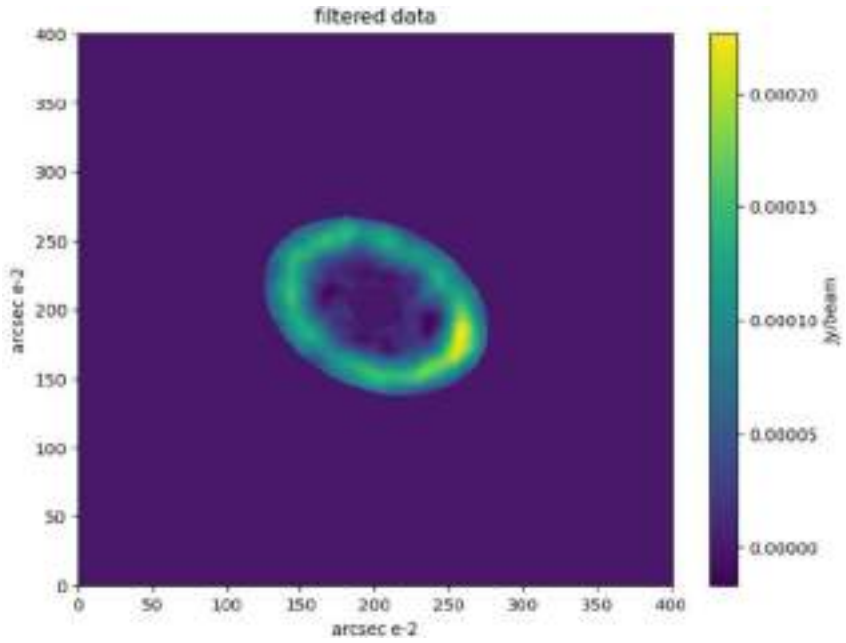

Figure III.9: Original image with inner (0-20 arcsec e-2) and outer (80-200 arsec e-2) filters applied. The result is an elliptical mask.

The final azimuthal profile, with errors calculated as for the radial profile, is shown in Figure III.11.

The plot in Figure III.11 clearly shows the presence of a clump that can also be seen as a brighter spot in the original image in Figure III.1 in correspondence of the zero angle. On the other side of the disk the structure is much more irregular but the aim is to model the biggest clump which constitutes the most important structure of the disk.

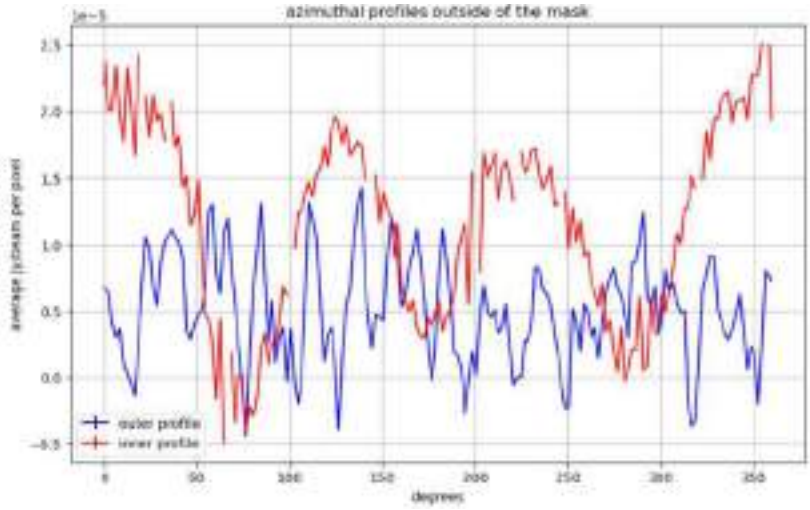

Figure III.10: Azimuthal profiles outside of the mask.

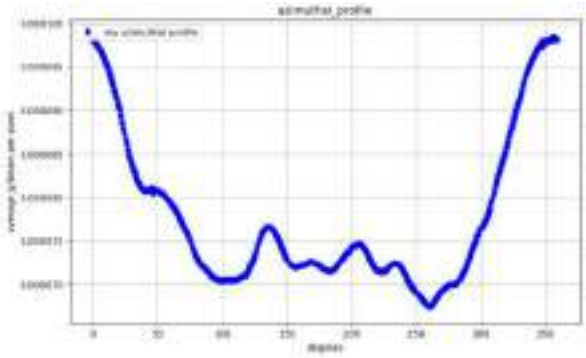

Figure III.11: The azimuthal profile of the disk.

IV. EXPLORING THE PARAMETERS SPACE

In this chapter we will explain how the modeling software was used, together with the theory outlined in Chapter 1, to explain the clump characterized by the analysis in Chapter 2. Out of the ten input parameters of the modeling software four were already determined in the previous description. In the first section of this chapter initial guesses for m_{pl} and $\dot{a}_{pl}$, which are the determining parameters for the azimuthal structure, will be discussed. In the second section the same will be done for a_{pl1}, a_{pl2}, a_{min} and a_{max}, which are the parameters that determine the radial structure. In the third and last section a best-fit to estimate these parameters will be performed.

In this chapter we will explain how the modeling software was used, together with the theory outlined in Chapter 1, to explain the clump characterized by the analysis in Chapter 2. Out of the ten input parameters of the modeling software four were already determined in the previous description. In the first section of this chapter initial guesses for m_{pl} and $\dot{a}_{pl}$, which are the determining parameters for the azimuthal structure, will be discussed. In the second section

the same will be done for a_{pl1}, a_{pl2}, a_{min} and a_{max}, which are the parameters that determine the radial structure. In the third and last section a best-fit to estimate these parameters will be performed.

4.1. Initial guess for azimuthal parameter

By looking at the azimuthal profile it is clear that the most important structure present in the disk is the very bright clump that can be seen in correspondence of the major axis in the HD 121617's original image. As mentioned before in Section 1.2, the 2:1 resonance is the only one with a single clump. This can also be seen in Figure 2.1. The optimal region of the μ vs θ graph shown in Figure II.2 would thus be the one encompassed by the 2:1, 5:3 and 2:1(l) lines. Being above the 2:1 lines would mean that the probability for a planetesimal to end up in the 2:1 resonance is less than 0.1. On the other hand, being below the 2:1(l) line would imply the presence of two clumps, one being twice as bright as the other, due to the asymmetric libration described in Section 2.2. The same reasoning applies to the 5:3 lines, below which three clumps of equal brightness would be observed. However, the described region of the graph is also below the triplets of the 4:3 and 3:2 resonances which means that a three clumps pattern from the 4:3 would also be showing. The 3:2 resonance only contributes in equal parts to the peaks of the 2:1(u) and 2:1(l) resonances. This issue will be discussed more in depth in the next

section. From this analysis one gets that, for a fixed value of μ[35], θ[36] can assume a restricted set of values. A sensible choice for μ, similar to the one made in the case of Vega in[37], would be 10. A value of 10 for μ, knowing that the star is 1.9 solar masses[38], would mean that the planet is 19 earth's masses heavy which is around the same mass of Neptune[39]. It is affirmed in[40] that a migration of Neptune could be responsible for the resonant trapping of Pluto and other trans-Neptunian objects in a 3:2 resonance, which further reinforces the choice for μ. The restricted set of values of θ is then $10^{-1} - 10^{0}$. By choosing μ and θ, initial guesses for m_{pl} and a_{pl} follow. As an example, one could choose $\theta = 0.5$ which, by using its definition, means a rate of migration for the planet $\dot{a}_{pl} = \theta \times \sqrt{m_*/a} = 0.08$[41].

4.2. Initial guess for radial parameters

Based on the study of the radial structure of the HD 121617's disk it is possible to give estimates for the remaining four parameters. By fitting a Gaussian to the graph in Figure III.7, as shown in Figure IV.1, it is possible to obtain a first estimate for a_{min} and a_{max}.

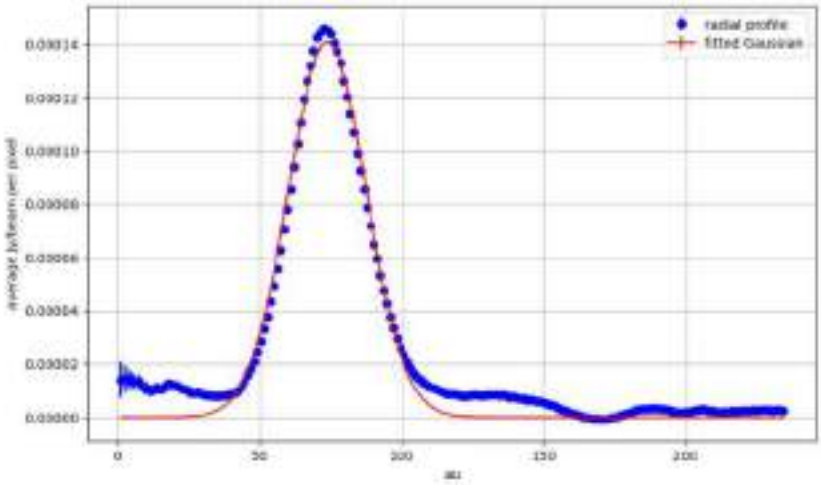

Figure IV.1: Radial profile with fitted Gaussian

[35] $\mu = mpl/m*$.
[36] $\theta = \dot{a}apl\sqrt{a}/m*$.
[37] M. C. Wyatt, "Resonant trapping of planetesimals by planet migration: debris disk clumps and Vega's similarity to the solar system", in *The Astrophysical Journal*, 2003.
[38] M. Cure, A. Kospal, A. Moor, et al., "Molecular Gas in Debris Disks around Young A-type Stars", in *The Astrophysical Journal*, 2017.
[39] 17 earth's masses.
[40] G. Bryden, T. Hidekazu, S. Ida, D. N. C. Lin, "Orbital Migration of Neptune and Orbital Distribution of Trans-Neptunian Objects", in *The Astrophysical Journal*, 2000.
[41] In this calculation, the mean of the fitted Gaussian in Section 4.2 was used as semi-major axis.

The mean and standard deviation of the fitted Gaussian are shown in Table IV.1.

Parameter	Value	Error
mean (au)	73.8	0.2
standard deviation (au)	13.6	0.2

Table IV.1: Estimated mean and standard deviation.

By assuming that at a distance of two standard deviations from the mean there are no more planetesimals, the first estimate is as shown in Table 4.2.

Parameter	Value	Error
a_{min} (au)	46.6	0.6
a_{max} (au)	101	0.6

Table IV.2: Estimated radial parameters.

In order to estimate the remaining two parameters some physical considerations are needed. First, the migration distance of the planet, determined by $\Delta a_{pl} = a_{pl2} - a_{pl1}$, is restricted by the age of the system which is 16 million years. This is because, given the migration rate, the duration of the migration can be calculated as $\Delta t = \Delta a / \dot{a}_p l$ and it cannot be greater than the age of the system. Second, knowing that the disk only shows one clump, it is possible to eliminate the three clumps pattern due to the 4:3 resonance by looking at Table 2.1. This table shows that for a starting distance of the planet greater than $a_{min}/1.59$ only the 2:1 resonance is possible. Remembering that the chosen region of Figure II.2 lies above the 5:3 triplet of lines, it is evident that we are led to selecting exclusively the 2:1 resonance. Based on the previous arguments a good first guess for the starting position of the planet is $a_{pl1} = a_{min}/1.41 = 23.4$ au, while for the final position $a_{pl2} = \dot{a}_{pl} \cdot 16 + a_{pl1} = 24.68$ au.

4.3. Fitting of the image

Based on the arguments outlined in the previous sections it is now possible to make a first simulation of the system through the numerical model and confront its result with the original image. To confront the two images some considerations must be made. The simulated system's image, as shown in Figure 2.3, represents numerical density per pixel, whereas the observed image represents flux density per pixel. To convert between these two units it is sufficient to divide the value of each pixel of the simulation by the square root of its distance from the center

of the disk[42]. The simulated system's image is then convolved with the bidimensional Gaussian distribution of the parameters given in the header of the FITS file. As explained in Section 3.1 the data observed by ALMA is convolved with this Gaussian because of the properties of the interferometer. It is therefore necessary to also convolve the simulation with the Gaussian in order to confront the two images. Then, instead of actually comparing the two images, it is more convenient to compare the radial and azimuthal profiles. To get the radial and azimuthal profiles of the simulation I used the same functions defined in Chapter 3[43] with the only difference that each pixel is divided by the square root of its distance.

4.3.1. Azimuthal fit

The fits were made with Python's Scipy least squares function which uses the chi-squared method with a trust region reflective algorithm. The first of these fits was done by comparing the azimuthal profiles of the simulations and the data with the least squares function. The aim was to determine the best choice for the azimuthal structure's determining parameters, m_{pl} and $\dot{a}_{pl}$, whose values are reported in Table IV.3. A third best-fit parameter regarding the scaling of the flux was also used. This is due to the fact that the total flux of the simulation depends on the number of planetesimals considered[44] which in turn cannot be too high for reasons of optimization of the best-fit algorithm. This scaling parameter is simply defined as the multiplying factor needed to re-scale the total flux of the simulation's profiles to match the data's total flux and is not of physical interest. A fourth parameter which represents the angle of rotation of the main clump with respect to the major-semiaxis was also included. All the other parameters are set equal to the first guesses given in the previous sections. The results of the fit are shown in Figure IV.2:

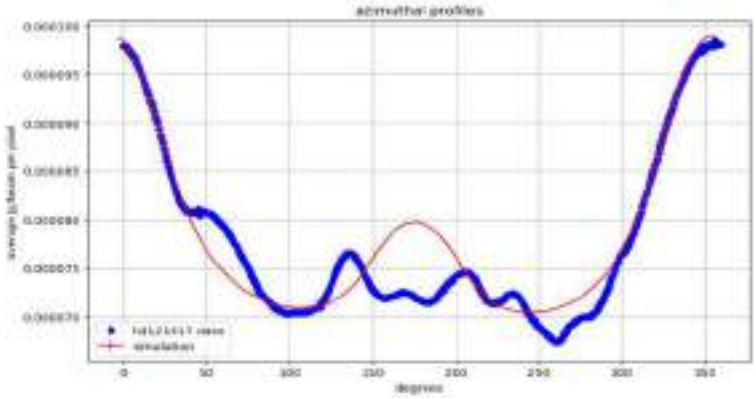

Figure IV.2: The azimuthal profile of the simulation in red over the azimuthal profile of the disk in blue.

[42] As discussed at the end of Section 3.1.

[43] This time with circular coordinates instead of elliptical ones, because the simulated disks are viewed face-on.

[44] Represented by the input parameter n_{pp} which was set equal to 200 during the best-fit process.

Parameter	Value
m_{pl} (earth's masses)	21
$\dot{a}_{pl}$ (au/Myr)	0.7
rotation angle (deg)	-3

Table IV.3: Estimated azimuthal parameters.

By observing the graphs in Figure IV.2 it can be seen that the brighter clump at -3° is very well fitted. Around 180° a second clump due to the 2:1(l) resonance can be seen. The data in this region is quite noisy and therefore difficult to fit. While the planet's mass is close to the first guess, the migration rate is higher than its first guess value. However $\theta = 3.7$ for the average planetesimal which is still very close to the same region of the graph in Figure II.2. A physical explanation is that a higher migration rate allows for a longer migration distance which in turn allows for a larger number of planetesimals to be trapped in resonance and therefore a brighter peak.

4.3.2. Radial fit

A second best fit was done with the aim of estimating the four parameters that determine the radial structure of the disk. Again by using the least squares function, the radial profiles of the simulations and the data were compared. The total number of parameters was reduced from four to two in order to simplify the parameter space. The two migration defining parameters a_{pl1} and a_{pl2} were defined as functions of a_{min} through:

$$a_{pl1} = a_{min}/1.41 \qquad \text{(IV.1)}$$

$$a_{pl2} = a_{pl1} + \dot{a}_{pl} \cdot 10 \qquad \text{(IV.2)}$$

Equation (IV.1) is based on the discussion of section 4.2 where it is explained that this particular choice only selects the pattern due to the 2:1 and 5:3 resonances. Equation (IV.2) sets the final semi-major axis of the planet equal to the initial semi-major axis plus the rate of migration multiplied by 10 Myr, which is a sensible guess on the duration of the migration, bounded by the age of the system of 16 Myr. As before, a new parameter was introduced so that the flux of the simulation would match the one of the original data. The remaining parameters, that determine the azimuthal structure, are taken from the previous section. The resulting best-fit values are reported in Table 4.3.2, while they are shown pictorially in Figure IV.3.

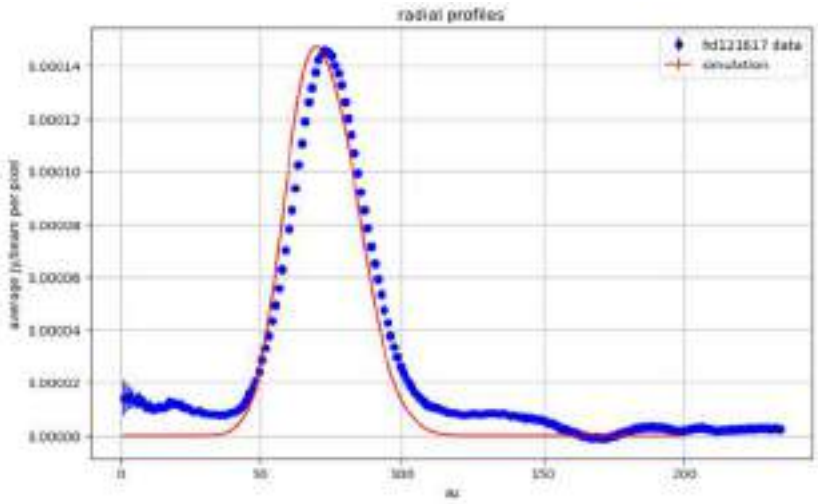

Figure IV.3: The radial profile of the simulation in red and the radial profile of the disk in blue.

Parameter	Value
a_{pl1} (au)	43
a_{pl2} (au)	50
a_{min} (au)	60
a_{max} (au)	85

Table IV.4: Estimated radial parameters.

It can be seen from Figure IV.3 that the simulation reproduces the radial profile of the disk for distances between 25 and 85 au. Outside of this interval the fit is not very close to the data which could be due to the absence of noise in the simulation and to the difficulty of fitting these lower emissions. The azimuthal profile of the resulting simulated system was also plotted in Figure IV.4. This Figure shows that, even if the radial parameters have been changed after the fit, the azimuthal profile is still well fitted.

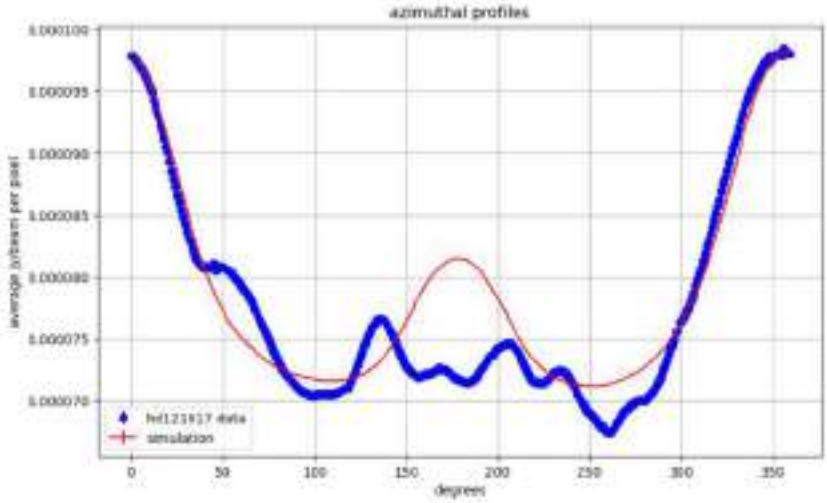

Figure IV.4: The azimuthal profile of the final simulation

V. CONCLUSIONS

In Chapter 2, the theory of gravitational resonance and a numerical model were presented. In Chapter 3, HD 121617's debris disk was analyzed. In Chapter 4, a best fit of the numerical model to the observations was conducted. The result of the simulation and estimation of the parameters is shown in Figure V.1.

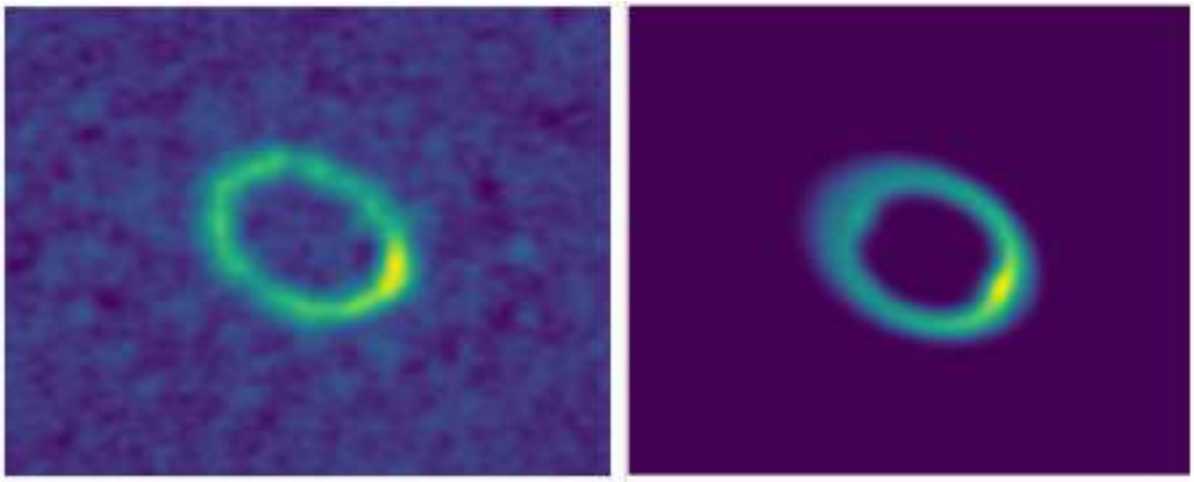

Figure V.1: The image on the left shows the original data. The image on the right is the product of the best fit which was also convolved with the beam size.

Figure V.1 shows that the best-fit parameters generate a simulation which is quite similar to the original disk. Based on the theory of resonance discussed in chapter 2, the migrating planet would be located at around 90° after the clump in an anticlockwise rotation, 50 au from the center of the disk. Figure V.2 shows how the system evolves from the beginning to the end of the migration.

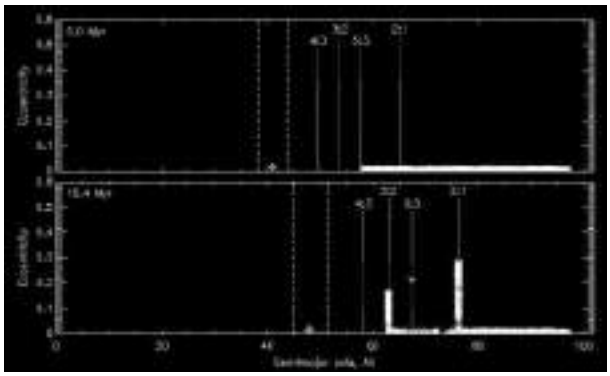

Figure V.2: The beginning of the migration (up) and its end (down).

In Figure V.2 the asterisks represent the planetesimals and the cross represents the planet. The dashed lines around the planet represent the extent of the overlap region. The dotted lines represent the locations of the resonances. The x-axis is the distance from the star, while y-axis is the eccentricity of the orbits. Even though the planet was initialized at 41 au which is

precisely a_{min}/1.41, some planetesimals still ended up in the 3:2 resonance. This is probably due to the length of the migration which was such that the 3:2 resonance location reached the disk.

This paper has showed that the brightest clump found in the HD 121617's debris disk can be explained by a migrating planet. The planet was characterized in mass and location, a result that could be effectively verified with more precise observations.

BIBLIOGRAPHY

M. Cure, A. Kospal, A. Moor, et al., ”Molecular Gas in Debris Disks around Young A-type Stars”, in *The Astrophysical Journal*, 2017.

M. C. Wyatt, ”Resonant trapping of planetesimals by planet migration: debris disk clumps and Vega’s similarity to the solar system”, in *The Astrophysical Journal*, 2003.

D. Murrey, F. Stanley, ”Solar System Dynamics”, *Cambridge University Press*, 1st edition, 2000.

G. Bryden, T. Hidekazu, S. Ida, D. N. C. Lin, ”Orbital Migration of Neptune and Orbital Distribution of Trans-Neptunian Objects”, in *The Astrophysical Journal*, 2000.

Classe di Scienze della Vita

Disentangling the Prognostic Landscape of Chronic Myeloid Leukemia: From Epigenetic Regulators to Inflammatory and Immune Markers

Lidia Trombello

Abstract

Chronic myeloid leukemia (CML) is characterized by the BCR::ABL1 fusion protein, which transforms hematopoietic stem cells into leukemic cells. Monitoring BCR::ABL1 transcript levels by quantitative PCR remains the gold standard for assessing response to tyrosine kinase inhibitors (TKIs). However, a significant proportion of patients show suboptimal response or develop resistance, even in the absence of BCR::ABL1 TKD domain mutations, suggesting the involvement of alternative molecular mechanisms.

In this study, we analyzed 21 patients with chronic-phase CML, evaluating gene expression of BMI1, EZH2, ROCK2, IGFBP6 and PD-L1 by digital droplet PCR (ddPCR) at diagnosis and after 12 months of TKI therapy. Additionally, PD-L1 polymorphisms were genotyped using RT-PCR. A significant positive correlation was observed between ROCK2 and PD-L1 expression ($\rho = 0.74$, $p < 0.001$) at diagnosis, which persisted after one year of treatment. In patients achieving deeper molecular responses, we observed a decrease in EZH2 and BMI1 expression levels, alongside increased ROCK2 and PD-L1 levels. Lower baseline EZH2 expression was associated with prolonged event-free survival.

These findings suggest the existence of a ROCK2–PD-L1 regulatory axis involved in immune evasion and treatment response, similar to mechanisms described in solid tumors. The integration of epigenetic and immunologic biomarkers may open new perspectives for combined therapeutic strategies in CML.

I. CHRONIC MYELOID LEUKEMIA (CML): BACKGROUND AND CLINICAL FRAMEWORK

Chronic Myeloid Leukemia (CML) is a hematologic malignancy characterized by the malignant transformation of a pluripotent hematopoietic stem cell. This transformation leads to excessive clonal proliferation, resulting in the hyperproduction of myeloid cells within the bone marrow. Although the granulocytic line (neutrophils, eosinophils, basophils) is predominantly affected, uncontrolled expansion also involves red blood cells, megakaryocytes (platelets), and monocytes, at varying levels of maturation. Initially, the stem cells retain the ability to mature into normal cells, but over time they lose this capacity, leading to the release of immature cells into the bloodstream (Jabbour & Kantarjian, 2020).

CML is referred to as "chronic" due to the slow progression of the disease, which often remains asymptomatic in its early stages. The disease may present with non-specific symptoms such as fatigue, weight loss, and a sensation of abdominal fullness, which often fail to raise concerns in the patient, explaining why most diagnoses occur during routine checkups. Rarely, bleeding episodes (due to low platelet count), thrombotic events, or gouty arthritis may occur. The most notable manifestation is splenomegaly, which can worsen as the disease progresses and is observed in 20-40% of cases (Jabbour & Kantarjian, 2020).

1.1. Epidemiology and Risk Factors

CML is the most common form of chronic myeloproliferative syndromes, representing 1520% of all leukemia cases. Its incidence is between 1.5-2 new cases per 100,000 individuals annually (Castoldi, 2013). It is more frequent in males, with a male-to-female ratio of approximately 1.7:1. The disease tends to present in the fifth and sixth decades of life, although all age groups, including children, can be affected (Faderl et al., 1999). In Western countries, the median age at diagnosis is 57 years, with 20% of cases occurring in individuals over 70 years old, while less than 5% are diagnosed in children and adolescents. In contrast, the median age of diagnosis is lower in Asia and Africa, reflecting the generally younger populations in these regions (Jabbour & Kantarjian, 2020). In Italy, approximately 1,000 new cases are diagnosed annually. CML is considered a disease of the elderly, with the median age at onset being around 65 years.

Although most cases of CML are acquired, there have been exceptional instances of familial cases, with no clinical, cytogenetic, or molecular alterations observed in the offspring of affected individuals. These findings suggest that CML is not a hereditary disease (Faderl et al., 1999).

CML does not appear to be an inherited disease, with rare familial occurrences. Factors such as older age, male sex, exposure to ionizing radiation or formaldehyde, and immunosuppression have been identified as potential risk factors for the development of CML (Siegel et al., 2024). Notably, the advent of tyrosine kinase inhibitors (TKIs) in the early 2000s has significantly altered the course of the disease, making it a chronic condition with life expectancy comparable to that of the general population (Jabbour & Kantarjian, 2020).

1.2. The Philadelphia Chromosome

The presence of a "minute chromosome" in blood samples from patients with CML was first described by Nowell and Hungerford in the 1960s (Nowell P C, Hungerford D A, 1960). That alteration, which we now refer to as the Philadelphia Chromosome, is currently considered the molecular hallmark of CML. In detail, this chromosomal abnormality consists of a balanced translocation between chromosomes 9 and 22 (t(9;22)(q34;q11.2)) that results in the fusion of the Abelson tyrosine-protein kinase 1 (*ABL1*) gene and breakpoint cluster region (*BCR*) gene. The product is the *BCR::ABL1* chimeric gene, which encodes for a constitutively active tyrosine-kinase (J. Cortes et al., 2021). The Philadelphia Chromosome is identified in more than 80% of patients with CML (Longmore et al. 2014), but also in 15% of children and 15- 30% of adults with Acute Lymphoblastic Leukemia (ALL), and in approximately 2% of patients with Acute Myeloblastic Leukemia (AML) (Faderl et al., 1999). As shown in **Fig. 1**, according to the localisation of the breakpoints on chromosome 9 and 22 several different transcript types of the *BCR::ABL1* gene can be generated. The breakpoint in chromosome 9, where the *ABL1* gene is located, is relatively constant between exons 1 and 2, whereas the breakpoint in chromosome 22 can vary more in location (J. Cortes et al., 2021). In most patients the breakpoints on chromosome 22 are located in the major break point cluster region (M-BCR), between intron 13 or 14, and produce two different protein products of the same molecular weight (210 kDa), known as e13a2 (previously b2a2) and e14a2 (previously b3a2) (J. Cortes et al., 2021). The

e14a2 transcript is found in approximately two thirds of patients with CML and seems to be associated with a better probability to achieve a deep molecular response and longer survival (P. Jain et al., 2016). 5 to 10% of patients with CML co-express both the e13a2 and e14a2 transcripts (J. Cortes et al., 2021), whereas other less common variants can be observed in the remaining portion of patients. These rarer gene products include a BCR::ABL1 protein of 190 kDa that is generated when the breakpoint is located proximal to exon 2 (e1a2), in the minor break point cluster region (m-BCR), and it is observed more commonly in Philadelphia-positive ALL patients (J. Cortes et al., 2021). Other possibilities include the e19a2 transcript, which corresponds to a BCR::ABL1 protein of 230 kDa, is called Chronic Neutrophilic Leukemia, and is associated with enhanced neutrophil differentiation , and the absence of a detectable translocation, which is associated with a poorer prognosis (Longmore M. et al., 2014). Lastly, in some patients the Philadelphia Chromosome there is evidence of a so called "masked" translocation, which by definition is detectable only by molecular -and not cytogenetic- techniques (Longmore M. et al., 2014). From a structural point of view, as shown in **Fig. 2**, the N-terminal segment of the ABL1 protein includes two SRC homology domains (SH2 and SH3), the catalytic domain, and a myristoylation sequence, whereas the C-terminal portion includes a DNA-binding domain, nuclear localisation signals and an actin-binding site (Faderl et al., 1999). The addition of the BCR segment interferes with the regulatory function of the SH3 domain of ABL1, which results in constitutive activation of the kinase portion of ABL1. This activation, in turn, increases dimerization, tetramerization, and autophosphorylation, thus enhancing binding of the SH2 domains of other proteins (Pendergast et al., 1991, 1993). In fact, several BCR domains are recognised by adapter proteins such as growth factor receptor–bound protein 2 (GRB2), which links BCR::ABL1 to RAS, CRK-oncogene–like protein (CRKL), casitas Blineage lymphoma protein (CBL), and SRC homology 2–containing protein (SHC) (Faderl et al., 1999).

Lastly, besides the Philadelphia Chromosome, additional chromosomal abnormalities and genetic mutations can be found in patients with CML (J. Cortes et al., 2021). These alterations have been observed more frequently in patients transitioning from chronic to blast phase CML and will thus be discussed in more detail in later sections.

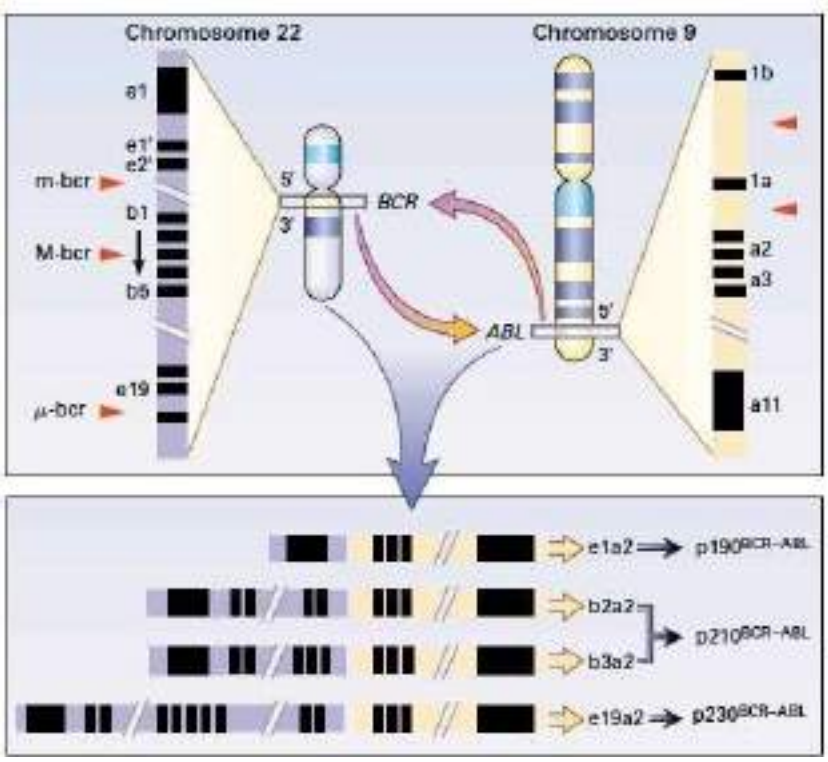

Figure 1: **The Translocation of t(9;22)(q34;q11) in CML**. Breakpoints (arrowheads) on the ABL1 gene are located 5' (toward the centromere) of exon a2 in most cases. Various breakpoint locations have been identified along the BCR gene on chromosome 22. Depending on which breakpoints are involved, different-sized segments from BCR are fused with the 3' sequences of the ABL1 gene. This results in fusion messenger RNA molecules (e1a2, b2a2, b3a2, and e19a2) of different lengths that are transcribed into chimeric protein products (p190, p210, and p230) with variable molecular weights and presumably variable function. The abbreviation mbcr denotes minor breakpoint cluster region and M-BCR major breakpoint cluster region. Figure adapted from Faderl et al.

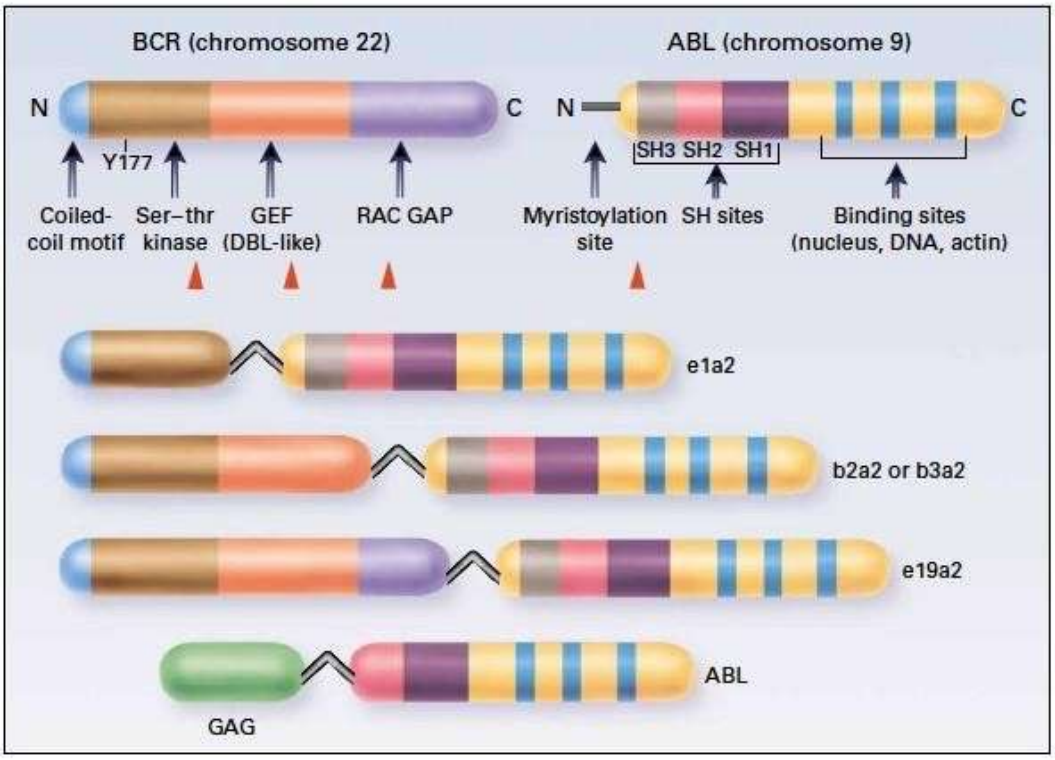

Figure 2: **Functional Domains of BCR, ABL1, and BCR::ABL1.** Important functional domains of the BCR and ABL1 gene products are shown. Breakpoints are indicated by arrowheads. N denotes N-terminal amino acid sequence, C C-terminal amino acid sequence, Ser–thr serine–threonine, GDP guanosine diphosphate, GTP guanosine triphosphate, GEF GDP–GTP exchange factor, DBL diffuse B-cell lymphoma oncogene, RAC a RAS-like GTPase, GAP guanosine triphosphatase–activating function, and SH SRC homology domain. Figure adapted from Faderl et al.

1.3. Pathways and Cellular Biology

The acquisition of the *BCR::ABL1* fusion gene is thought to occur in a single hematopoietic stem cell (HSC), known as the leukemia stem cell (LSC) (Bavaro et al., 2019). Through the activation of a variety of intracellular signalling cascades, which are summarised in **Fig. 3**, this molecular event induces changes in proliferation, perturbations of the balance between self-renewal and differentiation, and suppression of apoptosis. Ultimately, these cellular events lead to the clinical and laboratory features observed in CML patients, including the expansion of myeloid progenitors in various stages of maturation, a premature release in the peripheral blood, and homing to extramedullary locations (Faderl et al., 1999). Multiple molecular mechanisms

are responsible for changes in these essential cellular processes, with many preclinical studies now suggesting that the key, and potentially targetable, signalling cascades altered in CML are the Mitogen-activated Protein Kinase (MAPK), Janus Kinase (JAK)/ Signal Transducer and Activator of Transcription (STAT), Phosphoinositide 3-kinases (PI3K)/AKT, and Hedgehog pathways, and the C-X-C chemokine receptor type 4 (CXCR4)/ Stromal Cell-Derived Factor 1 (SDF1) axis (Cilloni & Saglio, 2012).

As stated, a pivotal role in the activation of these downstream signalling cascades is played by the tyrosine-phosphorylated site located in the BCR region that binds the SH2 domain of the adaptor protein GRB2 (Pendergast et al., 1991). In fact, this complex recruits the Son of Sevenless (SOS) protein (Cortez et al., 1997), which in turn stimulates the conversion of RAS GDP (inactive) to RAS-GTP (active form) (Ren, 2005) and the activation of GRB2-associated binding protein 2 (GAB2) (Sattler et al., 2002). The GRB2/GAB2/SOS complex then triggers the activation of RAS, hence resulting in abnormal proliferation, and of the PI3K/AKT pathways (Skorski et al., 1995), which promotes survival by suppressing FOXO (Cilloni & Saglio, 2012). It is worth pointing out, though, that the BCR::ABL1 might regulate the PI3K/AKT pathway through more than one mechanism, as also Crk and Crkl have been shown to connect the chimeric oncoprotein to PI3K (S. K. Jain et al., 1996). Additionally, the constitutive activation of the key transcription factors STAT1 and STAT5 was observed in both BCR::ABL1-positive cell lines and in primary cells from CML patients (Carlesso et al., 1996; Ilaria & Van Etten, 1996). However, instead of the usual activation mediated by the receptor-associated JAK kinases, these transcription factors are induced via direct association of the SH2 domain on STAT with the phosphorylated tyrosines on BCR::ABL1 (Carlesso et al., 1996). The activation of STAT5 in these models was shown to upregulate BCLxL and downregulate Bad, hence contributing to the suppression of apoptosis (Carlesso et al., 1996).

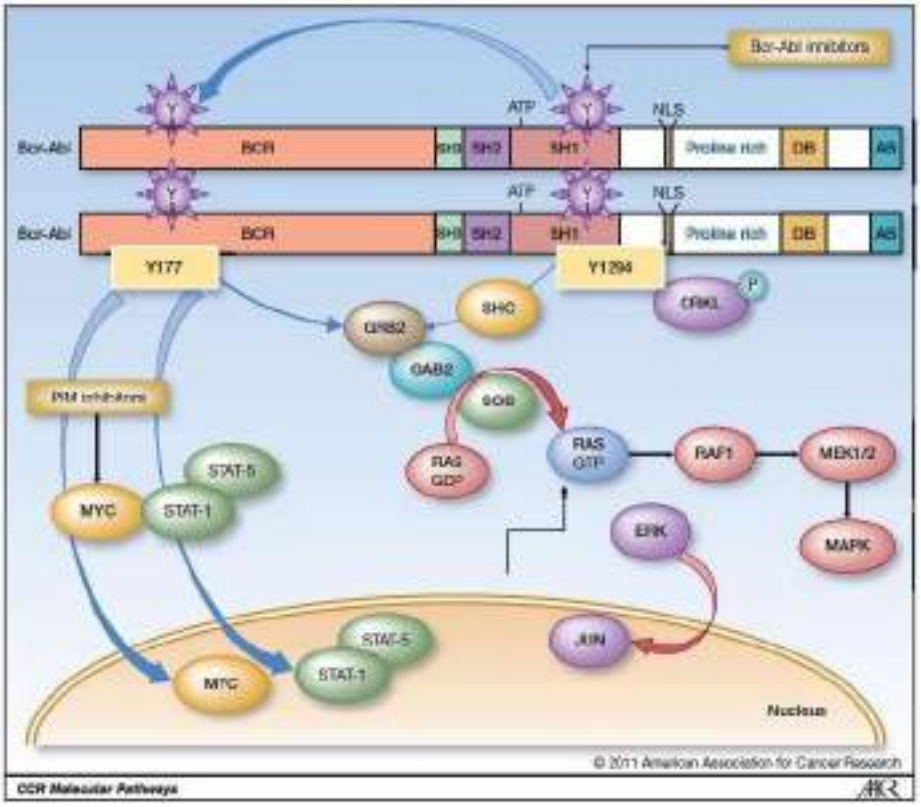

Figure 3: **Schematic representation of the molecular pathway activated by BCR::ABL1**. The BCR::ABL1/GRB2 complex recruits SOS, which is associates with the GRB2 SH3 domain. The BCR::ABL1/GRB2/SOS complex stimulates conversion of the inactive GDP-bound form of Ras to its active GTP-bound state, and activation of the scaffold adapter GAB2. The GRB2/GAB2/SOS complex causes constitutive activation of the RAS downstream Pathway, thereby activating the MAPK proteins and resulting in abnormal cell proliferation. In addition, this complex activates the PI3K/AKT pathway. Figure adapted from Cilloni and Saglio

1.4. Clinical Presentation of Chronic Myeloid Leukemia

Chronic Myeloid Leukemia (CML) is a clonal myeloproliferative neoplasm that arises from the neoplastic transformation of a pluripotent hematopoietic stem cell. This transformation leads to uncontrolled proliferation and accumulation of mature and immature myeloid cells, including promyelocytes, myelocytes, metamyelocytes, and occasionally megakaryocytes, culminating in massive infiltration of the bone marrow (Apperley, 2015). Peripheral blood findings typically include leukocytosis, thrombocytosis, basophilia, and eosinophilia. The

differential count of leukocytes, the percentage of circulating blasts, and spleen size hold diagnostic and prognostic relevance (Castoldi & Liso, 2013).

Clinically, CML is often insidious in onset. Approximately 30–40% of patients are asymptomatic at diagnosis, which is frequently incidental, discovered during routine blood counts showing unexplained neutrophilic leukocytosis, sometimes accompanied by anemia and thrombocytosis (Sawyers, 1999; Castoldi & Liso, 2013). When symptoms are present, they are usually non-specific and reflect systemic hypermetabolism or the effects of splenomegaly due to myeloid cell infiltration. These may include fatigue, malaise, weight loss, anorexia, low-grade fever, night sweats, and early satiety or discomfort in the left upper quadrant due to splenic enlargement (Apperley, 2015).

Splenomegaly is a hallmark finding, present in over 50% of cases at diagnosis. In marked cases, it may cause abdominal pain, early satiety, or signs of splenic infarction and perisplenitis due to organ compression (Apperley, 2015). Laboratory findings may reveal hyperuricemia, which can result in gout-like symptoms (Apperley, 2015).

Extreme leukocytosis (>300,000–400,000/mm³) can lead to hyperviscosity syndrome with neurological (paresthesias, dizziness, visual disturbances), pulmonary (dyspnea, cyanosis), ocular (papilledema, diplopia), and vascular manifestations such as priapism due to sluggish circulation in penile vessels (Castoldi & Liso, 2013).

Traditionally, CML has been described as a triphasic disease:

- The Chronic Phase (CP), which is the initial and most commonly diagnosed stage, is characterized by <10% blasts in the bone marrow and peripheral blood, with preserved myeloid maturation. Most patients in this phase respond well to treatment with Tyrosine Kinase Inhibitors (TKIs), which have significantly improved the prognosis and altered the disease's natural course (Apperley, 2015).
- The Accelerated Phase (AP) represents a transitional state, associated with progressive resistance to therapy and acquisition of additional chromosomal abnormalities by the malignant clone. Clinical features often include worsening anemia, thrombocytopenia, low-grade fever, and general deterioration. According to the European LeukemiaNet (ELN), AP is defined by one or more of the following: 15–29% blasts in blood or bone marrow; ≥20% basophils in peripheral blood; persistent thrombocytopenia (<100 x

10^9/L) despite treatment; or appearance of new cytogenetic abnormalities in the Phpositive clone (Baccarani et al., 2013).

- The Blast Crisis (BC) mimics an acute leukemia and occurs when blasts exceed 30% in the bone marrow or peripheral blood, or there is evidence of extramedullary blast proliferation (excluding spleen). This final phase can present as myeloid (≈50%), lymphoid (≈25%), or biphenotypic/undifferentiated (25%) leukemia, highlighting the disease's stem cell origin (Apperley, 2015). Clinically, BC is associated with severe anemia, thrombocytopenia, increased susceptibility to infections, bleeding, and constitutional symptoms. The prognosis is poor, with a median survival of about six months. Reversion to chronic phase can occur in 10–30% of cases, especially in lymphoid blast crises, but is generally transient and treatment-refractory (Castoldi & Liso, 2013).

The development and widespread use of TKIs, such as imatinib and its successors, have significantly reduced progression to AP and BC, leading to near-normal life expectancy in many patients diagnosed in CP. Nevertheless, timely recognition of symptomatic evolution or hematological progression remains critical for early intervention and effective disease management.

1.5. Diagnosis and Disease Staging

The complete blood count (CBC) plays a pivotal role in the diagnosis of chronic myeloid leukemia (CML), as it is often the first routine examination that raises suspicion of a myeloproliferative disorder and prompts further specific investigations. A hallmark of CML is marked leukocytosis, which can exceed 300 × 10^9/L, sometimes leading to leukostasis that may necessitate emergent leukapheresis. Red blood cell and platelet counts vary depending on the disease phase. While mild erythrocytosis may be seen in the early stages, normocytic normochromic anemia is almost invariably present in advanced stages. Thrombocytosis is frequently observed at presentation, with platelet counts often reaching 500,000/μL and, in approximately 30% of cases, as high as 1,000,000/μL. However, thrombocytopenia tends to appear in the advanced phases due to extensive bone marrow infiltration by the leukemic clone (Ahmed et al., 2009).

The differential white blood cell count typically shows an increase in neutrophils, basophils, and eosinophils, along with the presence of immature myeloid precursors. Morphological examination of a peripheral blood smear stained with May-Grünwald-Giemsa reveals a predominance of more mature granulocyte precursors—such as myelocytes, metamyelocytes, and band forms—during the chronic phase, whereas earlier precursors like myeloblasts and promyelocytes become more evident as the disease progresses.

The high cellular turnover characteristic of CML results in elevated serum levels of uric acid, lactate dehydrogenase (LDH), histamine, and vitamin B12. These markers correlate with the leukocyte burden. The rise in vitamin B12 and its binding proteins (both the physiologic transporter transcobalamin II and the storage protein transcobalamin I) reflects granulocyte proliferation, while increased histamine levels are primarily associated with basophilia.

Bone marrow aspiration (BMA) reveals marked hypercellularity and granulocytic hyperplasia due to clonal proliferation. Early stages may also exhibit megakaryocytic hyperplasia, whereas erythroid lineage hyperplasia is rare. Bone marrow biopsy (BMB) allows for the assessment of marrow architecture and typically demonstrates granulocytic predominance with a reduction of adipose tissue and erythroid elements. The reticulin network is usually normal or only mildly increased in the early phases but becomes more fibrotic in the later stages, resembling primary myelofibrosis.

CML should be suspected in cases of unexplained splenomegaly, unintentional weight loss, and fatigue; however, many patients are asymptomatic at diagnosis, and the disease is often discovered incidentally through routine blood tests revealing leukocytosis. The diagnostic approach involves four levels of assessment:

1. Clinical history and physical examination, including palpation of the spleen to determine its size and distance from the costal margin.
2. Laboratory testing, including CBC with differential and biochemical markers such as LDH and uric acid.
3. Bone marrow analysis (aspiration and biopsy), assessing cellular composition, blast percentage, and fibrosis.
4. Cytogenetic and molecular testing, crucial for confirming the diagnosis.

Peripheral blood smears typically demonstrate marked leukocytosis with the so-called “left shift” and increased eosinophils and basophils. Myeloblasts and promyelocytes are rare in

chronic phase (CP) but increase in accelerated (AP) and blast phases (BP). Bone marrow evaluation is critical to quantify blasts and detect fibrosis, which has prognostic implications.

Conventional cytogenetics confirms the presence of the Philadelphia chromosome (Ph) in ≥20 metaphases from marrow cells and can reveal additional chromosomal abnormalities (ACAs), which may indicate clonal evolution. In cases where the t(9;22) translocation is cryptic or the transcript is atypical, fluorescence in situ hybridization (FISH) with specific fluorochromelabeled DNA probes is employed.

The definitive diagnosis rests on the molecular detection of the BCR::ABL1 fusion transcript via reverse transcriptase PCR (RT-PCR), which may be qualitative (at diagnosis) or quantitative (for treatment monitoring).

Special cases include:

- Ph-negative, BCR::ABL1-positive CML, where patients show typical clinical features but lack cytogenetic evidence of Ph; diagnosis requires PCR or FISH. Prognosis and therapeutic response are similar to Ph-positive cases.
- Ph-negative, BCR::ABL1-negative (atypical CML), a distinct entity lacking both Ph chromosome and BCR::ABL1 transcript. These patients usually do not exhibit basophilia and have poor response to tyrosine kinase inhibitors (TKIs), with a median survival of 2–3 years. Accurate differential diagnosis using cytogenetics, PCR, and FISH is therefore critical.

Differential diagnoses include leukemoid reactions (typically symptomatic, with WBC count <50,000/μL and without basophilia or circulating precursors), other chronic myeloproliferative neoplasms (particularly primary myelofibrosis and post-polycythemia vera or post-essential thrombocythemia myelofibrosis), and myelodysplastic syndromes. The absence of BCR::ABL1 and the presence of JAK2, CALR, or MPL mutations may support alternative diagnoses, though rare cases may present with concurrent mutations.

According to the 2022 International Consensus Classification of Myeloid Neoplasms and Acute Leukemias, the criteria for accelerated phase (AP) include any of the following: 10–19% blasts in peripheral blood or bone marrow, ≥20% basophils in peripheral blood, or the presence of ACAs in Ph+ cells. Blast crisis (BC) is defined by ≥20% blasts in blood or marrow (≥30% according to the ELN) or extramedullary blast proliferation.

1.6. Risk Stratification

Following the advent of TKI therapy, prognostic scoring systems have gained importance to guide clinical management. The most widely used in chronic phase is the Sokal score, which stratifies patients into low-, intermediate-, and high-risk groups based on age, spleen size, platelet count, and peripheral blood basophil and blast percentages at diagnosis. This score correlates with both treatment response and progression risk (Giuliani et al., 2020).

Over time, additional risk models have been introduced. The Hasford/EURO score, initially developed to predict overall survival in patients treated with interferon-α, uses similar variables and maintains the three-tiered risk classification (Giuliani et al., 2020). The EUTOS score, in contrast, is simpler and includes only spleen size and basophil percentage, classifying patients into high- or low-risk groups (Giuliani et al., 2020). The most recent and refined model, the EUTOS Long-Term Survival (ELTS) score, was developed to predict disease-specific mortality, distinguishing between CML-related and unrelated deaths. It incorporates age, spleen size, peripheral blood blasts, and platelet count, and again stratifies patients into low-, intermediate-, and high-risk categories (Giuliani et al., 2020).

1.7. Emerging Prognostic Factors: Epigenetic, Inflammatory, and Immune Markers

Despite the clinical success of tyrosine kinase inhibitors (TKIs) in treating chronic myeloid leukemia (CML), a subset of patients experiences resistance or suboptimal responses. While mutations in the BCR::ABL1 kinase domain explain some resistance mechanisms, other molecular alterations are emerging as relevant contributors to disease persistence and progression. Recent studies have highlighted the involvement of epigenetic regulators, inflammatory mediators, and immune checkpoint molecules as potential prognostic markers and therapeutic targets in CML.

1.7.1. Epigenetic Regulators: EZH2 and BMI1

Polycomb group (PcG) proteins are fundamental epigenetic regulators in the organism, capable of modifying chromatin structure and consequently DNA accessibility through epigenetic modifications. An abnormality in PcG function leads to cellular transformation and malignant growth. These proteins can be overexpressed or aberrantly expressed, resulting in

uncontrolled proliferation and resistance to apoptosis, typical features of tumor cells (Wang et al., 2015).

Numerous PcG proteins, belonging to the PRC1 and PRC2 complexes, are involved in cancer development and progression, among which the most studied are BMI1 and EZH2.

1.7.1.1. EZH2

EZH2 is the catalytic core subunit of the PRC2 complex and consists of five main domains: EED Interaction Domain (EID), Domain I (whose role is still not well understood), Domain II (which interacts with SUZ12), a cysteine-rich domain (CXC), and the SET domain (Enhancer Domain of Zest and Trithorax), responsible for methyltransferase activity (Liu & Yang, 2023). EZH2 regulates vital processes such as cell differentiation, cell cycle, apoptosis, and DNA repair. Its abnormal expression is associated with various neoplasms due to increased cell proliferation (Duan et al., 2020).

In tissues with high proliferative activity, such as hematopoietic tissues, EZH2 regulates the balance between self-renewal of hematopoietic stem cells (HSCs) and their differentiation, protecting HSCs from cell death by repressing pro-apoptotic genes (p21, WIG1, NOXA) (Herviou et al., 2015).

EZH2 dysregulation manifests in several ways:

- Overexpression, which increases H3K27me3 levels and silences tumor suppressor genes.
- Mutations in the SET domain (Y641, A677G, A687V) that enhance methyltransferase activity, observed in follicular lymphomas and DLBCL.
- Interaction with lncRNAs that enhances its repressive activity.
- Inactivating mutations or deletions that reduce H3K27me3 and activate target genes (Völkel et al., 2015).

EZH2 overexpression is more common in solid tumors (prostate, breast, esophagus, stomach), whereas EZH2 mutations are frequent in hematological malignancies, suggesting a dual role of EZH2 as both an oncogene and tumor suppressor (Rinke et al., 2020).

In murine models, EZH2 overexpression in hematopoietic stem cells is associated with myeloproliferative neoplasms (MPN). In chronic myeloid leukemia (CML), EZH2 mutations are rare, whereas its overexpression in leukemic stem cells (LSCs) contributes to treatment resistance and disease persistence (Xie et al., 2016). EZH2 transcription is mediated by BCRABL1 STAT5 signaling, with STAT5A binding to the EZH2 promoter, increasing its expression in leukemic cells (Nishioka et al., 2016).

1.7.1.2. BMI1

The BMI1 protein (PCGF4), a component of canonical PRC1, mediates monoubiquitination of histone H2A (H2A119Ub), promoting chromatin compaction and gene repression. BMI1 is structured with two nuclear localization signals (NLS1, NLS2) and three main domains: an Nterminal RING domain, a central domain (UBL or RAWUL), and a PEST domain, which regulates protein stability and turnover (Sahasrabuddhe, 2016).

Its control occurs at the transcriptional level (activators: Sp1, Twist1, FoxM1, Myc; repressors: Mel18, Nanog) and post-transcriptionally, mainly via microRNAs that regulate its expression (Sahasrabuddhe, 2016).

BMI1 regulates fundamental processes such as cell growth and differentiation, embryonic development, DNA repair, apoptosis, and stem cell self-renewal (Bhattacharya et al., 2015). Considered a proto-oncogene, BMI1 promotes cell proliferation by repressing the Ink4a/Arf locus, which encodes the tumor suppressors p16Ink4a and p14Arf/p19Arf involved in cell cycle arrest and apoptosis induction (Wagner & Wagner, 2022).

BMI1 overexpression is frequent in solid carcinomas, leukemias, and lymphomas, promoting uncontrolled proliferation and resistance to apoptosis (Liu et al., 2006). In patients with acute myeloid leukemia (AML) and CML, BMI1 levels are significantly increased compared to healthy donors (Mohty et al., 2007; Saudy et al., 2014).

In CML, BMI1 represents a key biomarker for leukemic transformation of CD34+ cells through collaboration with BCR-ABL1, protecting tumor cells from apoptosis and promoting their self-renewal (Rizo et al., 2009). Increased BMI1 expression has been linked to Imatinib resistance, suggesting alternative epigenetic therapeutic approaches (Crea et al., 2015).

Moreover, co-expression of BMI1 and CD26 in leukemic stem cells suggests possible resistance to TKIs and enhanced quiescence capacity, with implications for disease relapse (Galimberti et al., 2018).

1.7.2. Inflammatory Genes: ROCK2 and IGFBP6

1.7.2.1. ROCK2

Rho-associated coiled-coil containing kinases (ROCKs) are major effectors of the small GTPase RhoA and belong to the AGC family of serine/threonine kinases, which also includes protein kinases A, G, and C (PKA, PKG, PKC) (Matsui et al., 1996). The ROCK family consists of two main isoforms, ROCK1 and ROCK2, which share 65% overall homology and 92% conservation within the kinase domain. The structure of these proteins includes an Nterminal serine/threonine kinase domain, followed by a central coiled-coil region containing the Rho-binding domain (RBD), and finally a C-terminal Pleckstrin Homology (PH) domain associated with a cysteine-rich (CR) sequence. The kinase domain is about 300 amino acids long, while the RBD, approximately 80 amino acids, interacts with active Rho GTPases such as RhoA, RhoB, and RhoC. The PH domain has binding sites for specific lipid mediators, such as arachidonic acid (AA) and sphingosylphosphorylcholine (SPC). In its inactive form, ROCK exhibits autoinhibitory activity due to interactions between the C-terminal PH domain and the RBD with the kinase domain, forming an inhibitory loop that blocks enzymatic activity. ROCK activation can occur via RBD binding to Rho GTPases, PH domain interaction with lipid mediators, or autophosphorylation induced by dimerization (Julian & Olson, 2014).

ROCK activation regulates fundamental cellular processes such as contractility, permeability, migration, proliferation, and apoptosis. Recent studies have highlighted the key role of ROCK2 in the inflammatory response, essential for T cell functions including movement and proliferation (Zanin-Zhorov & Blazar, 2021). In particular, ROCK2 is crucial for the acquisition of the effector phenotype in Th17 cells, maintaining the balance with regulatory T cells (Tregs). During Th17 polarization, ROCK2 phosphorylates IRF4 (Interferon Regulatory Factor 4), a transcription factor essential for the production of proinflammatory cytokines IL17 and IL-21 (Biswas et al., 2010). Furthermore, ROCK2 regulates the formation of the ROCK2/STAT3

(Signal Transducer and Activator of Transcription 3)/JAK2 (Janus Kinase 2) complex, necessary for optimal STAT3 activation and transcription of Th17-specific genes (Chen, 2018)

In non-hematopoietic cells, ROCK proteins participate in TGF-β signaling, a critical mediator in the balance between proinflammatory Th17 and immunosuppressive Treg cells (Edlund et al., 2002; Bettelli et al., 2006). Selective pharmacological inhibition of ROCK2 increases STAT5 phosphorylation, boosting the percentage of Tregs and IL-10 production, while reducing Th17 and T follicular helper (Tfh) cells (Zanin-Zhorov et al., 2014; Weiss et al., 2016). These immunomodulatory effects, observed in cell cultures, animal models, and patients, indicate that ROCK2 inhibition can improve symptoms in autoimmune diseases. For example, in patients with psoriasis vulgaris, ROCK2 inhibition reduced the Th17-dependent autoimmune response while increasing IL-10 and Treg cells (Zanin-Zhorov et al., 2017). ROCK2 is overexpressed in several autoimmune diseases such as rheumatoid arthritis (He et al., 2008), systemic lupus erythematosus (PubMed, 2013), multiple sclerosis (Zhang et al., 2011), and type 1 diabetes (PubMed, 2011). Although the role of ROCK2 in immunity is well established, its involvement in the inflammatory cascade in CAR-T therapy patients is not yet defined and requires further study (Zanin-Zhorov & Blazar, 2021).

1.7.2.2. IGFBP6

Insulin-like Growth Factor Binding Protein 6 (IGFBP6), a member of the IGFBP family, regulates the activity of IGFs. IGFBP6 is a glycoprotein of about 216 amino acids with three main domains: a conserved N-terminal domain, a less conserved central domain, and a cysteine-rich C-terminal domain that provides structural stability. Its three-dimensional structure, stabilized by disulfide bridges, allows a high binding affinity for IGF-II, approximately 50 times greater than that for IGF-I (Mohan & Baylink, 1990).

IGFBP6 modulates the biological activity of IGF-II by acting as a competitive inhibitor for binding to the IGF1R receptor, regulating cell proliferation, survival, and migration. Recent studies have highlighted IGFBP6's role in inflammatory processes: it modulates the inflammatory microenvironment through both IGF-II-dependent and -independent mechanisms. IGFBP6 influences recruitment and activation of immune cells such as macrophages and T lymphocytes, but not B lymphocytes. Moreover, it stimulates neutrophil

activation, promoting maximal release of reactive oxygen species (ROS) and degranulation of primary granules containing myeloperoxidase (MPO) (Conese, 2018).

A recent study showed that hyperthermia (39 °C) induces timely production of IGFBP6 by dendritic cells (DCs) (Liso, 2017). In autoimmune diseases such as rheumatoid arthritis, IGFBP6 modulates T cell proliferation and activation, with direct effects on the inflamed joint microenvironment (Alunno, 2017). Overexpression of IGFBP6 RNA has been observed in eosinophils of patients with allergic asthma, suggesting a role in the Th2 response (Venuto, 2023).

Despite these findings, the precise role of IGFBP6 in inflammation modulation is not yet fully clarified, and it remains to be determined whether its effects are a direct consequence of binding IGF-II or involve other molecules and receptors.

1.7.3. Immune Checkpoint Molecule: PD-L1

The immune system plays a crucial role in controlling leukemic stem cells (LSCs), particularly CD26+ LSCs in CML. One of the main immune evasion strategies employed by tumor cells is mediated by the PD-1/PD-L1 pathway, which acts as an adaptive mechanism to resist immune response (Butte et al., 2008). It has been shown that leukemic cells express the PD-L1 antigen, although specific information about CD26+ LSCs in CML is still limited (Sehgal et al., 2015; Christiansson et al., 2013; Mumprecht et al., 2009).

The expression and stabilization of PD-L1 on the cell surface can be regulated by complex molecular mechanisms. Recently, it has been demonstrated that moesin phosphorylation, mediated by Rho-associated protein kinase (ROCK), is required for PD-L1 stabilization in tumor cells, such as in breast cancer (Meng et al., 2020). This suggests that similar processes might influence the amount of PD-L1 expressed by LSCs in CML, thereby modulating their ability to evade immune control.

The level of PD-L1 expression on CD26+ LSCs could significantly affect the effectiveness of immune control exerted by the patient. In turn, PD-L1 expression can be conditioned by genetic polymorphisms that regulate the amount of protein expressed and thus the capacity of leukemic cells to escape immune attack (Wu et al., 2018).

In summary, the PD-1/PD-L1 signaling pathway constitutes a key mechanism by which leukemic cells evade immune control, and post-translational regulation of PD-L1, such as moesin phosphorylation, represents an important level of control of this evasion.

These emerging molecular markers not only deepen our understanding of CML pathogenesis but may also hold clinical value as prognostic indicators or therapeutic targets. Their relevance in treatment response and immune evasion mechanisms forms the basis for the experimental work presented in the following chapters.

II. RATIONALE AND OBJECTIVES

Chronic myeloid leukemia (CML) treatment has dramatically improved with the advent of tyrosine kinase inhibitors (TKIs), yet a notable proportion of patients exhibit resistance or suboptimal responses. While mutations in the BCR::ABL1 kinase domain account for some cases of resistance, many patients lack such mutations, indicating that other molecular mechanisms contribute to disease persistence and progression. Emerging evidence highlights the role of epigenetic regulators (such as BMI1 and EZH2), inflammatory mediators (ROCK2 and IGFBP6), and immune checkpoints (including PD-L1) in influencing CML biology, treatment response, and immune evasion.

The rationale of this thesis is to explore the interplay between these molecular pathways in CML, aiming to identify novel biomarkers of treatment response and potential therapeutic targets. Specifically, the study focuses on quantifying the expression of epigenetic and inflammatory genes and investigating the correlation with immune checkpoint regulation, in order to understand mechanisms underlying TKI resistance and disease progression.

The objectives are:

1. To analyze the expression patterns of BMI1, EZH2, ROCK2, IGFBP6 and PD-L1 in CML patients at diagnosis and during TKI therapy.
2. To evaluate the relationship between PD-L1 polymorphisms and gene expression levels.
3. To assess the potential regulatory axis between ROCK2 and PD-L1 and its implications for immune evasion.
4. To contribute to the identification of integrative biomarkers that may inform combinatorial therapeutic strategies.

III. MATERIALS AND METHODS

3.1. Patient Cohort

Patients included in this study were enrolled as part of the cohort of the project supported by the Tuscany Region (2018–2024), entitled *"The achievable cure in Chronic Myeloid Leukemia: unravelling CD26+ leukemia stem cell features to enable safe tyrosine kinase inhibitor discontinuation"* (acronym: stemCMLcure).

Enrollment was conducted between 2019 and 2023 according to the following inclusion criteria: age between 18 and 80 years, diagnosis of chronic phase chronic myeloid leukemia (CML), and frontline treatment with tyrosine kinase inhibitors (TKIs). All patients were followed at the Hematology Unit of the University of Pisa and were enrolled after reading and signing a written informed consent form allowing the use of biologic samples collected for diagnostic purposes in future non-profit scientific research.

Peripheral blood samples for gene expression analysis were collected at four timepoints: at diagnosis, and at 3, 6, and 12 months after the initiation of treatment. A total of 10 mL of blood was drawn into four 2.5 mL EDTA tubes at each timepoint.

Patients were stratified based on their molecular response to TKI therapy into three categories, in accordance with the 2020 European Leukemia Network (ELN) recommendations:

1. Optimal responders, i.e., patients achieving a deep and stable molecular response to ongoing therapy;
2. Warning, indicating a suboptimal response that may require closer monitoring or therapeutic adjustments;
3. Failure, referring to patients with insufficient or lost response requiring treatment change.

3.2. Isolation of Leukocytes from Buffy Coat

The peripheral blood (PB) sample is collected in four tubes containing the anticoagulant ethylenediaminetetraacetic acid (EDTA). The tubes are then centrifuged, and at the end of this

step, the whole blood is visibly separated into three distinct layers (**Fig. 4**): a yellow fluid layer at the top (plasma), a red layer at the bottom (erythrocytes), and a whitish intermediate layer ("ring-like"), known as the Buffy Coat. The Buffy Coat is a by-product obtained from the centrifugation of uncoagulated whole blood and consists of a thin layer of leukocytes and platelets. While plasma and red blood cells account for the majority of blood volume, the Buffy Coat comprises less than 1% of the total volume.

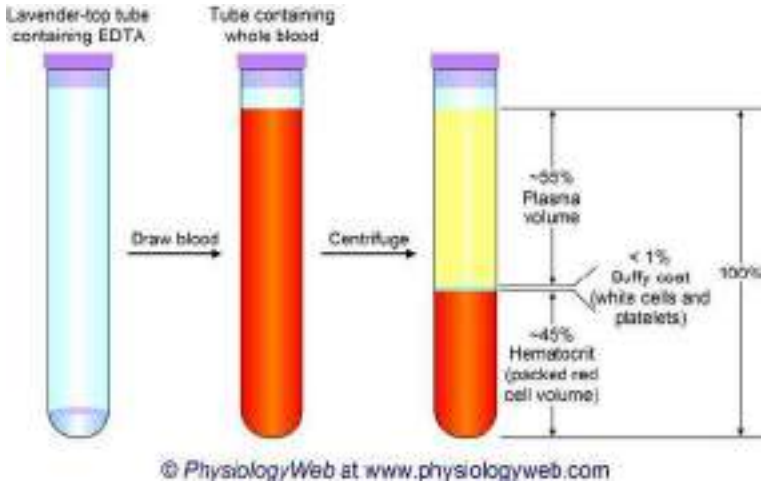

Figure 4 Components of blood after centrifugation (urly.it/311d05)

To isolate the Buffy Coat, proceed as follows:

- Centrifuge the EDTA whole blood tubes at 1500 × g for 15 minutes.
- Using a Pasteur pipette and circular movements, aspirate the Buffy Coat ring from each tube and transfer the entire volume into a single 50 ml Falcon tube.

Since the aspiration of the Buffy Coat inevitably carries with it a small portion of the underlying red blood cells, red blood cell lysis steps are required. This allows for the obtainment of a cleaner cell pellet.

Once the Buffy Coat has been aspirated and transferred to the 50 ml Falcon tube, proceed as described below:

- Add Erythrocyte Lysis Solution to the Falcon tube in a volume equal to twice the volume of the collected Buffy Coat, in order to degrade the red blood cell membranes.

- Seal the Falcon tube tightly and invert it 3–4 times.
- Incubate at room temperature for 10–15 minutes.
- Centrifuge at 200 × g for 10 minutes and discard the supernatant.
- Add an additional 10 mL of Erythrocyte Lysis Solution.
- Centrifuge at 200 × g for 10 minutes and discard the supernatant.
- Add 5 mL of physiological saline (to remove residual erythrocyte debris that could interfere with subsequent RNA extraction).
- Centrifuge at 200 × g for 10 minutes and discard the supernatant.
- Add 1 mL of physiological saline and resuspend the resulting pellet using a Pasteur pipette to make it more homogeneous.
- Transfer the resuspended pellet to a 1.5 mL Eppendorf tube and adjust the volume with physiological saline.
- Centrifuge at 4000 × g for 3 minutes in an ultracentrifuge for an additional wash and discard the supernatant.

At this point, a pellet consisting solely of white blood cells and platelets is obtained. The pellet is then resuspended in 300 µL of OMG (Homogenization Solution, Promega, USA) + thioglycerol (Stock solution: 600 µL of thioglycerol + 30 mL of OMG). This solution stabilizes the leukocyte pellet. RNA extraction and purification can now be performed, or the cell pellet can be stored at –80 °C.

3.3. RNA Extraction Using the Maxwell RSC Extractor

The RNA extraction procedure is carried out using a semi-automated system, which operates on the principle of selective capture and purification of nucleic acids (in this case, mRNA) through paramagnetic beads. The instrument used is the Maxwell® RSC (Promega), shown in **Fig. 5**, and the kit employed is the Maxwell® RSC simplyRNA Blood Kit.

Figure 5 Maxwell® RSC Instrument (urly.it/3126qp)

The extraction process consists of four main phases:

- Lysis of leukocytes and release of nucleic acid (mRNA).
- Binding of the nucleic acid to paramagnetic beads.
- Washing of the sample.
- Elution of the final product.

This instrument can process up to 16 samples simultaneously using cartridges with pre-filled wells.

First, sample preparation is carried out:

- Vortex the sample previously resuspended in OMG.
- Add 300 µL of Lysis Buffer, which degrades the leukocyte cell membranes, releasing the mRNA.
- Add 30 µL of Proteinase K, an enzyme that degrades cellular proteins.
- Vortex for 10 seconds to homogenize the sample.
- Incubate for 10 minutes at room temperature.

Next, the instrument must be set up to ensure correct execution of the automatic extraction process:

- Turn on the instrument and the connected tablet.
- Select the "simplyRNA blood" protocol.
- Indicate the positions where the cartridges will be placed and identify them.
- Remove the cartridge holder and insert the cartridges into the positions previously assigned by the instrument.

Each cartridge consists of 8 wells, each with a specific function. They are inserted into the metal holder using a snap-lock mechanism. Well no. 1 (the largest well in the cartridge) is adjacent to the locking lever; therefore, it is positioned far from the elution tube, which has its own designated slot in the metal holder. All cartridges are hermetically sealed with a protective film and should be opened only at the time of use.

For each cartridge, proceed as follows:

- Carefully remove the sealing film.
- Insert the plunger into the last well (no. 8).
- Place the 0.5 mL elution tubes, adding 50 µL of elution buffer to each.
- Once incubation is complete, load the processed sample into the first well of the cartridge (**Fig. 6**).

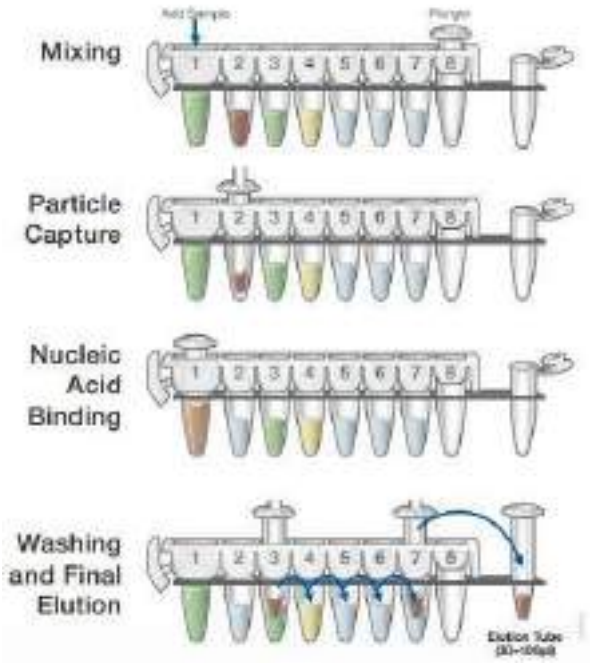

Figure 6 Structure of the cartridge used for nucleic acid extraction and the workflow with paramagnetic beads (Maxwell® RSC Promega, Instruments Guide)

Once all the samples have been loaded, insert the cartridge holder into the instrument and start the run. The duration is approximately 1 hour.

3.4. RNA Quantification with NanoDrop2000

Once the nucleic acid, in this case RNA, has been extracted, it undergoes a spectrophotometric reading using the NanoDrop2000 instrument (**Fig. 7**), which can both quantify the amount of RNA within the sample and assess its purity.

The NanoDrop2000 is a UV-visible spectrophotometer (light detector between 220 and 750 nm) that works based on the surface tension of liquids when placed between two closely spaced surfaces, such as two optical fibers. This instrument consists of:

- A light source that emits a high and constant amount of energy.
- A filter that separates the light into various wavelengths.

- A sample holder.
- A CCD camera that detects the light after it passes through the sample (detector).

Additionally, the instrument is connected to software on the PC, where the obtained data are processed and stored.

Figure 7: NanoDrop2000 Spectrophotometer from Thermo Fisher Scientific (urly.it/311m4d)

The light source emits a beam of light through a solution (sample), and a detector measures the intensity of the light that passes through the sample (unabsorbed light). The difference in light intensity before and after passing through the solution is used to calculate the absorbance of the substance in the solution. Therefore, the more light absorbed by the sample, the higher the concentration of nucleic acid present.

Nucleic acids absorb light at specific wavelengths, ranging from 230 to 280 nm, with an absorption peak at 260 nm. This absorption is due to the nitrogenous bases and is characteristic of both DNA and RNA. The absorbance is measured at 260 nm (A260), and at sufficiently low concentrations, it is directly proportional to the concentration of the sample.

This linear relationship is described by Lambert-Beer's law, which correlates the light absorbed by the substance—in this case, nucleic acid—with its concentration. The equation that describes this relationship is as follows: $A = \varepsilon \cdot C \cdot l$ where:

- A = Absorbance
- ε = Molar extinction coefficient, which indicates how strongly a substance absorbs light at a specific wavelength. For RNA, this coefficient is 25.
- l = Optical path length, which refers to the thickness of the sample the light travels through, measured in centimeters.

- C = Concentration of the analyte, which absorbs the light.

From the measurement of light absorption, a graph is obtained (**Fig. 8**), where the wavelengths are plotted on the X-axis, and the absorbance values are plotted on the Y-axis. The concentration of nucleic acid is calculated based on the area under the absorption peak at 260 nm.

The spectrophotometer is also useful for determining the purity of the sample, which is done by measuring absorbance at different wavelengths and calculating the ratios. Since proteins strongly absorb at 280 nm and chemical contaminants (such as phenol) absorb at 230 nm, two key ratios are established to assess purity:

- The A260/A280 ratio: indicates protein contamination. For RNA, the optimal value should be between 1.8 and 2.0.
- A260/A230 ratio: This ratio indicates the level of contamination from carbohydrates and phenols. The optimal value for this ratio should be around 2.2.

Additionally, absorbance at 320 nm (A260/A320) can be measured to check for any particulate contamination.

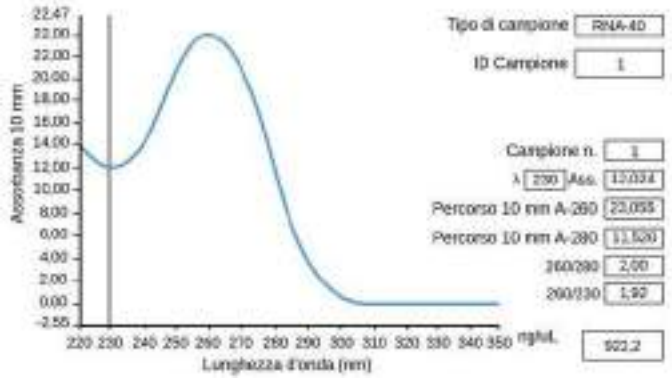

Figure 8: Example of a high-quality sample graph representing the result of a spectrophotometric RNA quantification (urly.it/311md4).

3.5. Reverse Transcription (RT) Step

Reverse transcription is the process that allows the synthesis of a double-stranded complementary DNA (cDNA) molecule from a single-stranded RNA template. The enzyme responsible for this process is reverse transcriptase (RT), an RNA-dependent DNA polymerase of retroviral origin (**Fig. 9**).

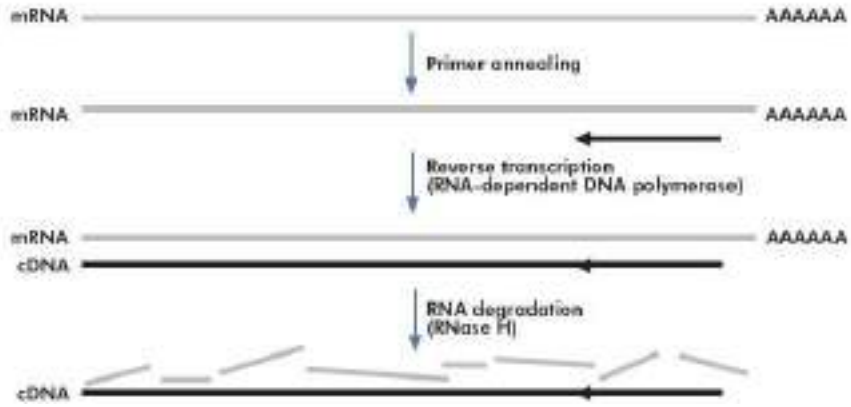

Figure 9: Action of reverse transcriptase during the synthesis of cDNA from mRNA (Bennici et al., 2015).

In vitro replication of the RNA strand involves using "random hexamers" as primers for reverse transcriptase: these are six-nucleotide sequences that randomly pair with RNA and initiate the reverse transcription reaction at multiple points.

The kit used is the BCR::ABL1 Mbcr IS MMR (QIAGEN®, Valencia, CA, USA), which includes the following reagents necessary for preparing the reverse transcription mix:

- 5X Transcriptase Buffer;
- dNTPs;
- Random hexamers;
- Reverse Transcriptase (RT);
- RNase Inhibitor and dithiothreitol (DTT).

In the same session, a calibrator, used as a positive endogenous control at a known concentration, and a negative RT control are reverse transcribed. The calibrator is transcribed

during the reverse transcription to ensure that the reverse transcription process and the subsequent RNA quantification are accurate, reliable, and standardized.

Procedure

During sample handling, it is recommended to work under a sterile hood to avoid contamination of the material.

- Dilute RNA samples with H2O to achieve a final concentration of 100 ng/µL in a final volume of 10 µL.
- Load the samples into the T100 Thermal Cycler (Bio-Rad, Hercules, California, USA) (**Fig.10**) and set the protocol suggested by the manufacturer.
- Denature at 65°C for 5 minutes.
- Prepare the reaction mixture for reverse transcription using the following reagents (**Tab. 1**):

Table 1 Reagents for the reverse transcription mix.

Reagents	**Quantity**
5X Transcriptase Buffer	5 µL
dNTPs	2 µL
Random esameri	5,25 µL
Rnasi inhibitor	0,5 µL
Reverse Transcriptase (RT)	1 µL
DTT (o ditiotreitolo)	1,25 µL

Pause the T100 thermal cycler and place the samples on ice for 5 minutes:

- Dispense 15 µL of the mix into each sample.
- Load the samples onto the T100 thermal cycler (**Fig. 10**) and restart the run.

Figure 10 T100 Thermal Cycler (T100 Thermal Cycle – Instruction Manual).

The thermal protocol continues with the following steps:

Step	Temperature (°C)	Time (Minutes)
Step 1	25	10
Step 2	50	60
Step 3	85	5
Step 4	4	5

Once the cDNA is obtained, it can be stored at -20°C for a short period of time.

3.6. Real-Time PCR (qPCR)

Gene expression is assessed by quantifying the messenger RNA (mRNA) level of the target gene. mRNA serves as an intermediary between the gene and the protein, and its quantification is a useful tool to evaluate the transcription of the target gene. The most commonly used technique to assess gene expression is Real-Time PCR (qPCR), which allows for the real-time detection and quantification of amplified products using fluorophores. The procedure is the same as that of conventional PCR (denaturation, annealing, extension), using the same reagents necessary for amplification: dNTPs, reaction buffer, heat-resistant polymerase (Taq polymerase). The only addition is a detection system that enables accurate quantification of a specific transcript.

Detection systems can be fluorescent DNA intercalators (SYBR® Green) or fluorophorelabeled probes (TaqMan). The main difference between the two lies in specificity: SYBR® Green emits fluorescence when it intercalates into DNA but is nonspecific and binds to any double-stranded DNA; on the other hand, TaqMan probes are complementary to the target product and emit fluorescence only when they bind to their target, making them more specific than SYBR® Green. Additionally, the two systems differ in cost: TaqMan probes are more expensive, making them less accessible for some laboratories. In this study, TaqMan probes were used to study the quantification of the BCR::ABL1 transcript. The probe is an oligonucleotide, a DNA fragment complementary to the target to be amplified, conjugated with

two different molecules: a high-energy fluorophore Reporter (R) at the 5' end and a lowenergy Quencher (Q) at the 3' end. The Quencher absorbs the signal emitted by the Reporter when it is excited by light. At the start of the Real-Time PCR reaction (**Fig. 11**), the probe is intact, and no fluorescence is emitted: the Quencher shields the Reporter, absorbing all its emission spectrum.

During the denaturation phase, when the DNA strands are separated, both the primers (Forward and Reverse) and the probe bind specifically to the DNA strand. Then, Taq polymerase will polymerize the new strand until it encounters the probe, and through its 5' → 3' exonuclease activity, it degrades the probe. In this way, the Reporter and Quencher separate, and the emission of the Reporter can be detected by a detector without being blocked by the Quencher. The fluorescence signal is directly proportional to the amount of target DNA present in the sample.

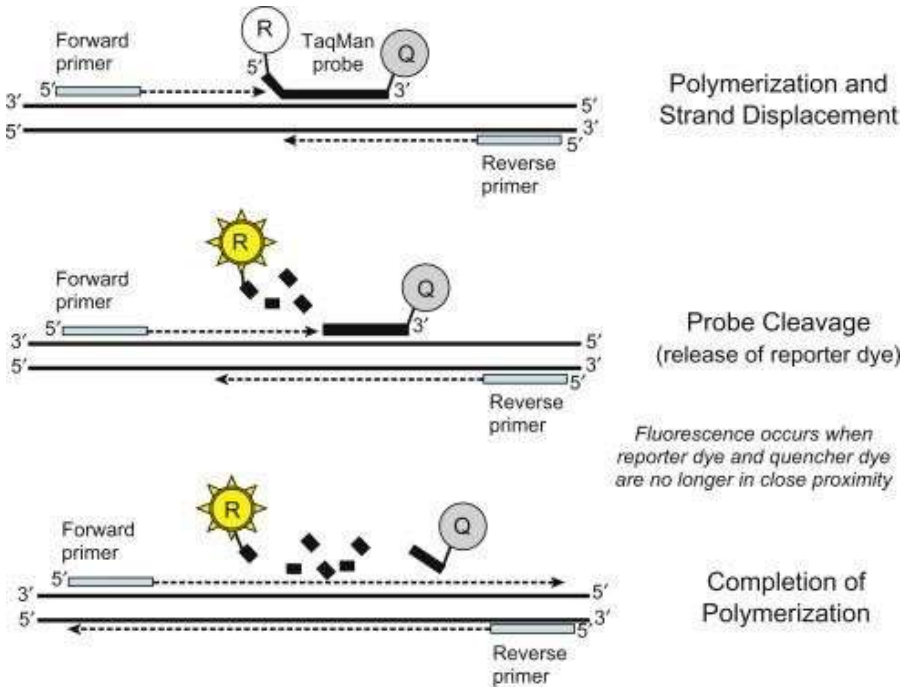

Figure 11: Action of the TaqMan probe in RT-PCR (Butler, 2012).

Additionally, TaqMan probes can be used for multiplex qPCR, allowing for the evaluation of the expression of multiple genes simultaneously. To do this, the probes must be labeled with different fluorophores so that the reading instrument can detect different signals.

Quantitative Signal Analysis

The signal analysis involves studying the amplification curves of each template in order to obtain an actual quantitative result. A graph is generated that displays the various amplification curves (**Fig.12**), each describing the increase in fluorescence of the template as a function of the number of PCR cycles. All ideal curves have a sigmoid shape, which can be broken down into the exponential phase, linear phase, and final plateau phase.

In the early cycles of PCR, the fluorescence is observed to be very low due to the small amount of product, which is still too low to be detected by the optical system. Only after a certain number of cycles, the fluorescence begins to increase, becoming measurable, until it surpasses a pre-set threshold or one chosen by the operator.

The point where the amplification curve intersects the threshold line ("Threshold") is called the threshold cycle (Ct), and it represents the number of cycles required to reach the set Threshold, as well as the point where the fluorescence is distinguished from the falsely detected signal due to background noise.

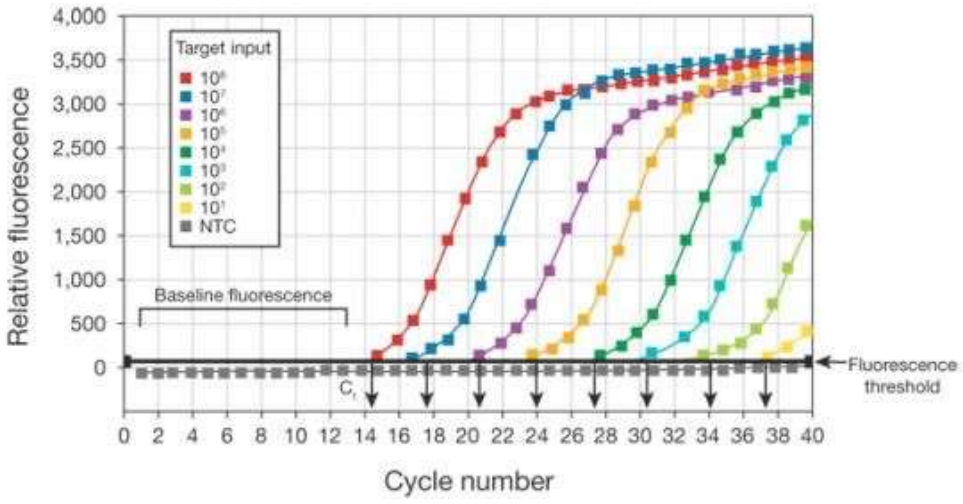

Figure 12: Examples of amplification curves in relation to the Threshold line and their corresponding Ct (Thermo Fisher Scientific, Real-Time Handbook).

The Ct values for the different dilutions, a standard curve is generated by plotting the logarithm of the starting DNA amount (on the x-axis) against the Ct values (on the y-axis). This

curve is used to determine the initial concentration of the target gene in unknown samples based on their Ct values.

The standard curve allows the calculation of the target gene copy number in the sample, as the relationship between the Ct value and the DNA amount is linear. The formula derived from the standard curve enables the quantification of the gene expression in the samples being analyzed.

The quantitative values of each standard and their corresponding Ct values allow the software to construct a calibration curve (**Fig. 13**), correlating the Ct values on the y-axis with the concentration values on the x-axis (Ct/Log [ ]).

In general, the expression of the target gene is normalized relative to the expression of a housekeeping gene, which is consistently expressed in all cells, with expression levels remaining stable across treated and control samples. The housekeeping gene undergoes the same procedure as the samples, using the same detection system.

By interpolating from the calibration curve, it is possible to determine the concentrations of both the target gene and the housekeeping gene. From the standard curve, three parameters can be derived, providing important information about the performance of the analysis:

- Slope (M): Represents the value of the slope (coefficient), or the number of cycles between two dilutions of the standard. It directly measures the reaction efficiency, with the range typically between -3.20 and -3.60.
- Y-intercept (B): Represents a measure of the method's sensitivity, where the highest measurable Ct corresponds to the lowest number of copies detectable by the instrument. Above this threshold, the signal becomes negative.
- Correlation coefficient (R^2): Correlated with the reproducibility of the data. The closer it is to 1 (the ideal value), the more accurately the line represents the experimental data trend.

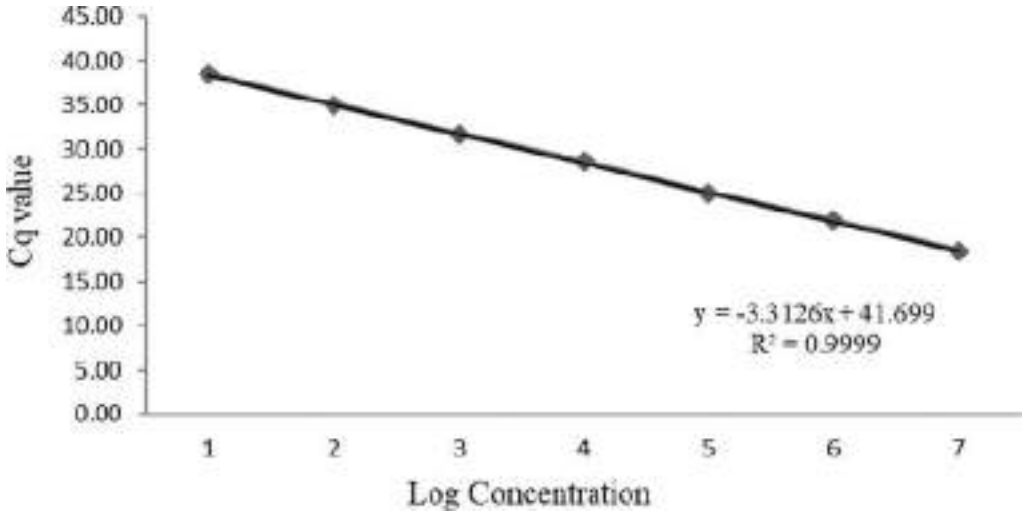

Figure 13: Example of a standard curve in RT-qPCR (urly.it/311xwt).

3.7. Gene Expression Analysis by Droplet Digital PCR (ddPCR)

Gene expression analysis of BM1 and EZH2 genes was performed using ddPCR, a thirdgeneration PCR technique. ddPCR divides the samples into many compartments, allowing absolute quantification without the use of standards. The term “droplet” refers to the water-oil emulsion that divides the samples into approximately 20,000 droplets using a droplet generator. PCR amplification occurs in each droplet, and the compartments containing the target molecule are read by a device, classifying them into a binary response (yes/no), which is where the term "digital" comes from. The binary response in ddPCR is based on the presence or absence of fluorescence in each droplet, where a positive signal indicates the detection of the target gene; conversely, droplets without fluorescence are considered negative.

Subsequently, statistical analysis is performed through the Poisson distribution, which accurately estimates the concentration of the target DNA by correcting for the randomness in the distribution of positive and negative droplets, ensuring absolute quantification.

As shown in **Fig.14** , the steps involved in ddPCR are:

- ddPCR Setup and Droplet Generation: The preparation of the Mastermix containing the combination of primers/probes specific for the amplification of the genes under study is carried out. The Mastermix is then added to the diluted samples in predetermined

volumes. Next, an aliquot of the prepared mix and the specific oil for droplet generation are loaded into the wells of the cartridge. This cartridge is then placed in a droplet generator capable of dividing the sample into droplets using microfluidic mechanisms.

- Plate Transfer and PCR Amplification: The resulting emulsion is placed in a 96-well plate. It is sealed with an aluminum sheet and placed in the thermal cycler for amplification.
- Droplet Reading and Data Analysis: Unlike qPCR, where the signal is read at each amplification cycle to create a curve, in ddPCR the fluorescent signal is read only once at the end of the reaction. For fluorescence reading, a 'droplet reader' is used, which aligns the droplets to record their respective fluorescence signals. Statistical analysis using the Poisson distribution is then performed, followed by the evaluation of the resulting graphs.

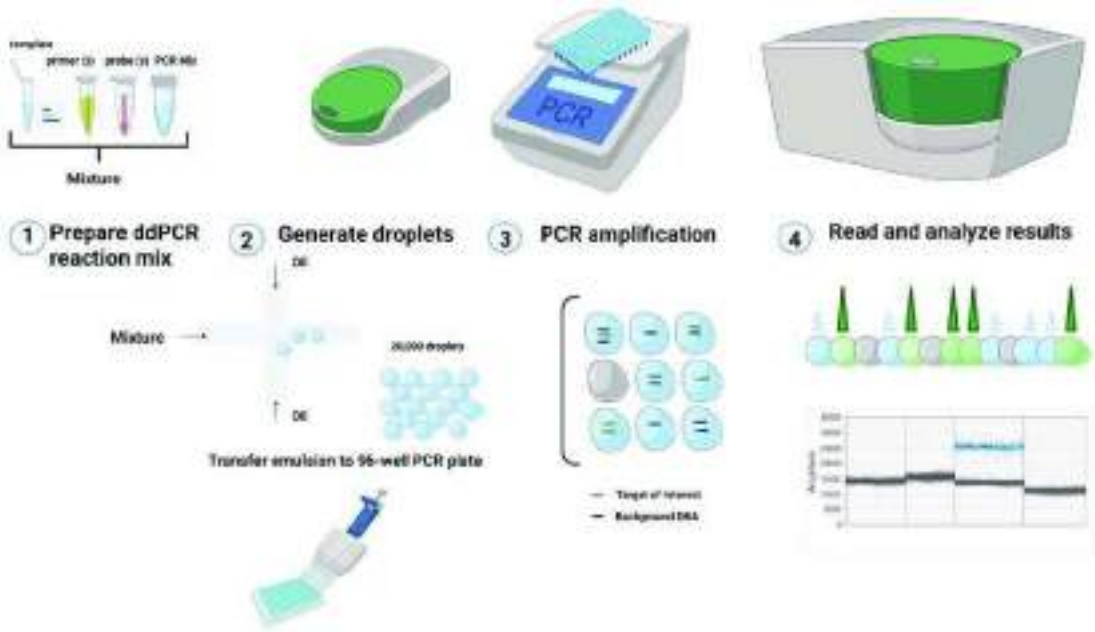

Figure 20: ddPCR Workflow (Lambrescu et al., Figure 14 ddPCR Workflow (Lambrescu et al., 2022).2022).

In our study, we used multiplex ddPCR, which extends the concept of ddPCR. Multiplex analysis with ddPCR is based on two key principles:

- The ability of the instrument to read two different fluorophores.

- The possibility of adding different relative quantities of "primers/probe" combinations specific for the different targets to the reaction mix.

This second point was crucial for discriminating the three signals associated with the different targets of interest.

In our case, we considered three genes: BMI1, EZH2, and GAPDH. As mentioned earlier, for each target, a specific combination of primers/probe was used to achieve amplification and signal emission. Since the instrument has only two fluorescence channels, the probes for BMI1 and EZH2 were labeled with the fluorophore "FAM," while the GAPDH probe was labeled with the fluorophore "HEX."

To distinguish signals for targets with probes labeled with the same fluorophore, we decided to focus on the signal intensity associated with each (**Fig. 15**). Indeed, the "droplet reader," in addition to discriminating the type of signal (FAM or HEX), can recognize different intensity levels (high or "High" and low or "Low").

Theoretically, the fluorescence signal intensity associated with a target at the end of the reaction (end-point) depends on the relative amount of the "primers/probe" combination in the reaction mix. This is because the greater the amount of primers, the more amplification can occur, and therefore, the more probe will be degraded during the amplification cycles, resulting in a stronger final signal. Conversely, the signal for a target associated with a lower amount of the "primers/probe" combination will be weaker, as there will be less amplification, leading to less probe degradation and thus a weaker final signal.

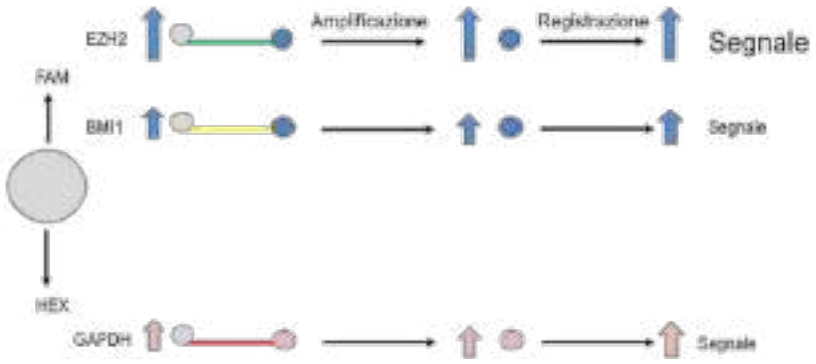

Figure 15: Schematic representation of the difference in signal intensity of the same fluorophore towards different targets as a function of primer/probe quantity.

Sample Preparation

RNA samples were reverse transcribed using the iScript™ gDNA Clear cDNA Synthesis Kit from Biorad. This kit allows for the completion of two essential steps for gene expression analysis: the first step removes any genomic DNA (gDNA) contamination, and the second step involves the reverse transcription of RNA into cDNA.

The kit enables accurate analysis with an initial RNA quantity range from 1µg to 1ng. In our case, 250ng of RNA was initially used.

In the first phase, the samples were treated with DNase to remove any residual gDNA contamination, following the proportions listed in **Tab.2**:

Table 2: DNase Treatment

Components	**Volume for 1 reaction, µl**
IScript DNAsi	0,5
iScript DNAsi buffer	1,5
RNA	14 (250ng totali)

Subsequently, the samples were subjected to the following thermal protocol:

Step	**Temperature (°C)**	**Time (Minutes)**
DNA digestion	25	5
DNAsi inactivation	75	5
Storage	4	Until retrotranscription

To the 16 µl of DNase-treated sample, 4 µl of iScript RT Supermix were added, and the mixture was subjected to the following thermal protocol:

Step	Temperature (°C)	Time (Minutes)
Priming	25	5
Retrotranscription	46	20
Inactivation RT	95	1
Storage	4	-

The samples were used for analysis via ddPCR. After diluting the cDNA at a 1:15 ratio, the Mastermix for the ddPCR assay was prepared. Each sample was analyzed in duplicate, and a negative control (H_2O) was included in every run to check for potential contamination. The probes used for BMI1 and EZH2 are TaqMan probes labeled with the FAM fluorophore, while the probe for GAPDH is labeled with the HEX fluorophore.

As observed, both BMI1 and EZH2 share the same fluorophore. To distinguish which target the emitted fluorescence corresponds to, the signal intensity associated with each is examined.

The Mastermix is composed of the components listed in **Tab 3**.

Table 3: Mastermix Components for ddPCR Amplification.

Component	**Volume in µL (per single reaction)**
4x Supermix (specific for multiplex ddPCR assay)	5.50
BMI1 primer/probe (900 nM primers; 250 nM FAM probe)	0.50
EZH2 primer/probe (900 nM primers; 250 nM FAM probe)	1.00
GAPDH primer/probe (900 nM primers; 250 nM HEX probe)	1.00
DTT	0.29
Nuclease-Free Water	5.71
Diluted cDNA	8.00
Final Volume	**22.00**

Droplet Generation

Following sample preparation, the droplet generation phase was carried out. The samples were loaded into a specific cartridge called the DG8™ cartridge (**Fig. 17**):

It consists of 3 rows with 8 wells each and is placed into its cartridge holder using a snap-in system. The samples (20 µL from the previously prepared mix) are loaded into the middle row of the DG8™ cartridge, taking care to avoid forming air bubbles inside the wells. In each well of the bottom row, 70 µL of oil (Droplet Generation Oil for Probes) are loaded, which is necessary for generating the emulsion. After covering the cartridge with the seal provided in the kit, it is inserted into the Droplet Generator (Bio-Rad), shown in **Figure 16**.

Approximately 20,000 droplets are generated per sample in 2.5 minutes.

Figure 17 Image of the DG8™ cartridge used to create the emulsion (Droplet Digital™ PCR – Application Guide).

Figure 16 QX200™ Droplet Generator instrument (Droplet Generator, IVD, Instruction Manual).

-

Transfer to Plate and Amplification

In the upper row, through a microfluidic mechanism, the emulsion containing the droplets (50 µL) is generated. The samples are then transferred to a 96-well PCR plate by gently aspirating with a pipette. If this step is performed incorrectly, the droplets may be disrupted, compromising the test results. Next, the plate is sealed with a foil sheet and placed inside the thermal cycler for amplification, following the thermal protocol below:

Step	**Temperature (°C)**	**Time**	**Cycles**
Enzyme Activation	95	10 min	1
Denaturation	94	30 sec	45
Primer Annealing / Extension	58	1 min	
Enzyme Deactivation	98	10 min	1
Hold	4	10 min	
Storage	12	∞	

Plate Reading and Data Analysis

After amplification, the plate is inserted into the droplet reader (Droplet Reader – QX200), which scans the contents of each well and analyzes each droplet using a dual-color detection system: one channel for FAM and one for HEX. Thus, ddPCR detects fluorescence only once at the end of the amplification reaction, which is why it is referred to as *end-point* detection.

Equipped with separate channels for different fluorophores, the instrument measures the signals individually and classifies each droplet based on the detected intensity. The signal intensity depends on the amount of fluorophore released after degradation of the labeled probe, which in turn depends on the presence of the target gene.

Some droplets will show a signal, some none, and others may contain more than one signal. This is due to the random distribution of cDNA among the droplets, which can be corrected using the *Poisson equation*.

This statistical Poisson correction is applied by the Quantasoft software, which processes the raw data from the optical reader and allows for proper interpretation. PCR-positive and PCRnegative droplets are counted to provide an *absolute quantification*, which is then visualized through scatter plots and histograms.

Before accessing values and plots, a kind of *quality control* must be performed: for each sample, the total number of events—i.e., the total number of droplets read by the instrument regardless of classification—is calculated. This value is crucial for statistical calculations and significantly affects the reliability of the result. A test is considered reliable if at least 10,000 droplets are detected. Fewer events may indicate poor emulsification or droplet loss (rupture) during the process.

Data can be visualized in 1-D (**Fig. 18**) or 2-D (**Fig. 19**):

- 1-D Plot: Displays fluorescence intensity for a single fluorophore, FAM or HEX, on one axis. It allows for the visualization of positive and negative droplets for one fluorophore, separated by a threshold line. This threshold is set automatically by the software but can be adjusted by the user.

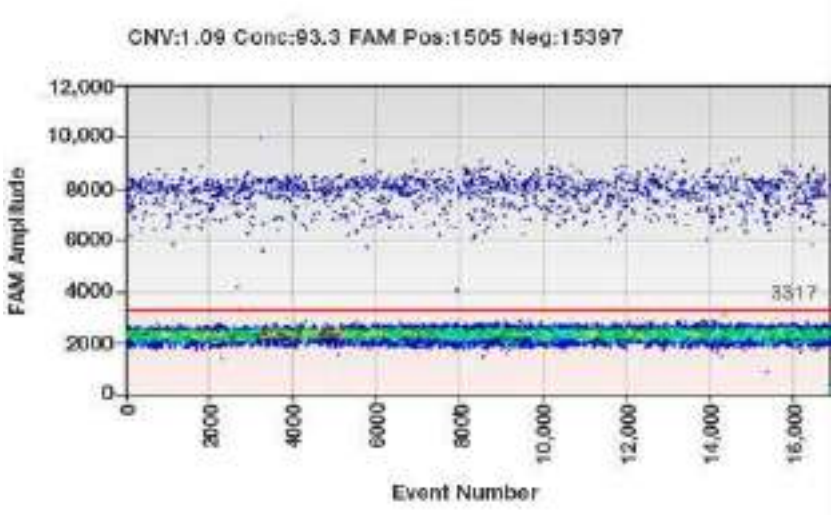

Figure 18: Example of the 1-D plot for FAM. The red line represents the threshold, above which the positive droplets reside (Digital Droplet PCR-technology).

- 2-D Plot, where two fluorescence channels are used simultaneously to represent the intensity of both signals on two distinct axes (e.g., FAM on the X-axis and HEX on the Y-axis). The axes of the plot divide the droplets into various clusters, which are distributed into 4 quadrants depending on the type of fluorescence and intensity: in the first quadrant (+/+) are the double-positive droplets, indicating the presence of both target genes within the droplets; in the second and fourth quadrants (+/- or -/+) droplets are positive for one of the fluorophores; finally, in the third quadrant (-/-) are the double-negative droplets, where no target is present. This two-dimensional representation allows for a clearer view of the distribution of the generated droplets.

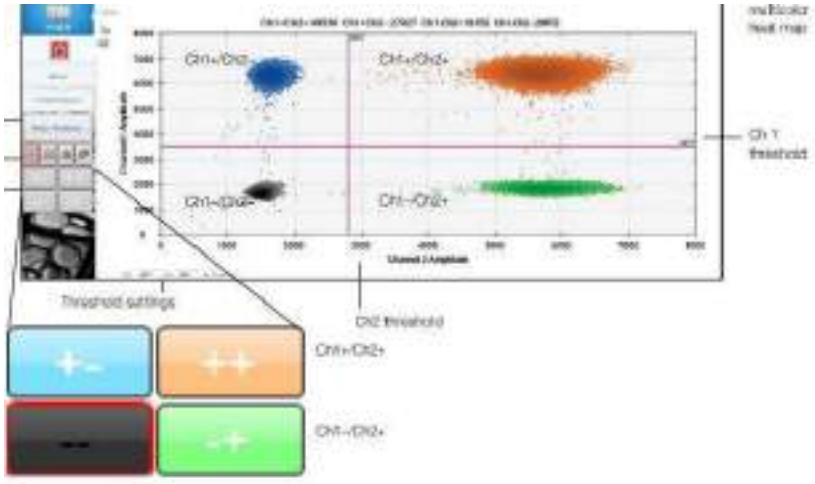

Figure 19: Representative 2D graphical plot showing the distribution of clusters across four quadrants: (+/+), (-/+), (-/-), and (+/-).

Starting from the data on the number of positive and negative droplets for each target, the instrument automatically calculates the concentration (copies/µl) of that specific target at the beginning of the reaction. After determining the concentration, it is possible to calculate the ratio, which takes on different meanings depending on the context. In the case of gene expression, it is defined by the expression of the target gene (A) normalized according to that of the housekeeping gene (B), which in our case is represented by GAPDH. In the case of mutation analysis, it is represented by the concentration of the mutated target (A) over the sum of the concentrations of the mutated target and the wild-type (A+B).

Plate reading and result analysis in Multiplex ddPCR

Each run is then visualized using the "QuantaSoft Analysis Pro™" software to analyze the obtained data. To use this software, we need to set the type of analysis to be performed (Gene Expression) and the type of assay used (Amplitude multiplex). A window then opens (**Fig. 20**), where it is possible to set the name of the target gene and the associated signal in qualitative terms (FAM or HEX) and quantitative terms (Low or High). Three possible signals are obtained: FAM low, FAM High, and HEX;

Figure 20: Interface for setting the run parameters in QuantaSoft Analysis Pro™

it is also possible to specify whether the target is an unknown (BMI1, EZH2) or a reference gene (GAPDH).

Following the analysis of the results, we can perform an analysis using the 1D plot (**Fig. 21**), where the fluorescence intensity for each individual channel is shown separately (FAM or HEX). In the FAM channel, we can identify:

- A low fluorescence signal, where droplets without the specific fluorophore are present (gray, background signal);
- A first level of fluorescence, where we find droplets associated with a low signal;
- A second level of fluorescence, where droplets associated with a higher intensity are shown.

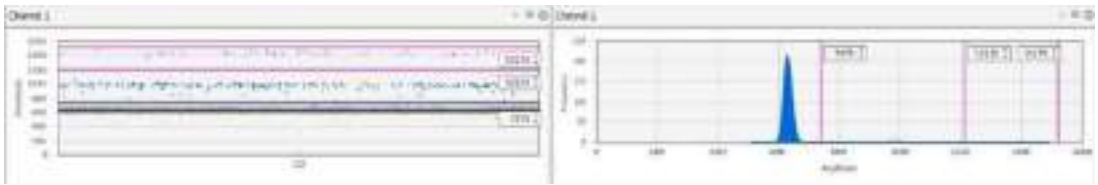

*Figure 21:*1D Plot graph, in this case showing fluorescence associated with the FAM channel. On the left, the distribution of droplets is shown according to the signal intensity, and on the right, the frequency distribution of droplets

In the 2D graph (**Fig. 22**), the fluorescence intensity for the HEX channel is shown on the Xaxis, and the fluorescence intensity for the FAM channel is shown on the Y-axis. The figure displays the distribution of the obtained clusters.

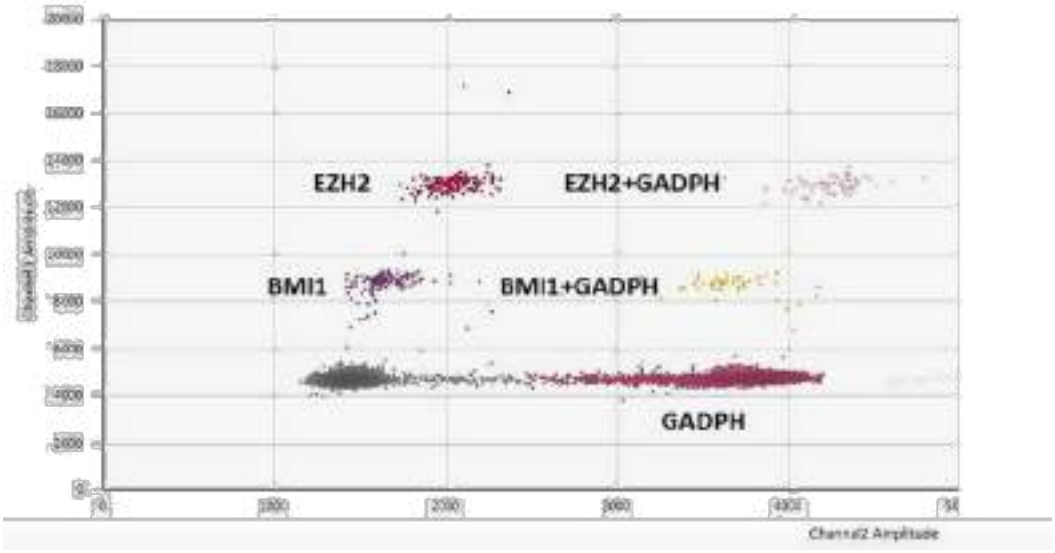

Figure 22: 2D Plot showing a sample analyzed with the multiplex assay using ddPCR. In 2D Plot showing a sample analyzed with the multiplex assay using ddPCR. In our case, our case, 6 clusters are observed.6 clusters are observed.

Once the graphical analysis has been performed, allowing the assignment of individual droplets to their respective clusters, it is possible to derive the data related to the concentration of individual targets and their relative expression.

3.8. Analysis of ROCK, IGFBP6 and PD-L1 gene expression by multiplex ddPCR

RNA samples were reverse transcribed into cDNA using the iScript™ gDNA Clear cDNA Synthesis Kit by BioRad. This kit allows for two essential steps in gene expression analysis: the first step removes any genomic DNA (gDNA) contamination, and the second step involves reverse transcription of RNA into cDNA.

The kit allows for accurate analysis over a range of initial RNA quantities between 1µg-1ng. In our case, 250 ng of RNA were reverse transcribed.

As previously mentioned, the samples were treated with DNase to remove any residual gDNA contamination, following the proportions outlined in the table (**Tab.4**).

Table 4: Components of the mix used for DNase treatment of RNA samples

Components	**Volume per reaction, µl**
iScript DNase	0.5
iScript DNase buffer	1.5
RNA	14 (250 ng total)

The samples were then subjected to the following thermal protocol (**Tab.5**):

Table 5: Thermal protocol for DNase treatment

Step	**Temperature (°C)**	**Time (Minutes)**
DNA digestion	25	5
DNase inactivation	75	5
Storage	4	Until reverse transcription

To the 16 µl of DNase-treated sample, 4 µl of iScript RT Supermix were added and subjected to the following thermal protocol (**Tab.6**):

Table 6 Thermal protocol for reverse transcription reaction

Step	**Temperature (°C)**	**Time (Minutes)**
Priming	25	5
Reverse transcription	46	20
RT inactivation	95	1
Storage	4	-

The reverse-transcribed samples were appropriately diluted with water (1:15 dilution) and used for the ddPCR reaction. For the analysis of ROCK2, IGFBP6, PD-L1 gene expression, we used multiplex ddPCR, which extends the concept of ddPCR. Multiplex ddPCR analysis relies on two fundamental principles:

- The instrument's ability to read two different fluorophores.
- The ability to add different relative amounts of specific "primer/probe" combinations for the different targets in the mix.

This second point is crucial for discriminating the three signals associated with the different targets of interest.

In our case, we examined four genes: ROCK2, IGFBP6, PD-L1 and GAPDH (glyceraldehyde-3-phosphate dehydrogenase) as the reference gene. As mentioned earlier, a specific primer/probe combination was used for each target to achieve amplification and signal emission. Since the instrument has only two fluorescence channels, the probes for ROCK2 and IGFBP6 were labeled with the "FAM" fluorophore, while PD-L1 and GAPDH were labeled with the "HEX" fluorophore.

To recognize the signals of the targets whose probes were labeled with the same fluorophore, we decided to act on the intensity of the associated signal (**Fig. 22**). In fact, the "droplet reader," in addition to discriminating the type of signal (FAM or HEX), is able to recognize different intensity levels: High and Low.

Theoretically, the intensity of the fluorescence signal associated with a target, at the end of the reaction (end-point), depends on the relative amount of "primer/probe" combination present in the reaction mix. This is because the greater the amount of primers, the greater the amplification that can occur, and thus the greater the amount of probe that will be degraded during the amplification cycles, resulting in a stronger final signal. Conversely, the signal associated with a target that has a lower amount of "primer/probe" combination will be weaker; this is because the amplification will be lower, leading to less probe degradation and consequently a weaker final signal.

As we mentioned, in our experiments, the probes used for ROCK2 and IGFBP6 are TaqMan probes labeled with the FAM fluorophore, while those used for PD-L1 and GAPDH are labeled with the HEX fluorophore. To discriminate the signal, we used different volumes of the primer/probe combination for each analyzed target. The volumes used to create the mastermix are shown in the table (**Tab. 7**).

Components Volume in µL *(x1 per single reaction)*

Table 7: Components of the mastermix with respective volumes used for the multiplex ddPCR to monitor ROCK2, IGFBP6 and PD-L1

Component	Volume (µL)
ddPCR Multiplex 4X Supermix (BioRad)	5.50
ROCK primer/probe (900 nM primers; 250 nM probe FAM) [Assay ID: dHsaCPE5056316, BioRad]	0.50
IGFBP6 primer/probe (900 nM primers; 250 nM probe FAM) [Assay ID: dHsaCPE5040160, BioRad]	1.00
PD-L1 (CD274) primer/probe (900 nM primers; 250 nM probe FAM) [Assay ID: dHsaCPE5058503, BioRad]	1.25
GAPDH primer/probe (900 nM primers; 250 nM probe HEX) [Assay ID: dHsaCPE5031596, BioRad]	0.65
DTT	0.29
Nuclease-Free Water	8.81
Diluted cDNA	4.00
Final Volume	22.00

Each sample was analyzed in duplicate, and a negative control (H2O) was included in each run to assess potential contamination. Once the samples were prepared, the droplets were generated, the emulsion was transferred to a plate, and amplification was carried out according to the following thermal protocol (**Tab. 8**).

Table 8 Thermal protocol for multiplex ddPCR used to study IGFBP6, ROCK2, PD-L1.

Step	Temperature (°C)	Time	Cycles
Enzyme Activation	95	10 min	1
Denaturation	94	30 sec	
Primer Annealing / Extension	58	1 min	45
Termination	98	10 min	1
Storage	4	10 min	

Final Storage	12	∞	-

After amplification, the droplets are read by the Droplet Reader and analyzed.

From the "QuantaSoft Analysis Pro™" software (Bio-Rad), to use this software, we must first set the type of analysis to be performed (Gene Expression) and the type of assay used (Amplitude multiplex). At this point, we can set the name of the target gene and the associated signal in both qualitative (FAM or HEX) and quantitative terms (Low or High), obtaining 4 possible signals: FAM low, FAM High, HEX low and HEX high. It is also possible to indicate whether the target is unknown (ROCK2, IGFBP6, PD-L1) or the reference gene (GAPDH).

At this point, we can perform an analysis using the 1D plot (**Fig. 23**), where the fluorescence intensity for each individual channel is shown separately (FAM or HEX). In the FAM channel, we can identify:

- A signal with very low fluorescence, where no target is present (in gray, background signal);
- A first level of fluorescence, where droplets with a low signal are found;
- A second level of fluorescence, where droplets with a higher signal intensity are found.

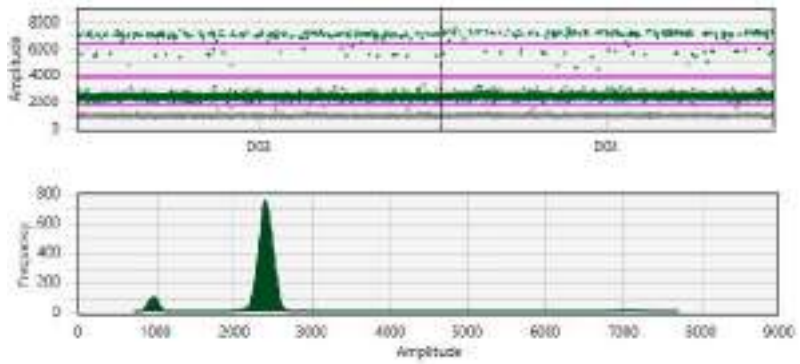

Figure 23: 1D Plot Graph. In this case, the fluorescence associated with the FAM channel is shown. At the top, the distribution of droplets as a function of signal intensity is displayed; at the bottomt, the frequency distribution of the droplets based on the signal is shown

In the 2D plot, the X-axis shows the fluorescence intensity related to the HEX channel, while the Y-axis displays the fluorescence related to the FAM channel. The figure shows the distribution of the resulting clusters (**Fig. 24**).

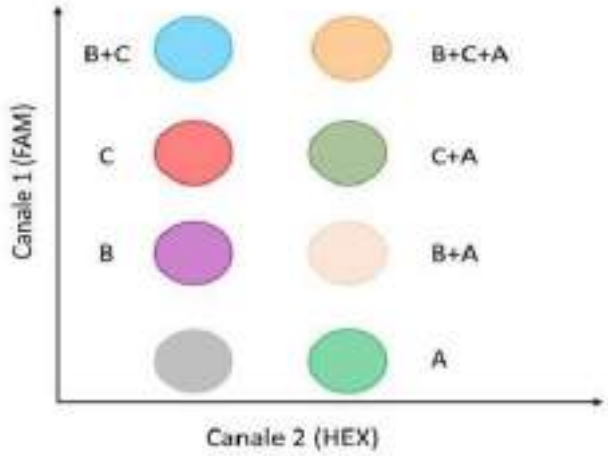

Figure 24: Arrangement of Potential Clusters Obtained with Multiplex ddPCR

Also in this case, all samples that did not reach a total number of 10,000 events were excluded from the analysis. In the graph below (**Fig. 25**), an example of the droplet distribution provided by the analysis software can be observed.

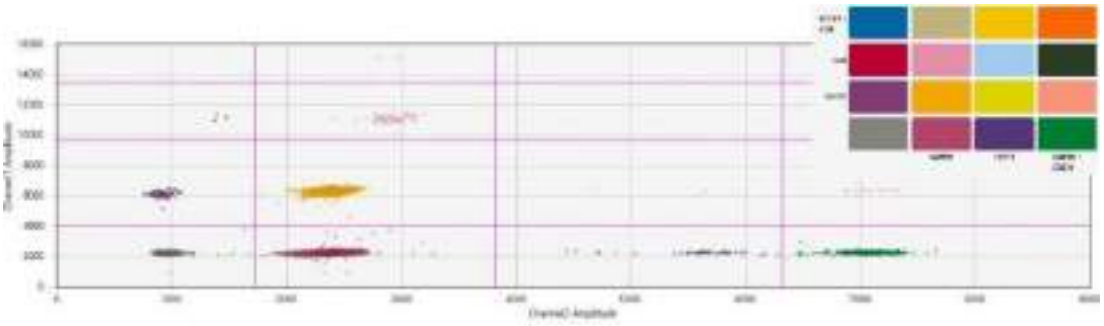

Figure 25: Cluster distribution of droplets provided by the software. In the 2-D representation, droplets positive for ROCK2 (light purple), for IGFBP6 (red), for GAPDH (bright magenta), for PD-L1 (deep purple), double positives for ROCK2 and IGFBP6 (blue), double positives for GAPDH and PD-L1 (green).

The software, in addition to providing the number of positive events for each gene, is able to calculate the target concentration (copies/µl) as shown in the figure and provide a ratio relative to GAPDH used as the reference gene (**Fig. 26**).

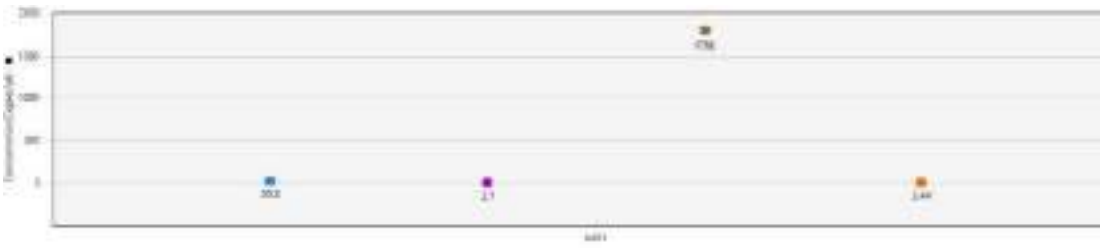

Figure 26: Graph provided by the software showing the concentration of the genes under study (ROCK2, IGFBP6, PD-L1 and GAPDH).

3.9. Genotyping of PD-L1 Polymorphisms

Genotyping of PD-L1 single nucleotide polymorphisms (SNPs), rs2282055 (T>G), rs4143815

(G>C), and rs10815225 (G>C), was performed by real-time polymerase chain reaction (RTPCR) using allele-specific TaqMan® SNP Genotyping Assays (Applied Biosystems, Foster City, CA, USA).

Each PCR reaction was prepared in a final volume of 10 µL, as detailed in **Tab. 9**, and consisted of 2X TaqMan Genotyping Master Mix, SNP assay mix (containing allele-specific primers and probes), and genomic DNA at a concentration of 2 ng/µL (9 ng per reaction).

Amplification and fluorescence detection were carried out on a QuantStudio™ 5 Real-Time PCR System (Applied Biosystems). The thermal cycling protocol consisted of an initial denaturation at 95 °C for 10 minutes, followed by 40 cycles of 95 °C for 15 seconds and 60 °C for 1 minute.

No-template controls (NTCs) were included to monitor contamination. Approximately 10% of the samples were randomly selected and re-genotyped, yielding 100% concordant results.

Table 9: Composition of the PCR Reaction Mix for SNP Genotyping

Component	**Volume per Reaction (µL)**	**Final Concentration / Note**
2X TaqMan Genotyping Master Mix	5.0	Supplied by Applied Biosystems
TaqMan SNP Assay Mix (primers + probes)	0.5	Allele-specific mix (Applied Biosystems)
Genomic DNA (2 ng/µL)	4.5	Total 9 ng of DNA per reaction
Total Volume	**10.0**	

Allelic Discrimination and Data Analysis

After PCR amplification, a post-PCR plate read was performed using the QuantStudio™ 5 Real-Time PCR System (Applied Biosystems). The instrument software measured fluorescence signals for each well and plotted normalized reporter signals (Rn values) to generate allelic discrimination plots. These plots displayed each sample as a data point on a scatter plot of VIC® (Allele 1) versus FAM™ (Allele 2) fluorescence intensities (**Fig. 27**).

Allele calling was conducted using QuantStudio Design & Analysis Software, which automatically assigned genotypes based on signal clustering. In cases where clustering was ambiguous or borderline, allele calls were manually reviewed and verified. The accuracy of genotyping was confirmed by duplicate analysis of randomly selected samples, which showed 100% concordance.

No pre-read background subtraction was performed, as no pre-read data were available. The overall workflow followed the standard procedure recommended by the manufacturer, including:

- Setting up a post-PCR plate read document,
- Performing the plate read,
- Automatic and manual allele discrimination,
- Verification of genotypes.

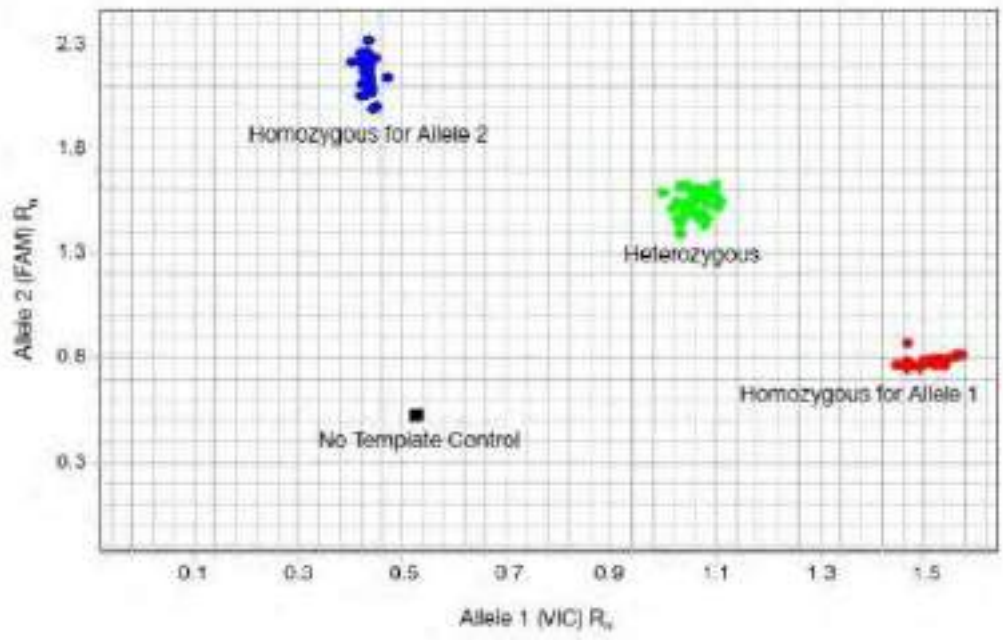

Figure 27: Example of an allelic discrimination plot

3.10. Statistical Methods Used

Event-Free Survival (EFS) was defined as the time, measured in months from diagnosis, without clinical events such as tyrosine kinase inhibitor (TKI)-related toxicities leading to treatment discontinuation or disease relapse. Survival curves were estimated using the Kaplan–Meier method, and differences between groups were assessed with the Log-Rank (Mantel–Cox) test. Survival analyses were stratified by the number of comorbidities (1–2 vs. ≥3), first-line therapy (nilotinib vs. imatinib), gene expression levels of EZH2 and BMI1 (stratified by the median), SIRI inflammatory index (above vs. below the median), and the presence of PD-L1 gene polymorphisms. Additional clinical and molecular factors—including age, sex, ELTS score, and expression levels of candidate genes (ROCK2, IGFBP6, PD-L1), were also evaluated for their impact on EFS. A p-value < 0.05 was considered statistically significant.

Associations between gene expression levels and molecular response (MR) at various timepoints (3, 6, 9, and 12 months) were assessed using the Pearson's chi-square test. Continuous gene expression values were dichotomized (high/low) based on either ROC analysis thresholds or median values.

To assess the correlation between inflammatory parameters (neutrophil, lymphocyte, and platelet counts) and gene expression levels, as well as correlations among the expression profiles of different genes, Spearman's rank correlation coefficient was used. The choice of non-parametric tests was based on variable distribution, verified using the Shapiro–Wilk normality test.

The association between PD-L1 expression levels and the selected single nucleotide polymorphisms (SNPs) was tested by stratifying patients according to median PD-L1 expression at diagnosis and at 12 months (high vs. low), and comparing genotype distributions using the Pearson's chi-square test.

All statistical analyses were performed using SPSS v.28. All tests were two-tailed, and statistical significance was set at $p < 0.05$.

3.11. Systemic Inflammation Response Index (SIRI)

Recent evidence highlights the prognostic relevance of systemic inflammation in various malignancies, including hematological neoplasms. In this context, composite hematologic indexes that reflect the balance between pro-tumoral inflammation and anti-tumoral immune function have gained increasing attention.

Among these, the Systemic Inflammation Response Index (SIRI) has emerged as a novel and promising biomarker. It integrates key components of both the innate immune system (neutrophils and monocytes) and the adaptive immune system (lymphocytes), offering a dynamic insight into the host–tumor interaction and the overall inflammatory state.

SIRI was calculated for each patient at diagnosis according to the following formula:

SIRI=Neutrophil count×Monocyte count\Lymphocyte count

Peripheral blood counts were obtained from diagnostic complete blood count (CBC) results. Patients were stratified into two groups based on the median SIRI value, to evaluate its association with Event-Free Survival (EFS).

Originally developed as a general marker of systemic inflammation, SIRI has been shown to be an independent prognostic factor in several clinical conditions, including cancer, rheumatoid arthritis, hyperuricemia, intracerebral hemorrhage, and acute ischemic stroke (AIS) (Dang, 2023). However, its prognostic utility in hematologic malignancies remains underexplored.

In this study, we investigated the potential role of SIRI as a prognostic factor in Chronic Myeloid Leukemia (CML) by assessing its correlation with event-free survival.

IV. RESULTS

4.1. Clinical Characterization of the Patient Cohort

A total of 21 patients diagnosed with chronic myeloid leukemia (CML) were included in this study. All diagnoses were made between June 2019 and December 2023. The cohort consisted of 14 males and 7 females, with a median age of 54 years (range: 21–83 years) at the time of diagnosis. According to the EUTOS Long-Term Survival (ELTS) score, 11 patients (52%) were classified as low-risk, 6 (29%) as intermediate-risk, and 4 (19%) as high-risk. (**Tab.10**)

Additional cytogenetic abnormalities (ACAs) were identified in 2 out of 21 patients (9.5%). Regarding comorbidities, 6 patients (28.6%) presented with three or more comorbid conditions at diagnosis.

As first-line therapy, 11 patients (52%) were treated with imatinib, 9 patients (43%) with nilotinib, and 1 patient (5%) with dasatinib. At the time of analysis, the median follow-up was 40 months (range: 13–67 months). Peripheral blood samples for gene expression analysis were collected at four timepoints: diagnosis, 3, 6, and 12 months after the initiation of treatment.

Table 10: Clinical and demographic characteristics of the study cohort (n = 21)

Characteristic	**Value**
Sex (M:F)	14:7
Median age (range)	54 years (21–83)
ELTS risk group	Low: 11 (52%) Intermediate: 6 (29%) High: 4 (19%)
Additional cytogenetic abnormalities (ACAs)	2/21 (9.5%)
≥3 comorbidities	6/21 (28.6%)
First-line TKI therapy	Imatinib: 11 (52%) Nilotinib: 9 (43%) Dasatinib: 1 (5%)
Median follow-up (range)	40 months (13–67)

Five patients (24%) required a change in first-line TKI therapy: two due to resistance and three due to intolerance. Of these, two patients also underwent a second-line TKI change, one due to both resistance and intolerance, and one due to intolerance alone (**Tab.11**).

Table 11: Summary of treatment line changes and their reasons in the study population

Reason for Change	**Number of Patients Who Changed First-Line**	**Number of Patients Who Also Changed Second-Line**
Resistance	2	1
Intolerance	3	1
Total	**5**	**2**

4.2. Clinical Outcomes: Event-Free Survival (EFS)

4.2.1. Event-Free Survival (EFS) Analysis

Event-free survival (EFS) was calculated considering both TKI-related toxicities that led to treatment discontinuation and disease recurrence as events. Time was measured in months from the date of diagnosis.

At the time of analysis, with a median follow-up of 40 months, the estimated EFS at 40 months was 75%, and the median EFS was not reached. The Kaplan–Meier curve (**Fig. 28**) displayed a notable decline in EFS between 15 and 18 months, followed by a plateau phase extending approximately from 20 to 60 months.

These findings indicate that most adverse events or relapses occur within the first 1–2 years of treatment, while a majority of patients maintain an event-free status in the long term once that critical period is surpassed.

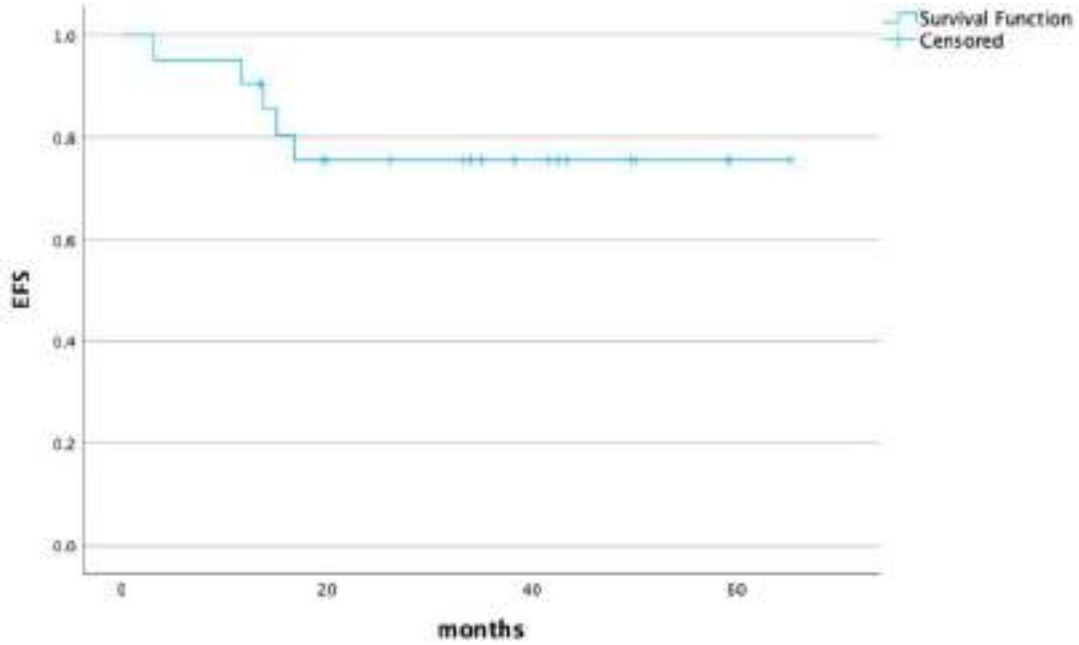

Figure 28: Kaplan–Meier curve showing event-free survival (EFS). The X-axis represents time (months) from diagnosis, and the Y-axis shows the cumulative event-free survival probability. Events included TKI-related toxicity and disease recurrence. A marked drop in EFS is observed between 15 and 18 months, followed by a plateau from 20 to 60 months

4.2.2. EFS Comparison Between Patients with 1-2 and 3 or More Comorbidities

A Kaplan–Meier survival analysis was conducted to compare the EFS between patients with 1-2 comorbidities and those with 3 or more comorbidities (**Fig. 29**). The X-axis represents time (months) from diagnosis, and the Y-axis shows EFS, defined as the cumulative probability of being free from treatment discontinuation or disease recurrence.

The analysis revealed a significant difference in survival between the two groups. Patients with 1-2 comorbidities had a significantly better EFS compared to those with 3 or more comorbidities. The Log-Rank Mantel-Cox test resulted in a p-value of 0.017, indicating that the survival distributions of the two groups are significantly different.

These findings suggest that a higher number of comorbidities is associated with a worse Event-Free Survival, highlighting the impact of comorbidity burden on treatment outcomes in this patient cohort.

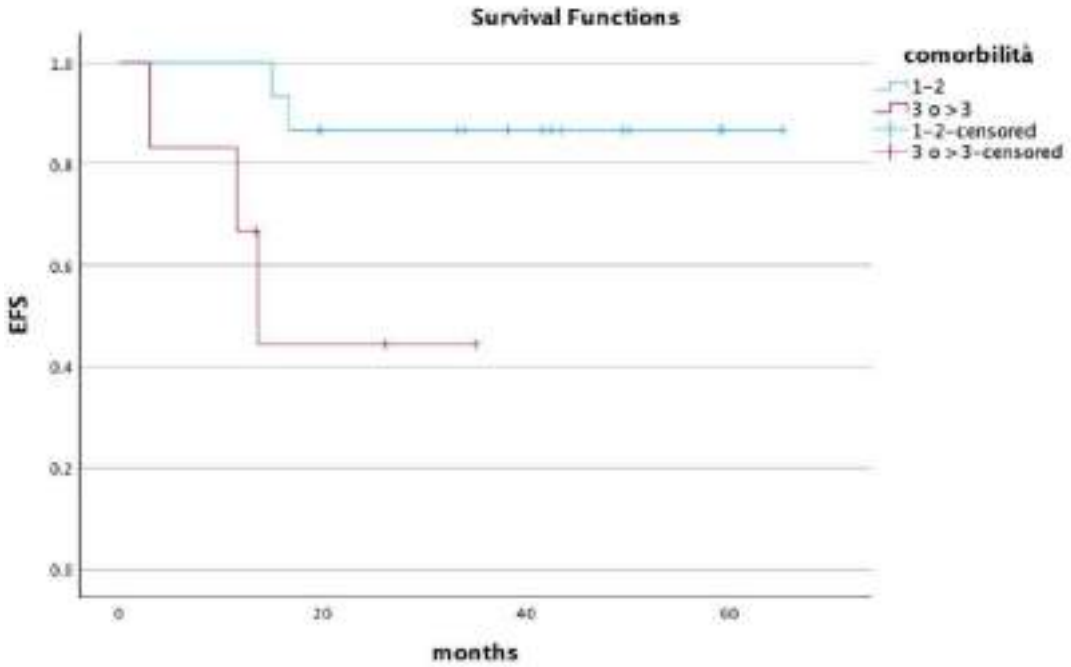

Figure 29: Kaplan–Meier curve comparing event-free survival (EFS) between patients with 1–2 comorbidities and those with 3 or more comorbidities. The X-axis represents time (months), and the Y-axis shows cumulative event-free survival. A significant difference in EFS was observed between the two groups (p-value = 0.017, LogRank Mantel-Cox test).

4.2.3. EFS Comparison Based on SIRI Score at Diagnosis

A Kaplan–Meier survival analysis was conducted to compare the EFS between patients with a SIRI score below the median and those with a SIRI score above the median at diagnosis (**Fig. 30**). The X-axis represents time (months) from diagnosis, and the Y-axis shows EFS, indicating the cumulative probability of being free from treatment discontinuation or disease recurrence.

Although patients with a higher SIRI score at diagnosis exhibited worse EFS compared to those with a lower score, the difference was not statistically significant. The Log-Rank Mantel-Cox test yielded a p-value of 0.206, indicating that the survival distributions of the two groups are not significantly different.

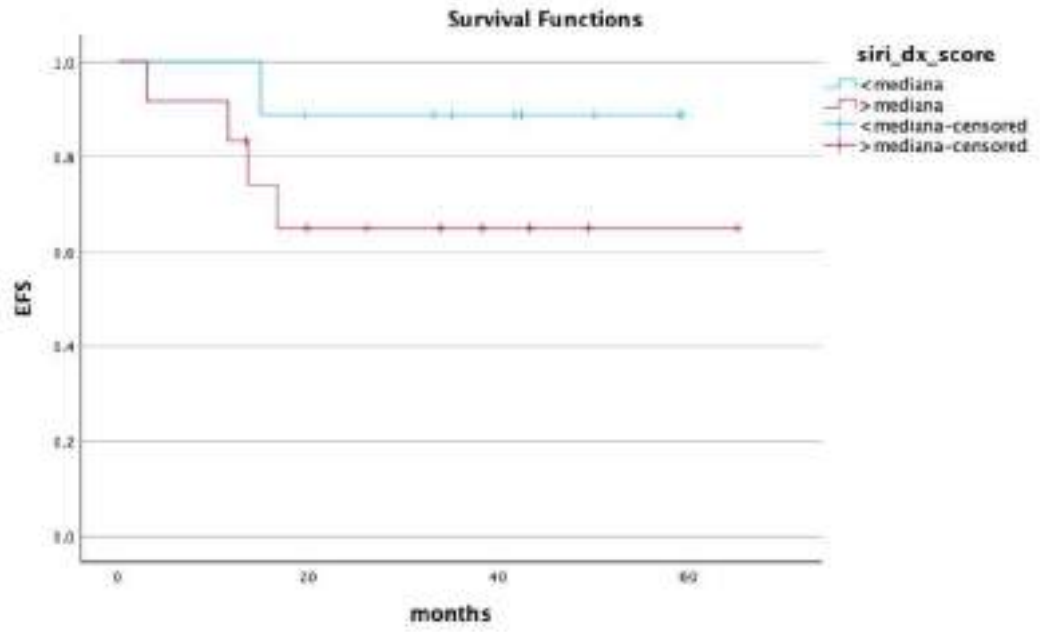

Figure 30: Kaplan–Meier curve comparing event-free survival (EFS) based on the SIRI score at diagnosis. Patients with a SIRI score below the median are compared with those with a SIRI score above the median. The X-axis represents time (months), and the Y-axis shows cumulative event-free survival. No statistically significant difference was observed between the two groups (p-value = 0.206, Chi-square = 1.597, df = 1, Log-Rank Mantel-Cox test).

4.2.4. EFS Comparison Based on First-Line TKI Used

A Kaplan–Meier survival analysis was conducted to compare the EFS between patients treated with nilotinib and those treated with imatinib as their first-line therapy (**Fig. 31**). The X-axis represents time (months) from diagnosis, and the Y-axis shows the EFS, indicating the cumulative probability of being free from treatment discontinuation or disease recurrence.

Patients treated with imatinib showed a worse EFS compared to those treated with nilotinib. Specifically, at 20 months, imatinib-treated patients had an EFS of approximately 60%, after which the survival rate plateaued. In contrast, nilotinib-treated patients maintained a 100% EFS throughout the entire follow-up period.

The comparison between the two groups was statistically significant, with a p-value of less than 0.001, further supporting the conclusion that the survival distributions of the two groups are significantly different.

This result suggests that, in this cohort, nilotinib may offer a better event-free survival compared to imatinib, at least within the context of this study.

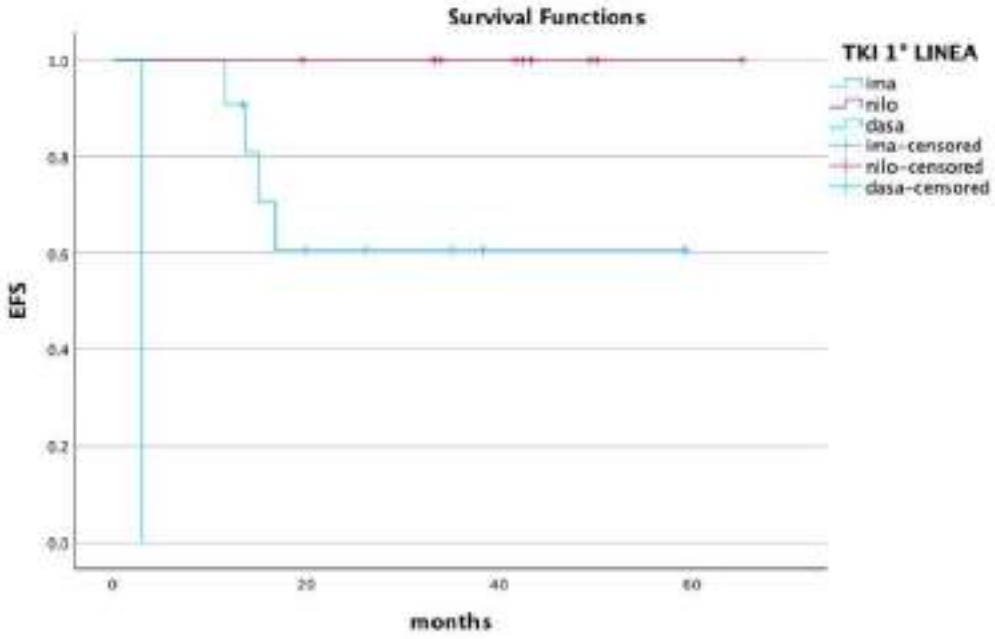

Figure 31: Kaplan–Meier curve comparing event-free survival (EFS) based on first-line TKI therapy. Patients treated with nilotinib are compared with those treated with imatinib. The X-axis represents time (months), and the Y-axis shows cumulative event-free survival. At 20 months, the EFS for patients treated with imatinib was approximately 60%, after which it plateaued. In contrast, nilotinib-treated patients maintained a 100% EFS throughout the follow-up period. A statistically significant difference was observed between the two groups (p-value < 0.001, Chi-square = 23.39, df = 2, Log-Rank Mantel-Cox test).

4.2.5. Event-Free Survival Based on EZH2 Expression Levels at diagnosis

A Kaplan–Meier survival analysis was performed to evaluate the EFS according to the expression level of the EZH2 gene at diagnosis. Patients were stratified into two groups based on whether their EZH2 expression was above or below the median value (0.017) (**Fig. 32**).

The X-axis represents time in months from diagnosis, and the Y-axis indicates cumulative EFS. Patients with EZH2 expression above the median showed significantly worse EFS compared to those with lower expression. The comparison between the survival curves yielded a p-value of 0.010 using the Log-Rank Mantel-Cox test.

These findings suggest that higher EZH2 expression at diagnosis may be associated with poorer event-free survival in this cohort.

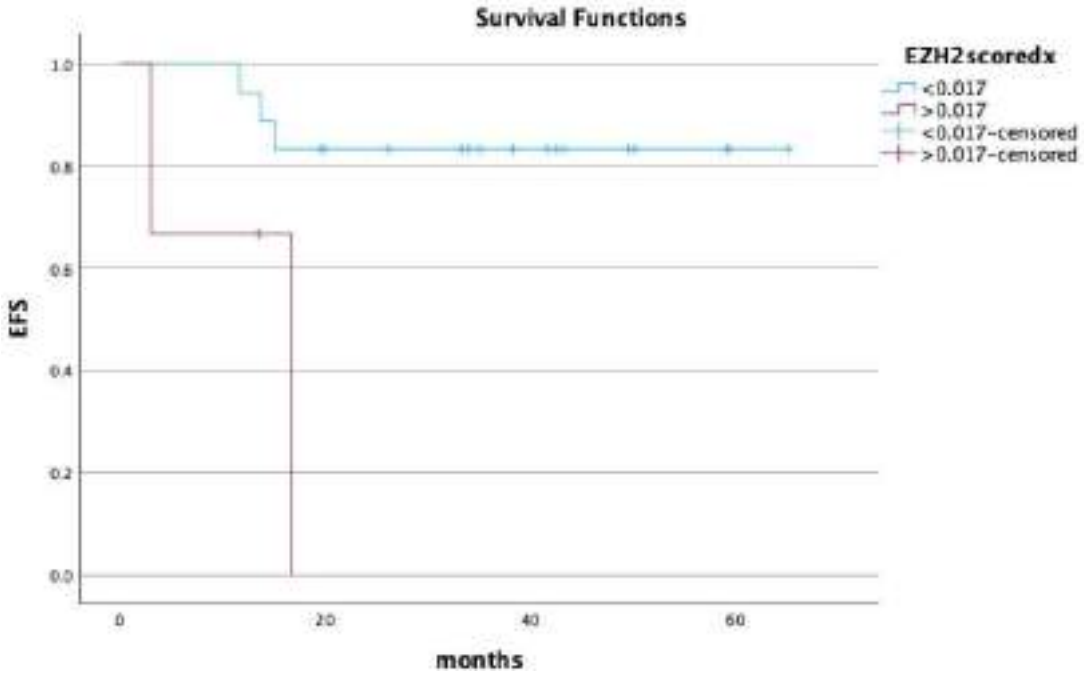

Figure 32: Kaplan–Meier curve comparing event-free survival (EFS) based on EZH2 gene expression at diagnosis. Patients were divided according to whether EZH2 expression was above or below the median value (0.017). The X-axis shows time in months, and the Y-axis represents cumulative EFS. A statistically significant difference was observed between the two groups (p = 0.010, Chi-square = 6.591, df = 1; Log-Rank Mantel-Cox test).

4.2.6. Event-Free Survival Based on EZH2 Expression Levels at 3 months

A Kaplan-Meier survival analysis was performed to assess the impact of EZH2 expression at 3 months post-treatment on EFS in CML patients. Patients were stratified based on EZH2 expression levels, with a cutoff value of 0.006. The analysis revealed that patients with EZH2 expression levels greater than the cutoff had a significantly worse EFS compared to those with lower EZH2 expression (**Fig. 33**). The p-value for this comparison was 0.014, indicating a statistically significant difference in survival distributions, further supporting the conclusion that higher EZH2 expression at 3 months is associated with poorer event-free survival.

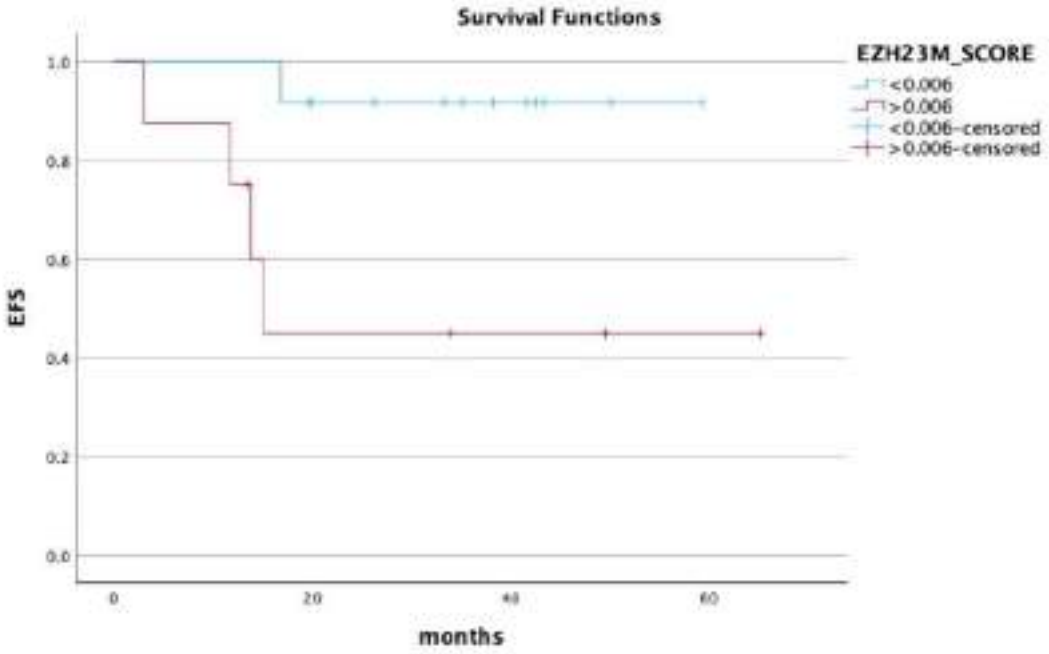

Figure 33: Kaplan–Meier curve comparing event-free survival (EFS) based on EZH2 expression at 3 months post-treatment. Patients with EZH2 expression greater than the cutoff value of 0.006 are compared with those below the cutoff. A statistically significant difference was observed between the two groups (p-value = 0.014, Chi-square = 6.02, df = 1, Log-Rank Mantel-Cox test).

4.2.7. Event-Free Survival Based on BMI1 Expression Levels at Diagnosis

A Kaplan–Meier survival analysis was performed to compare EFS between patients with high and low BMI1 expression levels at diagnosis (**Fig. 34**). The median cutoff value for BMI1 expression was set at 0.005. Although patients with higher BMI1 expression appeared to have worse EFS compared to those with lower expression, the difference was not statistically significant. The Log-Rank Mantel-Cox test yielded a p-value of 0.202, indicating that there was no significant difference in EFS between the two groups.

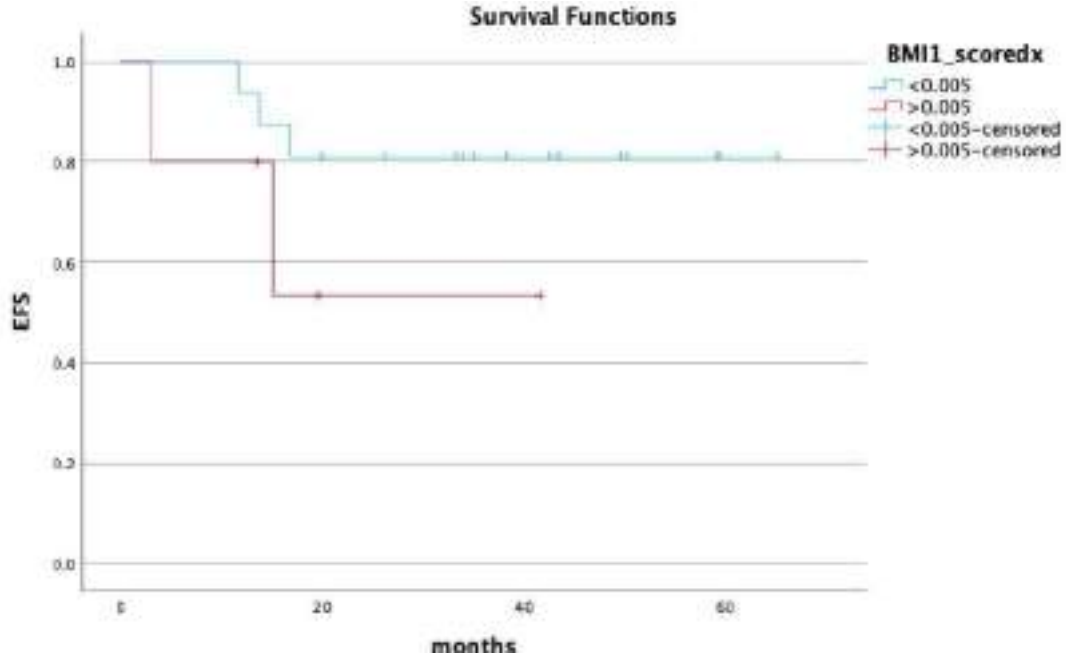

Figure 34: Kaplan–Meier curve comparing event-free survival (EFS) based on BMI1 expression levels at diagnosis. Patients with high BMI1 expression are compared with those with low BMI1 expression, using a median cutoff value of 0.005. The X-axis represents time (months), and the Y-axis shows cumulative event-free survival. No statistically significant difference was observed between the two groups (p-value = 0.202, Chisquare = 1.628, df = 1, Log-Rank Mantel-Cox test).

4.2.8. Event-Free Survival Based on PD-L1 Polymorphism

A Kaplan–Meier survival analysis was conducted to compare the EFS between patients with the homozygous PD-L1 polymorphism (2282055 T>G) and those with wild-type (WT) or heterozygous genotypes (**Fig. 35**). The X-axis represents time (months), while the Y-axis shows the cumulative EFS. The analysis was performed for all three investigated PD-L1 polymorphisms (2282055 T>G, 4143815 G>C, and 10815225 G>C); however, the only graph in which the survival curves appeared to diverge was that of the 2282055 T>G variant. Even though this separation was not statistically significant, it was visually more pronounced compared to the other two polymorphisms, whose curves overlapped almost completely. In the 2282055 T>G analysis, the curves for the homozygous PD-L1 polymorphism and the combined WT and heterozygous groups separated well, with the homozygous PD-L1 polymorphism group exhibiting worse EFS. However, no statistically significant difference was observed between the two groups (p-value = 0.087).

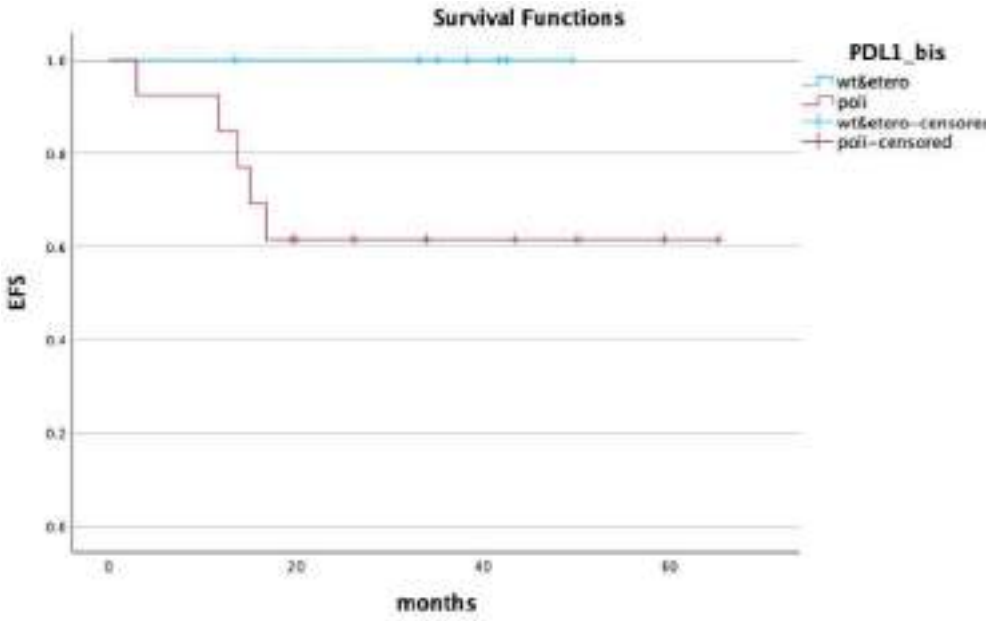

Figure 35: Kaplan–Meier curve comparing event-free survival (EFS) based on PD-L1 polymorphism. The homozygous PD-L1 group is compared with wild-type (WT) and heterozygous groups. The X-axis represents time (months), and the Y-axis shows cumulative event-free survival. Although the curves separate, no statistically significant difference was observed between the groups (p-value = 0.087, Chi-square = 2.931, df = 1, Log-Rank Mantel-Cox test)

4.2.9. Event-Free Survival and Other Factors

In this study, no statistically significant differences in EFS were observed for several factors, including ROCK gene expression, sex, age over 65 years, the EUTOS Long-Term Survival (ELTS) risk score, IGFBP6 gene expression, and PD-L1 gene expression. The analysis indicated that these factors did not significantly impact EFS outcomes in patients with chronic myeloid leukemia treated with tyrosine kinase inhibitors. Despite the possible biological relevance of these factors, none of them showed a clear association with event-free survival, as evidenced by the lack of significance in the statistical tests performed.

4.3. Molecular Response

4.3.1. Kinetics of BCR::ABL1 Transcript Reduction Over Time

Molecular response, assessed via quantitative PCR (qPCR) for BCR::ABL transcript levels, was monitored at 3, 6, and 12 months following treatment initiation. A notable reduction in BCR::ABL levels was observed between 3 and 6 months, with a p-value of 0.05, suggesting statistical significance. However, the difference between 6 and 12 months was not statistically

significant (p = 0.814), indicating that the reduction in transcript levels between these timepoints was minimal and not significant.

4.3.2. Overall distribution of molecular responses

Molecular response (MR) was defined according to BCR::ABL1 transcript levels measured on the International Scale (IS), as follows:

- MR1: BCR::ABL1 transcript between 10% and 1%
- MR2: BCR::ABL1 transcript between 1% and 0.1%
- MR3: BCR::ABL1 transcript between 0.1% and 0.01%, also referred to as major molecular response (MMR)
- MR4: BCR::ABL1 transcript ≤ 0.01%

The overall distribution of molecular responses across different timepoints is illustrated in **Fig. 36**, which shows the number of patients achieving MR1, MR2, MR3, or MR4. at 3, 6, 9, and 12 months of treatment, regardless of the type of TKI used. A progressive shift toward deeper molecular responses was observed over time, with an increasing number of patients reaching MR3 and MR4 by month 12. This dynamic reflects the expected cumulative efficacy of TKI therapy in chronic myeloid leukemia.

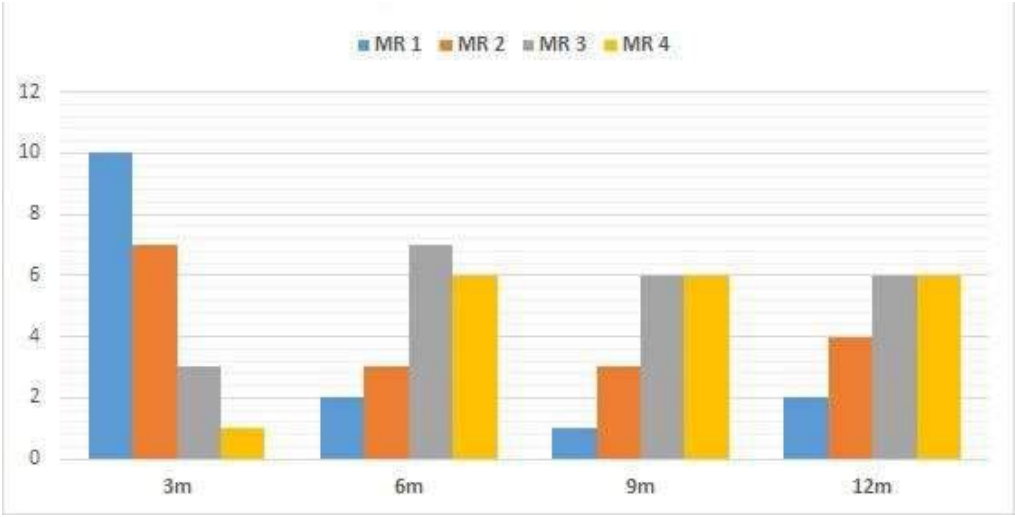

Figure 36: Global distribution of molecular responses (MR1 to MR4) at 3, 6, 9, and 12 months of treatment. The histogram shows the number of patients achieving each molecular response level at the indicated timepoints, independent of the TKI received. A progressive increase in the depth of molecular response over time is evident.

4.3.3. Best Molecular Response and Time to Achievement

During a median follow-up period of 40 months, the best molecular response achieved by each patient was recorded. Among the cohort, 14 patients reached MR4 as their best response, 6 patients achieved MR3, and 1 patient reached MR2. The time required to achieve the best molecular response is summarized in **Fig. 37**. The majority of patients (7/21) attained their best response within 6 months of treatment, followed by 4 patients at 12 months, 2 patients at 24 months and only one patient at 3 months. A smaller number of patients required longer durations to reach their best response: one patient each at 36, 40, 43, 48, 56, 63, and 65 months. For visualization purposes, in **Fig. 37**, all responses achieved beyond 48 months are grouped into a single bar labelled ">48 months". This distribution illustrates the heterogeneity in treatment response dynamics among patients, with a relevant portion achieving deep molecular remission early, while others required prolonged therapy.

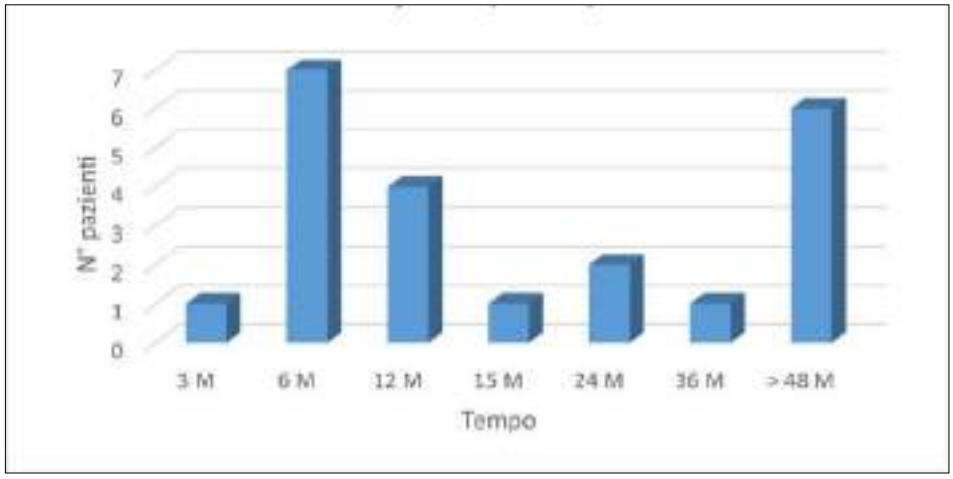

Figure 37: Time to best molecular response. Histogram showing the number of patients who achieved their best molecular response at each indicated timepoint. Responses occurring after 48 months were grouped into the ">48 months" category for clarity. The data reflect variability in response kinetics, with most patients reaching their best response within the first year of treatment

4.3.4. Molecular Response According to First-line TKI

The distribution of molecular responses at each timepoint did not significantly differ based on the type of first-line tyrosine kinase inhibitor (TKI) used imatinib or nilotinib (**Tab.12**). However, a trend toward deeper molecular responses at 12 months was observed in patients treated with nilotinib, particularly in achieving MR4, although this difference did not reach statistical significance. Specifically, 5 out of 6 patients who reached MR4 were receiving nilotinib, whereas 5 out of 6 patients in MR1 or MR2 were treated with imatinib ($p = 0.1$). This

trend is visually represented in **Fig. 38**, where the number of patients (Y-axis) is plotted against the depth of molecular response (MR1 to MR4, X-axis), with separate bars for imatinib- and nilotinib-treated patients. Despite the lack of statistical significance, these findings may suggest a tendency for nilotinib to induce deeper molecular responses within the first year of treatment.

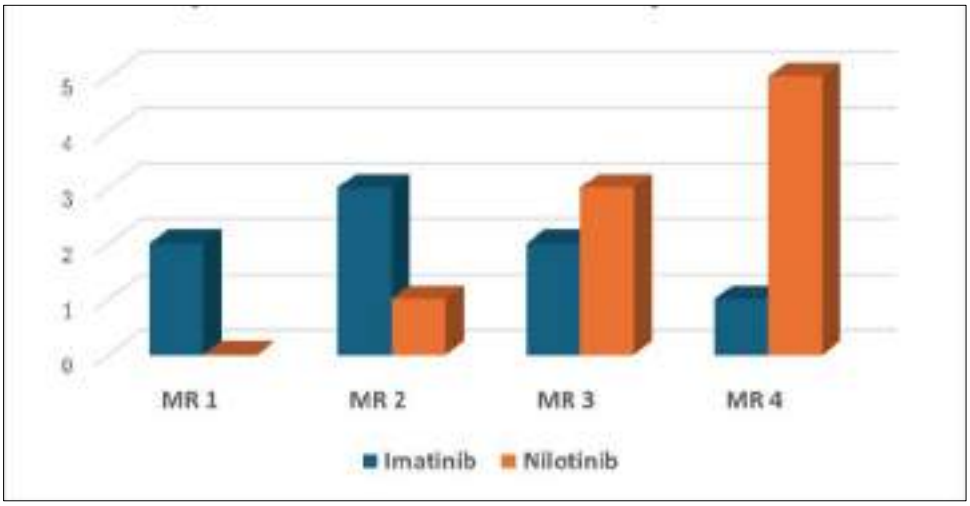

Figure 38: Distribution of molecular responses (MR1 to MR4) at 12 months according to first-line TKI. Bars represent the number of patients achieving each molecular response level, stratified by treatment with imatinib (blue) or nilotinib (orange). A trend toward deeper responses (MR4) was observed in patients treated with nilotinib.

Table 12: *Distribution of Molecular Response (MR) by Timepoint and First-line TKI*

Timepoint	**TKI**	**MR1**	**MR2**	**MR3**	**MR4**
3 months	Imatinib	7	2	2	0
	Nilotinib	2	5	1	1
	Dasatinib	1	0	0	0
Total Patients		10	7	3	1
6 months	Imatinib	1	2	3	3
	Nilotinib	1	1	4	3
Total Patients		2	3	7	6
12 months	Imatinib	2	3	2	1
	Nilotinib	0	1	3	5

Total Patients		2	4	5	6

Legend

- **MR1**: BCR::ABL1 transcript 10-1%
- **MR2**: BCR::ABL1 transcript 1-01%
- **MR3**: BCR::ABL1 transcript 0.1-0.01% (MMR)
- **MR4**: BCR::ABL1 transcript ≤0.01%

4.4. Gene Expression Analysis

4.4.1. Baseline Gene Expression at Diagnosis (EZH2, BMI1, ROCK2, IGFBP6, PD-L1)

At diagnosis, the expression patterns of the analyzed genes were as follows:

- BMI1: 100% of the patients were expressors of BMI1.
- EZH2: 100% of the patients were expressors of EZH2.
- IGFBP6: 20 out of 21 patients were expressors of IGFBP6.
- ROCK2: 100% of the patients were expressors of ROCK2.
- PD-L1: 20 out of 21 patients were expressors of PD-L1.

4.4.2 EZH2 Expression Trends at four timepoints

The expression levels of the EZH2 gene were evaluated at four timepoints: diagnosis, 3 months, 6 months, and 12 months after initiation of therapy. Paired sample statistics were used to assess changes in expression levels over time within the same patients. No statistically significant differences were observed between diagnosis and 3 months (two-sided $p = 0.36$), between 3 and 6 months ($p = 0.056$), or between diagnosis and 6 months ($p = 0.19$). However, the comparison between 3 and 6 months revealed a non-significant trend toward decreased expression ($p = 0.056$), suggesting a possible transient downregulation.

In contrast, a significant increase in EZH2 expression was observed at 12 months when compared to all earlier timepoints, with statistically significant differences between diagnosis and 12 months, 3 and 12 months, and 6 and 12 months (all two-sided $p < 0.001$).

A line graph (**Fig.40**) depicting EZH2 expression from diagnosis to 12 months illustrates this progressive upregulation, particularly pronounced after the 6-month timepoint. A separate graph (**Fig.39)** focusing on the period from diagnosis to 6 months shows a mild downward trend in EZH2 expression, although the observed changes do not reach statistical significance. These

findings suggest a delayed but marked increase in EZH2 expression during the second half of the first treatment year.

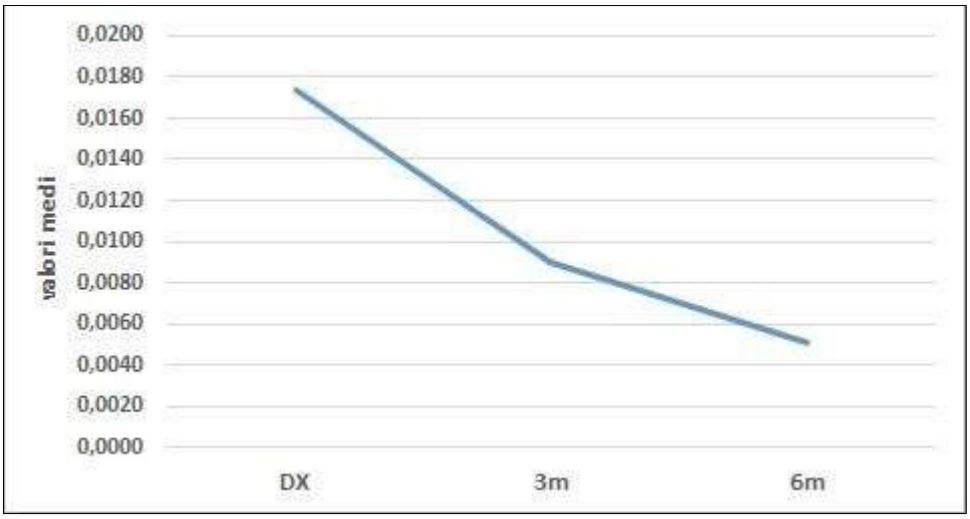

Figure 39: EZH2 expression trend from diagnosis to 6 months. Detailed view of EZH2 gene expression levels at the first three timepoints. Although a mild downward trend is observed between diagnosis and 6 months, the differences are not statistically significant ($p = 0.36$ for diagnosis vs 3 months, $p = 0.056$ for 3 vs 6 months, $p = 0.19$ for diagnosis vs 6 months).

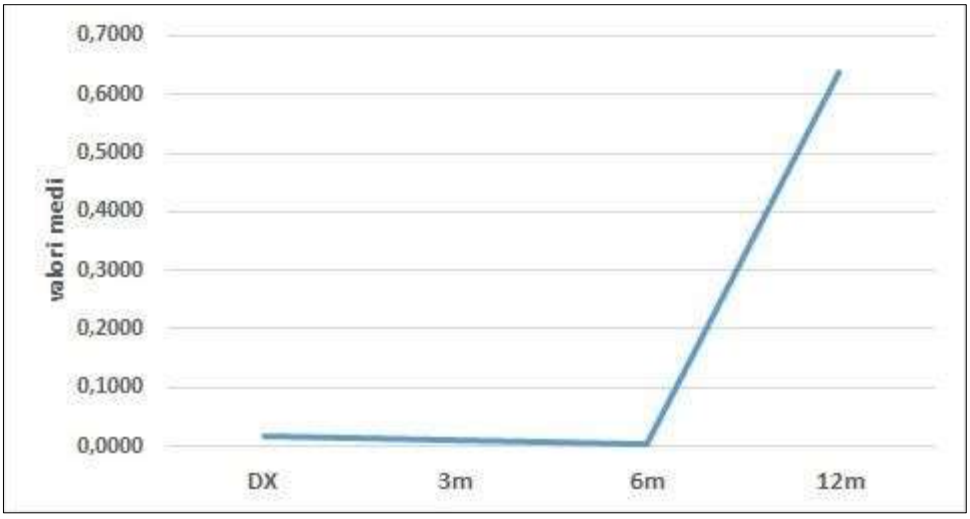

Figure 40: EZH2 expression over time from diagnosis to 12 months. Line graph illustrating the median EZH2 gene expression levels at four timepoints: diagnosis, 3 months, 6 months, and 12 months. A significant increase in EZH2 expression is observed at 12 months compared to all earlier timepoints ($p < 0.001$ for comparisons with diagnosis, 3 months, and 6 months).

4.4.3. BMI1 Expression Trends at four timepoints

The expression levels of the BMI1 gene were analyzed at four different timepoints: diagnosis, 3 months, 6 months, and 12 months after the initiation of treatment. A significant increase in

BMI1 expression was observed between diagnosis and 3 months (two-sided $p < 0.001$) (**Fig.42**), with BMI1 levels rising during the early phases of treatment. Between 3 and 6 months, no significant changes were noted (two-sided $p = 0.28$), suggesting a stabilization in expression. However, significant increases were observed when comparing diagnosis to 6 months (two-sided $p < 0.001$), diagnosis to 12 months (two-sided $p < 0.001$), 3 months to 12 months (two-sided $p < 0.001$), and 6 months to 12 months (two-sided $p < 0.001$) (**Fig.41**).

These findings indicate a progressive and consistent upregulation of BMI1 expression over time, with the most significant changes occurring between diagnosis and 3 months, and between 6 and 12 months. The increase in BMI1 expression over the course of treatment may reflect its involvement in adaptive or compensatory mechanisms in response to therapy.

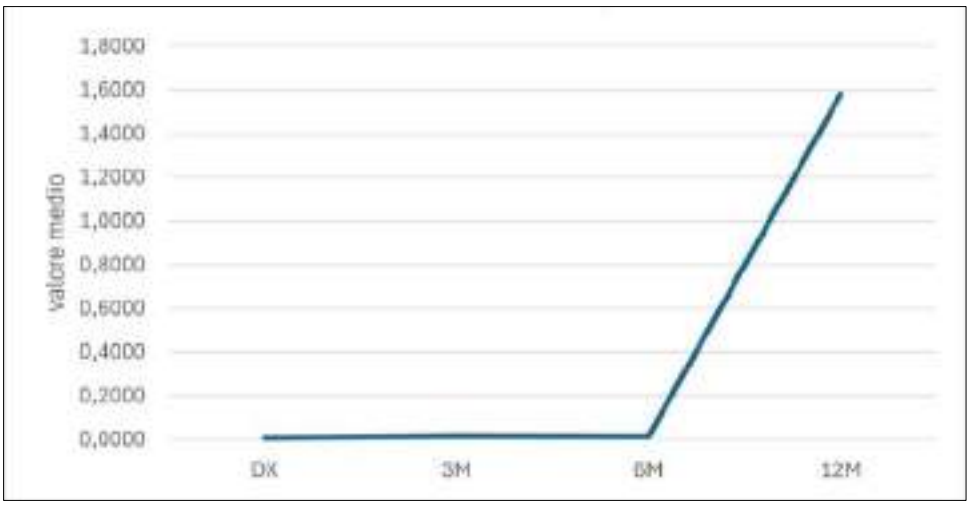

Figure 41: BMI1 Gene Expression from Diagnosis to 12 Months Line graph illustrating the median expression levels of BMI1 at four timepoints: diagnosis, 3 months, 6 months, and 12 months. A significant increase in BMI1 expression is observed at 12 months compared to earlier timepoints ($p < 0.001$).

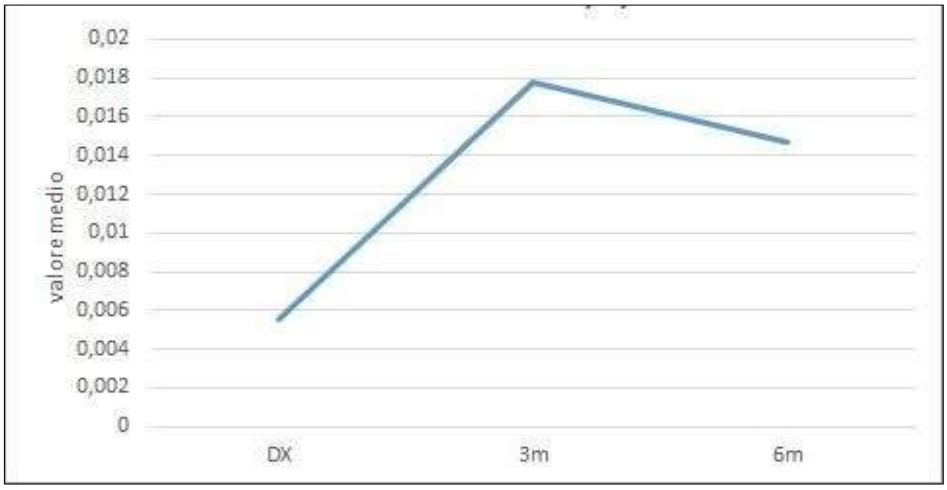

Figure 42: BMI1 Gene Expression from Diagnosis to 6 Months Line graph depicting the median expression of BMI1 at three timepoints: diagnosis, 3 months, and 6 months. A significant increase is

observed between diagnosis and 3 months ($p < 0.001$), but no significant change is noted between 3 and 6 months ($p = 0.28$). This suggests an early upregulation followed by stabilization in the first 6 months of treatment.

4.4.4. Gene Expression Trends: ROCK2, IGFBP6, PD-L1

The expression levels of the ROCK2, IGFBP6, and PD-L1 genes were evaluated between diagnosis and 12 months of treatment. For ROCK2, a significant increase in expression was observed at 12 months ($p = 0.002$). In contrast, no significant difference was found for IGFBP6 between diagnosis and 12 months ($p = 0.52$), suggesting stable expression over time. The expression of PD-L1 showed a statistically significant change with a p-value of 0.05, indicating a significant alteration in PD-L1 expression between diagnosis and 12 months (**Fig.43**).

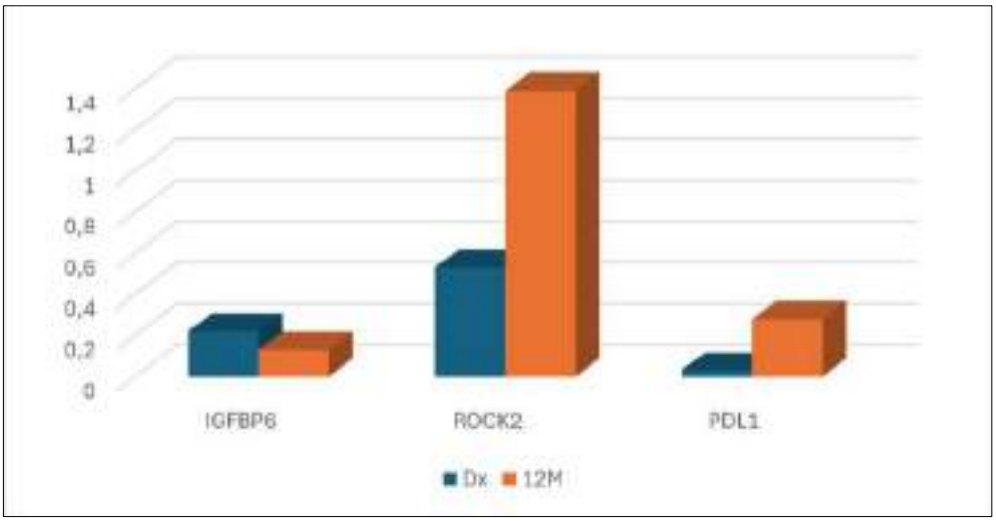

Figure 43: Gene expression changes between diagnosis and 12 months.
Histogram showing the expression levels of ROCK2, IGFBP6, and PD-L1 at diagnosis and 12 months of treatment. The data indicate a significant increase in ROCK2 expression at 12 months ($p =0.002$), while IGFBP6 expression remained stable over time ($p = 0.52$). For PD-L1, a significant increase was observed at 12 months ($p= 0.05$).

4.5. Correlation Analyses

4.5.1. Correlation Between Gene Expression and Molecular Response

4.5.1.2. BMI1 and MR at 9 Months

A significant correlation was observed between BMI1 expression greater than 0.005 and a deeper molecular response at 9 months. The analysis, conducted using Pearson's chi-square test, yielded a p-value of 0.038, indicating a statistically significant association. This suggests that

higher BMI1 expression levels at baseline may be linked to a more profound molecular response over time, potentially offering a prognostic marker for treatment outcomes in patients undergoing therapy.

4.5.1.3. EZH2 and MR at 6

A statistically significant correlation was observed between EZH2 expression levels below 0.017 and a deeper molecular response at 6 months. The Pearson's chi-square test yielded a pvalue of 0.031, indicating a significant association. This suggests that lower EZH2 expression at baseline may be linked to a more profound molecular response at 6 months, which could be useful for predicting treatment efficacy and monitoring patient progress during therapy.

4.5.1.4. EZH2 and MR at 12 Months

A significant correlation was found between EZH2 expression levels below 0.017 and a deeper molecular response at 12 months. The Pearson's chi-square test resulted in a p-value of 0.037, suggesting a meaningful association. This indicates that lower EZH2 expression at baseline may be associated with a more profound molecular response after 12 months of treatment, highlighting the potential role of EZH2 as a predictive marker for long-term therapeutic outcomes.

4.5.1.5. Lack of Correlation Between MR and IGFBP6, ROCK2, PD-L1

No significant correlation was observed between molecular response and the expression levels of IGFBP6, ROCK2, or PD-L1 at any of the timepoints considered. These findings suggest that the molecular response is not directly associated with the expression patterns of these genes in the studied cohort.

4.5.2. Correlation Between Gene Expression and Inflammatory Parameters

4.5.2.1. At Diagnosis

Spearman correlation analysis was performed to explore the associations between gene expression levels (BMI1, EZH2, IGFBP6, PD-L1, ROCK2, BCR::ABL1) and inflammatory parameters (neutrophil count, lymphocyte and platelets) at diagnosis. A significant positive correlation was observed between BMI1 and the following genes:

- EZH2 ($\rho = 0.57$, $p = 0.007$),
- IGFBP6 ($\rho = 0.44$, $p = 0.048$),

- PD-L1 ($\rho = 0.57$, $p = 0.007$),
- ROCK2 ($\rho = 0.68$, $p < 0.001$).

Regarding immune cell counts, a significant negative correlation was found between PD-L1 and neutrophil count ($\rho = -0.49$, $p = 0.026$), and between PD-L1 and lymphocyte count ($\rho = -0.51$, $p = 0.022$).

Finally, a strong positive correlation was noted between ROCK2 and PD-L1 expression levels ($\rho = 0.74$, $p < 0.001$).

These findings suggest coordinated regulation among certain genes implicated in stemness and immune modulation, as well as a potential inverse relationship between PD-L1 expression and systemic inflammatory markers.

4.5.2.2. At 12 months

At the twelve-month follow-up, several significant positive correlations were identified. The expression levels of BMI1 and EZH showed a significant correlation ($p = 0.011$), with a Spearman's rho coefficient of 0.54, indicating a moderate to strong positive association. Additionally, a significant correlation was observed between EZH2 and IGFBP6 ($p = 0.007$, rho = 0.58), as well as between ROCK2 and PD-L1 ($p = 0.005$, rho = 0.59). These findings suggest potential co-regulation or shared inflammatory pathways among these genes, which may play a role in the long-term molecular dynamics observed in the study cohort.

4.5.3. Correlation Among Gene Expression Profiles

4.5.3.1. At 3 months

At the three-month follow-up, a significant positive correlation was observed between the expression of BMI1 and EZH2, with a p-value of 0.045. The Spearman's rho coefficient for this correlation was 0.45, indicating a moderate positive relationship between these two genes at this time point. This suggests that higher expression levels of BMI1 are associated with increased expression of EZH2, highlighting a potential link between these genes in the context of epigenetics.

4.5.3.2. At 6 months

At the six-month follow-up, a significant positive correlation was found between the expression levels of BMI1 and EZH2, with a p-value of 0.024. The Spearman's rho coefficient

was 0.49, indicating a moderate positive relationship between these two genes. This result further strengthens the observation that BMI1 and EZH2 may be interconnected.

4.6. Lack of Association Between PD-L1 Expression Levels and SNP Variants

To investigate a potential association between PD-L1 expression levels and the three selected single nucleotide polymorphisms (SNPs), patients were stratified based on the median PD-L1 expression values at two timepoints: at diagnosis (median = 0.009) and at 12 months (median = 0.068). Expression levels were classified as either above or below the median. The chisquare test was applied to evaluate the distribution of genotypes across high and low expression groups for each SNP. At both timepoints, the p-values obtained were greater than 0.05, indicating that no statistically significant association was observed between the PD-L1 expression levels and the genotypic variants of the three polymorphisms analyzed.

V. DISCUSSION

The treatment of chronic myeloid leukemia (CML) has been profoundly revolutionized by the introduction of the tyrosine kinase inhibitor (TKI) imatinib in 1996, which demonstrated effective antileukemic activity by targeting CML cells in both peripheral blood and bone marrow. Imatinib significantly increased the number of patients achieving deep molecular responses. Subsequently, second- and third-generation TKIs, such as dasatinib, nilotinib, bosutinib, ponatinib, and more recently asciminib, have expanded therapeutic options. However, approximately 25–30% of patients in the chronic phase do not respond adequately to TKI therapy. In about half of these patients, mutations in the BCR::ABL1 TKD domain have been identified, whereas the causes of therapeutic failure in the remaining half remain unknown. In addition to the well-characterized role of the BCR::ABL1 gene, increasing attention is being paid to epigenetic regulators (e.g., EZH2 and BMI1), inflammation-related genes such as ROCK2 and IGFBP6, and immune evasion mechanisms mediated by PD-L1 expression.

Epigenetics is emerging as a key field in understanding the biology of CML. Alterations in epigenetic regulation may contribute to leukemogenesis and treatment resistance by silencing tumor suppressor genes or promoting oncogene expression, not only via structural DNA changes but also through chromatin remodeling mechanisms. BMI1 and EZH2 are core components of the Polycomb Repressive Complexes 1 and 2 (PRC1 and PRC2), respectively, which control gene silencing via chromatin modification. These complexes exhibit dynamic changes in composition and function during cellular differentiation and disease progression (Xu et al., 2020). Recent studies have shown a strong interconnection between BMI1 and EZH2 in lymphomas and leukemias, with correlated overexpression patterns contributing to aggressive phenotypes (Lusci Gemignani et al., 2025).

In our study, we observed that BMI1 expression significantly increased after 3 months of TKI therapy, and remained elevated at 6 and 12 months, suggesting a sustained activation of PRC1 induced by treatment (Crea, Di Paolo, et al., 2015). Additionally, we confirmed the strong correlation between BMI1 and EZH2 expression, consistent with previous findings in hematological malignancies (Lusci Gemignani et al., 2025). This association may result from EZH2-mediated suppression of miR-200c, which in turn leads to the upregulation of BMI1 (Xu et al., 2020).

Recent evidence has further clarified the functional role of EZH2 in the maintenance of leukemic stem cells (LSCs), which represent a major obstacle to disease eradication in CML. EZH2 is significantly overexpressed in CML LSCs compared to normal hematopoietic stem

cells, and this overexpression contributes to therapy resistance and disease persistence (Xie et al., 2016). Pharmacological inhibition of EZH2 using GSK126 has been shown to selectively reduce CML LSCs while sparing normal stem cells, partly by reactivating the tumor suppressor gene PTEN, which is epigenetically silenced by EZH2-mediated H3K27 trimethylation (Zhou et al., 2018). These findings highlight the central role of EZH2 in preserving LSC identity and support its potential as a therapeutic target to prevent relapse and achieve deeper, more durable remissions.

From a methodological perspective, our use of a multiplex digital droplet PCR (ddPCR) assay enabled the simultaneous and quantitative measurement of four target genes with high sensitivity and reproducibility, overcoming the limitations of conventional real-time PCR, particularly in the absence of standardized references.

Regarding inflammatory and immune parameters, IGFBP6 is known to act as a proinflammatory mediator, whose expression is upregulated under hyperthermic conditions and which promotes neutrophil activation and oxidative burst (Conese et al., 2018). ROCK2 regulates inflammatory responses by influencing the Th17/Treg cell balance, promoting Th17 polarization through activation of STAT3 and IRF4 (Zanin-Zhorov & Blazar, 2021).

Correlation analysis between gene expression and inflammatory markers at diagnosis revealed a strong positive correlation between ROCK2 and PD-L1 expression ($\rho = 0.74$, $p < 0.001$). This suggests possible co-regulation of inflammatory and immune escape pathways. Interestingly, this link is supported by recent evidence in solid tumors: ROCK-dependent moesin phosphorylation was shown to stabilize PD-L1 expression on the tumor cell membrane, enhancing immune evasion (Meng et al., 2020). Our finding may reflect a similar mechanism in CML pathophysiology.

Furthermore, PD-L1 expression correlated negatively with neutrophil counts ($\rho = –0.49$, $p = 0.026$) and lymphocyte counts ($\rho = –0.51$, $p = 0.022$), supporting its role in systemic immune suppression. Notably, the ROCK2–PD-L1 correlation persisted even after 12 months of TKI therapy ($\rho = 0.59$, $p = 0.005$), suggesting that these immunoregulatory pathways may remain active despite hematologic remission.

Importantly, pro-inflammatory and oxidative stress changes have been documented during nilotinib treatment, potentially contributing to cardiovascular and metabolic side effects (Sicuranza et al., 2022). These systemic alterations might also influence immune dynamics and epigenetic regulation in CML, further reinforcing the need for integrative biomarkers.

In conclusion, our results highlight the central role of Polycomb group proteins BMI1 and EZH2 in CML progression and treatment response, suggesting their potential as both

biomarkers and therapeutic targets. The interaction between ROCK2, IGFBP6, and PD-L1 points to a complex interplay between inflammation and immune evasion in disease maintenance and resistance. Combinatorial therapeutic strategies targeting epigenetic regulators and immune pathways may offer a promising direction to overcome current limitations in TKI monotherapy.

Further investigations are warranted to elucidate the molecular mechanisms underlying these epigenetic and immunologic alterations and to determine the specific effects of different TKIs on these regulatory networks.

REFERENCES

Abruzzese E, Breccia M, Latagliata R. Second-generation tyrosine kinase inhibitors in firstline treatment of chronic myeloid leukaemia (CML). BioDrugs. 2014;28(1):17–26.

Ahmed R, Naqi N, Hussain I, Khattak BK, Nadeem M, Iqbal J. Presenting phases of chronic myeloid leukemia. J Coll Physicians Surg Pak. 2009;19(8):469–472.

Alshemmari SH, Rajan R, Emadi A. Molecular pathogenesis and clinical significance of driver mutations in primary myelofibrosis: A review. Med Princ Pract. 2016;25:501–509.

Alunno A, et al. Insulin-like growth factor binding protein 6 in rheumatoid arthritis: A possible novel chemotactic factor? Front Immunol. 2017;8:1–9.

Apperley JF. Chronic myeloid leukaemia. Lancet. 2015;385(9976):1447–1459.

Arber DA, Orazi A, Hasserjian R, et al. The 2016 revision to the WHO classification of myeloid neoplasms and acute leukemia. Blood. 2016;127(20):2391–2405.

Baccarani M, Deininger MW, Rosti G, Hochhaus A, Soverini S, Apperley JF, et al. European LeukemiaNet recommendations for the management of chronic myeloid leukemia: 2013. Blood. 2013;122(6):872–884.

Bach LA. Recent insights into the actions of IGFBP-6. J Cell Commun Signal. 2015;9:189–200.

Barbui T, Thiele J, Vannucchi AM, Tefferi A. Rationale for revision and proposed changes of the WHO diagnostic criteria for polycythemia vera, essential thrombocythemia and primary myelofibrosis. Blood Cancer J. 2015;5:e337.

Bavaro L, Martelli M, Cavo M, Soverini S. Mechanisms of disease progression and resistance to tyrosine kinase inhibitor therapy in chronic myeloid leukemia: An update. Int J Mol Sci. 2019;20(24):6141.

Bettelli E, et al. Reciprocal developmental pathways for the generation of pathogenic effector TH17 and regulatory T cells. Nature. 2006;441:235–238.

Biswas PS, et al. Phosphorylation of IRF4 by ROCK2 regulates IL-17 and IL-21 production and the development of autoimmunity in mice. J Clin Invest. 2010;120:3280–3295.

Biswas PS, Gupta S, Chang E, Bhagat G, Pernis AB. Aberrant ROCK activation promotes the development of type I diabetes in NOD mice. Cell Immunol. 2011;266(2):111–115.

Brave M, Gootenberg J, Kaminskas E, Farrell A. Sprycel for chronic myeloid leukemia and Philadelphia chromosome-positive acute lymphoblastic leukemia resistant to or intolerant of imatinib mesylate. Clin Cancer Res. 2008;14(2):352–359.

Butte MJ, Peña-Cruz V, Kim MJ, Freeman GJ, Sharpe AH. Interaction of human PD-L1 and B7-1. Mol Immunol. 2008;45(13):3567–3572.

Campo E, Swerdlow SH, Harris NL, Pileri S, Stein H, Jaffe ES. The 2008 WHO classification of lymphoid neoplasms and beyond. Hematology Am Soc Hematol Educ Program. 2008:341–358.

Carlesso N, Frank DA, Griffin JD. Tyrosyl phosphorylation and DNA binding activity of signal transducers and activators of transcription (STAT) proteins in hematopoietic cell lines transformed by Bcr/Abl. J Exp Med. 1996;183(3):811–820.

Castoldi G, Collaboratori. Malattie del sangue e degli organi emopoietici. 2013.

Chen W, Nyuydzefe MS, Weiss JM, Zhang J, Waksal SD, Zanin-Zhorov A. ROCK2, but not ROCK1 interacts with phosphorylated STAT3 and co-occupies TH17/TFH gene promoters in TH17-activated human T cells. Sci Rep. 2018;8(1):16636.

Christiansson L, Söderlund S, Svensson E, Mustjoki S, Bengtsson M, Simonsson B, et al. Increased level of myeloid-derived suppressor cells, programmed death receptor ligand 1/programmed death receptor 1, and soluble CD25 in Sokal high risk chronic myeloid leukemia. PLoS One. 2013;8(1):e55818.

Cilloni D, Saglio G. Molecular pathways: BCR-ABL. Clin Cancer Res. 2012;18(4):930–937.

Conese M, et al. Insulin-like growth factor-6 (IGFBP-6) stimulates neutrophil oxidative burst, degranulation and chemotaxis. Inflamm Res. 2018;67:107–109.

Cortes J, Pvlovsky C, Saußele S. Chronic myeloid leekaemia. Lancet. 2021 ;398/10314):1914-1926.

Cortez D, Reuther G, Pendergast AM. The Bcr-Abl tyrosine kinase activates mitogenic signaling pathways and stimulates G1-to-S phase transition in hematopoietic cells. Oncogene. 1997;15(19):2333–2342.

Crea F, Di Paolo A, Liu HH, Polillo M, Clermont PL, Guerrini F, Ciabatti E, Ricci F, Baratè C, Fontanelli G, Barsotti S, Morganti R, Danesi R, Wang Y, Petrini M, Galimberti S, Helgason CD. Polycomb genes are associated with response to imatinib in chronic myeloid leukemia. Epigenomics. 2015;7(5):757–769.

Dameshek W. Some speculations on the myeloproliferative syndromes. Blood. 1951;6(4):372–375.

Dang H, Mao W, Wang S, Sha J, Lu M, Cong L, Meng X, Li H. Systemic inflammation response index as a prognostic predictor in patients with acute ischemic stroke: A propensity score matching analysis. Front Neurol. 2023;13:1049241.

Deeks ED. Asciminib: First approval. Drugs. 2022;82:219–226.

Deininger M, O'Brien SG, Guilhot F, et al. International randomized study of interferon vs STI571 (IRIS) 8-year follow-up: sustained survival and low risk for progression or events in patients with newly diagnosed chronic myeloid leukemia in chronic phase (CML-CP) treated with imatinib. Blood. 2009;114:462.

Duan R, Du W, Guo W. EZH2: A novel target for cancer treatment. J Hematol Oncol. 2020;13(1):104.

Edlund S, Landström M, Heldin CH, Aspenström P. Transforming growth factor-beta-induced mobilization of actin cytoskeleton requires signaling by small GTPases Cdc42 and RhoA. Mol Biol Cell. 2002;13:902–914.

Eechoute K, Sparreboom A, Burger H, et al. Drug transporters and imatinib treatment: implications for clinical practice. Clin Cancer Res. 2010;17(3):406–415.

Faderl S, Talpaz M, Estrov Z, O'Brien S, Kurzrock R, Kantarjian HM. The biology of chronic myeloid leukemia. N Engl J Med. 1999;341(3):164–172.

Galimberti S, Grassi S, Baratè C, et al. The polycomb BMI1 protein is co-expressed with CD26+ in leukemic stem cells of chronic myeloid leukemia. Front Oncol. 2018;8:555.

Gandhi V, Plunkett W, Cortes JE. Omacetaxine: a protein translation inhibitor for treatment of chronic myelogenous leukemia. Clin Cancer Res. 2014;20(7):1735–1740.

Giuliani N, Others. Ematologia per Medicina – Scienze Biologiche – Biotecnologie Mediche. 2020.

Guglielmelli P, Lasho TL, Rotunno G, Score J, Mannarelli C, Pancrazzi A, et al. The number of prognostically detrimental mutations and prognosis in primary myelofibrosis: an international study of 797 patients. Leukemia. 2014.

He Y, et al. Antiinflammatory effect of Rho kinase blockade via inhibition of NFκB activation in rheumatoid arthritis. Arthritis Rheum. 2008;58:3366–3376.

Herrmann H, et al. Dipeptidylpeptidase IV (CD26) defines leukemic stem cells (LSC) in chronic myeloid leukemia. Blood. 2014;123:3951–3962.

Herviou L, Cavalli G, Cartron G, Klein B, Moreaux J. EZH2 in normal hematopoiesis and hematological malignancies. Oncotarget. 2015;7(3):2284-2296.

Hochhaus A, Baccarani M, Silver RT, Schiffer C, Apperley JF, Cervantes F, Hehlmann R. European LeukemiaNet 2020 recommendations for treating chronic myeloid leukemia. Leukemia. 2020;34:966-984.
Ilaria RL, Van Etten RA. P210 and P190 induce the tyrosine phosphorylation and DNA binding activity of multiple specific STAT family members. J Biol Chem. 1996;271(49):31704-31710.
Iqbal N, Iqbal N. Imatinib: A breakthrough of targeted therapy in cancer. Chemother Res Pract. 2014;2014:1-9.

Isgro J, Gupta S, Jacek E, et al. Enhanced rho-associated protein kinase activation in patients with systemic lupus erythematosus. Arthritis Rheum. 2013;65(6):1592-1602.
Jabbour E, Kantarjian H. Chronic myeloid leukemia: 2020 update on diagnosis, therapy, and monitoring. Am J Hematol. 2020;95(6):691-709.

Jain P, Kantarjian H, Patel KP, et al. Impact of BCR-ABL transcript type on outcome in patients with chronic-phase CML treated with tyrosine kinase inhibitors. Blood. 2016;127(10):1269-1275.

Jain SK, Susa M, Keeler ML, Carlesso N, Druker B, Varticovski L. PI 3-kinase activation in BCR/abl-transformed hematopoietic cells does not require interaction of p85 SH2 domains with p210 BCR/abl. Blood. 1996;88(5):1542-1550.

Julian L, Olson MF. Rho-associated coiled-coil containing kinases (ROCK). Small GTPases. 2014;5:e29846.

Kantarjian HM, Keating MJ, Freireich EJ. Toward the potential cure of leukemias in the next decade. Cancer. 2018;124(22):4301-4313.

Khoury JD, Solary E, Abla O, Akkari Y, Alaggio R, Apperley JF, Bejar R, Berti E, Busque L, Chan JKC, Chen W, Chen X, Chng W-J, Choi JK, Colmenero I, Coupland SE, Cross NCP, De Jong D, Elghetany MT, et al. The 5th edition of the World Health Organization Classification of Haematolymphoid Tumours: Myeloid and histiocytic/dendritic neoplasms. Leukemia. 2022;36(7):1703-1719.

Liso A, Capitanio N, Gerli R, Conese M. From fever to immunity: A new role for IGFBP-6? J Cell Mol Med. 2018;22:4588-4596.

Liso A, Castellani S, Massenzio F, et al. Human monocyte-derived dendritic cells exposed to hyperthermia show a distinct gene expression profile and selective upregulation of IGFBP6. Oncotarget. 2017;8(37):60826–60840.

Liu Y, Yang Q. The roles of EZH2 in cancer and its inhibitors. Med Oncol. 2023;40(6):167.
Longmore M, et al. Oxford Handbook of Clinical Medicine. 9th ed. Oxford: Oxford University Press; 2014.

Lusci Gemignani A, Papotti R, Bomben R, et al. A new digital droplet PCR method for looking at epigenetics in diffuse large B-cell lymphomas: The role of BMI1, EZH2, and USP22 genes. Int J Lab Hematol. 2025 Feb;47(1):101-109.

Matsui T, Amano M, Yamamoto T, et al. Rho-associated kinase, a novel serine/threonine kinase, as a putative target for small GTP binding protein Rho. EMBO J. 1996;15(9):2208–16.

Meng F, Su Y, Xu B. Rho-associated protein kinase-dependent moesin phosphorylation is required for PD-L1 stabilization in breast cancer. Mol Oncol. 2020 Nov;14(11):2701-2712.
Mohan S, Baylink DJ. IGF-binding proteins are multifunctional and act via IGF-dependent and -independent mechanisms. J Endocrinol. 2002;175:19–31.

Mohty M, Yong ASM, Szydlo RM, Apperley JF, Melo JV. The polycomb group BMI1 gene is a molecular marker for predicting prognosis of chronic myeloid leukemia. Blood. 2007;110(1):380–383.

Mumprecht S, Schürch C, Schwaller J, et al. Programmed death 1 signaling on chronic myeloid leukemia-specific T cells results in T-cell exhaustion and disease progression. Blood. 2009;114(8):1528–36.

Nishioka C, Ikezoe T, Yang J, Yokoyama A. BCR/ABL increases EZH2 levels which regulates XIAP expression via miRNA-219 in chronic myeloid leukemia cells. Leuk Res. 2016;45:24–

32.

Nowell PC, Hungerford DA. A minute chromosome in human chronic granulocytic leukemia. Science. 1960;132(3438):1497–1501.
O'Brien SG, Guilhot F, Larson RA, et al; IRIS Investigators. Imatinib compared with interferon and low-dose cytarabine for newly diagnosed chronic-phase chronic myeloid leukemia. N Engl J Med. 2003;384:994–1004.

Pendergast AM, Muller AJ, Havlik MH, Maru Y, Witte ON. BCR sequences essential for transformation by the BCR-ABL oncogene bind to the ABL SH2 regulatory domain in a nonphosphotyrosine-dependent manner. Cell. 1991;66(1):161–171.

Pendergast AM, Quilliam LA, Cripe LD, et al. BCR-ABL-induced oncogenesis is mediated by direct interaction with the SH2 domain of the GRB-2 adaptor protein. Cell. 1993;75(1):175–185.

Rea D, Nicolini FE, Rousselot P, et al. Discontinuation of dasatinib or nilotinib in chronic myeloid leukemia patients with stable undetectable Bcr-Abl transcripts: Results from the French CML group (FILMC). Blood. 2011;114:608.

Reddy EP, Aggarwal AK. The ins and outs of BCR-ABL inhibition. Genes Cancer. 2012;3(5–6):447–454.

Ren R. Mechanisms of BCR–ABL in the pathogenesis of chronic myelogenous leukaemia. Nat Rev Cancer. 2005;5(3):172–183.

Rinke J, Chase A, Cross NCP, Hochhaus A, Ernst T. EZH2 in myeloid malignancies. Cells. 2020;9(7):1639.

Rizo A, Olthof S, Han L, Vellenga E, de Haan G, Schuringa JJ. Repression of BMI1 in normal and leukemic human CD34(+) cells impairs self-renewal and induces apoptosis. Blood. 2009;114(8):1498–1505.

Rossari F, Minutolo F, Orciuolo E. Past, present, and future of BCR-ABL inhibitors: From chemical development to clinical efficacy. J Hematol Oncol. 2018;11(1):84.

Rousselot P, Cony-Makhoul P, Nicolini F, et al. Loss of major molecular response is accurate for restarting imatinib after imatinib discontinuation in CP-CML patients with long-lasting CMR: Importance of fluctuating values of MRD and interferon. Haematologica. 2012;97(4):619–625.

Saglio G, Kim DW, Issaragrisil S, Le Coutre P, Etienne G, Lobo C, Pasquini R, Clark RE, Hochhaus A, Hughes TP, Gallagher N, Hoenekopp A, Dong M, Haque A, Larson RA, Kantarjian HM. Nilotinib versus imatinib for newly diagnosed chronic myeloid leukemia. N Engl J Med. 2010;362(24):2251–2259.

Sahasrabuddhe AA. BMI1: A biomarker of hematologic malignancies. Biomark Cancer. 2016;8:65–72.

Sattler M, Mohi MG, Pride YB, Quinnan LR, Malouf NA, Podar K, Gesbert F, Iwasaki H, Li S, Van Etten RA, Gu H, Griffin JD, Neel BG. Critical role for Gab2 in transformation by BCR/ABL. Cancer Cell. 2002;1(5):479–492.

Saudy NS, Fawzy IM, Azmy E, Goda EF, Eneen A, Abdul Salam EM. BMI1 gene expression in myeloid leukemias and its impact on prognosis. Blood Cells Mol Dis. 2014;53(4):194–198.
Savage D, Antman K. Imatinib mesylate—A new oral targeted therapy. N Engl J Med. 2002;346(9):683–693.
Sehgal A, Whiteside TL, Boyiadzis M. Programmed death-1 checkpoint blockade in acute myeloid leukemia. Expert Opin Biol Ther. 2015;15(8):1191–1203.
Shallis RM, Wang R, Davidoff A, Ma X, Podoltsev NA, Zeidan AM. Epidemiology of the classical myeloproliferative neoplasms: The four corners of an expansive and complex map. Blood Rev. 2020;42:100706.

Sholikah TA. Fusion gene BCR-ABL: From etiopathogenesis to the management of chronic myeloid leukemia. J Kedokt Kesehat Indones. 2017;8(1):29–37.

Sicuranza A, Ferrigno I, Abruzzese E, Iurlo A, Galimberti S, Gozzini A, Luciano L, Stagno F, Russo Rossi A, Sgherza N, Cattaneo D, Zuanelli Brambilla C, Marzano C, Fava C, Mulas O, Cencini E, Santoni A, Sammartano V, Gozzetti A, Puccetti L, Bocchia M. Pro-Inflammatory and Pro-Oxidative Changes During Nilotinib Treatment in CML Patients: Results of a Prospective Multicenter Front-Line TKIs Study (KIARO Study). Front Oncol. 2022 Feb 1;12:835563.

Siegel RL, Giaquinto AN, Jemal A. Cancer statistics, 2024. CA Cancer J Clin. 2024;74(1):12–49.

Skorski T, Kanakaraj P, Nieborowska-Skorska M, Ratajczak MZ, Wen SC, Zon G, Gewirtz AM, Perussia B, Calabretta B. Phosphatidylinositol-3 kinase activity is regulated by BCR/ABL and is required for the growth of Philadelphia chromosome-positive cells. Blood. 1995;86(2):726–736.

Talpaz M, Mercer J, Hehlmann R. The interferon-alpha revival in CML. Ann Hematol. 2015;94(Suppl 2):S195–207.

Venuto S, et al. IGFBP-6 network in chronic inflammatory airway diseases and lung tumor progression. Int J Mol Sci. 2023;24:4804.

Völkel P, Dupret B, Le Bourhis X, Angrand P-O. Diverse involvement of EZH2 in cancer epigenetics. Am J Transl Res. 2015;7(2):175–193.

Wagner K-D, Wagner N. The senescence markers p16INK4A, p14ARF/p19ARF, and p21 in organ development and homeostasis. Cells. 2022;11(12):1966.

Wang W, Qin JJ, Voruganti S, Nag S, Zhou J, Zhang R. Polycomb group (PcG) proteins and human cancers: Multifaceted functions and therapeutic implications. Med Res Rev. 2015;35(6):1220–1264.

Weiss JM, et al. ROCK2 signaling is required to induce a subset of T follicular helper cells through opposing effects on STATs in autoimmune settings. Sci Signal. 2016;9:ra73.

Wu Y, Zhao T, Jia Z, Cao D, Cao X, Pan Y, Zhao D, Zhang B, Jiang J. Polymorphism of the programmed death-ligand 1 gene is associated with its protein expression and prognosis in gastric cancer. J Gastroenterol Hepatol. 2018.

Xie H, Peng C, Huang J, Li BE, Kim W, Smith EC, Fujiwara Y, Qi J, Cheloni G, Das PP, Nguyen M, Li S, Bradner JE, Orkin SH. Chronic myelogenous leukemia initiating cells require polycomb group protein EZH2. Cancer Discov. 2016;6(11):1237–1247.

Xu L, Lin J, Deng W, Luo W, Huang Y, Liu CQ, Zhang FP, Qin YF, Wong PP, Liu C. EZH2 facilitates BMI1-dependent hepatocarcinogenesis through epigenetically silencing microRNA-200c. Oncogenesis. 2020;9(11):101.

Zanin-Zhorov A, Blazar BR. ROCK2, a critical regulator of immune modulation and fibrosis has emerged as a therapeutic target in chronic graft-versus-host disease. Clin Immunol. 2021;230:108823.

Zanin-Zhorov A, et al. Cutting edge: Selective oral ROCK2 inhibitor reduces clinical scores in patients with psoriasis vulgaris and normalizes skin pathology via concurrent regulation of IL-17 and IL-10. J Immunol. 2017;198:3809–3814.

Zhang X, Tao Y, Troiani L, Markovic-Plese S. Simvastatin inhibits IFN regulatory factor 4 expression and Th17 cell differentiation in CD4+ T cells derived from patients with multiple sclerosis. J Immunol. 2011;187:3431–3437.

Zhou J, Nie D, Li J, Du X, Lu Y, Li Y, Liu C, Dai W, Wang Y, Jin Y, Pan J. PTEN Is Fundamental for Elimination of Leukemia Stem Cells Mediated by GSK126 Targeting EZH2 in Chronic Myelogenous Leukemia. Clin Cancer Res. 2018;24(1):145–157.

Proprietà di connettività e small-world del Default Mode Network e dei suoi due sottosistemi: un prototipo di studio con dati e strumenti *open-source*

Lorenzo Murace

Abstract

Il Default Mode Network (DMN) è una delle reti cerebrali più studiate nel contesto della cognizione umana, responsabile di processi quali l'elaborazione del sé, la memoria episodica e la rappresentazione di stati mentali altrui. Nonostante la sua importanza funzionale, restano ancora aperte domande sul modo in cui le singole regioni che ne fanno parte si organizzino per garantire efficienza ed integrazione dell'informazione.

In questo lavoro, abbiamo indagato le proprietà connettive del DMN e dei suoi due principali sottosistemi – il componente anteriore dorso-mediale (dMPFC) e quello posteriore temporo-parietale (TML) – applicando tecniche di analisi network a dati fMRI (risonanza magnetica funzionale) *open-source*. Utilizzando una parcellazione fine basata sull'atlante di Schaefer, abbiamo estratto la matrice di correlazione funzionale per tre soggetti e costruito grafi pesati interpretando i coefficienti come pesi di adiacenza. In particolare, tramite l'analisi network, abbiamo individuato i due sottosistemi principali del DMN - con risultanti concordanti con studi precedenti, condotti con tecniche statistiche - e abbiamo indagato le proprietà della rete quanto a trasmissione e integrazione dell'informazione. Abbiamo, inoltre, osservato le proprietà combinate di alta connettività globale e specializzazione locale del DMN, caratteristiche dei network cosiddetti *small-world*. Congiuntamente, abbiamo approfondito le proprietà di centralità di ciascuna regione della rete.

I valori riscontrati con questo studio, pur attuato in forma di prototipo, vista la quantità ridotta dei dati presi a campione e le tecniche basilari impiegate, suggeriscono come l'efficienza funzionale del DMN nell'elaborazione rapida e simultanea di informazioni complesse derivi da una distribuzione equilibrata delle connessioni piuttosto che dalla presenza di pochi *hub* dominanti.

Parole-chiave: Default Mode Network; small-worldness; network analysis; connettività funzionale; Community detection.

I. INTRODUZIONE

1.1. Il Default Mode Network (DMN)

Quando un individuo non è impegnato nell'esecuzione di un compito specifico (ossia, in gergo tecnico, quando è "a riposo"), nel suo cervello si attivano diverse regioni neurali che invece risultano meno attive durante la persecuzione attiva di uno scopo.

Tale rete di regioni è stata inizialmente osservata nelle scansioni di controllo di studi che impiegavano la risonanza magnetica per indagare l'attivazione di determinate aree del cervello durante l'esecuzione di specifiche azioni. Durante tali scansioni di controllo, infatti, all'individuo non veniva sottoposto alcun compito specifico, ma veniva semplicemente invitato a pensare liberamente, in maniera spontanea. Un gruppo di ricerca[1], nel 2001, ha condotto uno studio specifico sulla rete neurale attiva in condizioni di riposo, osservando che si disattivava quando si rivolgeva l'attenzione a uno scopo specifico esterno, e hanno dunque nominato quella forma di attività neurale «modalità di default» («*Default mode of brain function*»). Questo studio ha aperto alla ricerca su queste regioni, di cui è stata approfondita sempre più la connettività, la funzionalità e la collocazione anatomica, in particolare dal 2007 in poi[2]. Successivamente, sono state individuate anche altre reti neurali attive in stato di riposo (*resting state networks*, RSN). Si ipotizza una connettività mono-sinaptica a lungo raggio per la rete neurale associata alla *default mode* (Default Mode Network, DMN)[3]. La connettività funzionale del DMN a cui si farà riferimento in seguito è stata originariamente indagata con tecniche di ICA (Independent component analysis) e *seed-based*. Definizioni più recenti del DMN, in realtà, si fondano sulla teoria dei grafi (GT), che permette di ovviare alla specificità nelle connessioni considerate tramite il metodo *seed-based*, tenendo conto dell'integrità del network individuato proprio grazie alla valutazione di metriche small-world, e su modelli di connettività meta-analitici (MACM), che consentono di integrare i dati da diverse rilevazioni, anche di soggetti non a riposo, filtrando i *bias* introdotti dall'eventuale compito specifico (*task*) in cui i vari soggetti considerati potrebbe essere stati impegnati durante la rilevazione.[4]

Il DMN si attiva quando si lascia "vagare la mente" (lit. «*mind-wandering*»), nel pensiero introspettivo - ossia il pensiero su di sé e sui propri stati mentali - e nel pensare a sé in relazione al tempo, come ad esempio

[1] M. E. RAICHLE, A. M. MACLEOD, A. Z. SNYDER, W. J. POWERS, D. A. GUSNARD, G. L. SHULMAN, "A default mode of brain function", in *Proceedings of the National Academy of Sciences*, 98, 2, 2001, pp. 676–682.
[2] J. R. ANDREWS-HANNA, "The Brain's Default Network and Its Adaptive Role in Internal Mentation", in *The Neuroscientist*, 18, 3, 2012, pp. 251–270.
[3] *Ibidem*.
[4] E. SANZ-MORALES, H. MELERO, "Advances in the fMRI analysis of the default mode network: a review" in *Brain Struct Funct*, **230**, 22, 2025.

nell'organizzazione personale per una giornata futura. Il DMN risulta attivo anche durante l'esecuzione di attività dirette allo scopo che richiedono un'elaborazione introspettiva, come ad esempio compiti di relazione autobiografica o di elaborazione concettuale o semantica. Per questa ragione, il DMN suscita particolare interesse anche negli studi relativi alla coscienza umana, sebbene non si abbiano sufficienti conoscenze per determinare chiaramente quale ruolo abbia nella sua insorgenza[5].

1.2. Lo studio di Andrews-Hanna et al. (2010)

Un gruppo guidato da Andrews-Hanna, nel 2010, ha condotto uno studio in tre esperimenti per indagare in maggiore profondità l'organizzazione del DMN[6]. Con il primo esperimento inizialmente hanno individuato 11 regioni cerebrali corrispondenti alle zone di attività del DMN, tramite tecniche *seed-based*[7]. Successivamente hanno indagato la connettività funzionale delle regioni individuate, applicando analisi network e clustering gerarchico. Hanno così individuato nella regione anteromediale della Corteccia Pre-Frontale (aMPFC) e nella Corteccia Cingolata Posteriore (PCC) due hub del network. Hanno anche mostrato l'esistenza di due sottosistemi del DMN: uno associato alla Corteccia Pre-Frontale dorso-mediale (dMPFC) e uno associato al Lobo Temporale Mediale (TML). L'intero network ha comunque mostrato un'elevata connettività globale.

Con il secondo esperimento, hanno messo in evidenza come il sottosistema legato alla dMPFC venga attivato durante la riflessione su di sé nel momento presente, oltre che nel tentativo di interpretare lo stato emotivo altrui, aspetto che apre a speculazioni sull'integrazione del DMN in alcune teorie della coscienza. Il sottosistema legato al TML risulta stimolato dal pensiero episodico di sé nel futuro. Gli hub (aMPFC e PCC) hanno mostrato attività in entrambi i tipi di attività, mostrando sensibilità a stimoli relativi al sé in generale, piuttosto che alla temporalità.

Il terzo esperimento mostra come, in uno stato di riposo totale, in cui gli individui sono invitati ad abbandonarsi al flusso spontaneo del pensiero, senza vincoli, i due sistemi tendono a operare in maniera integrata, e questo suggerisce come il senso del sé e della temporalità siano collegati nella riflessione spontanea, quando non si richiede esplicitamente di considerarli separatamente.

---

[5] A. LUPPI, D. LYU, E. A. STAMATAKIS, "Core of consciousness: the default mode network as nexus of convergence and divergence in the human brain", in *Current Opinion in Behavioral Sciences*, 65, 2025, p. 101545.

[6] J. R. ANDREWS-HANNA, J. S. REIDLER, J. SEPULCRE, R. POULIN, R. L. BUCKNER, "Functional-Anatomic Fractionation of the Brain's Default Network", in *Neuron*, 65, 4, 2010, pp. 550–562.

[7] La metodologia *seed-based* consiste nel selezionare una o più regioni cerebrali di interesse (dette *seed*) e calcolare la correlazione temporale della loro attività (BOLD) con quella di tutte le altre regioni del cervello, al fine di identificare pattern di connettività funzionale.

Considerando la disattivazione delle regioni associate al DMN durante i compiti rivolti a uno scopo, si può avere un'interpretazione funzionale dello stato di «flow»[8] (lett. "flusso"), durante il quale si eseguono attività con una sensazione di totale immersione, come in un automatismo, in cui si riduce la consapevolezza di sé e del tempo. Pare infatti che l'inibizione del DMN nello stato di *flow* sia una risposta evolutiva sviluppatasi per ridurre la consapevolezza di sé durante la prestazione. Questo porterebbe a una minore considerazione delle minacce alla propria persona (fisiche, come in una prestazione sportive, o sociali, come nello svolgimento di un compito intellettuale), e di conseguenza a una maggiore facilità di azione, ulteriormente accentuata da un'elevata attivazione del sistema neurobiologico della ricompensa[9].

1.3 Propositi per questo prototipo di studio

In questo articolo, si propone un prototipo di analisi delle proprietà connettive del DMN e dei suoi due sottosistemi, in maniera analoga a quanto attuato nella seconda parte del primo esperimento dello studio del gruppo di Andrews-Hanna del 2010[10], tramite strumenti e dati *open-source* ad elevata accessibilità. Si precisa che, per la limitatezza degli strumenti impiegati per l'analisi, abbiamo preso in analisi un campione estremamente ridotto (ulteriori dettagli nella sezione II. MATERIALE E METODI). Pertanto, intendiamo questo studio come un *proof of concept* o un'indicazione di prospettive, un prototipo con il quale intendiamo suggerire una via alternativa di indagine, con la piena consapevolezza di non poter presentare conclusioni forti a partire da quanto osservato.

Con tale premessa, dunque, proponiamo l'utilizzo di metodi di analisi network per lo studio dei sottosistemi funzionali del DMN, altrimenti indagati con mezzi di elaborazione statistica nello studio di riferimento. In particolare, ci proponiamo di individuare le regioni cerebrali che risultano appartenere a ciascuno dei due sottosistemi del DMN secondo l'algoritmo di Louvain [11] per l'individuazione di *community* e di determinare quali siano le regioni essenziali per la comunicazione

[8] J. GOLD, J. CIORCIARI, "A neurocognitive model of flow states and the role of cerebellar internal models", in *Behavioural Brain Research*, 407, 2021, p. 113244.
[9] *Ibidem*.
[10] J. R. ANDREWS-HANNA et al., "Functional-Anatomic Fractionation…", cit., pp. 550–562.
[11] L'algoritmo di Louvain è un metodo di ottimizzazione gerarchica della modularità che consente di individuare comunità all'interno di una rete. Funziona in due fasi iterative: nella prima, i nodi vengono assegnati alle comunità massimizzando localmente la variazione di modularità; nella seconda, le comunità individuate vengono compresse in super-nodi, generando una nuova rete su cui ripetere il procedimento. Questo approccio, efficiente anche su grafi di grandi dimensioni, restituisce una suddivisione che bilancia coesione interna e separazione tra comunità.

efficiente sia a livello globale nella rete sia tra i suoi due sottosistemi e in quale misura il DMN stesso e i suoi due sottosistemi possano essere considerati network small-world.

I network small-world presentano caratteristiche "intermedie" tra un reticolo regolare, caratterizzato da elevata coesione locale (ogni nodo è collegato a *n* suoi vicini) ma da percorsi globali molto lunghi, e un grafo random, il quale offre cammini brevi a scapito della coerenza tra vicini. I network small-world, pertanto, presentano alta densità di connessioni all'interno di cluster locali congiuntamente ad alcune "scorciatoie" che riducono drasticamente la distanza media tra qualsiasi coppia di nodi[12]. Questa configurazione ibrida permette di bilanciare segregazione funzionale e integrazione efficiente, rendendo il network capace di elaborare informazioni specializzate a livello locale e al tempo stesso di trasmetterle rapidamente su scala globale. Dimostrare che il DMN possiede queste caratteristiche significa dimostrare che la rete unisce specializzazione e cooperazione: ogni sottoinsieme di regioni mantiene un forte legame reciproco senza sacrificare la rapidità con cui le informazioni possono attraversare l'intero network.

Tale equilibrio small-world potrebbe spiegare la capacità del DMN di supportare localmente diversi processi cognitivi evoluti — dall'auto-riflessività alla simulazione mentale di stati altrui — e di integrarli in modo efficiente segnali tra centri cerebrali distanti.

Conducendo l'analisi con una parcellazione delle regioni del network in 46 regioni, intendiamo proporre l'osservazione degli effetti di una maggiore risoluzione parcellare rispetto a quanto ottenuto dal gruppo di Andrews-Hanna nel 2010[13] con una parcellazione a 11 regioni.

II. MATERIALE E METODI

2.1 Materiale

In questo studio abbiamo condotto un'analisi funzionale connettiva del DMN tramite analisi network. Le scansioni impiegate per l'analisi sono state reperite tramite la piattaforma OpenNeuro. In particolare, sono state selezionati i dati relativi a tre *run* di tre soggetti distinti (una *run* per ciascun soggetto, per un totale complessivo di tre *run*)[14] dal dataset ds004787[15]. Pur non offrendo descrizioni

[12] D. J. WATTS, S. H. STROGATZ, "Collective dynamics of 'small-world' networks", in *Nature*, 393, 6684, 1998, pp. 440–442.

[13] J. R. ANDREWS-HANNA et al., "Functional-Anatomic Fractionation…", cit., pp. 550–562.

[14] Il riferimento specifico alle *run* selezionate è disponibile all'interno della cartella allegata all'articolo, che contiene anche il listato impiegato per l'elaborazione dei dati.

[15] D. NIELSON, A. ZUGMAN, M. ZELENINA, D. PINE, *NIMH METeR (Multi-Echo Test-Retest)*, 2023.

più accurate, gli autori delle scansioni dichiarano che le *run* fornite sono state eseguite su soggetti a riposo.

I dati sono stati elaborati in python tramite l'utilizzo delle librerie Nibabel[16], Nilearn[17] e NetworkX[18]. Il programma e i dati utilizzati per questo studio possono essere forniti dall'autore su richiesta.

2.2 Elaborazione dei dati

Innanzitutto, per ciascuna *run*, abbiamo integrato i dati da ciascuna delle quattro *echo*, tramite la libreria Nibabel, con una procedura del tutto equivalente a una semplice media ponderata dei valori, la quale consente una prima riduzione del rumore. Abbiamo poi integrato i dati di ciascuna delle tre *run* in regioni funzionali secondo l'atlante Schaefer 2018 a 200 regioni, codificato nella libreria Nilearn. Da tale organizzazione, abbiamo estratto soltanto le serie temporali delle 46 regioni[19] già categorizzate come appartenenti al DMN nell'atlante stesso (Fig. 1). Per ciascuna regione dell'atlante, abbiamo considerato come valore di attivazione in ogni istante il valore medio dell'attivazione nel dato istante di tutte le sezioni che la compongono (il cui valore è registrato dalla scansione). Abbiamo successivamente estratto la matrice di correlazione funzionale relativa all'attivazione delle regioni del DMN. Abbiamo dunque ricavato un grafo interpretando la matrice di correlazione come una matrice di adiacenza pesata, tramite una funzione di NetworkX.

Abbiamo proceduto al calcolo della *betweenness centrality* di ogni regione, indice che rappresenta la frazione di cammini minimi tra coppie di altre regioni che passano per la regione in esame[20]. In altre parole, la *betwenness centrality* è una misura dell'essenzialità della regione per la massima efficacia nella trasmissione dell'informazione nella rete. La funzione di NetworkX che calcola la *betweenness centrality*[21], nel calcolare i cammini minimi, interpreta il peso associato all'arco come una distanza.

---

[16] NIBABEL CONTRIBUTORS, *nibabel*, 2024. (doi: 10.5281/zenodo.13936989)

[17] NILEARN CONTRIBUTORS, *nilearn*, s.d. (doi: https://doi.org/10.5281/zenodo.8397156)

[18] A. A. HAGBERG, D. A. SCHULT, P. J. SWART, "Exploring Network Structure, Dynamics, and Function using NetworkX", in *Proceedings of the 7th Python in Science Conference*, 2008, pp. 11–15.

[19] Per una visualizzazione che consenta di individuare ciascuna regione, si rimanda a un programma realizzato allo scopo, inserito nella cartella allegata all'articolo.

[20] Più rigorosamente, la *betweenness centrality* di un nodo v è definita come la somma, per tutte le coppie di nodi distinti s, t del rapporto fra il numero di cammini minimi che collegano s e t passando per v ($\sigma_{st}(v)$) e il numero totale di cammini minimi fra s e t (σ_{st}): $C_B(v) = \sum_{s \neq v \neq t} \frac{\sigma_{st}(v)}{\sigma_{st}}$.

[21] Per ulteriori dettagli sulla funzione, si consulti il link https://networkx.org/documentation/stable/reference/algorithms/generated/networkx.algorithms.centrality.betweenness_centrality.html.

Siccome, nel nostro modello, tanto più è alto il peso associato ad un arco, tanto più i due nodi sono associati e lo scambio di informazione tra i due è favorito, abbiamo calcolato la *betweenness centrality* associando a ciascun arco un peso pari a $w_i' = 1 - w_i$ per i soli $w_i > 0$, in cui w_i è l'indice di correlazione funzionale tra le due regioni (peso nel grafo originale), dunque per le sole regioni la cui interazione è eccitatoria, e si osserva dunque co-attivazione.

Abbiamo sono altresì individuato le regioni componenti di ciascun sottosistema del DMN, tramite l'algoritmo di Louvain per l'individuazione di comunità[22], e le regioni che fungono da ponte principale per lo scambio di informazioni tra le community individuate, tramite il calcolo della *betweenness centrality* tra subset (una *betweenness centrality* che prende cioè in considerazione soltanto i cammini minimi in cui punto di partenza e punto di arrivo appartengono a subset dati, nel nostro caso le community individuate, tramite una funzione della libreria NetworkX[23]).

Infine, abbiamo indagate le proprietà *small-world* del DMN e di ciascuno dei suoi due sottosistemi. In particolare, cioè, per il grafo del DMN e per ciascuno dei due sotto-grafi abbiamo ricavato delle versioni "sogliate", in cui, cioè, si sono considerati soltanto gli archi con peso (coefficiente di correlazione) maggiore di 0.1: in questo modo abbiamo escluso le connessioni più deboli, che non sono sufficientemente stabili nel tempo per essere considerate collegamenti fissi. Abbiamo selezionato il valore di 0.1 in quanto risulta il massimo valore di sogliatura per il quale i grafi di tutti e tre i soggetti risultano completamente connessi, dunque il massimo valore per il quale risulta possibile una successiva analisi small-world. Su tali grafi abbiamo poi calcolato:

- Il coefficiente di clustering medio (C), che rappresenta quanto, in una scala tra 0 e 1 il grafo sia completamente connesso[24];

[22] V. D. BLONDEL, J.-L. GUILLAUME, R. LAMBIOTTE, E. LEFEBVRE, "Fast unfolding of communities in large networks", in *Journal of Statistical Mechanics: Theory and Experiment*, 2008, 10, p. P10008.

[23] Per ulteriori dettagli sulla funzione, si consulti il link https://networkx.org/documentation/stable/reference/algorithms/generated/networkx.algorithms.centrality.betweenness_centrality_subset.html

[24] Più rigorosamente, il coefficiente di clustering medio (C) è definito come la media dei coefficienti di clustering locali C_i dei nodi della rete, con: $C_i = \frac{2E_1}{k_i\,(k_i - 1)}$, dove k_i è il grado del nodo i ed E_i è il numero di archi effettivamente presenti tra i vicini di i.

- Cammino minimo medio (L), la lunghezza media dei cammini più brevi che collegano ogni coppia di nodi del grafo, e quantifica l'efficienza globale della rete nel trasmettere informazioni tra le sue componenti[25].

In un grafo completamente connesso, il cammino minimo medio è esattamente 1; mentre è proporzionale al logaritmo del numero di nodi in un grafo casuale alla Erdos-Renyi, il che porta comunque a valori piccoli rispetto al numero di nodi. In effetti, i grafi small-world possono essere intesi come "intermedi" tra grafi casuali e grafi completamente connessi o regolari[26]. Detti C_{rand} e L_{rand} rispettivamente il coefficiente di clustering medio e il cammino minimo medio di un grafo casuale con lo stesso numero di nodi e grado medio del grafo in oggetto e C_{latt} il coefficiente di clustering medio di un grafo regolare con stesso numero di nodi e grado medio), per quantificare il livello di *small-worldness*, abbiamo impiegato i parametri $\sigma = \frac{\frac{C}{C_{rand}}}{\frac{L}{L_{rand}}}$ e $\omega = \frac{L_{rand}}{L} - \frac{C}{C_{latt}}$, calcolati tramite le funzioni della libreria Networkx. Il primo indice può assumere valori positivi, e valori maggiori di 1 indicano small-worldness. Il secondo può assumere valori compresi tra -1 per grafici regolari e 1 per grafici casuali: tanto più il suo valore si approssima a 0, tanto più il grafo ha proprietà *small-world*.

Infine, abbiamo riportato le regioni che, distintamente, per tutti i tre soggetti sono risultate:

- Hub dell'intera rete;
- Appartenenti alla stessa comunità;
- Hub tra le comunità.

III. RISULTATI

3.1 Estrazione del DMN

Le regioni individuate come appartenenti al DMN hanno le seguenti denominazioni nell'atlante Schaefer 2018[16]:

[25] Più rigorosamente, il cammino minimo medio (L) è la media della lunghezza $d(i, j)$ dei cammini minimi tra tutte le coppie di nodi i, j della rete: $L = \frac{1}{N(N-1)} \sum_{i \neq j} d(i, j)$, dove N è il numero dei nodi e $d(i, j)$ indica la distanza fra i e j nella rete pesata secondo $w_{ij}' = 1 - w_{ij}$ in cui w_{ij} è l'indice di correlazione tra le regioni i e j.

[26] D. J. WATTS, S. H. STROGATZ, "Collective dynamics of 'small-world' networks", cit., pp. 440–442.

- Regioni temporali:
    - L-Temp_1, L-Temp_2, L-Temp_3, L-Temp_4, L-Temp_5, R-Temp_1, R-Temp_2, R-Temp_3, R-Temp_4, R-Temp_5;
- Regioni parietali:
    - L-Par_1, L-Par_2, L-Par_3, L-Par_4, R-Par_1, R-Par_2, R-Par_3;
- Regioni della corteccia pre-frontale:
    - L-PFC_1, L-PFC_2, L-PFC_3, L-PFC_4, L-PFC_5, L-PFC_6, L-PFC_7, L-PFC_8, L-PFC_9, L-PFC_10, L-PFC_11, L-PFC_12, L-PFC_13, R-PFCv_1;
    - R-PFCdPFCm_1, R-PFCdPFCm_2, R-PFCdPFCm_3, R-PFCdPFCm_4, R-PFCdPFCm_5, R-PFCdPFCm_6, R-PFCdPFCm_7 (corteccia frontale dorsomediale);
- Regioni del precuneo e corteccia cingolata posteriore:
    - L-pCunPCC_1, L-pCunPCC_2, L-pCunPCC_3, L-pCunPCC_4, R-pCunPCC_1, RpCunPCC_2, R-pCunPCC_3;
- Giro paraippocampale:
    - L-PHC_1.

La procedura di associazione tra regioni dell'atlante e dati fMRI forniti è andata a buon fine per ciascun soggetto.

Una visualizzazione sommaria di alcune regioni del DMN individuate in ciascun soggetto è fornita Fig. 1. Si osservi che per tutti i tre soggetti la mappa risulta completa in queste regioni (come in realtà nelle altre non mostrate), a indicare la buona risuscita della procedura di sovrapposizione della "maschera" dell'atlante sui dati fMRI utilizzati.

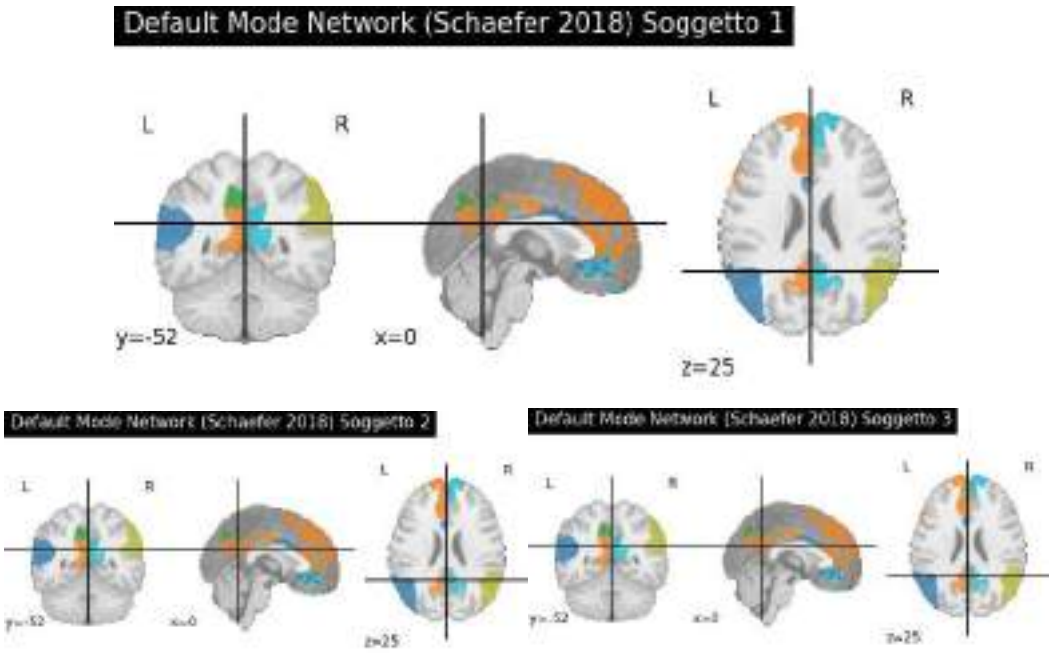

Fig. 1 – Sezioni del cervello comprendenti regioni del DMN (sono stati individuati dati di attività funzionale per ciascuna regione fornita dall'atlante, perciò le regioni visualizzate sono le stesse per tutti e tre i soggetti).

	Soggetto 1	Soggetto 2	Soggetto 3
Community dMPFC	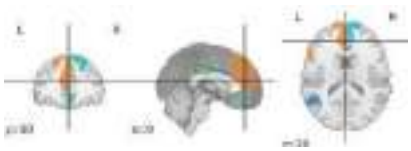	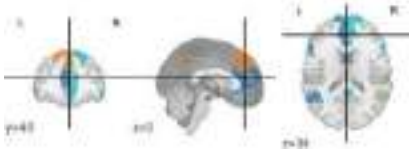	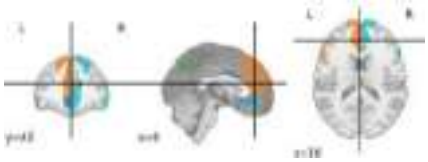
Community TML	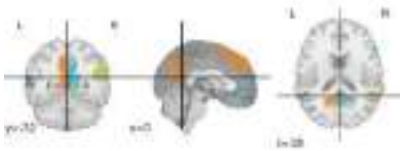	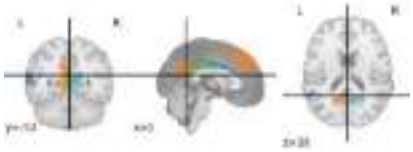	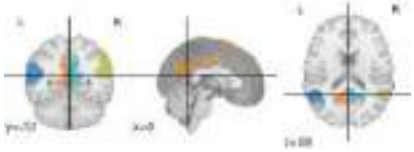

3.2 Estrazione delle *Community*

Tabella 1- rappresentazione di sezioni significative di ciascuna community per ciascun soggetto.

Si riportano i risultati dell'estrazione di community tramite l'algoritmo di Louvain. L'identificazione delle due community in *Community dMPFC e Community TML*, riportata in Tabella 2, è stata fatta per analogia con la nomenclatura utilizzata dal gruppo di Andrews-Hanna nello studio di riferimento[27]. Per una rappresentazione tramite immagini delle regioni individuate per ciascun soggetto, si veda la Tabella 1. Si veda sotto per un elenco delle regioni che sono risultate appartenenti a una delle due community nell'analisi dei dati di tutti e tre i soggetti.

Community dMPFC	Community TML
L-PFC_12, R-PFCdPFCm_4, R-PFCdPFCm_7, L-PFC_6, R-PFCdPFCm_6, L-PFC_7, L-PFC_4, R-PFCdPFCm_2, L-PFC_8, L-PFC_11, R-Par_2, R-PFCdPFCm_5, L-PFC_9	L-PFC_2, L-Par_1, L-Temp_3, R-pCunPCC_2, L-pCunPCC_3, L-pCunPCC_2, L-Temp_2, R-pCunPCC_1, L-Par_3, L-pCunPCC_1

Tabella 2 – Regioni che sono risultate appartenere alla stessa community per tutti i soggetti analizzati

3.3 Valori di Centralità

Nessuna regione è risultata essere un hub per l'intera rete o semplicemente di connessione tra le due community in tutti e tre i soggetti.

A scopo esemplificativo, si riportano nella Tabella 3 le regioni che sono risultate hub per il primo soggetto, con i relativi valori di *betweenness centrality*. Nelle Fig. 2 e Fig. 3, le rappresentazioni grafiche (ottenute tramite un algoritmo di *sping layout* fornito dalla libreria NetworkX) del DMN del soggetto 1, rispettivamente senza e con sogliatura.

[27] J. R. ANDREWS-HANNA et al., "Functional-Anatomic Fractionation…", cit., pp. 550–562.

Hubs dell'intero DMN – Soggetto 1	Hubs di collegamento tra i sottosistemi – Soggetto 1
L-pCunPCC_3: 0.019	L-pCunPCC_3: 0.010
L-PFC_8: 0.012	L-PFC_8: 0.006
L-Par_1: 0.011	L-Par_1: 0.006
L-PFC_2: 0.009	L-PFC_2: 0.005
R-PFCv_1: 0.005	R-PFCv_1: 0.003
L-PFC_1: 0.004	L-PFC_1: 0.002
R-PFCdPFCm_3: 0.004	R-PFCdPFCm_3: 0.002
L-PFC_3: 0.003	R-Par_2: 0.002
R-Par_2: 0.003	R-Temp_5: 0.002
R-Temp_5: 0.003	R-PFCdPFCm_1: 0.001
R-PFCdPFCm_1: 0.002	L-PFC_7: 0.001
L-PFC_7: 0.001	L-PFC_10: 0.001
L-PFC_10: 0.001	R-pCunPCC_1: 0.001
R-pCunPCC_1: 0.001	

Tabella 3 – Regioni che sono risultate hub per tutta la rete indistintamente e hub principali di collegamento tra le due sezioni per il Soggetto 1, con associati i relativi valori di betweenness centrality standardizzata.

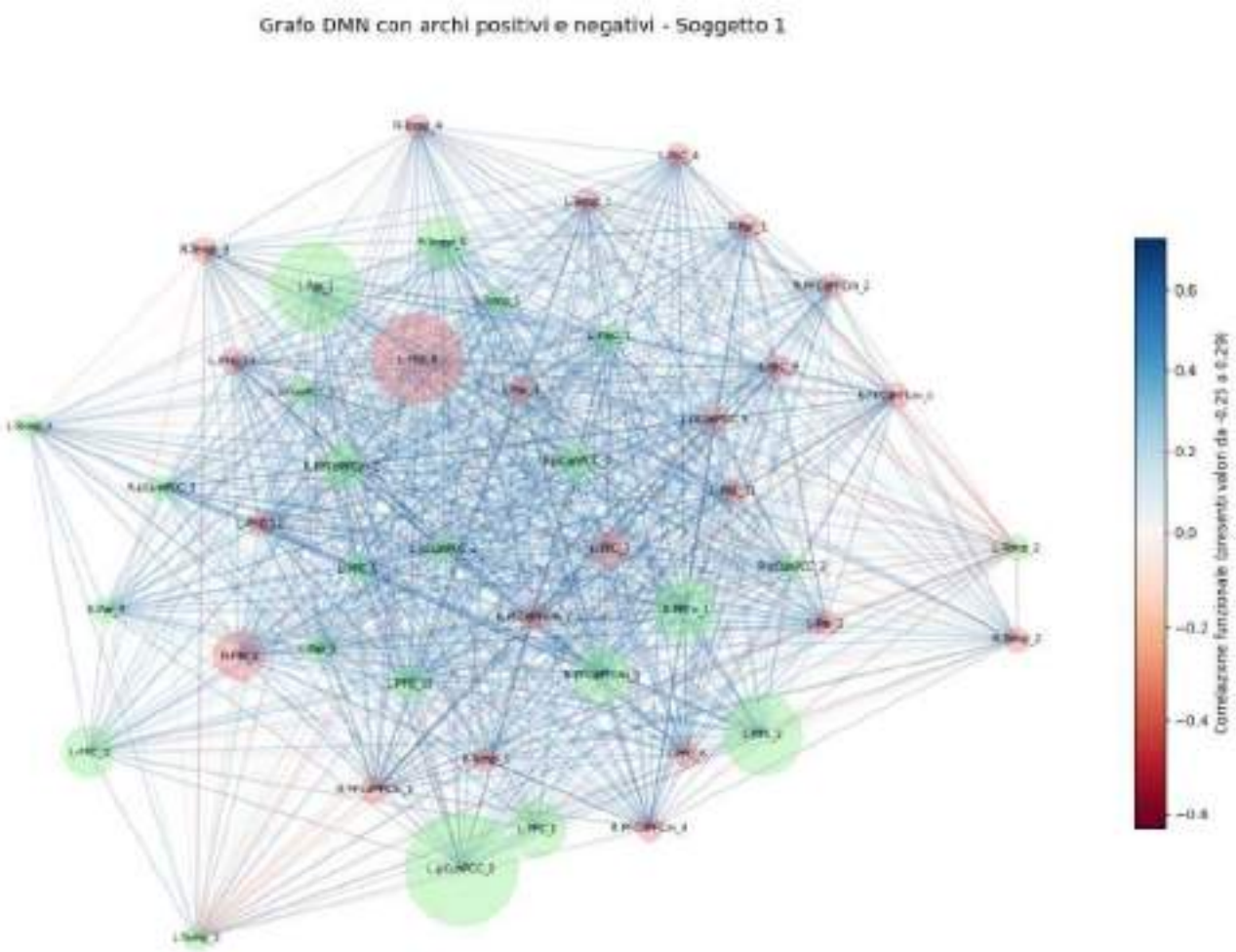

Fig. 2 – Grafo del DMN del soggetto 1, rappresentato con algoritmo spring layout. Gli archi con pesi positivi (in blu) rappresentano una correlazione funzionale positiva, quelli con pesi negativi una negativa. La dimensione di ogni nodo è determinata da una funzione lineare crescente della betweenness centrality. I nodi colorati in rosa appartengono alla comunità dMPFC, quelli colorati in verde alla TML.

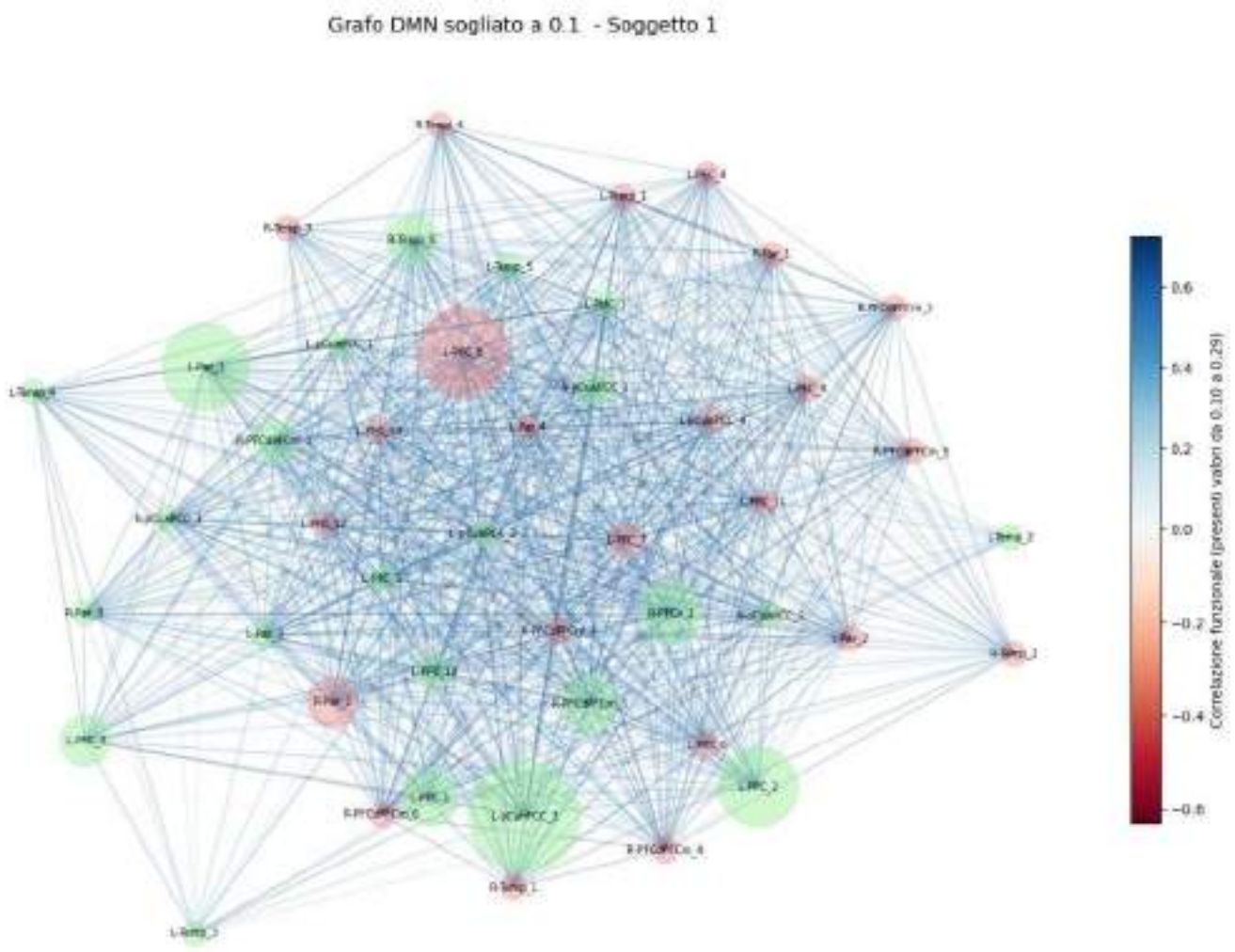

Fig. 3 - Grafo del DMN del soggetto 1, sogliato al valore di 0.1, rappresentato con algoritmo spring layout. Sono stati esclusi gli archi con valore di correlazione inferiore a quello di soglia fissato a 0.1, perché fossero messe in evidenza le attivazioni simultanee più stabili. La dimensione di ogni nodo è determinata da una funzione lineare crescente della *betweenness centrality*. I nodi colorati in rosa appartengono alla comunità dMPFC, quelli colorati in verde alla TML.

3.4 Analisi *small-world*

Si riportano nella Tabella 4 i valori relativi all'analisi small-world per il grafo e i sottosistemi per ciascun soggetto.

	Soggetto 1	Soggetto 2	Soggetto 3
DMN	Coefficiente di clustering: 0.898 Cammino minimo medio: 1.202 σ: 1.030 ω: -0.006	Coefficiente di clustering: 0.906 Cammino minimo medio: 1.169 σ: 1.025 ω: 0.000	Coefficiente di clustering: 0.928 Cammino minimo medio: 1.149 σ: 1.010 ω: -0.003
Community dMPFC	Coefficiente di clustering: 0.959 Cammino minimo medio: 1.067 σ: 1.004 ω: 0.000	Coefficiente di clustering: 0.991 Cammino minimo medio: 1.009 σ: 1.000 ω: -0.000	Coefficiente di clustering: 0.966 Cammino minimo medio: 1.047 σ: 1.000 ω: 0.000
Community TML	Coefficiente di clustering: 1.000 Cammino minimo medio: 1.000 σ: 1.000 ω: 0.000	Coefficiente di clustering: 0.981 Cammino minimo medio: 1.021 σ: 1.000 ω: -0.000	Coefficiente di clustering: 0.997 Cammino minimo medio: 1.003 σ: 1.000 ω: 0.000

Tabella 4 – Valori relative all'analisi small world per il DMN e ciascuna sua community per ciascun soggetto

IV. DISCUSSIONE

4.1 Osservazione critica dei risultati

L'individuazione delle regioni appartenenti alla Default Mode Network (DMN) è avvenuta con successo, confermando la validità del processo di analisi condotto sul dataset selezionato, per quanto ridotto. Le community rilevate mediante l'algoritmo di Louvain mostrano una buona corrispondenza con i sottosistemi associati alle regioni dMPFC e TML, già evidenziati nello studio di riferimento[28] e noti rispettivamente anche come DMN anteriore (aDMN) e posteriore (pDMN). Le regioni

[28] *Ivi*.

rappresentate nella Tabella 1, che risultano appartenere alla medesima community in tutti e tre i soggetti analizzati, possono essere considerate le più rappresentative dei due sottosistemi.

Non sono emersi nodi che fungano da hub in modo sistematico tra tutti i soggetti, sebbene se ne siano individuati alcuni per ciascun soggetto, e alcuni risultassero comuni a due dei tre soggetti. Questo dato si discosta da quanto osservato dal gruppo di Andrews-Hanna[29], dove l'impiego di una parcellazione in 11 regioni ha portato all'individuazione di hub condivisi, a differenza della parcellazione in 46 regioni utilizzata in questo prototipo di studio. Un'ipotesi ragionevole, che a nostro avviso meriterebbe approfondimento, è che una maggiore risoluzione parcellare potrebbe far emergere connessioni dirette tra regioni di dimensioni ridotte, altrimenti aggregate in macroaree, evidenziando legami che appaiono deboli a una scala più grossolana, perché temporalmente attivi per intervalli ridotti rispetto a quelli di attivazione simultanea di altre aree di dimensione maggiore. Così tali relazioni non sarebbero prese in considerazione nel calcolo dei cammini minimi tra coppie di regioni, portando alla conclusione fuorviante che l'informazione segua preferenzialmente cammini mediati da regioni "ponte". Tale fenomeno sarebbe compatibile con l'esistenza di connessioni mono-sinaptiche a lungo raggio, come riportato nello studio di Andrews-Hanna del 2012[30]. A questo proposito, uno studio del 2013[31] ha indagato proprio quale sia la risoluzione parcellare più adeguata al fine di garantire la massima omogeneità nell'attivazione funzionale di ciascuna regione. Integrando i dati di diverse scansioni fMRI, tramite tecniche di analisi network, gli autori hanno ricavato atlanti dell'intero cervello a 100, 200 e 300 regioni dall'elevata coerenza e applicabilità generale. D'altra parte, una parcellazione più fine di quella a 300 regioni è risultata critica in quanto la risoluzione consentita dallo scanner a 3T e dagli algoritmi di imaging da loro impiegati non consentivano una risoluzione migliore di quella ottenuta, con voxel di lato 3mm.Ad ogni modo, da recenti *review*[32], non risulta essere consolidata la pratica di un impiego di una risoluzione parcellare a più di 11-17 regioni per il DMN, in favore di una più agevole identificazione delle regioni.

Un'altra interpretazione possibile riguarda la variabilità soggettiva nelle connessioni funzionali, suggerita anche dalla distribuzione non perfettamente sovrapponibile delle regioni tra i due

[29] *Ibidem*.
[30] J. R. ANDREWS-HANNA, "The Brain's Default Network…", cit., pp. 251–270.
[31] X. SHEN, F. TOKOGLU, X. PAPADEMETRIS, R.T. CONSTABLE, "Groupwise whole-brain parcellation from restingstate fMRI data for network node identification" in *Neuroimage*, 15, 82, 2013, pp. 403-415.
[32] A. LUPPI, D. LYU, E. A. STAMATAKIS, "Core of consciousness…", cit., p.101545; E. SANZ-MORALES, H. MELERO, "Advances in the fMRI analysis…", cit.

sottosistemi nei diversi soggetti: diverse forme di pensiero, di soggettività, potrebbero derivare dall'attivazione simultanea di regioni diverse allo stesso stimolo, portando a diverse forme di elaborazione dell'esperienza, comunque entro gli schemi comuni, riconducibili ai collegamenti comuni riscontrati tra i soggetti. Infatti, si osserva in tutti i casi un nucleo centrale condiviso all'interno di ciascun sottosistema, confermando la presenza di una struttura funzionale comune, seppur parzialmente modulata da caratteristiche individuali.

Dal punto di vista delle proprietà topologiche della rete, l'analisi suggerisce che il DMN, così come i suoi sottosistemi, possiedano caratteristiche riconducibili a una rete small-world, nonostante presentino un cammino minimo medio prossimo a quello di una più banale rete completamente connessa. Sebbene i valori dell'indice σ si collochino in prossimità della soglia critica ($\sigma \approx 1$), introducendo una certa ambiguità interpretativa, l'indice ω fornisce indicazioni più affidabili: i valori prossimi allo zero suggeriscono una chiara tendenza small-world, sia a livello dell'intera rete DMN che dei suoi due sottosistemi considerati separatamente. Va tuttavia ricordato che l'indice σ, non confrontando esplicitamente il grafo con una controparte regolare, non consente da solo una valutazione esaustiva, rendendo necessario un approccio integrato per interpretare esaustivamente la struttura della rete. Una più solida individuazione delle caratteristiche small-world del DMN, già ampiamente attuata da numerosi studi[33] - per quanto a risoluzioni parcellari inferiori – ha aperto a profonde interpretazioni delle proprietà di connettività funzionale. Una tale configurazione topologica, infatti, consentendo una trasmissione rapida e una comunicazione efficace tra regioni anche distanti, favorisce l'integrazione di grandi moli di informazioni, quali i contenuti interni complessi che portano ai modelli individuali dell'io e agli stati mentali autoriferiti, nonché alla coscienza stessa, secondo la teoria dell'*Integrated Information* (IIT)[34]. Questo risulterebbe compatibile con la presenza di hub caratterizzati da valori di centralità estremamente ridotti, come quelli osservati nel presente studio, suggerendo che l'efficienza della rete non dipenda necessariamente dalla centralità di pochi nodi dominanti, ma piuttosto da una distribuzione bilanciata dei collegamenti, in linea con quanto ipotizzato da Watts e Strogatz in riferimento sia alla corteccia visiva, sia alla rete neurale del nematode *C. Elegans*[35].

[33] B. ZHANG, S. LIU, S. CHEN, X. LIU, Y. KE, S. QI, X. WEI, D. MING, "Disrupted small-world architecture and altered default mode network topology of brain functional network in college students with subclinical depression" in *BMC Psychiatry*. 25, 1, 2025, p. 193

[34] A. LUPPI, D. LYU, E. A. STAMATAKIS, "Core of consciousness…", cit., p. 101545

[35] D. J. WATTS, S. H. STROGATZ, "Collective dynamics of 'small-world' networks", cit., pp. 440–442.

Le proprietà small-world dell'intera rete forniscono un'interpretazione funzionale di alto livello per la tendenza spontanea del DMN ad attivarsi simultaneamente, integrando in maniera variabile le funzioni di ponderazione sul sé presente, sul sé futuro e di inferenza dello stato mentale altrui, come osservato nel terzo esperimento del gruppo di Andrews-Hanna[36]. Le forti proprietà small-world delle due "sottoreti" e il loro costituire *community* separate (aDMN e pDMN), d'altra parte, corrispondono pienamente alla tendenza osservata all'attivazione in forma preferenzialmente distinta delle due diverse macroaree in processi mentali differenti, in risposta a stimoli distinti, come osservato nel secondo esperimento.

4.2 Limiti e possibili sviluppi di questo studio

Come già segnalato, questo studio ha integrato una quantità estremamente limitata di dati, tra l'altro non generati specificamente per lo scopo, e ha impiegato strumenti *open-source* ad alta accessibilità per l'analisi. Per questo lo si propone come un *prototipo* di studio. I pochi dati presi in analisi non permettono di trarre conclusioni generali. I dati di fMRI funzionale utilizzati non sono associati al tipo di "attività" a riposo attuata dal soggetto. Si assume che il soggetto sia stato invitato a pensare in maniera spontanea, che secondo quanto ricavato nelle osservazioni relative al terzo esperimento dello studio di riferimento[37], dovrebbe portare a un'attivazione complessiva del DMN. Tuttavia, non avendo informazioni più dettagliate sullo stato del soggetto, non abbiamo garanzia che l'attivazione fosse bilanciata tra le due comunità, e che non siano rimaste inespresse eventuali connessioni tra i due sottosistemi.

Perciò, si auspica che un futuro studio su questi aspetti ricavi i dati da scansioni realizzate per lo scopo. Strumenti di analisi più sofisticati, inoltre, potrebbero permettere di ridurre al minimo il rumore, e ad integrare in maniera più efficace le informazioni tra tutti i soggetti presi in analisi. In questo studio, infatti, si sono integrate le diverse *echo* di ogni *run* tramite una semplice media ponderata sui tempi di eco (che consente un compromesso tra la sensibilità al segnale BOLD e al rumore), mentre un software più raffinato potrebbe ottenere un segnale pulito in maniera più accurata. Una valutazione accurata del rapporto segnale-rumore (SNR) dei dati forniti potrebbe dare informazioni sull'opportunità o meno di una risoluzione parcellare fine come quella scelta o più. Un confronto dei risultati ottenuti con dati surrogati potrebbe fornire ulteriori indicazioni sulla significatività e generalità di quanto osservato. Inoltre, per considerare le regioni risultate parte dello stesso sottosistema, o le regioni hub, in questo

[36] J. R. ANDREWS-HANNA et al., "Functional-Anatomic Fractionation…", cit., pp. 550–562. [37] *Ibidem*.

studio abbiamo semplicemente considerato l'intersezione degli insiemi individuati per ciascun soggetto, mentre per un dataset più ampio si dovrà mettere a punto un algoritmo di integrazione più complesso, che escluda eventuali casi estremali.

In ogni caso, la descrizione del DMN come network, in particolare come network small-world, può aprire a ulteriori indagini sulle proprietà connettive di ciascuna sua regione (scelto l'adeguato livello di finezza parcellare), fornendo nuove ipotesi sui percorsi di integrazione dell'informazione.

Ci auguriamo che, in ragione della sua semplicità concettuale, l'elevata accessibilità dell'analisi qui condotta sia di stimolo ad altri per condurne una più rigorosa per discutere le ipotesi che abbiamo avanzato a conclusioni di carattere generale.

CONCLUSIONI

L'analisi esplorativa condotta sulla Default Mode Network (DMN), mediante una parcellazione a risoluzione più fine rispetto a quella adottata nello studio del 2010 del gruppo di Andrews-Hanna[37], ha permesso di individuare, attraverso l'algoritmo di Louvain, i nuclei funzionali dei due sottosistemi associati rispettivamente alla corteccia prefrontale dorso-mediale (dMPFC) e al lobo temporale mediale (TML). Tuttavia, a differenza dello studio di riferimento, non sono emerse regioni che svolgano sistematicamente la funzione di hub o che rappresentino punti di collegamento stabili tra i due sottosistemi nei diversi soggetti analizzati. Questo risultato, unito alla variabilità nella composizione dei sottosistemi stessi tra i partecipanti, pone l'accento sulla necessità di ulteriori approfondimenti basati su dati raccolti *ad hoc*, strumenti di analisi più avanzati e campioni più estesi, al fine di valutare con maggiore affidabilità la stabilità e la generalizzabilità delle configurazioni osservate. In ogni caso, però, i risultati ottenuti mostrano che il DMN e i suoi sottosistemi esibiscono una topologia small-world: da un lato conservano cluster locali coesi, dall'altro introducono alcune "scorciatoie" che riducono drasticamente la distanza media tra aree distanti. Tale configurazione ibrida giustifica l'elevata efficienza funzionale osservata nel sistema, anche in assenza di hub con betweenness centrality predominante, perché è proprio l'equilibrio tra segregazione locale e integrazione globale a favorire una circolazione dell'informazione rapida e robusta, piuttosto che il ruolo ponte di alcune regioni che fungerebbero da zone di integrazione dell'informazione. Secondo quanto osservato, cioè, l'informazione sarebbe integrata, a vario livello, in quasi tutte le regioni del DMN, e non solo in alcune zone ponte. La comparsa di community distinte, che si attivano durante

[37] 38 *Ivi*.

processi mentali differenti indica comunque una specializzazione funzionale di alcune aree e la combinazione preferenziale di alcuni processi. Tuttavia, l'elevata variabilità inter-soggettiva e intrasoggettiva (a livello temporale) dei cammini di collegamento tra le varie aree pare aprire a più complesse possibilità di integrazione delle funzioni cerebrali al livello del DMN e di ciascuno dei suoi due sottosistemi.

Alla luce di questi riscontri, auspichiamo che studi futuri conducano un'analisi sistematica dell'effetto della finezza della parcellazione delle aree del DMN sull'osservazione di regioni a elevata centralità. Un simile approfondimento permetterebbe di stabilire se la riduzione degli hub osservata in questo studio rifletta un mero effetto metodologico o, al contrario, il manifestarsi genuino di un'organizzazione small-world nel DMN al livello di piccole regioni. In tal modo si potrebbero collocare le nostre osservazioni in un quadro teorico più esteso che descriva il bilanciamento tra modularità locale e comparsa di scorciatoie globali su differenti scale. A tale scopo, questo studio potrebbe suggerire la validità di un approccio tramite analisi network come valida alternativa al metodo statistico impiegato nello studio di riferimento di Andrews-Hanna.

Nonostante i limiti intrinseci di un'analisi basata su dati e strumenti *open-source* ad alta accessibilità, questo studio propone una semplice esplorazione delle capacità di integrazione dell'informazione e attivazione simultanea spontanea che caratterizzano il DMN. Queste proprietà risultano centrali in processi "mentali" estremamente complessi e raffinati, che quindi richiedono differenti e variabili forme di rielaborazione dell'informazione, come la costruzione del sé, la percezione degli stati mentali interni e la comprensione inferenziale di quelli altrui, funzioni che costituiscono il nucleo dell'esperienza soggettiva della realtà.

BIBLIOGRAFIA

ANDREWS-HANNA J. R., “The Brain’s Default Network and Its Adaptive Role in Internal Mentation”, in *The Neuroscientist*, 18, 3, 2012, pp. 251–270.

ANDREWS-HANNA J. R., REIDLER J. S., SEPULCRE J., POULIN R., BUCKNER R. L., “Functional-Anatomic Fractionation of the Brain’s Default Network”, in *Neuron*, 65, 4, 2010, pp. 550–562.

BLONDEL V. D., GUILLAUME J.-L., LAMBIOTTE R., LEFEBVRE E., “Fast unfolding of communities in large networks”, in *Journal of Statistical Mechanics: Theory and Experiment*, 2008, 10, p. P10008.

GOLD J., CIORCIARI J., “A neurocognitive model of flow states and the role of cerebellar internal models”, in *Behavioural Brain Research*, 407, 2021, p. 113244.

HAGBERG A. A., SCHULT D. A., SWART P. J., “Exploring Network Structure, Dynamics, and Function using NetworkX”, 2008, pp. 11–15.

LUPPI A., LYU D., STAMATAKIS E. A., “Core of consciousness: the default mode network as nexus of convergence and divergence in the human brain”, in *Current Opinion in Behavioral Sciences*, 65, 2025, p. 101545

NIBABEL CONTRIBUTORS, “nibabel”, 2024. (doi: 10.5281/zenodo.13936989)

NIELSON D., ZUGMAN A., ZELENINA M., PINE D., “NIMH METeR (Multi-Echo Test-Retest)”, 2023.

NILEARN CONTRIBUTORS, “nilearn”, s.d. (doi: https://doi.org/10.5281/zenodo.8397156)

RAICHLE M. E., MACLEOD A. M., SNYDER A. Z., POWERS W. J., GUSNARD D. A., SHULMAN G. L., “A default mode of brain function”, in *Proceedings of the National Academy of Sciences*, 98, 2, 2001, pp. 676–682.

SANZ-MORALES E., MELERO H., “Advances in the fMRI analysis of the default mode network: a review” in *Brain Struct Funct*, 230, 22, 2025.

SHEN X., TOKOGLU F., PAPADEMETRIS X., CONSTABLE R.T. “Groupwise whole-brain parcellation from resting-state fMRI data for network node identification” in *Neuroimage,* 15, 82, 2013, pp. 403-415

WATTS D. J., STROGATZ S. H., “Collective dynamics of ‘small-world’ networks”, in *Nature*, 393, 6684, 1998, pp. 440–442.

ZHANG B., LIU S., CHEN S., LIU X., KE Y., QI S., WEI X., MING D., “Disrupted small-world architecture and altered default mode network topology of brain functional network in college students with subclinical depression” in *BMC Psychiatry*. 25, 1, 2025, p. 193